

# UC Irvine

## UC Irvine Electronic Theses and Dissertations

### Title

Understanding NO<sub>3</sub> oxidation of monoterpenes at different scales: Insights from molecular modeling, chamber experiments, and field observations

### Permalink

<https://escholarship.org/uc/item/4z06s084>

### Author

Draper, Danielle

### Publication Date

2021

Peer reviewed|Thesis/dissertation

UNIVERSITY OF CALIFORNIA,  
IRVINE

Understanding NO<sub>3</sub> oxidation of monoterpenes at different scales: Insights from molecular modeling, chamber experiments, and field observations

DISSERTATION

submitted in partial satisfaction of the requirements  
for the degree of

DOCTOR OF PHILOSOPHY

in Chemistry

by

Danielle Catherine Draper

Dissertation Committee:  
Professor James N. Smith, Chair  
Associate Professor Ann Marie G. Carlton  
Professor Barbara J. Finlayson-Pitts

2021



# DEDICATION

To all my teachers who have expanded my mind in weird directions

...

...

...

and all of the cats.

# TABLE OF CONTENTS

	Page
<b>LIST OF FIGURES</b>	<b>vi</b>
<b>LIST OF SCHEMES</b>	<b>ix</b>
<b>LIST OF TABLES</b>	<b>xi</b>
<b>ACKNOWLEDGMENTS</b>	<b>xii</b>
<b>CURRICULUM VITAE</b>	<b>xiv</b>
<b>ABSTRACT OF THE DISSERTATION</b>	<b>xx</b>
<b>1 Introduction</b>	<b>1</b>
1.1 Background . . . . .	1
1.1.1 Precursors . . . . .	4
1.1.2 Ambient observations . . . . .	10
1.1.3 SOA yields . . . . .	12
1.1.4 Gas-phase oxidation mechanisms . . . . .	14
1.1.5 New particle formation & growth . . . . .	18
1.2 Research goals . . . . .	21
1.3 General Methods . . . . .	23
1.3.1 Theoretical Approach . . . . .	23
1.3.2 Experimental approach . . . . .	27
1.3.3 Instrumentation . . . . .	29
1.4 Overview of Dissertation . . . . .	31
<b>2 Exploring the diversity of monoterpene oxidation via computational comparison of nitroxy-alkyl and nitroxy-alkoxy radical bond scissions</b>	<b>34</b>
2.1 Abstract . . . . .	35
2.2 Introduction . . . . .	35
2.3 Methods . . . . .	38
2.4 Results & Discussion . . . . .	41
2.4.1 Nitroxy alkyl radical ring opening reactions . . . . .	41
2.4.2 Nitroxy alkoxy radical $\beta$ -scission reactions . . . . .	44
2.4.3 Proposed fate of each monoterpene . . . . .	47

2.5	Conclusions . . . . .	57
<b>3</b>	<b>Formation of Highly Oxidized Molecules from NO<sub>3</sub> Radical Initiated Oxidation of <math>\Delta</math>-3-Carene: A Mechanistic Study</b>	<b>60</b>
3.1	Abstract . . . . .	61
3.2	Introduction . . . . .	62
3.3	Methods . . . . .	67
3.3.1	Computational . . . . .	67
3.3.2	Experimental . . . . .	70
3.4	Results & Discussion . . . . .	71
3.4.1	Derived Reaction Mechanism . . . . .	71
3.4.2	RO <sub>2</sub> Fate . . . . .	72
3.4.3	RO <sub>2</sub> H-shifts . . . . .	74
3.4.4	RO <sub>2</sub> Ring Closing . . . . .	76
3.4.5	RO Fate . . . . .	76
3.4.6	Computational Summary . . . . .	79
3.4.7	Chamber Experiments . . . . .	80
3.4.8	Implications for SOA Formation . . . . .	82
3.5	Conclusions . . . . .	83
<b>4</b>	<b>Observations of semi-volatile organonitrates in nanoparticles in the boreal atmosphere</b>	<b>85</b>
4.1	Abstract . . . . .	86
4.2	Introduction . . . . .	86
4.3	Methods . . . . .	88
4.3.1	Description of Field Site . . . . .	88
4.3.2	Instrumentation . . . . .	88
4.3.3	Gas / Particle Partitioning Analysis . . . . .	90
4.3.4	Calculations . . . . .	91
4.4	Results . . . . .	93
4.4.1	TDCIMS Ambient Observations . . . . .	93
4.5	Discussion . . . . .	97
4.5.1	Proposed Mechanism . . . . .	97
4.5.2	Partitioning Modeling . . . . .	102
4.5.3	Alternative Mechanisms . . . . .	109
4.6	Conclusions . . . . .	111
4.7	Ongoing & Future Work . . . . .	112
<b>5</b>	<b>Conclusions</b>	<b>114</b>
5.1	Future Directions . . . . .	115
	<b>Bibliography</b>	<b>117</b>
	<b>Appendix A Abstract for Dummies</b>	<b>137</b>

<b>Appendix B Supplementary Information for Chapter 3</b>	<b>138</b>
B.1 Computational . . . . .	138
B.2 Experimental . . . . .	146
B.3 NO <sub>3</sub> <sup>-</sup> Clustering Calculations . . . . .	150
B.4 Estimated vapor pressures . . . . .	151

# LIST OF FIGURES

	Page
1.1 Modeled global emission rates for speciated monoterpenes. Estimates of emissions in Tg yr <sup>-1</sup> (out of 1089 Tg yr <sup>-1</sup> total non-methane BVOC) [64] . . . . .	7
1.2 Regional emissions percentages of six different monoterpenes in the US. Image adapted from Geron et al. (2000) [59] . . . . .	8
1.3 Diurnal profiles of NO <sub>2</sub> and total monoterpene concentrations from two forested locations. BEACHON-RoMBAS data from Fry et al. (2013) [55] and SOAS data from Ayres et al. (2015) [9]. . . . .	9
1.4 Mass percentage of organic nitrate in ambient submicron organic aerosol, shown in blue, measured at different locations in North America and Europe. Image reproduced from Ng et al. (2017) [124]. . . . .	12
1.5 General VOC oxidation schematic, highlighting potential closed-shell products. Image reproduced from Ziemann et al. (2012) [180] . . . . .	16
1.6 Schematic of RO <sub>2</sub> H-shift, or “autoxidation” reactions. Image reproduced from Crouse et al. (2013) [27]. . . . .	17
1.7 Schematic highlighting the processes that occur during nucleation, including the typical chemical composition and size range for each stage. J <sub>1.5</sub> and J <sub>3</sub> are the nucleation rates of 1.5 and 3 nm particles, respectively. Image reproduced from Kulmala et al. 2013 [91]. . . . .	19
1.8 Schematic showing possible particle mass accommodation processes. Image reproduced from Smith et al. 2021 [154] . . . . .	20
1.9 Illustration of the likely shift in composition of nanoparticles as they grow from 1-100 nm. Image reproduced from Ehn et al. (2014) [39]. . . . .	21
1.10 Potential energy diagram showing reactant (R), transition state (TS), and product (P). . . . .	25
1.11 Generic ion-molecule clustering reaction scheme . . . . .	26
1.12 Schematic of the reaction chamber and associated suite of instrumentation. . . . .	29
1.13 Sectional view of the TDCIMS inlet (Image by J.N. Smith). . . . .	31
1.14 Overview schematic highlighting the reactions and processes explored in this work. Chapter 2 shown in red surveys first generation alkyl and alkoxy radical fates for several cyclic monoterpenes. Chapter 3 shown in blue explores the unimolecular reaction pathways available to second generation peroxy and alkoxy radicals from Δ-3-carene. Chapter 4 shown in green considers gas-to-particle conversion processes to explain observations of ambient nanoparticle composition. . . . .	33



2.1	Overview schematic: Chapter 2 focuses on the first generation alkyl radical and alkoxy radical fates for seven cyclic monoterpenes. . . . .	34
2.2	Molecular structures of nitroxy-alkoxy stereoisomers of limonene, $\alpha$ -thujene, sabinene, $\beta$ -pinene, and camphene assessed in this study. . . . .	39
2.3	Zero-point corrected energy diagram calculated at the $\omega$ B97X-D/aug-cc-pVTZ level (a) and species time evolution profile from MESMER simulation at 298.15 K and 760 Torr (b) comparing the sabinene + $\text{NO}_3$ alkyl ring-opening reaction vs. $\text{O}_2$ addition . . . . .	44
2.4	Reaction labeling scheme for nitroxy-alkoxy scission reactions. Rate constants were calculated for the “right” and “left” C–C scissions for endocyclic monoterpenes and for the “right,” “left,” and “top” C–C scissions for exocyclic monoterpenes with all molecules drawn in comparable orientation, as shown in Figure 2.2 above.. . . .	45
3.1	Overview schematic: Chapter 3 explores the second generation peroxy radical and alkoxy radical unimolecular reactions available to $\Delta$ -3-carene following $\text{NO}_3$ oxidation. . . . .	60
3.2	(a) Structures of $\alpha$ -pinene and $\Delta$ -3-carene highlighting the secondary rings in red to show the only structural variation between the two prevalent monoterpenes, and (b) the general oxidation scheme of $\text{NO}_3$ oxidation of volatile organic compounds (VOCs) in the atmosphere. We note that not all pathways are available to all VOCs and some pathways may only become available for later generations of chemistry. . . . .	64
3.3	Schematic showing the RO scission of $\alpha$ -pinene + $\text{NO}_3$ mechanism (black) compared to $\Delta$ -3-carene + $\text{NO}_3$ mechanism (red), comparing scission of the right (top) or left (bottom) C–C bond. The dashed arrow for the left scission of the $\alpha$ -pinene RO indicates this reaction is not expected to be competitive with the right scission due to the unfavorability of the alkyl radical on the strained ring. All other reactions (solid arrows) are expected to occur with an approximate 50/50 branching for the two $\Delta$ -3-carene RO pathways [94]. . . . .	65
3.4	(a) Radical end points from $\Delta$ -3-carene + $\text{NO}_3$ mechanism in Kurtén et al. (2017), which comprise our reactants in this study with the hydrogens investigated in this study labeled and color-coded to differentiate Reactant 1 and Reactant 2, and (b) schematic showing types of rearrangement reactions included in this study. . . . .	66
3.5	(a) Monomer region of average mass spectrum from $\Delta$ -3-carene + $\text{NO}_3$ chamber experiment with structures for highest intensity peaks consistent with computational mechanism. M/z values reflect $\text{NO}_3^-$ adducts (M ( $\text{NO}_3^-$ )) as detected, and labeled peaks reflect the product (M) alone. $\text{C}_7\text{H}_{11}\text{NO}_8$ was not included in the mechanism in this study but is expected to be a third generation product related to $\text{C}_7\text{H}_{10}\text{NO}_6$ . (b) Time series of the five highest intensity observed peaks as well as $\text{C}_7\text{H}_{11}\text{NO}_6$ as it is the closed-shell product of one of our explicitly calculated intermediates. (c) Dimer region of mass spectrum with highest intensity peak formulas labeled. . . . .	81

4.1	Overview schematic: Chapter 4 assesses gas-to-particle partitioning from probable $\text{NO}_3$ oxidation of monoterpenes based on ambient nanoparticle composition measurements. . . . .	85
4.2	Ambient aerosol size distribution ( $\text{dN}/\text{dlogDp}$ ), showing particle sizes collected for TDCIMS analysis. Darker markers show volume median diameter of collected particles assessed by direct measurements. Crosses represent the range of particle sizes composing 90% of the total collected mass. . . . .	94
4.3	TDCIMS-derived average daytime (a) and nighttime (b) mass spectra. Lower plot (c) shows the difference spectrum of nighttime - daytime and highlights the species that dominate nanoparticle composition during each period. . . . .	95
4.4	Time series of $\text{C}_{10}\text{H}_{15}\text{O}_2^-$ and $\text{C}_{10}\text{H}_{17}\text{O}_2^-$ from TDCIMS measurements of nanoparticle composition. . . . .	96
4.5	Supporting measurements of $[\text{O}_3]$ , $[\text{NO}_2]$ , estimated concentrations of $\alpha$ -pinene (see text), $\text{PM}_{2.5}$ , temperature, and photosynthetically active radiation during the observation period, plotted along with the time series of $\text{C}_{10}\text{H}_{15}\text{O}_2^-$ and $\text{C}_{10}\text{H}_{17}\text{O}_2^-$ . . . . .	98
4.6	Mechanism for $\text{NO}_3$ initiated oxidation of $\alpha$ -pinene. Shaded compounds are key intermediates that are discussed in the text and shown again in Figure 4.7. . . . .	99
4.7	Proposed steps that demonstrate the formation of observed ions from key organonitrate precursors show in Figure 4.6. Calculated EA are shown for observed ions as well as minor ions. . . . .	101
4.8	Calculated steady state $\text{NO}_3$ radical time series, overlayed on photosynthetically active radiation (PAR) data to indicate daylight. . . . .	103
4.9	The calculated instantaneous and cumulative time series for the $\alpha$ -pinene-derived hydroxynitrate product during the observation period. . . . .	105
4.10	Estimated vapor pressures for the ketonitrate product ( $\text{C}_{10}\text{H}_{15}\text{NO}_4$ ) and the hydroxynitrate product ( $\text{C}_{10}\text{H}_{17}\text{NO}_4$ ) using COSMOtherm and SIMPOL.1. . . . .	107
4.11	Modeled fraction that each compound contributes to the total particle-phase overlayed with the TDCIMS data represented as fraction of total ion signal. . . . .	108

## LIST OF SCHEMES

	Page
2.1 Ring opening radical rearrangement reactions for nitroxy-alkyl radicals from bicyclic monoterpenes . . . . .	43
2.2 Proposed fate of limonene + NO <sub>3</sub> beginning from the 1 <sup>st</sup> -generation nitroxy-alkoxy radical outlined in black. Bold arrows show the $\beta$ -scission reactions studied here, including calculated, stereoisomer-averaged branching ratios. Dashed boxes indicate selected products observed experimentally. . . . .	49
2.3 Proposed fate of $\alpha$ -thujene + NO <sub>3</sub> beginning from the 1 <sup>st</sup> -generation nitroxy-alkyl radical. The 1 <sup>st</sup> -generation nitroxy-alkoxy radical is outlined in black. Bold arrows show the reactions studied here, including calculated, stereoisomer-averaged branching ratios. Dashed boxes indicate predicted major product channels. . . . .	51
2.4 Proposed fate of sabinene + NO <sub>3</sub> beginning from the 1 <sup>st</sup> -generation nitroxy-alkyl radical. The 1 <sup>st</sup> -generation nitroxy-alkoxy radical is outlined in black. Bold arrows show the reactions studied here, including calculated, stereoisomer-averaged branching ratios. Dashed boxes indicate predicted major product channels. . . . .	52
2.5 Proposed fate of $\beta$ -pinene + NO <sub>3</sub> beginning from the 1 <sup>st</sup> -generation nitroxy-alkyl radical. The 1 <sup>st</sup> -generation nitroxy-alkoxy radical is outlined in black. Bold arrows show the reactions studied here, including calculated, stereoisomer-averaged branching ratios. Dashed boxes indicate predicted major product channels. . . . .	54
2.6 Proposed fate of camphene + NO <sub>3</sub> beginning from the 1 <sup>st</sup> -generation nitroxy-alkyl radical. The 1 <sup>st</sup> -generation nitroxy-alkoxy radical is outlined in black. Bold arrows show the reactions studied here, including calculated, stereoisomer-averaged branching ratios. Dashed boxes indicate predicted major product channels. . . . .	56
2.7 1 <sup>st</sup> -generation mechanism proposed in Kurtén et al. [94] for $\alpha$ -pinene + NO <sub>3</sub> beginning from the 1 <sup>st</sup> -generation nitroxy-alkyl radical. The 1 <sup>st</sup> -generation nitroxy-alkoxy radical is outlined in black. Bold arrows show the reactions corresponding to those studied here, including calculated, stereoisomer-averaged branching ratios. Dashed boxes indicate predicted major product channels. . . . .	57

2.8	1 <sup>st</sup> -generation mechanism proposed in Kurtén et al. [94] for $\Delta$ -3-carene + NO <sub>3</sub> beginning from the 1 <sup>st</sup> -generation nitroxy-alkyl radical. The 1 <sup>st</sup> -generation nitroxy-alkoxy radical is outlined in black. Bold arrows show the reactions corresponding to those studied here, including calculated, stereoisomer-averaged branching ratios. Dashed boxes indicate predicted major product channels. .	58
3.1	Summary of dominant pathways in $\Delta$ -3-carene+ NO <sub>3</sub> mechanism. Black structures and arrows indicate reactions inferred from literature, culminating in the radical endpoints in Kurtén et al. [94] which serve as the “reactants” in this study. Green and purple structures and arrows indicate reactions calculated in this study originating from Reactant 1 and Reactant 2, respectively. For complete mechanism, including all pathways assessed in this study, refer to Scheme B.1. . . . .	73

# LIST OF TABLES

	Page
1.1 Lifetimes of prevalent cyclic monoterpenes with respect to OH, NO <sub>3</sub> , and O <sub>3</sub> , assuming “typical” oxidant concentrations of: [OH] = 2.0 × 10 <sup>6</sup> molec cm <sup>-3</sup> (12 hr daytime avg); [NO <sub>3</sub> ] = 5.0 × 10 <sup>8</sup> molec cm <sup>-3</sup> (~20 ppt) (12 hr nighttime avg); [O <sub>3</sub> ] = 7.0 × 10 <sup>11</sup> molec cm <sup>-3</sup> (~30 ppb) (24 hr avg). Rate constants and average concentrations from Atkinson & Arey 2003 [7]. . . . .	10
1.2 Yields of SOA and oxidation products from monoterpene + NO <sub>3</sub> chamber studies. Compiled data from Ng et al. (2017) [124]. . . . .	15
2.1 Barriers (zero-point corrected transition state - reactant electronic energy) and Multi-Conformer Transition State Theory (MC-TST) rate constants calculated at the ωB97X-D/aug-cc-pVTZ level for alkoxy β-scission reactions at 298.15 K. . . . .	46
3.1 Barriers and LC-TST Rate Constants <sup>a</sup> . . . . .	72
3.2 Barriers and LC-TST Rate Constants <sup>a</sup> . . . . .	74

# ACKNOWLEDGMENTS

Financial support for this work was provided by NSF Grant AGS-1762098, NSF Graduate Research Fellowship Grant DGE-1321846, and an NSF GROW travel grant.

The body of work discussed in this dissertation would not have been possible without the help of a number of fantastic co-authors. Chapter 2 includes significant contributions from Thomas Almeida, Nanna Myllys, Jim Smith, and Theo Kurtén, with Thomas in particular performing approximately half of the calculations shown. The text in Chapter 3 of this dissertation is a reprint of the material as it appears in *ACS Earth & Space Chemistry* and includes contributions from Nanna Myllys, Noora Hyttinen, Kristian Møller, Henrik Kjaergaard, Julie Fry, Jim Smith, and Theo Kurtén. And last but not least, Mike Lawler, Theo Kurtén, and Jim Smith all contributed to the work discussed in Chapter 4, for which Mike made the measurements and provided significant analysis support.

On a personal level, this work would not have been possible without the support of many teachers, colleagues, friends, family, and cats. I am grateful for a number of past teachers who have shaped my trajectory through academia. My middle school science teacher Mr. Walsh, who introduced me to the inquisitive and creative side of science, and my high school chemistry teacher Mr. Cook, who showed me how fun chemistry itself can be, thereby significantly influencing my college trajectory later on. Ms. Knake steered me on a sharp left turn, igniting a love for history and research-based writing that has certainly immensely benefited my science writing. The incredible chemistry faculty at Reed College, especially Arthur Glasfeld, Maggie Geselbracht, and Julie Fry clinched my decision to actually major in chemistry, and Julie Fry has played a monumental role in shaping my career trajectory. She sparked my excitement for atmospheric chemistry nearly ten years ago and has continued to be a phenomenal mentor, colleague, and friend ever since.

I am grateful that Jim and I made our way to UCI around the same time and I was able to be his first graduate student. His mentorship encouraged so much freedom to explore the scientific trajectories I found most interesting and gave me the incredible opportunity to be able to propose questions and lead collaborative efforts to answer them. Through combination of his research interests and appreciation for the value of students getting exposure to varied research experiences, I was extremely lucky to be able to travel frequently and work with multiple different groups of collaborators. This travel included the HISCALE campaign in Oklahoma, the CLOUD10 campaign at CERN, and numerous trips to Finland to learn how to be a computational chemist. During these Finland trips, I gained another fantastic mentor in Theo Kurtén. I am forever amazed by his unwavering enthusiasm, support, and confidence in his students, and I am hopeful we will continue to have opportunities to work together in the coming years.

It was so fun to help shape the Ultrafine Aerosol group and watch how it evolved as we grew to critical mass. Tuija, I very much appreciated your camaraderie in the first couple of years. Mike, Sabrina, Hayley, Deanna, Lia, and Adam, I adore everyone's unique quiriness, and I will miss our late night conversations, excursions to musicals, and investment in blind Jelly

Belly flavor identification, among other things. I am thrilled to have been able to brainwash Lia into being as excited about  $\text{NO}_3$  + monoterpene oxidation as I am. And I am so happy to have been able to be a part of the AirUCI community as a whole.

And then of course there are all the people (and cats) who helped keep me sane through all these years. Excellent roommates like Caitlin, Genia, and Veronica. Myself. Trapeze friends around the country. Support from several amazing women scientists. And surely many many more people. Thank you for helping me reach the finish line.

# CURRICULUM VITAE

Danielle Catherine Draper

## EDUCATION

**Doctor of Philosophy in Chemistry** **2021**  
University of California, Irvine *Irvine, California*

**Bachelor of Arts in Chemistry** **2013**  
Reed College *Portland, Oregon*

## RESEARCH EXPERIENCE

**Graduate Student Researcher** **2015–2020**  
University of California, Irvine *Irvine, California*

**Visiting Researcher** **2017–2018**  
University of Helsinki *Helsinki, Finland*

**Post-Baccalaureate Research Assistant** **2013–2014**  
Reed College *Portland, Oregon*

**Undergraduate Research Assistant** **2011–2013**  
Reed College *Portland, Oregon*

## TEACHING EXPERIENCE

**Tutor** **2018-present**  
High school level chemistry and physics  
Middle school level math and science  
Intelligentsia, Inc. *Los Angeles, California*

**Teaching Assistant** **2014-2015**  
General Chemistry 1LC, 1B discussion, 1C discussion  
University of California, Irvine *Irvine, California*



## SERVICE OUTREACH

<b>Co-organizer</b> <i>Near-Peer Mentoring Program: UCI &amp; Reed College</i>	<b>2019</b> <i>Irvine, California</i>
<b>Co-founder &amp; Co-organizer</b> <i>AirUCI Internal Symposium</i>	<b>2018-2019</b> <i>Irvine, California</i>
<b>ACS Climate Science Educator Volunteer</b> <i>Oregon Museum of Science and Industry</i>	<b>2013 &amp; 2014</b> <i>Portland, Oregon</i>
<b>Choreographer / Director / Dancer</b> <i>Dance Performance of Chemistry Undergraduate Thesis</i>	<b>2013</b> <i>Portland, Oregon</i>

## PUBLICATIONS (*italicized entries in preparation or submitted*)

19. *D. C. Draper, M. J. Lawler, J. N. Smith [et al.], "Observations of semi-volatile organonitrates in nanoparticles in the boreal atmosphere," in prep. 2020.*
18. *D. C. Draper, T. G. Almeida, N. Myllys, J. N. Smith, T. Kurtén, "Calculation of favorable alkoxy scission pathways for cyclic monoterpenes," in prep. 2020.*
17. J. N. Smith, D. C. Draper; S. Chee; M. Dam; H. Glicker; D. Myers; A. E. Thomas; M. J. Lawler; N. Myllys, "Atmospheric clusters to nanoparticles: Recent progress and challenges in closing the gap in chemical composition," *Journal of Aerosol Science*, accepted 2020.
16. M. Simon, et al. [CLOUD Consortium including **D. C. Draper**], "Molecular understanding of new particle formation from  $\alpha$ -pinene between  $-50$  and  $+25$  °C," *Atmos. Chem. Phys.*, 20, 9183-9207, August 2020.
15. C. Yan, et al. [CLOUD Consortium including **D. C. Draper**], "Size-dependent influence of  $\text{NO}_x$  on the growth rates of organic aerosol particles," *Sci. Adv.*, May 2020.
14. M. J. Lawler, **D. C. Draper**, J. N. Smith, "Atmospheric Fungal Nanoparticle Bursts," *Sci. Adv.*, January 2020.
13. **D. C. Draper**, N. Myllys, N. Hyttinen, K. H. Møller, H. G. Kjaergaard, J. L. Fry, J. N. Smith, T. Kurtén, "Formation of Highly Oxidized Molecules from  $\text{NO}_3$  Radical Initiated Oxidation of  $\Delta$ -3-carene: A Mechanistic Study," *ACS Earth and Space Chem.*, July 2019.
12. K. Lehtipalo, et al. [CLOUD Consortium including **D. C. Draper**], "Multicomponent new particle formation from sulfuric acid, ammonia, and biogenic vapors," *Sci. Adv.*, December 2018.

11. D. Stolzenburg, et al. [CLOUD Consortium including **D. C. Draper**], "Rapid growth of organic aerosol nanoparticles over a wide tropospheric temperature range," *Proc. Natl. Acad. Sci.*, August 2018.
10. N. M. Kreisberg, S. R. Spielman, A. Eiguren-Fernandez, S. V. Hering, M. J. Lawler, **D. C. Draper**, J. N. Smith, "Water-Condensation Based Nano-Particle Charging System: Physical and Chemical Characterization," *Aerosol Sci. and Tech.*, September 2018.
9. R. Wagner, et al. [CLOUD Consortium including **D. C. Draper**], "The role of ions in new particle formation in the CLOUD chamber," *Atmos. Chem. Phys.*, 17, 15181-15197, December 2017.
8. B. B. Palm, P. Campuzano-Jost, D. A. Day, A. M. Ortega, J. L. Fry, S. S. Brown, K. J. Zarzana, W. Dube, N. L. Wagner, **D. C. Draper**, L. Kaser, W. Jud, T. Karl, A. Hansel, C. Gutiérrez Montes, and J. L. Jimenez, "Secondary organic aerosol formation from in situ OH, O<sub>3</sub>, and NO<sub>3</sub> oxidation of ambient forest air in an oxidation flow reactor," *Atmos. Chem. Phys.*, 17, 5331-5354, April 2017.
7. P. S. Romer, K. C. Duffey, P. J. Wooldridge, H. M. Allen, B. R. Ayres, S. S. Brown, W. H. Brune, J. D. Crouse, J. DeGouw, **D. C. Draper**, P. Feiner, J. L. Fry, A. H. Goldstein, A. Koss, P. K. Misztal, T. B. Nguyen, K. Olson, A. P. Teng, P. O. Wennberg, R. J. Wild., L. Zhang, R. C. Cohen. "The lifetime of nitrogen oxides in an isoprene dominated forest," *Atmos. Chem. Phys.*, 16, 7623-7637, June 2016.
6. B. R. Ayres, H. M. Allen, **D. C. Draper**, S. S. Brown, R. J. Wild, J. L. Jimenez, D. A. Day, P. Campuzano Jost, W. Hu, J. de Gouw, A. Koss, R. C. Cohen, K. C. Duffey, P. Romer, K. Baumann, E. Edgerton, S. Takahama, J. A. Thornton, B. H. Lee, F. D. Lopez-Hilfiker, C. Mohr, A. H. Goldstein, K. Olson, and J. L. Fry, "Organic nitrate aerosol formation via NO<sub>3</sub> + biogenic volatile organic compounds in the southeastern United States," *Atmos. Chem. Phys.*, 15, 13377-13392, December 2015.
5. **D. C. Draper**, D. K. Farmer, Y. Desyaterik, J. L. Fry, "A qualitative comparison of secondary organic aerosol (SOA) yields and composition from ozonolysis of monoterpenes at varying concentrations of NO<sub>2</sub>," *Atmos. Chem. Phys.*, 15, 12267-12281, November 2015.
4. H. M. Allen, **D. C. Draper**, B. R. Ayres, A. Ault, A. Bondy, S. Takahama, R. L. Modini, K. Baumann, E. Edgerton, C. Knote, A. Laskin, B. Wang, and J. L. Fry, "Influence of crustal dust and sea spray supermicron particle concentrations and acidity on inorganic NO<sub>3</sub> aerosol during the 2013 Southern Oxidant and Aerosol Study," *Atmos. Chem. Phys.*, 15, 10669-10685, September 2015.
3. R. A. Washenfelder, A. R. Attwood, C. A. Brock, H. Guo, L. Xu, R. J. Weber, N. L. Ng, H. M. Allen, B. R. Ayres, K. Baumann, R. C. Cohen, **D. C. Draper**, K. C. Duffey, E. Edgerton, J. L. Fry, W. W. Hu, J. L. Jimenez, B. B. Palm, P. Romer, E. A. Stone, P. J. Wooldridge, and S. S. Brown, "Biomass burning dominates brown carbon

absorption in the rural southeastern United States," *Geophys. Res. Lett.*, 42, 653-664 January 2015.

2. J. L. Fry, **D. C. Draper**, K. C. Barsanti, J. N. Smith, J. Ortega, P. M. Winkler, M. J. Lawler, S. S. Brown, P. M. Edwards, R. C. Cohen, L. Lee, "Secondary Organic Aerosol Formation and Organic Nitrate Yield from NO<sub>3</sub> Oxidation of Biogenic Hydrocarbons," *Environ. Sci. Technol.*, 48, 11944-11953, September 2014.
1. J. L. Fry, **D. C. Draper**, K. J. Zarzana, P. Campuzano-Jost, D. A. Day, J. L. Jimenez, S. S. Brown, R. C. Cohen, L. Kaser, A. Hansel, L. Cappelin, T. Karl, A. Hodzic Roux, A. Turnipseed, C. Cantrell, B. L. Lefer, and N. Grossberg, "Observations of gas- and aerosol-phase organic nitrates at BEACHON-RoMBAS 2011," *Atmos. Chem. Phys.*, 13, 8585-8605, Sept. 2013.

## PRESENTATIONS (\* indicates talk, otherwise poster)

23. \***D. C. Draper**, T. G. Almeida, M. Dam, N. Myllys, T. Kurten, J. N. Smith, "Unlumping monoterpenes: Identification of unique first-generation oxidation pathways for the most prevalent cyclic monoterpenes," Atmospheric Chemical Mechanisms Conference (virtual), November 10, 2020.
22. \***D. C. Draper**, T. G. Almeida, M. Dam, N. Myllys, T. Kurten, J. N. Smith, "First-generation alkyl and alkoxy radical fates foreshadow SOA yields from cyclic monoterpenes," American Association for Aerosol Research Fall Meeting (virtual), October 8, 2020.
21. \***D. C. Draper**, M. L. Dam, "Using CIMS to help constrain organic oxidation mechanism development," ToF-CIMS Users Meeting, virtual meeting hosted by University of Helsinki, May 14, 2020.
20. \***D. C. Draper**, "Contribution of Semivolatile Organonitrates to Nanoparticles in the Boreal Forest: Questioning My Assumptions and Testing a Hypothesis," AirUCI Internal Symposium, Irvine, CA, November 21, 2019.
19. \***D. C. Draper**, N. Myllys, N. Hyttinen, K. H. Møller, H. G. Kjaergaard, J. L. Fry, J. N. Smith, T. Kurtén, M. J. Lawler, M. Dam, "My Quest to Understand SOA Formation Growth from NO<sub>3</sub> Radical Oxidation of Monoterpenes," Wennberg group meeting, Caltech, Pasadena, CA, November 1, 2019.
18. **D. C. Draper**, M. J. Lawler, T. Kurtén, J. N. Smith, "Assessing the Contribution of NO<sub>3</sub> Radical Chemistry to Nanoparticle Composition in the Boreal Atmosphere," American Association for Aerosol Research Fall Meeting, Portland, OR, October 2019.
17. \***D. C. Draper**, "Formation of Highly Oxidized Molecules from NO<sub>3</sub> Radical Oxidation of  $\Delta$ -3-Carene: A Computational Mechanism," Atmospheric Chemistry Mechanisms Conference, Davis, CA, December 6, 2018; AirUCI Internal Symposium, January 31, 2019.

16. \***D. C. Draper**, "In pursuit of highly oxidized molecules (HOMs) from NO<sub>3</sub> oxidation of Δ-3-carene," AirUCI retreat, Lake Arrowhead, CA, September 25, 2018.
15. J. N. Smith, J. L. Fry, T. Kurtén, **D. C. Draper** "Atmospheric Nanoparticle Growth from NO<sub>3</sub> Radical Initiated Oxidation of Monoterpenes," NSF-ATC and NCAR Atmospheric Chemistry Workshop, Boulder, CO, May 30-31, 2018. (*made poster, not in attendance*)
14. \***D. C. Draper**, "In pursuit of HOMs from NO<sub>3</sub> oxidation of Δ-3-carene, Part II: Honing a likely mechanism," CopenHel group meeting, University of Copenhagen, Denmark, May 17, 2018.
13. \***D. C. Draper**, "Making a case for NO<sub>3</sub> radical: impacts on SOA formation," University of Oulu Prisle group meeting, Finland, November 24, 2017. (*Invited*)
12. \***D. C. Draper**, "In pursuit of ELVOCs from NO<sub>3</sub> oxidation of Δ-3-carene," CopenHel group meeting, University of Helsinki, Finland, November 7, 2017.
11. \***D. C. Draper**, M. Lawler, J. Smith, "Influence of NO<sub>x</sub> on nanoparticle composition during CLOUD10: TDCIMS measurements," CLOUD data workshop meeting, Bad Zurzach, Switzerland, January 31, 2017.
10. **D. C. Draper**, M. J. Lawler, J. N. Smith, CLOUD consortium "Observation of particle-phase NO<sub>y</sub> and SO<sub>x</sub> species during nanoparticle growth events at CLOUD10," American Association for Aerosol Research Fall Meeting, Portland, OR, October 17 – 21, 2016. (*Poster award recipient*)
9. \***D. C. Draper**, M. Lawler, J. Smith, "Status of TDCIMS data from CLOUD10," CLOUD data workshop meeting, Hyytil, Finland, February 1, 2016.
8. \***D. C. Draper**, M. Lawler, J. Smith, "TDCIMS update," Collaboration Meeting for CLOUD Consortium, CERN, October 21, 2015.
7. **D. C. Draper**, D. K. Farmer, Y. Desyaterik, J. N. Smith, J. L. Fry, "Comparison of NO<sub>2</sub> Effects on Secondary Organic Aerosol (SOA) Formation from Ozonolysis of Four Monoterpenes," American Association for Aerosol Research Fall Meeting, Minneapolis, MN, October 12-16, 2015. (*Poster award recipient*)
6. \***D. C. Draper**, "Nighttime effects of NO<sub>2</sub> on secondary organic aerosol (SOA) formation," University of Washington Thornton group meeting, January 24, 2014; Reed College Chemistry Department Seminar, March 14, 2013.
5. B. R. Ayres, **D. C. Draper**, H. Allen, J. L. Fry, R. Wild, S. S. Brown, A. Koss, J. A. De Gouw, K. F. Olson, A. H. Goldstein, K. Baumann, E. Edgerton, "Reactive nitrogen fate in the southeastern U.S.: Preliminary results from the SOAS campaign," American Geophysical Union Fall Meeting, San Francisco, CA, December 9-13, 2013. (*co-presenter*)

4. **D. C. Draper**, D. Farmer, Y. Desyaterik, J. L. Fry, "SOA yield from ozonolysis of BVOC at varying NO<sub>2</sub> concentrations," American Association for Aerosol Research Fall Meeting, Portland, OR, September 30 – October 4, 2013.
3. **D. C. Draper** and J. L. Fry, "NO<sub>x</sub> effects on nighttime secondary organic aerosol (SOA) formation," Urban Ecology Conservation Symposium, Portland, OR, February 11, 2013; American Chemical Society National Meeting, New Orleans, LA, April 7-11, 2013. (*Poster award recipient*)
2. J. L. Fry, **D. Draper**, S. S. Brown, J. N. Smith, R. C. Cohen, K. J. Zarzana, B. B. Palm, J. L. Jimenez, L. Kaser, A. Hansel, T. Karl, J. Ortega, P. Winkler, K. C. Barsanti, "NO<sub>3</sub>-initiated oxidation of biogenic hydrocarbons: Nighttime sink of volatile organic compounds and source of secondary organic aerosol," Reed College Summer Science Poster Session, August 31, 2012. (*presenter*)
1. \*J.L. Fry and **D. Draper**, "Field and laboratory studies of secondary organic aerosol formation from biogenic VOCs," Biosphere-Atmosphere Interactions Group, Atmospheric Chemistry Division, National Center for Atmospheric Research, Oct. 10, 2011. (*co-presenter*)

## SELECTED HONORS & AWARDS

- **National Science Foundation Graduate Research Opportunities Worldwide**  
*Travel support grant to University of Helsinki, Finland 2017-2018*
- **Student Poster Award AAAR fall meeting 2016**
- **National Science Foundation Graduate Research Fellowship 2016-2019.**
- **Student Poster Award AAAR fall meeting 2015**
- **Class of '21 Award Reed College 2013**
- **Certificate of Merit American Chemical Society Division of Environmental Chemistry - ACS Spring Meeting 2013**

# ABSTRACT OF THE DISSERTATION

Understanding  $\text{NO}_3$  oxidation of monoterpenes at different scales: Insights from molecular modeling, chamber experiments, and field observations

By

Danielle Catherine Draper

Doctor of Philosophy in Chemistry

University of California, Irvine, 2021

Professor James N. Smith, Chair

It has been shown through numerous field studies, laboratory measurements, and the occasional modeling study that  $\text{NO}_3$  radical oxidation of monoterpenes is a significant, though often overlooked, source of secondary organic aerosol (SOA). However, this generalization is complicated by the fact that while most abundantly emitted monoterpenes (e.g.  $\beta$ -pinene,  $\Delta$ -carene, and limonene) have moderate-to-high SOA yields with  $\text{NO}_3$  radical, the *most* abundantly emitted monoterpene ( $\alpha$ -pinene) has a negligible SOA yield with  $\text{NO}_3$ . As a result, the contribution of  $\text{NO}_3$  chemistry to the global SOA budget relies strongly on regional variability in vegetation and is therefore quite difficult to parameterize into models. In this work we investigate how particles form and grow from monoterpene +  $\text{NO}_3$  chemistry.

SOA originates from gas-phase oxidized organics and therefore a major focus of this work is mechanism development of reaction pathways not previously characterized for this system. In chapter 2, we use quantum chemical calculations to determine the fate of first-generation alkyl and alkoxy radicals for five cyclic monoterpenes. The fate of these radical intermediates determine whether these species are able to undergo additional radical propagation reactions that would lead to highly oxidized products or if the radicals terminate at relatively low oxidation states. We find that in spite of structural similarities between many of the cyclic

monoterpenes studied, they all favored different combinations of alkyl and alkoxy radical pathways, likely playing a role in the large variability of SOA yields observed from these precursors.

In chapter 3, we continue using quantum chemical methods to explore the fates of second-generation peroxy and alkoxy radicals for a single monoterpene,  $\Delta$ -3-carene. At this stage of the reaction mechanism, intermediates are already somewhat highly oxidized and these species are more likely to contribute (directly) to SOA than those discussed in the previous chapter. Here we computed rate constants for a variety of unimolecular reactions and compared those rate constants to estimated bimolecular rates. We found that both unimolecular and bimolecular reactions play a significant role in radical propagation (or termination) from second-generation peroxy radicals. Additionally, the derived mechanism was compared to  $\text{NO}_3^-$  CIMS data from  $\Delta$ -3-carene +  $\text{NO}_3$  chamber experiments and we were able to identify products consistent with the dominant reaction pathways in the computational mechanism.

Finally, in chapter 4 we analyze ambient observations of nanoparticle composition collected using the Thermal Desorption Chemical Ionization Mass Spectrometer (TDCIMS) in the boreal forest (Hyytiälä, Finland). We identify two abundant ions in this dataset with a striking diurnal cycle, peaking sharply at night, that are consistent with oxidized monoterpenes, though with quite low oxidation states. We postulate that these ions originate from first-generation organonitrates from monoterpene +  $\text{NO}_3$  chemistry. We then assess the formation kinetics and partitioning thermodynamics using supporting, coincident measurements and find that the kinetics and partitioning of the hypothesized organonitrates are consistent with the TDCIMS observations, but the magnitude of these species in the particle-phase remains uncertain.

# Chapter 1

## Introduction

### 1.1 Background

Particulate matter in the atmosphere comes in many shapes and sizes. Some particles, like dust and sea spray, are generated via physical processes and tend to be on the larger end of what can reasonably be sent aloft. These “coarse mode” primary particles can range from a few to tens of microns in diameter. Other particles are borne from chemical processes, either directly as primary emissions (e.g. smoke), or as a result of secondary chemistry of reactive trace gases whose products can undergo gas-to-particle conversion. These “fine mode” particles are smaller, ranging anywhere from 1 nm to  $\sim 2.5 \mu\text{m}$ . This diversity of size, formation mechanism, and composition results in a great diversity of physical and chemical properties, which in turn leads to diverse effects on our planet and our health.

Generally, this particulate matter, or aerosol particles, can have both a direct and indirect effect on Earth’s radiative balance, thereby impacting climate. Most particles are colorless and scatter incoming solar radiation, leading to a direct cooling effect on the atmosphere. Other particles, for example black or brown carbon, have visible color properties that absorb



incoming radiation and therefore have a warming effect instead. In addition, an indirect cooling effect is attributed to the particles that seed cloud droplets, referred to as cloud condensation nuclei (CCN), since clouds are a major reflective surface in the atmosphere [119]. Cloud properties and therefore the magnitude of their cooling effect are influenced by the properties of their parent particle population. For example, a large concentration of smaller particles will yield brighter clouds than a small concentration of large particles, and the ability of a particle to become a CCN in the first place depends on both its size and composition [160, 152].

In addition to climate effects, aerosol particles can also cause health problems upon inhalation. Acute and chronic conditions affecting a variety of organ systems have been linked to both extreme air quality events and long term exposure to fine mode particulate matter [111, 138, 126]. These conditions include a multitude of cardiopulmonary issues as well as diabetes, cancer, Alzheimer's, stroke, and may ultimately lead to death [150, 80]. Adverse health effects tend to increase with decreasing particle size, as smaller particles are able to travel further into the body, for example passing through the "filter" of the upper respiratory tract to reach the lungs, and, for the smallest particles, permeating through the lung tissue and entering the bloodstream [150]. Additionally, research has shown that some fraction of inhaled ultrafine particles (diameter  $< 100$  nm) may directly impact the central nervous system via translocation to the brain along the olfactory nerve [127]. Composition of these particles is also an important factor contributing to morbidity. For example reactive oxygen species (ROS), which can be plentiful in organic aerosol, are known to contribute to problematic inflammatory responses that can lead to many of the conditions above [47].

In terms of both climate and health effects, we see that the smallest particles can be the most impactful. CCN tend to be of order  $\sim 100$  nm in diameter, and ultrafine aerosol particles are likely to be the most detrimental to human health. With a few exceptions of extremely small primary particulate emissions [96], ultrafine aerosol generally originates from gas-to-

particle nucleation and growth processes following gas-phase atmospheric chemistry. This gas-phase chemistry, again, is quite diverse, with an enormous number of potential precursors including both organic and inorganic species. Organic aerosol (OA) that forms from gas-phase chemistry followed by gas-to-particle conversion processes is referred to as secondary organic aerosol (SOA). SOA is globally ubiquitous and makes up a large fraction of total organic aerosol, which in turn makes up a large fraction of total submicron particulate mass [69, 81, 178]. SOA forms from the oxidation of volatile organic compounds (VOCs), which sounds straightforward but is an extremely complex process en masse. There are estimated to be tens of thousands of VOCs in the atmosphere [61], each of which can produce large numbers of oxidation products with highly variable volatilities, and the potential for this whole soup to form SOA is influenced by the surrounding ambient environmental conditions, e.g. temperature, humidity, atmospheric dynamics, etc [69]. So, in spite of a plethora of research directed toward understanding SOA formation, there is a great deal we are still working to understand.

Somewhat paradoxically, ambient SOA has been shown to correlate strongly with anthropogenic tracers (e.g. carbon monoxide, CO) [170, 30], but radiocarbon dating indicates that the carbon content is primarily modern and therefore most likely of biogenic origin [105, 104, 161]. This observation indicates that the majority of SOA arises from pollution interacting with natural emissions rather than human sources alone [21, 74]. In this work I explore the nitrate radical ( $\text{NO}_3$ ) oxidation of monoterpenes, a chemical system that exemplifies this paradox.  $\text{NO}_3$  forms from anthropogenic emissions, whereas monoterpenes are emitted by trees.  $\text{NO}_3 + \text{monoterpene}$  chemistry is thought to contribute to SOA formation in numerous locations globally, but has also been under-studied in comparison to monoterpene oxidation by other oxidants (OH or  $\text{O}_3$ ), so a number of open questions remain [124].

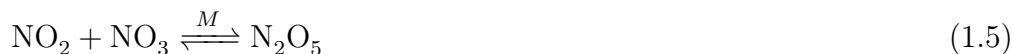
### 1.1.1 Precursors

**NO<sub>3</sub> radical** is a secondary product of reactions of nitrogen oxides ( $\text{NO}_x \equiv \text{NO} + \text{NO}_2$ ). There are a handful of different  $\text{NO}_x$  sources, including natural or biogenic processes such as lightning strikes or biological soil emissions from bacterial nitrification and denitrification processes [32, 5]. However, the significant majority of  $\text{NO}_x$  emissions – nearly 90 % in the US and only slightly less globally – come from fossil fuel combustion [32, 142, 41].  $\text{NO}_x$  is therefore an anthropogenic pollutant in its own right, and it also plays a huge role in the oxidative capacity of the troposphere as it is a precursor for both  $\text{NO}_3$  radical and ozone ( $\text{O}_3$ ), two of the three main atmospheric oxidants. As seen in equations 1.1-1.3,  $\text{NO}_x$  is constantly being interconverted between  $\text{NO}$  and  $\text{NO}_2$  during the day as  $\text{NO}_2$  is photolyzed to form  $\text{NO}$  and  $\text{NO}$  reacts with  $\text{O}_3$  to reform  $\text{NO}_2$ . Net  $\text{O}_3$  formation occurs when this cycle is intercepted by reactions that can convert  $\text{NO}$  to  $\text{NO}_2$  without consuming  $\text{O}_3$ , therefore allowing equation 1.2 to occur without 1.3.



$\text{NO}_3$  radical formation and loss pathways are shown in equations 1.4 - 1.9. These reactions are also occurring constantly, but if we note equations 1.6, 1.7, and 1.8 we can see that  $\text{NO}_3$  is photolyzed by the full spectrum of visible light, and it also reacts with  $\text{NO}$  (equation 1.8), which is photochemically sustained via equation 1.1. All three of these reactions are quite fast and convert  $\text{NO}_3$  back to  $\text{NO}_x$ . This means that  $\text{NO}_3$  is typically considered a nighttime oxidant since it is only really able to accumulate enough to react with VOCs in the absence

of daylight. That said, under certain circumstances e.g. when VOC concentrations are high enough that equation 1.9 is competitive with equations 1.6, 1.7, and 1.8,  $\text{NO}_3$  has been shown to contribute to daytime VOC oxidation as well [9].



**Monoterpenes** ( $\text{C}_{10}\text{H}_{16}$ ) are a class of biogenic volatile organic compound (BVOC) that comprise approximately 15 % of global BVOC emissions [64], an amount comparable to total global anthropogenic VOC emissions [63, 61]. Monoterpenes are something of a Goldilocks molecule with respect to SOA formation. They are large enough that they efficiently form SOA once oxidized, and they have high enough emissions that they contribute significantly to global SOA loading. This is in comparison to isoprene, which is more abundant (49%) but smaller ( $\text{C}_5\text{H}_8$ ) and therefore has fewer condensable oxidation products [22, 147], and sesquiterpenes, which are less abundant (2.7%) but larger ( $\text{C}_{15}\text{H}_{24}$ ) and therefore have a larger fraction of condensable oxidation products [78, 45]. Observations from the southeastern United States, a region with quite high isoprene and modest monoterpene emissions, suggest that monoterpenes are the largest individual contributor to submicron SOA, accounting for about half of the observed SOA mass [177]. The relative contribution of isoprene, monoterpenes, and sesquiterpenes to SOA formation will of course vary regionally, but these

observations demonstrate the possibility for major monoterpene contributions to SOA even in a region dominated by isoprene emissions.

Monoterpenes are emitted by coniferous trees and are produced to serve a variety of physiological functions, including defense against biotic or abiotic stressors such as herbivory, oxidative stress, or mechanical damage [45, 112]. As a class of compounds, they consist of a large number of structural isomers. This speciation is shown in Figure 1.1, highlighting in particular the eight most abundant isomers globally. While we can see that  $\alpha$ -pinene is the most abundant monoterpene emitted on average, this is not necessarily the case at the regional scale, since composition is dictated by the tree species and forest ecosystems are quite diverse across different regions of the earth. As an example of this regional monoterpene diversity, Figure 1.2 shows estimates of percent contribution of the six most abundant monoterpenes in the US. While  $\alpha$ -pinene clearly dominates in some regions, other regions are dominated by  $\beta$ -pinene or  $\Delta$ -3-carene. Understanding this regional diversity of monoterpenes and the unique reactivity of each is especially important as the climate changes and trees begin to emit different types and ratios of terpenoid compounds in response to physical and biological stressors [46].

### **Co-occurrence of precursors**

For the same reason that it seems paradoxical that much of SOA is likely *both* anthropogenic and biogenic in origin, it is important to justify that these two precursors exist together in both time and space in the ambient atmosphere. Temporally,  $\text{NO}_3$  radical's rapid photolysis generally allows it to only be a relevant oxidant at night.  $\text{NO}_x$  emissions tend to be higher during the day when the majority of on-road transportation and industrial processes take place, but  $\text{NO}_x$  has a long enough lifetime that it persists through the night. In the absence of nighttime  $\text{NO}$  emissions,  $\text{NO}$  is efficiently titrated to  $\text{NO}_2$  by  $\text{O}_3$  (equation 1.3), allowing  $\text{NO}_3$  to form efficiently with all major chemical sinks removed except for VOCs. Monoter-

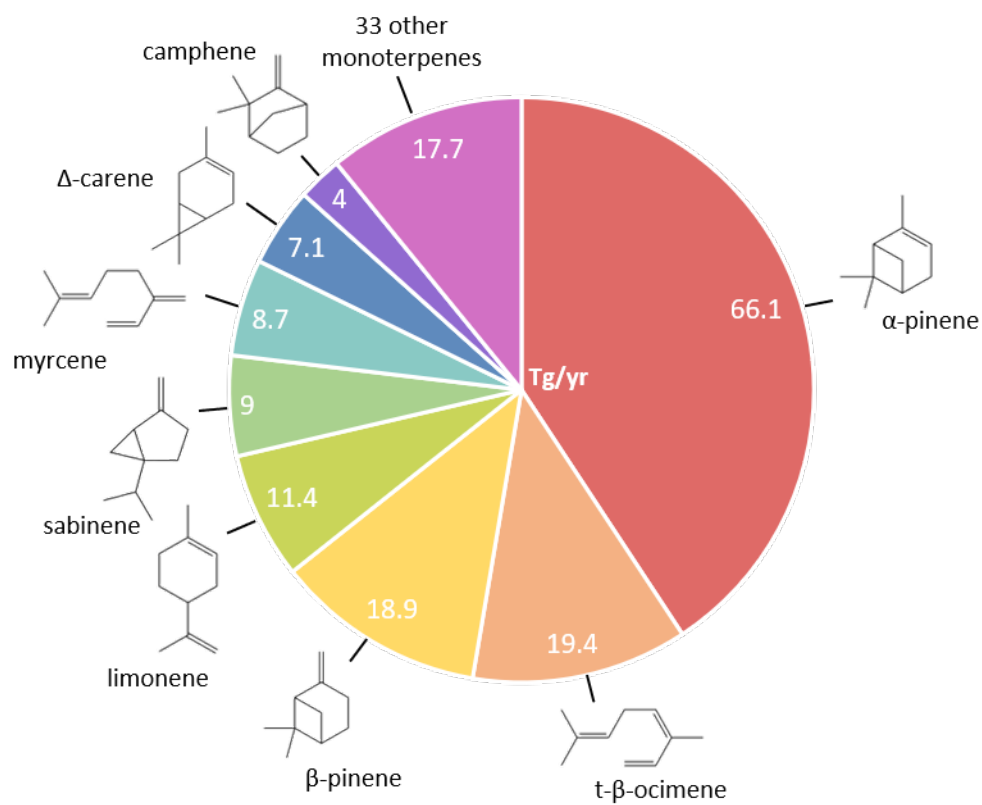


Figure 1.1: Modeled global emission rates for speciated monoterpenes. Estimates of emissions in  $\text{Tg yr}^{-1}$  (out of  $1089 \text{ Tg yr}^{-1}$  total non-methane BVOC) [64]

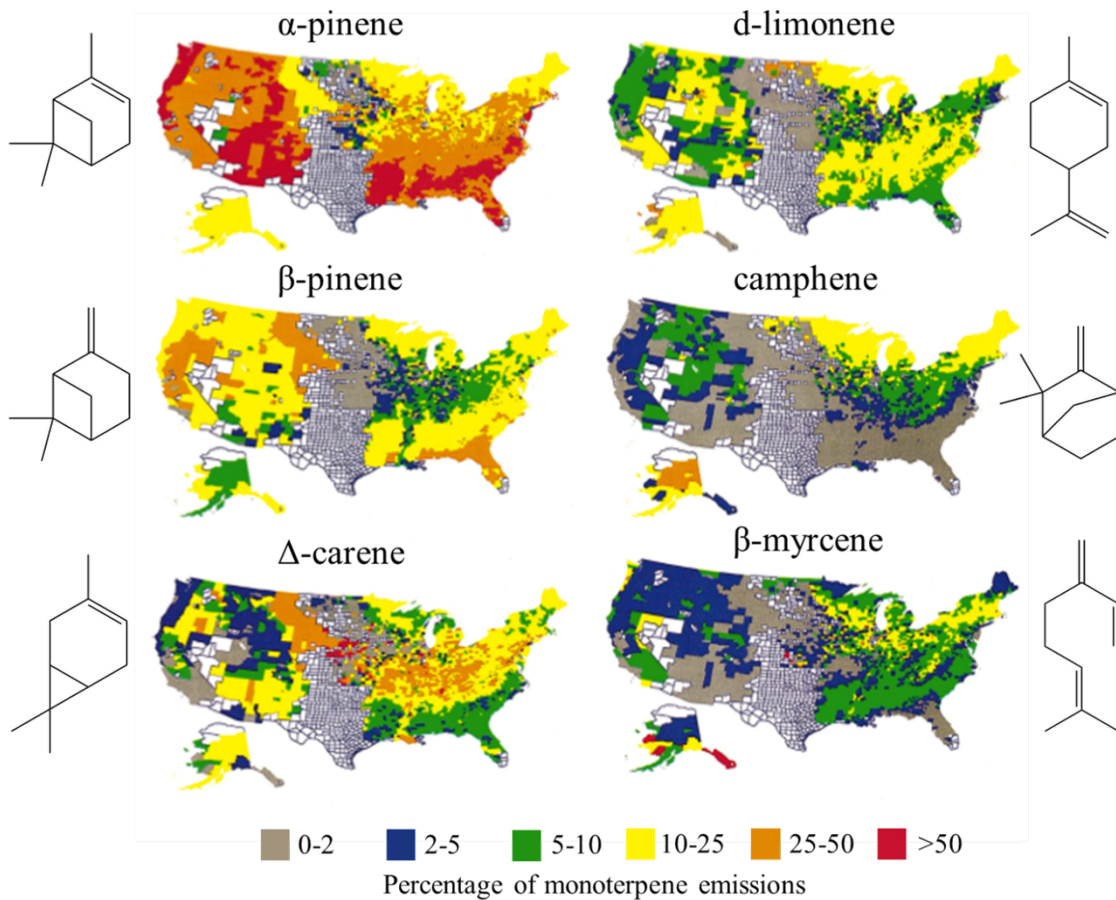


Figure 1.2: Regional emissions percentages of six different monoterpenes in the US. Image adapted from Geron et al. (2000) [59]

pene emissions are mainly temperature dependent, unlike isoprene, which is strongly light dependent [65]. Ambient temperature is generally cooler overnight than it is during the day, so monoterpene emissions are somewhat lower at night, but their emissions are continuous, so nighttime monoterpene chemistry can certainly occur as well.

As examples of spatial overlap, Figure 1.3 shows diurnal profiles of monoterpenes and  $\text{NO}_2$  at two relatively remote forested sites in the US: the Rocky Mountains in Colorado during the summer of 2011, and central Alabama in the summer of 2013. In spite of being “relatively remote,” we see that both  $\text{NO}_2$  and monoterpenes are present at comparable concentrations (of order 1 ppb). They both also have remarkably similar diurnal profiles, both peaking at night. This is likely the case for other forested regions with some local  $\text{NO}_x$  background, whether from small magnitude local emissions or longer range transport downwind from urban or industrial sources. Therefore monoterpene +  $\text{NO}_3$  chemistry is likely significant in many regions of the world even without being centered around major anthropogenic sources.

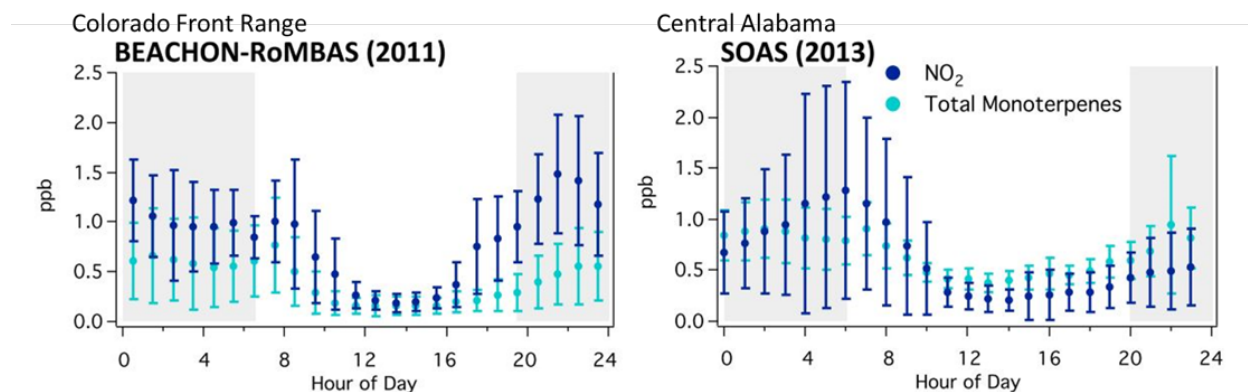


Figure 1.3: Diurnal profiles of  $\text{NO}_2$  and total monoterpene concentrations from two forested locations. BEACHON-RoMBAS data from Fry et al. (2013) [55] and SOAS data from Ayres et al. (2015) [9].

The reaction between monoterpenes and  $\text{NO}_3$  radical at night is further aided by the mixing conditions of the atmosphere. During the day, convective mixing driven by surface warming from incoming solar radiation enables a well mixed boundary layer. At night, however, the lack of solar radiation warming the surface creates a temperature inversion, turning off



the convective mixing. This, in effect, leads to a much more shallow boundary layer and surface emissions become concentrated in this now smaller volume closer to Earth’s surface. Therefore, even though  $\text{NO}_x$  and monoterpene emissions are generally lower at night, their boundary layer concentrations may end up being elevated at night, as seen in Figure 1.3, which in turn makes their reaction rates faster than they would otherwise be.

Given that this chemistry is both temporally and spatially feasible, it is worth comparing monoterpene reactivity with  $\text{NO}_3$  to that of OH and  $\text{O}_3$ . Table 1.1 shows the lifetimes of several monoterpenes with respect to a reasonable “typical” concentration of each oxidant. For each of these monoterpenes, the lifetime with respect to  $\text{NO}_3$  is significantly shorter than either OH or  $\text{O}_3$ . Clearly  $\text{NO}_3$  oxidation of monoterpenes is not only feasible, but it is potentially more significant than monoterpene oxidation by either OH or  $\text{O}_3$ .

Table 1.1: Lifetimes of prevalent cyclic monoterpenes with respect to OH,  $\text{NO}_3$ , and  $\text{O}_3$ , assuming “typical” oxidant concentrations of:  $[\text{OH}] = 2.0 \times 10^6 \text{ molec cm}^{-3}$  (12 hr daytime avg);  $[\text{NO}_3] = 5.0 \times 10^8 \text{ molec cm}^{-3}$  ( $\sim 20$  ppt) (12 hr nighttime avg);  $[\text{O}_3] = 7.0 \times 10^{11} \text{ molec cm}^{-3}$  ( $\sim 30$  ppb) (24 hr avg). Rate constants and average concentrations from Atkinson & Arey 2003 [7].

monoterpene	OH	$\text{NO}_3$	$\text{O}_3$
$\alpha$ -pinene	2.5 hr	5.4 min	4.7 hr
$\beta$ -pinene	1.9 hr	13 min	1.1 day
limonene	51 min	2.7 min	1.9 hr
sabinene	1.2 hr	3.3 min	4.8 hr
$\Delta$ -3-carene	1.6 hr	3.7 min	11 hr
camphene	2.6 hr	51 min	18 days

### 1.1.2 Ambient observations

Evidence of  $\text{NO}_3$  + monoterpene chemistry in the ambient atmosphere, specifically organic nitrates in the gas or particle phase, is becoming increasingly apparent as field-deployable instrumentation sensitive to low organonitrate concentrations has improved. The  $\text{NO}_3$  radical itself was first measured in the troposphere using long path differential optical absorption

spectroscopy in 1979 [137], and today is able to be measured in situ using cavity ring-down spectroscopy [18]. Early online techniques for detecting bulk organonitrates included Thermal Dissociation Laser Induced Fluorescence (TDLIF) detection of bulk peroxy and alkyl nitrates [29, 19, 55] and Aerosol Mass Spectrometry (AMS) analysis methods to parse total particulate nitrate signal into organic and inorganic contributions [48, 88]. Only recently have molecular organic nitrates been observed in ambient air using chemical ionization mass spectrometry (CIMS) [100, 113, 173, 99]. Even more recently an instrument has been developed to measure ambient  $\text{NO}_3$  reactivity [106, 107]. Figure 1.4 shows the submicron particulate mass fraction measured in ambient particles at numerous sites around the United States and Europe [124]. Every single site shows a non-trivial contribution from particulate organic nitrates, and in some locations these species actually dominate the submicron particle composition, demonstrating the ubiquity and importance of this chemistry.

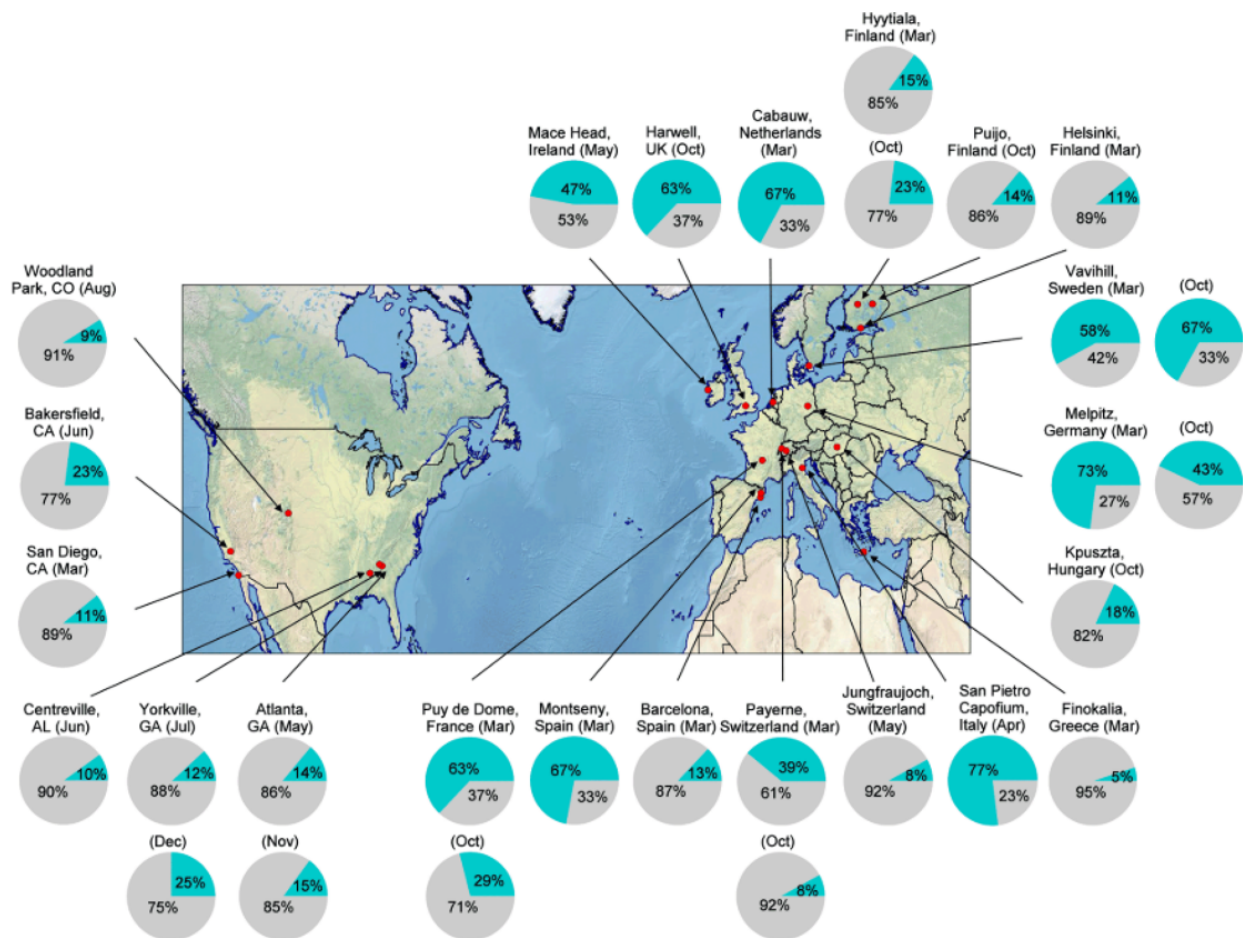


Figure 1.4: Mass percentage of organic nitrate in ambient submicron organic aerosol, shown in blue, measured at different locations in North America and Europe. Image reproduced from Ng et al. (2017) [124].

### 1.1.3 SOA yields

Laboratory experiments are crucial to help explain ambient observations and to eventually be able to model them. These often come in the form of chamber experiments where known concentrations of a simpler mixture of precursors – often a single VOC and oxidant – are injected into a chamber containing a large volume of air, and the gas- and/or particle-phase reaction products are monitored. SOA yields from individual VOCs are often determined from these kinds of experiments, where SOA yield is defined as the mass of SOA produced

divided by mass of VOC reacted. These yields are valuable especially for large scale modeling efforts in order to predict SOA mass formed based on gas-phase emissions and reactivity.

SOA yields have been measured for  $\text{NO}_3$  oxidation of a few of the most prevalent monoterpenes. These SOA yields as well as molar carbonyl and nitrate yields are compiled in Table 1.2. Most of the monoterpenes studied have moderate to high SOA yields from  $\text{NO}_3$  oxidation. However, the most prevalent monoterpene globally,  $\alpha$ -pinene, has anomalously low yields. This anomalous behavior for  $\alpha$ -pinene is not easily discernible based on its structure. Most of the monoterpenes with yield data shown are bicyclic with their double bond in one of two similar locations (see Figure 1.1). Limonene is the one that doesn't quite fit this description, but it is still cyclic and has two double bonds, one of which is in the same location as the others, so it should still react similarly. A more detailed description of this reactivity is discussed in the next section, but the wide variability in observed SOA and oxidation product yields suggests that their mechanisms are more nuanced than expected.

The variability in SOA yields across different monoterpenes is problematic for modeling efforts. Large scale chemical transport models are computationally onerous to run, and it is not possible to treat every reaction explicitly. Instead, classes of compounds are often lumped into a much simplified parameterization, tracking only a subset of products or types of products, and SOA formation is treated based on laboratory SOA yields [24, 140, 20]. Monoterpenes often get lumped into one or two "representative" tracers, and SOA yields for these tracers are likely to be parameterized according to only a handful of relevant experimental yields, for example,  $\alpha$ -pinene ozonolysis and  $\text{NO}_3$  radical oxidation of  $\beta$ -pinene [141]. Additionally, large scale models are unlikely to have the spatial resolution to capture important VOC spatial variability [85], which, if different terpenes all have different SOA yields, will affect the accuracy of SOA estimates. Several modeling efforts over the last few years have worked to incorporate more explicit monoterpene +  $\text{NO}_3$  chemistry to explain organonitrate observations in the southeastern US in particular. This expanded parameter-

ization is incredibly valuable to better predict organonitrate-related chemistry, but it tends to focus on the addition of new products rather than addressing complexity in monoterpene speciation [139, 51, 172, 176, 175]. The importance of monoterpene speciation is amplified for  $\text{NO}_3$  oxidation since the monoterpene with the most anomalous behavior is the monoterpene with the largest global emissions. This splits the  $\text{NO}_3$  oxidation of monoterpenes into two categories:  $\alpha$ -pinene, which has high emissions and a negligible SOA yield, and ‘other cyclic monoterpenes,’ which collectively have high emissions and moderate to high SOA yields. Not accounting for these two groups separately is therefore likely to be problematic.

#### 1.1.4 Gas-phase oxidation mechanisms

At a fundamental level, the anomalous behavior of  $\alpha$ -pinene compared to other cyclic monoterpenes may provide valuable insight into the mechanism for SOA formation more broadly. For two monoterpenes with different but moderate SOA yields, it is challenging to identify what factors cause that difference since they are structural isomers and therefore have a great deal of overlap in their product distribution. However, if one of those monoterpenes does not produce SOA at all, like  $\alpha$ -pinene, differences in product distributions are more likely to be telling of what features might be important for SOA formation.

While it is apparent we do not fully understand the details of monoterpene oxidation that lead to such diverse products, we do have a good understanding as a community of what pathways are possible during VOC oxidation. Figure 1.5 shows the general process and possibilities of VOC oxidation. For alkenes (including monoterpenes), the oxidant adds to (or across for  $\text{O}_3$ ) a double bond, initially forming a C-centered alkyl radical (R). This alkyl radical will typically undergo rapid  $\text{O}_2$  addition since we live in an oxygen rich environment, forming an O-centered peroxy radical ( $\text{RO}_2$ ). This peroxy radical has a few possible fates, either bimolecular reaction with another radical or isomerization, forming a new, more highly

Table 1.2: Yields of SOA and oxidation products from monoterpene + NO<sub>3</sub> chamber studies. Compiled data from Ng et al. (2017) [124].

Monoterpene	SOA yield	Organic nitrate molar yield	Carbonyl molar yield	Ref.
$\alpha$ -pinene	0.2-16 %	18-25%	65-72%	[68]
	4 or 16%	11-29%	39-58%	[157]
	0%	10%		[54]
	1.7-3.6%			[122]
	9%			[135]
			14% 12-18%	58-66% 69-81%
$\beta$ -pinene	10-52% (7-40%)*	51-74%	0-2%	[68] *[116]
	50%	40%		[57]
	33-44%	22%		[54]
	27-104%	45-74%		[16]
	32-89%			[62]
$\Delta$ -carene	15-62% (12-49%)*	51-74%	0-2%	[68] *[116]
	38-65%	77%		[54]
	13-72%			[62]
limonene	17% (14-24%)*	48%	69%	[68] *[116]
	21 or 40%	63-72%	25-33%	[157]
	25-40%	30%		[56]
	44-57%	54%		[54]
sabinene	14-76%			[62]
	25-45%			[54]

\*Moldanova and Ljungstrom 2000 modeled yields from Hallquist et al. 1999 dataset

oxidized alkyl radical. Bimolecular reaction with another radical (e.g.  $\text{RO}_2$ ,  $\text{HO}_2$ ,  $\text{NO}_3$ ,  $\text{NO}$ ) may either terminate the radical, leading to a closed-shell product, or continue propagating, forming an alkoxy radical ( $\text{RO}$ ). Like the peroxy radical, alkoxy radicals can also undergo bimolecular reactions leading to closed shell products, or they can isomerize or decompose, continuing the radical propagation and cycling back to a new alkyl radical. Therefore, the gas-phase oxidation mechanism for any VOC is a cycle of radical propagation until the radical terminates into a comparatively stable closed-shell product. These closed-shell products can also undergo additional generations of oxidation, restarting the radical propagation process.

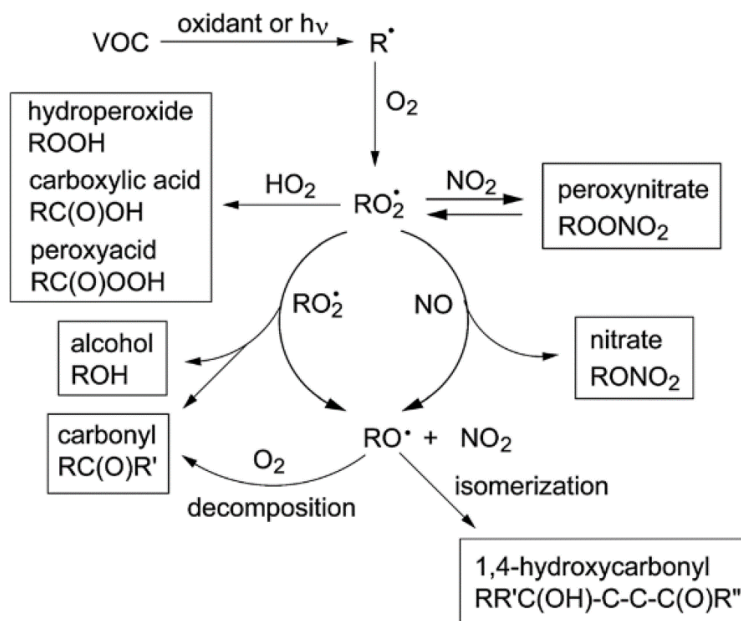


Figure 1.5: General VOC oxidation schematic, highlighting potential closed-shell products. Image reproduced from Ziemann et al. (2012) [180]

A lot of effort toward understanding SOA yields has been directed at measuring the distribution of closed-shell products and assessing the potential for partitioning into the particle-phase. This is important, but recently that conversation has started shifting to a slightly different perspective: consideration of the  $\text{RO}_2$  fate to assess whether isomerization is likely.

This  $\text{RO}_2$  isomerization, often referred to as autoxidation, has been observed in the atmosphere only in the last several years [27, 39, 14]. In these reactions,  $\text{RO}_2$  radicals with suf-

ficiently large carbon backbones can abstract an internal H, forming a hydroperoxide group and reforming an alkyl radical, which will rapidly add  $O_2$  and can potentially continue undergoing multiple cycles of oxidation without coming into contact with another radical. This mechanism is shown in Figure 1.6 and has been implicated to justify the extremely fast formation of very highly oxidized molecules (HOMs). These HOMs are likely a key contributor to SOA formation and growth due to their higher molecular weight and degree of oxidation compared to lesser oxidized products.

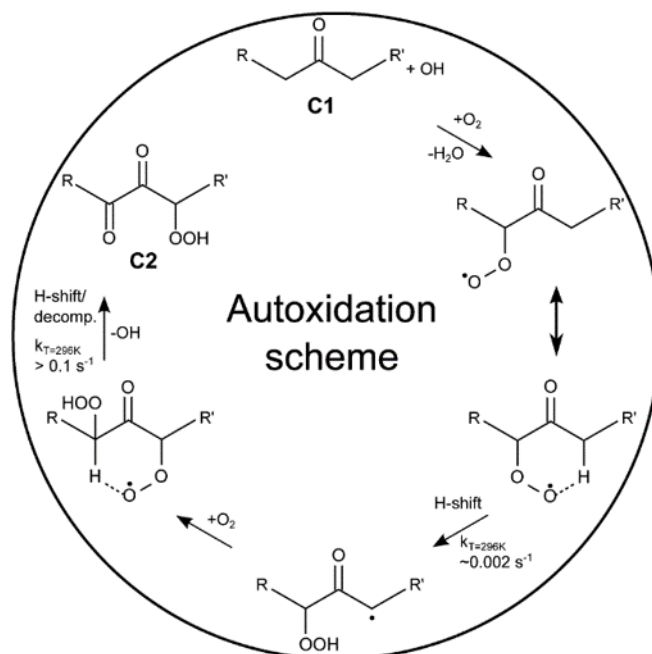


Figure 1.6: Schematic of  $RO_2$  H-shift, or “autoxidation” reactions. Image reproduced from Crouse et al. (2013) [27].

Peroxy radical autoxidation has been found to be fast enough to compete with bimolecular radical reactions, but this depends strongly on the specific geometry of the  $RO_2$  as well as the bimolecular reaction sink, making the  $RO_2$  fate a very important parameter to understand for individual systems and environments. Since we know similar isomerization reactions can also occur for alkoxy radicals, I prefer to broaden the focus on  $RO_2$  fate to radical fate more generally. Even if a specific peroxy radical does not isomerize, the subsequent bimolecular reaction does not lead to a 100% yield of radical termination products. Some



(often large) fraction of those products will be alkoxy radicals and some fraction of those will continue propagating until, at some stage, they terminate. As long as the organic radical is still a radical, it can continue propagating to form increasingly oxidized and lower volatility products that may be important in SOA formation and growth.

### 1.1.5 New particle formation & growth

Once gas-phase oxidation occurs, SOA is borne from gas-to-particle conversion of whichever oxidation products are able to participate. This transformation into the particle-phase includes both nucleation of new particles and growth onto existing SOA mass. Nucleation describes the formation of thermodynamically stable molecular clusters and their subsequent “activation” by extremely low volatility vapors to continue growing, as illustrated in Figure 1.7. The precise physicochemical mechanism of nucleation is still poorly understood, but correlations of nucleation rates with precursors have elucidated which chemical species can participate [90]. Most often nucleation is initiated by sulfuric acid ( $\text{H}_2\text{SO}_4$ ) along with ammonia, amines, and/or oxidized organics [91, 4, 103, 114], though nucleation has also been observed from oxidized organics alone [89].

SOA growth is perhaps even more complicated and less well understood than nucleation. This complexity arises from the large number of compounds that might contribute to growth and the multiple reaction pathways that could be involved. Figure 1.8 shows general processes that contribute to growth of newly formed particles. Gas-phase species can condense and re-evaporate to achieve thermodynamic equilibrium [131]. Particle-phase species may also react at the surface or in the bulk, either forming lower volatility or effectively non-volatile accretion products (e.g. oligomers or salts) that will not re-evaporate, or fragmenting to form higher volatility products, which may evaporate. These processes are additionally

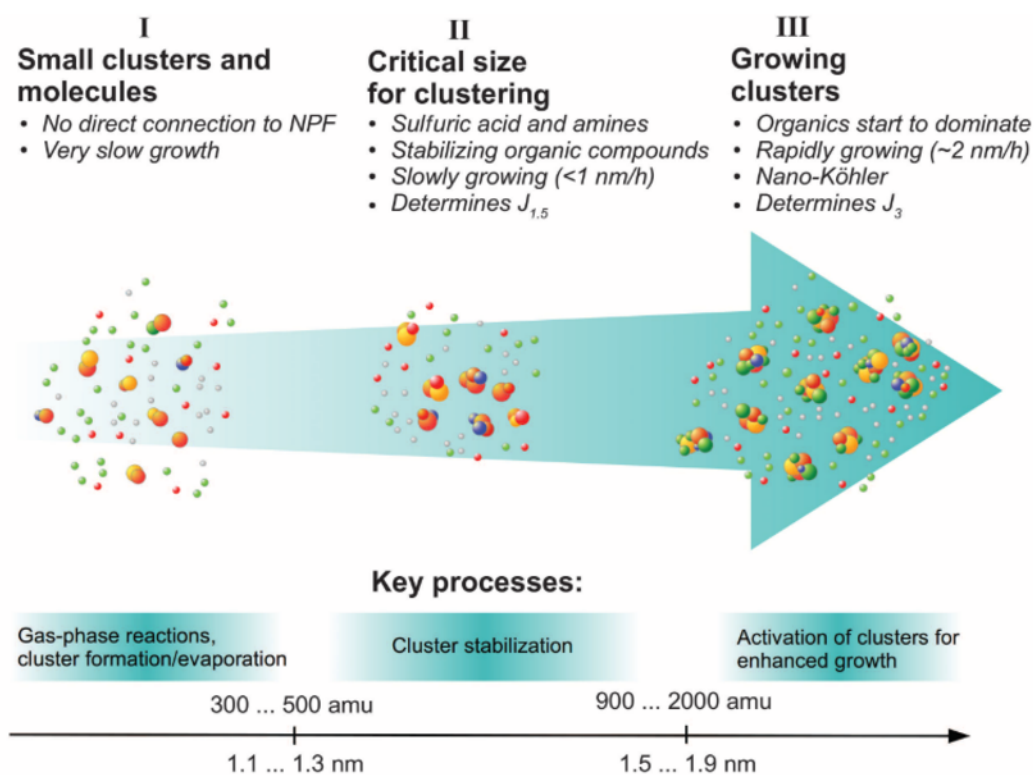


Figure 1.7: Schematic highlighting the processes that occur during nucleation, including the typical chemical composition and size range for each stage.  $J_{1.5}$  and  $J_3$  are the nucleation rates of 1.5 and 3 nm particles, respectively. Image reproduced from Kulmala et al. 2013 [91].

influenced by properties such as phase state of the particles, aerosol liquid water content, relative humidity, temperature, etc. [151, 153, 175, 49, 159].

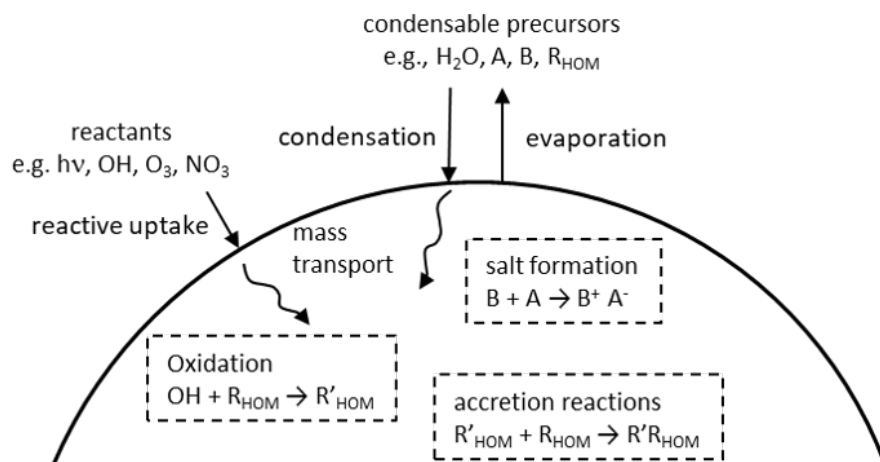


Figure 1.8: Schematic showing possible particle mass accommodation processes. Image reproduced from Smith et al. 2021 [154]

SOA growth is often treated using some version of the absorptive partitioning framework, which considers particle mass accommodation assuming thermodynamic equilibrium, so the partitioning of an individual compound is driven by its vapor pressure [131]. A larger fraction of a low volatility product will exist in the particle-phase than a higher volatility compound. In this framework, partitioning is also influenced by the background SOA mass. In the partitioning constant ( $K_p$ ) expression shown in equation 1.10, the particle-phase concentration of the species of interest ( $F$ ) is directly proportional to the mass concentration of total suspended particulate matter (TSP), where  $A$  is the gas-phase concentration of the same compound. This means that a higher fraction of a given compound partitions more into the particle-phase at higher background SOA mass loadings, and similarly, that as background SOA mass increases, increasingly high volatility products can partition into the particle-phase. Additionally, for the smallest sized particles that are already expected to contain mostly low volatility species, the Kelvin effect enhances evaporation from the surface of the particle due to the surface curvature reducing the number of intermolecular interactions at the surface of the particle. Therefore, the earliest steps of nucleation and growth are thought

to be dominated by extremely low volatility species. Figure 1.9 nicely illustrates how particle composition is likely to change as it grows from freshly nucleated particles ( $\sim 1$  nm) to cloud condensation nuclei (CCN) sizes ( $\sim 100$  nm).

$$K_p = \frac{F/TSP}{A} \quad (1.10)$$

For individual chemical systems, such as  $\text{NO}_3$  + monoterpenes, it is clear then that the details of the gas-phase chemistry, particularly the volatility distribution of products, will strongly influence the SOA formation potential including both nucleation and growth rates.

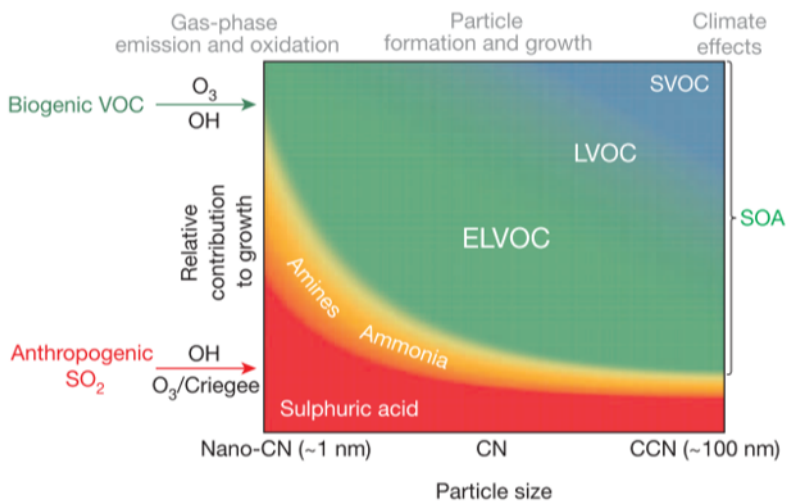


Figure 1.9: Illustration of the likely shift in composition of nanoparticles as they grow from 1-100 nm. Image reproduced from Ehn et al. (2014) [39].

## 1.2 Research goals

The primary research goal of my PhD research has been to better understand how particles form and grow from the  $\text{NO}_3$  oxidation of monoterpenes. As a community, we understand a great deal about both anthropogenic and biogenic emissions, gas-phase oxidation mech-

anisms, and particle-phase processes. We have done a great deal of work cataloguing and parameterizing observations such as SOA yields and kinetic and thermodynamic properties in order to accurately model these processes. Monoterpenes as a class of compounds have an enormous body of literature focused on them. And yet we still cannot fully explain or predict the observed differences in SOA yields across different monoterpenes. The wide range of SOA yields observed across monoterpenes oxidized by  $\text{NO}_3$  radical, in particular, is intriguing as it is suggestive of mechanistic nuances that can completely preclude SOA formation or very efficiently form high yields of SOA.

The details and effects of a single monoterpene +  $\text{NO}_3$  reaction depend greatly on the environment and scale in which it occurs. For that reason, I felt it was important to tackle this question from a variety of perspectives and on multiple scales ranging from molecular-scale mechanism development to relatively controlled laboratory experiments to ambient observations. The molecular-scale mechanism development provides a framework for what reactions can occur, but laboratory measurements are crucial to validate the developed mechanism as well as to constrain the relative contribution of different pathways under various conditions. Similarly, laboratory measurements give us information about how the oxidation reactions proceed and how these translate into SOA formation in a pristine and isolated environment, but ambient measurements are crucial for us to see how these bulk-scale mechanisms are impacted by interactions with everything else in the real atmosphere. Therefore, combination of all three of these scales help us gain a realistic picture of how a single monoterpene +  $\text{NO}_3$  reaction may exert a global influence on atmospheric chemistry and particle formation.

My specific goals in this work are to address two portions of the gas-phase oxidation mechanism to understand a) the structural features leading to different oxidation pathways across several different monoterpenes, and b) the detailed mechanism for a single monoterpene that would lead to highly oxidized, condensable products. I then seek to compare these mecha-

nisms to gas-phase observations during chamber experiments of the same monoterpenes, and finally I zoom out and investigate the significance of this chemistry in SOA formation and growth via ambient nanoparticle composition measurements. Through ab initio mechanism development, laboratory experiments, and ambient data analysis, all performed independently of one another, I wish to see how well “bottom-up” and “top-down” converge upon similar conclusions.

## 1.3 General Methods

### 1.3.1 Theoretical Approach

Quantum chemical calculations are a key component of the mechanism development in Chapters 2 and 3 and are also used to a lesser degree to assess detectability of certain compounds by chemical ionization mass spectrometry (CIMS) reagent ions. These calculations, while different in application, all required quite similar computational procedures: namely conformer sampling the structures of interest and running optimizations and frequency calculations to determine their electronic energy. Specific details are included in each chapter, so the following sections just give a general overview of the different applications for which quantum chemical calculations were used.

#### **Unimolecular Reaction Barrier Energies and Rate Constants**

The main application of theoretical calculations in this work was to calculate rate constants of unimolecular radical rearrangement reactions (e.g. Figure 1.10) using multiconformer transition state theory (MC-TST). For larger molecules with a number of conformers at thermal equilibrium, MC-TST provides more accurate rate constants than conventional transition

state theory by summing the rate constants from each conformer, weighted by the Boltzmann population of the corresponding reactant conformer. Conventional transition state theory (TST) is described by equation 1.11, where  $\kappa$  is the tunneling coefficient,  $k_B$  is the Boltzmann constant,  $T$  (K) is the temperature,  $h$  is Planck’s constant,  $Q_{TS}$  and  $Q_R$  are the total partition functions for the transition state (TS) and reactant (R),  $E_{TS}$  and  $E_R$  are electronic energies, and  $Z_{TS}$  and  $Z_R$  are the zero-point vibrational energies. The probability of a given reactant ( $R_i$ ) contributing to the overall Boltzmann reactant population is given in equation 1.12, where  $G_{R,0}$ ,  $G_{R,i}$ , and  $G_{R,j}$  are the Gibb’s free energies of the lowest energy,  $i^{th}$ , and  $j^{th}$  reactant conformers, respectively. Finally, the expression for the MC-TST rate constant is given in equation 1.13 [44, 43, 118].

$$k_{TST} = \kappa \frac{k_B T}{h} \frac{Q_{TS}}{Q_R} \exp\left(\frac{-(E_{TS} + Z_{TS} - E_R - Z_R)}{k_B T}\right) \quad (1.11)$$

$$p_{R,i} = \frac{\exp\left(\frac{-(G_{R,i} - G_{R,0})}{k_B T}\right)}{\sum_{j=1}^{N_R} \left(\exp\left(\frac{-(G_{R,j} - G_{R,0})}{k_B T}\right)\right)} \quad (1.12)$$

$$k_{MCTST} = \sum_{i=1}^{N_{TS}} p_{R,i} \times k_{TST,i} \quad (1.13)$$

Electronic energies, zero-point vibrational energies, partition functions, and Gibb’s free energies (which can also be expressed in terms of  $E$ ,  $Z$ , and  $Q$ ) for each reactant and transition state conformer can be calculated using density functional theory (DFT) methods. However, due to the large number of conformers for many atmospherically-relevant oxidized organics, it is computationally unreasonable to include every single conformer. Møller et al. developed a procedure that is followed closely in this work to approximate the MC-TST rate constant that reduces computational cost while maintaining high accuracy [118]. The goal of this procedure is to reduce the total number of conformers down to only the ones contributing most

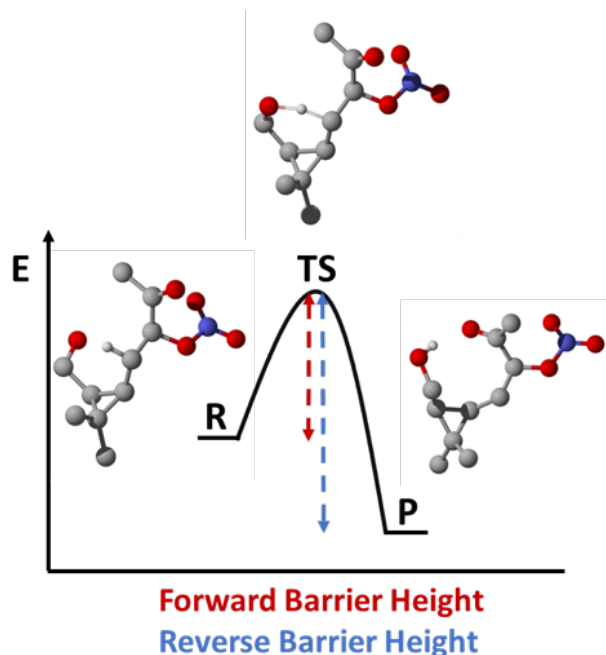


Figure 1.10: Potential energy diagram showing reactant (R), transition state (TS), and product (P).

significantly to the Boltzmann population and therefore overall reaction kinetics. This whitening down of conformers is achieved iteratively, beginning with cheaper (and less accurate) methods and applying relative energy cutoffs to reduce the total number of conformers as geometries are re-optimized at higher levels of theory. Conformer sampling procedures and energy cutoffs recommended in Møller et al. were tested rigorously and were not observed to miss important low-energy conformers that would strongly impact calculated rate constants.

This sequence of calculations begins with conformer sampling of reactant and transition state structures using Spartan'16 and Spartan'18 software using the MMFF force field and calculation of the single point energy at the B3LYP/6-31+G(d) level using Gaussian 09 and 16 [101, 12, 52]. Conformers within 5 kcal/mol of the lowest energy conformer were then fully optimized at the same level. The conformers within 2 kcal/mol of the lowest energy conformer (removing duplicates, determined by electronic energy and dipole moment) are the conformers to be included in the final MC-TST calculation. These conformers then underwent optimization and frequency calculations at the  $\omega$ B97X-D/aug-cc-pVTZ level, pro-



viding the final zero-point energy corrections and partition functions. Finally, the single point energy of the lowest energy conformer was calculated using a highly correlated wave function method, here ROHF-DLPNO-CCSD(T)/aug-cc-pVTZ since canonical coupled cluster (CCSD(T)) methods were prohibitively expensive for the size of molecules studied. This single point energy was used to correct the  $\omega$ B97X-D electronic energies, improving the absolute accuracy of calculated rate constants [118].

## Reagent Ion Clustering

Reagent ion clustering calculations were performed for a few specific products to determine whether they were likely to be detectable with the  $\text{NO}_3^-$  reagent ion during chemical ionization mass spectrometry (CIMS) analysis. A general schematic of this reaction is shown in Figure 1.11. In order for a reagent ion to bind to an analyte molecule, its clustering energy must be stronger than its clustering energy with itself. So in the case of a generic molecule M, clustering with  $\text{NO}_3^-$  will be favorable if  $\Delta E_M$  from Equation 1.15 is greater than  $\Delta E_{\text{HNO}_3}$  from Equation 1.14. Since qualitative interpretation of relative energies between these two is sufficient to predict whether or not a cluster will form, which is all that is being questioned in this work, the level of accuracy of the electronic energy calculations is not critical. Therefore, the  $\omega$ B97X-D functional, which better accounts for dispersion interactions, paired with the smaller 6-31+G\* basis set was sufficient for most clustering calculations.

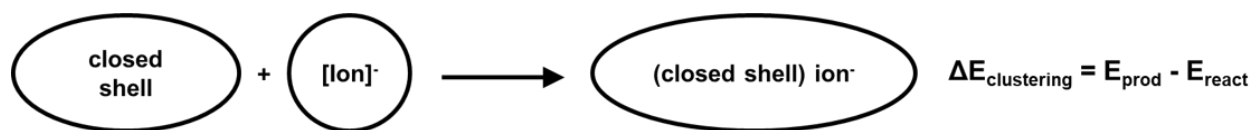
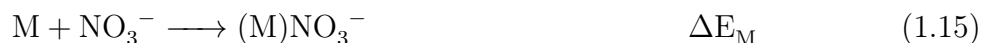


Figure 1.11: Generic ion-molecule clustering reaction scheme



## Electron Affinities

Electron affinities were calculated in a similar manner to the reagent ion clustering and were used to assess the likelihood of certain analyte species being ionized by electron transfer in the TDCIMS inlet. Equations 1.16 and 1.17 show the competing reactions for the negative mode reagent ion  $\text{O}_2^-$ . We expect electron transfer to occur if  $\text{EA}_{\text{M}} > \text{EA}_{\text{O}_2}$ . Similar to the reagent ion calculations above, we are only interested in relative energies between the two reactions, so low-level computational methods are sufficient.



### 1.3.2 Experimental approach

The experimental approaches implemented in this work include both laboratory chamber experiments (Chapter 3) and ambient measurements (Chapter 4). Specific details for each set of measurements are contained within the chapters themselves, while the following sections include a general overview of the chamber setup and instrumentation.

## Chamber Description

Chamber experiments were conducted in a 560 L stainless steel chamber, described in detail in DeHaan et al. [31]. The chamber is equipped with quartz windows and external UV lamps for photooxidation reactions, but for the nighttime  $\text{NO}_3$  radical experiments here, the windows were covered with opaque cloth to prevent any photochemistry from occurring. A schematic of the chamber is shown in Figure 1.12. Experiments were conducted in flow-through mode, continuously adding precursors to reach steady state conditions.  $\text{NO}_3$  radical was generated via reaction of  $\text{O}_3 + \text{NO}_2$ , and for a typical experiment, these two reagents were allowed to come to steady state before monoterpene was added. Once the oxidants came to steady state, resulting in equilibrium concentrations of  $\text{NO}_3$ ,  $\text{N}_2\text{O}_5$ ,  $\text{NO}_2$ , and  $\text{O}_3$ , monoterpene was added. Concentrations of precursors were chosen carefully to avoid appreciable  $\text{O}_3$  oxidation of the monoterpene, so the resulting product mixture should be dominated by monoterpene +  $\text{NO}_3$  products.

Precursors and products were monitored in real time by the suite of instrumentation shown in Figure 1.12 (except for the instruments marked by dashed boxes, which were not running during the experiments discussed in Chapter 3). This suite of instruments includes  $\text{NO}_x$  and  $\text{O}_3$  gas analyzers (Model 405nm and Model 106-L, 2B Technologies) as well as a scanning mobility particle sizer (SMPS) comprised of a differential mobility analyser (Model 3081, TSI, Inc.) and an ultrafine condensation particle counter (Model 3020, TSI, Inc.) to measure particle size distributions. The  $\text{NO}_3^-$  CIMS will be discussed in the next section.

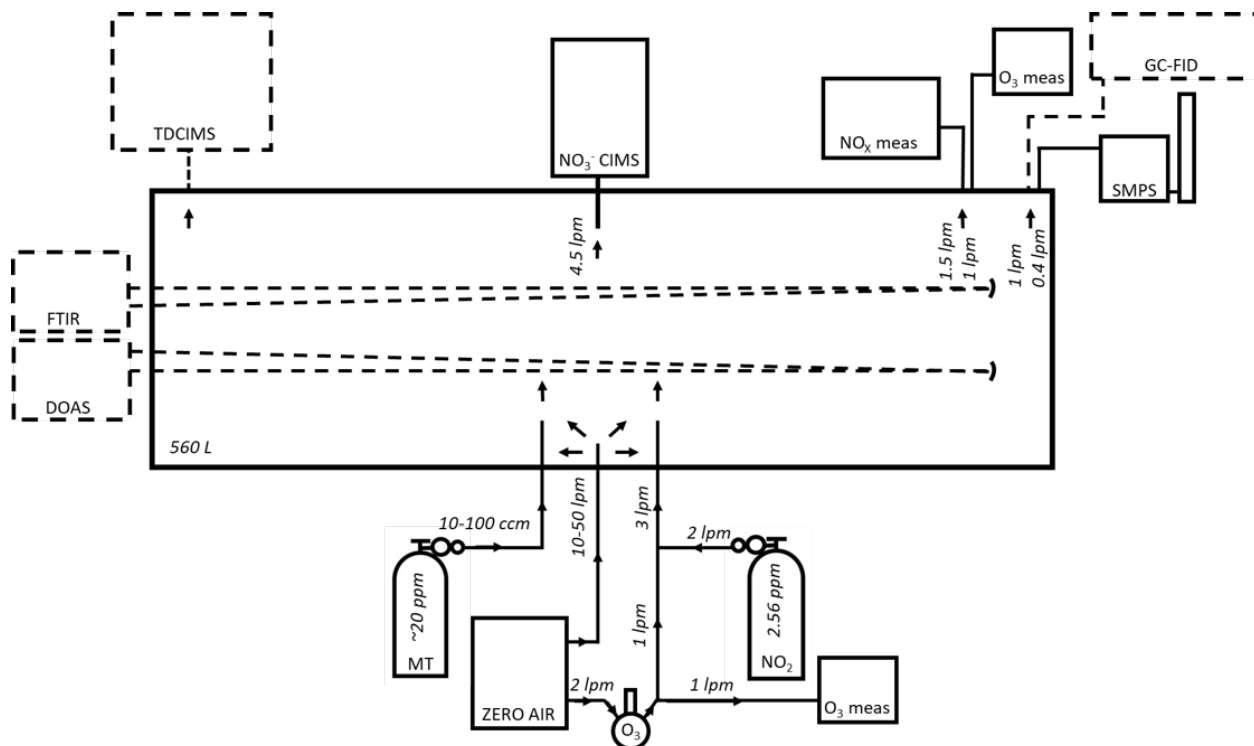


Figure 1.12: Schematic of the reaction chamber and associated suite of instrumentation.

### 1.3.3 Instrumentation

#### Chemical Ionization Mass Spectrometry (CIMS)

Gas-phase products were measured using chemical ionization mass spectrometry (CIMS) with the  $\text{NO}_3^-$  reagent ion. This instrument couples a commercially-available chemical ionization inlet (Aerodyne, Corp.) to a high resolution atmospheric pressure interface time of flight mass spectrometer (APi-TOF-MS) with an LTOF analyzer (Tofwerk, AG). The CIMS inlet is based on the design by Eisele and Tanner [40, 82] and consists of an atmospheric pressure drift tube with concentric flows. The sample flow is drawn through the center and  $\text{NO}_3^-$  ions are introduced to the outer sheath flow.  $\text{NO}_3^-$  ions are generated by flowing clean air over the headspace of a volume of  $\text{HNO}_3$  and exposing it to alpha radiation using a  $^{210}\text{Po}$  source. This  $\text{NO}_3^-$  flow is directed radially into the sample flow by an electric field, and

analyte ionization typically occurs via clustering with the  $\text{NO}_3^-$  ion for species less acidic than  $\text{HNO}_3$ , which encompasses the oxidized organics of interest in this work.

### **Thermal Desorption Chemical Ionization Mass Spectrometry (TDCIMS)**

Size-selected nanoparticle (<100 nm) composition was measured using the Thermal Desorption Chemical Ionization Mass Spectrometer (TDCIMS). The TDCIMS couples a home-built inlet to a high resolution atmospheric pressure interface time of flight mass spectrometer (Tofwerk, AG) identical to the one discussed in Junninen et al. [83]. The TDCIMS has been described in detail elsewhere [98, 156, 167], so I will only discuss its general principle of operation here. Ambient particles are charged via unipolar charger and size-selected downstream by nanoparticle differential mobility analyzers (nDMAs) set at a constant voltage corresponding to the diameter of interest. As shown in Figure 1.13, size-selected nanoparticles then travel toward a Pt collection filament. During collections, high voltage (+4000 V) is applied to the filament, collecting particles by electrostatic precipitation. After collection, the filament moves upward into the ion source, at which point it is resistively heated by a smooth ramp of the current over about 40 seconds, reaching a maximum temperature of  $\sim 600^\circ\text{C}$ . Nanoparticle constituents are volatilized during this temperature ramp. Reagent ions are generated by alpha radiation ionizing  $\text{H}_2\text{O}$  or  $\text{O}_2$  impurities in the  $\text{N}_2$  flowing over the  $^{210}\text{Po}$  ion source, leading to  $\text{H}_3\text{O}^+$  (or  $(\text{H}_2\text{O})_n\text{H}_3\text{O}^+$ ) reagent ions in positive mode and  $\text{O}_2^-$  (or  $(\text{H}_2\text{O})_n\text{O}_2^-$ ) reagent ions in negative mode. Reagent ions ionize the desorbed analyte molecules by proton transfer in positive mode and either proton transfer, electron transfer, or  $\text{O}_2^-$  clustering in negative mode. These analyte ions are then directed toward the entrance aperture to the mass spectrometer via an electric field, and they are analyzed with a time of flight mass analyzer. Backgrounds are run under identical conditions to the collections except no voltage is applied to the Pt filament during the “collection” period, which allows for subtraction of any gas-phase species adsorbed to the filament.

During operation, the size-selection diameter and the collection time are set by the user based on the ambient particle size distribution of interest. The TDCIMS is sensitive to picograms of sampled mass, so for larger diameter particles and/or large number concentrations, collection times can be quite short, and conversely, for smaller diameter particles and/or small number concentrations collection periods may be as long as 30 minutes in order to collect sufficient mass. Typical operation consists of alternating collection and background cycles and positive and negative ion mode (positive collection, positive background, negative collection, negative background). For 30 minute collections, this leads to time resolution of  $\sim 2$  hrs for each polarity.

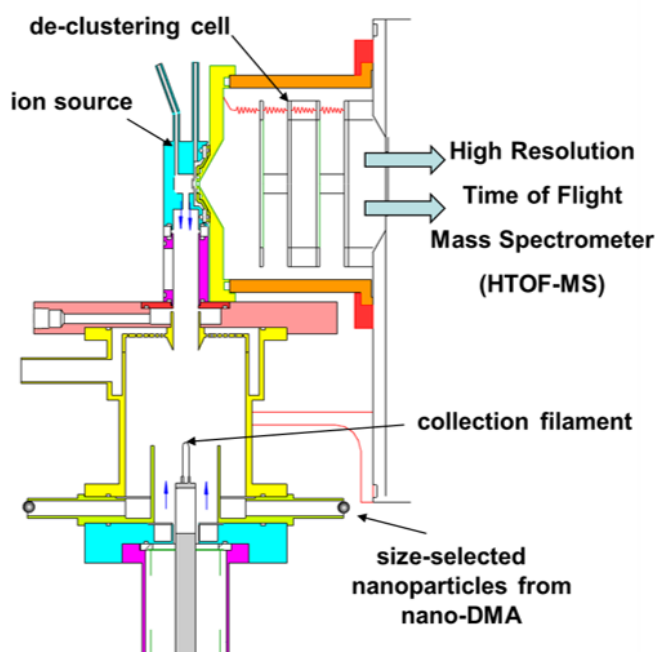


Figure 1.13: Sectional view of the TDCIMS inlet (Image by J.N. Smith).

## 1.4 Overview of Dissertation

The work presented in this dissertation discusses monoterpene +  $\text{NO}_3$  chemistry in order of increasing scale and complexity of its environment, beginning with molecular-level calculations, followed by laboratory measurements, and concluding with ambient observations.

Figure 1.14 highlights, using a different color for each chapter, the portion of the oxidation mechanism and/or gas-to-particle conversion process investigated in each chapter. Collectively, these works shed light on the entire process from the initial monoterpene +  $\text{NO}_3$  reaction to subsequent gas-phase chemistry to the partitioning of products into the particle phase.

Chapter 2 describes monoterpene +  $\text{NO}_3$  mechanism development using quantum chemical methods. In this chapter, we survey two critical reaction steps across five different cyclic monoterpenes (expanding upon published work by Kurtén et al. (2017) for  $\alpha$ -pinene and  $\Delta$ -3-carene). Specifically, we assess the fate of the first-generation alkyl and alkoxy radical by calculating the rate constants for all of the feasible unimolecular reaction pathways. The first-generation alkyl and alkoxy radical fates dictate whether radical propagation continues, enabling further oxidation, or if these intermediates terminate into a closed shell product. Understanding this balance between radical propagation and termination at the very early stages in this chemistry is important to be able to understand an individual monoterpene's potential to form SOA.

Chapter 3 expands upon the mechanisms developed in Chapter 2 by exploring the radical propagation pathways available to second-generation peroxy and alkoxy radicals for a single monoterpene ( $\Delta$ -3-carene). We calculate rate constants for peroxy and alkoxy H-shift reactions, peroxy and alkoxy addition over an internal double bond, and alkoxy decomposition. We then conducted  $\Delta$ -3-carene +  $\text{NO}_3$  chamber experiments, measuring the gas-phase oxidation products using CIMS with  $\text{NO}_3^-$  reagent ion, and compared the observed product distribution to our computationally-derived mechanism. This work identified which unimolecular pathways enable continued radical propagation and formation of highly oxidized products for  $\Delta$ -3-carene. These are some of the molecules we expect to be directly involved in SOA formation from this chemistry.

Chapter 4 moves away from the “bottom-up” approach somewhat and describes analysis of ambient nanoparticle composition taken using the TDCIMS in Hyytiälä, Finland, in the spring of 2014. In this dataset, we observe a handful of ions that exhibit a diel trend and we focus in particular on two major ions in the nighttime spectra that are likely thermally decomposed, semivolatile, monoterpene-derived organonitrates. To confirm the identity of these two ions and attempt to justify their presence in the nanoparticles, we built an observationally-constrained kinetics model to calculate the formation and partitioning of the proposed species. In contrast to Chapters 2 and 3 which explain the mechanisms leading to highly oxidized products, Chapter 4 indicates that even semivolatile organonitrates may be important in SOA formation and growth.

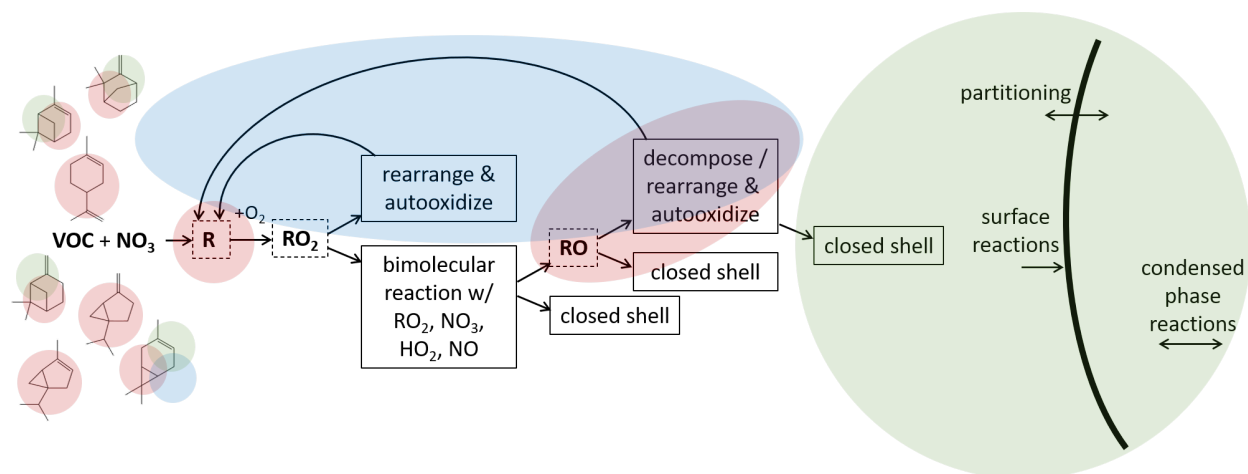


Figure 1.14: Overview schematic highlighting the reactions and processes explored in this work. Chapter 2 shown in red surveys first generation alkyl and alkoxy radical fates for several cyclic monoterpenes. Chapter 3 shown in blue explores the unimolecular reaction pathways available to second generation peroxy and alkoxy radicals from  $\Delta$ -3-carene. Chapter 4 shown in green considers gas-to-particle conversion processes to explain observations of ambient nanoparticle composition.



## Chapter 2

# Exploring the diversity of monoterpene oxidation via computational comparison of nitroxy-alkyl and nitroxy-alkoxy radical bond scissions

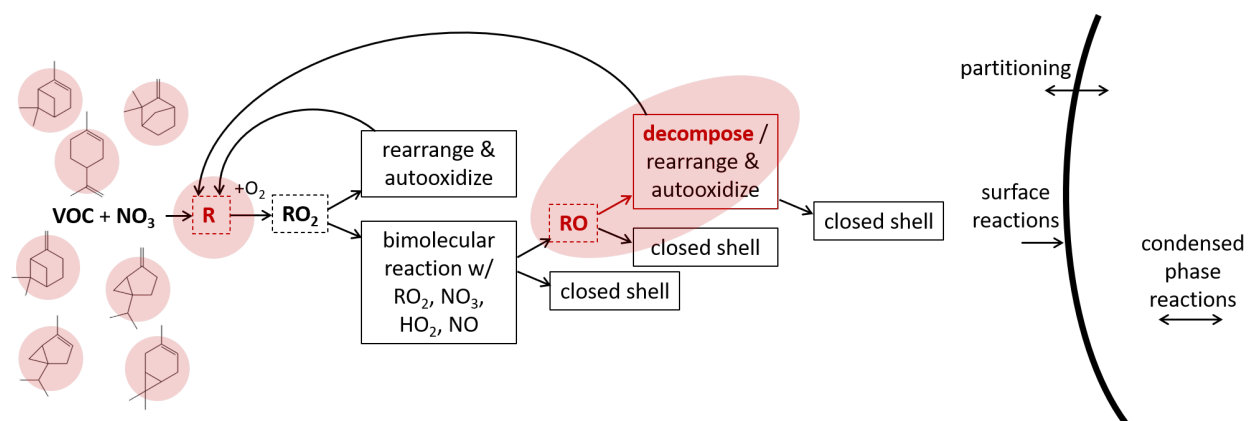


Figure 2.1: Overview schematic: Chapter 2 focuses on the first generation alkyl radical and alkoxy radical fates for seven cyclic monoterpenes.

## 2.1 Abstract

Monoterpene oxidation is an important atmospheric mechanism in many regions of the world, contributing to secondary organic aerosol (SOA) formation, ozone formation, and  $\text{NO}_x$  cycling. Results from laboratory studies suggest that in spite of structural similarities, different monoterpenes behave differently, for example forming drastically different yields of SOA from one to another. However, in models monoterpenes are often lumped into one or two parameterizations, assuming that the structurally similar species will behave similarly. Using quantum chemical calculations of unimolecular reaction kinetics, we have demonstrated that the fate of the first-generation alkyl and/or alkoxy radical following  $\text{NO}_3$  radical oxidation is quite different for 7 of the most prevalent cyclic monoterpenes:  $\alpha$ -pinene,  $\beta$ -pinene,  $\Delta$ -3-carene, sabinene, limonene, camphene, and  $\alpha$ -thujene. Radical intermediates such as these can either continue propagating through additional oxidation steps or may terminate through uni- or bi-molecular chemistry. Our results show in general that the monoterpenes with higher observed SOA yields generate radical intermediates with readily available radical propagation pathways, whereas those with lower yields have dominant termination pathways early in the oxidation mechanism, thus suggesting that the key inter-terpene differences affecting other atmospheric chemistry may occur quite early in the oxidation mechanism.

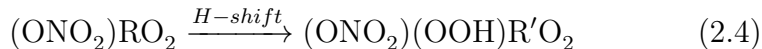
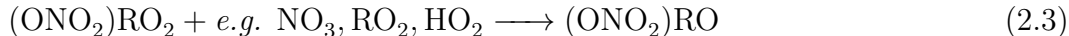
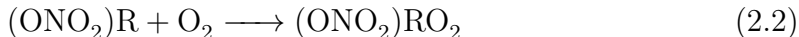
## 2.2 Introduction

Monoterpenes ( $\text{C}_{10}\text{H}_{16}$ ) have long been studied as a significant contributor to secondary organic aerosol (SOA) formation and growth. They are estimated to contribute approximately 15% of global biogenic (non-methane) volatile organic compound (VOC) emissions, and due to their relatively large and branched carbon backbone, monoterpenes tend to have a high yield of condensable products once oxidized [64]. Field observations around the world have

shown that a major fraction of organic aerosol (OA) is secondary (SOA) in nature [178], meaning that it forms from chemical reactions (e.g. oxidation) of gas-phase organic precursors, and individual field studies have been able to attribute substantial fractions of observed SOA to monoterpene-derived products specifically. For example, in the southeastern US it was estimated that monoterpene chemistry contributed to roughly half of the total observed submicron OA [177]. And in the boreal forest, condensation of oxidized monoterpene products are found to fully account for the growth of newly formed nanoparticles [115]. While we know that aerosol in the atmosphere plays an important role in the climate system by interacting with incoming solar radiation and seeding clouds, aerosol represents the largest source of uncertainty in estimates of radiative forcing in the atmosphere due to its complexity [119]. Many formation and aging processes as well as physicochemical properties are still poorly understood [69, 152, 14]. Further, small sized particles (i.e. size ranges often dominated by formation and growth of SOA) can have adverse effects on human health upon inhalation due to their ability to permeate lung tissue and enter the bloodstream [138, 150, 8], which gives an additional layer of urgency to better understand SOA formation and growth processes. Due to their structural similarities, oxidation of different monoterpenes proceed along quite similar mechanistic pathways. However, numerous studies have shown striking differences in SOA yields between different monoterpenes [68, 62, 54, 124], indicating that there must be impactful differences in their oxidation mechanisms.

In addition to monoterpene oxidation chemistry being an important component of ambient SOA formation,  $\text{NO}_3$  radical oxidation of monoterpenes in particular is expected to contribute significantly to SOA [141, 124], but this chemistry is under-studied compared to daytime oxidants OH and  $\text{O}_3$ . Kurtén et al. investigated the detailed oxidation mechanisms for two chemical systems with one of the most extreme SOA yield disparities: the  $\text{NO}_3$  radical oxidation of  $\alpha$ -pinene and  $\Delta$ -3-carene [94]. These two bicyclic monoterpenes differ only by the size and placement of their secondary ring structure, and yet  $\alpha$ -pinene has a negligible SOA yield from  $\text{NO}_3$  oxidation [68, 157, 122, 54, 135], while  $\Delta$ -3-carene has observed

SOA yields ranging from 12-74% [62, 68, 116, 54]. Computational modeling probing the kinetics of the known plausible 1<sup>st</sup> generation oxidation steps (reactions 2.1 - 2.5) revealed that the mechanisms for these two monoterpenes diverge at the nitroxy-alkoxy radical (RO) (reaction 2.5). The  $\alpha$ -pinene-derived RO decomposes at the C–C bond farther from the 4-membered ring, leading primarily to the closed-shell and relatively volatile product pinonaldehyde, whereas the  $\Delta$ -3-carene-derived RO preferentially decomposes at the C–C bond  $\alpha$  to the 3-membered ring, generating a primary alkyl radical [94] that can undergo further uni- and bi-molecular reactions, eventually leading to low enough volatility products which likely contribute to SOA [36].



In this study, we expand the work by Kurtén et al. to five more cyclic monoterpenes: limonene,  $\alpha$ -thujene, sabinene,  $\beta$ -pinene, and camphene. Our objective is to better characterize the structural nuances that lead to important mechanistic differences. For the bicyclic terpenes ( $\alpha$ -thujene, sabinene,  $\beta$ -pinene, and camphene), a ring-opening reaction from rearrangement of the original nitroxy-alkyl radical is possible in addition to the  $\beta$ -alkoxy scissions that were the focus of the Kurtén et al. study, and therefore we focus on both of these types of reactions here. Understanding the branching at these two steps provides indicators for what types of reactions remain available for each monoterpene, or conversely, which monoter-

penes are likely to terminate to a closed shell product earlier than others, producing higher volatility products and correspondingly lower SOA yields.

Large scale modeling approaches for predicting aerosol budgets must by necessity simplify this complex chemistry and typically do so by lumping together all monoterpenes and parameterizing the monoterpene SOA yield using laboratory yields from a few model compounds (often emphasizing  $\alpha$ -pinene) [84, 109]. This approach is problematic, however, given the enormous variability of SOA yields for different monoterpene and oxidation combinations. One modeling study showed that adjusting only the model monoterpene system by using  $\beta$ -pinene +  $\text{NO}_3$  to represent all monoterpene +  $\text{NO}_3$  yields instead of  $\alpha$ -pinene, more than 50% of the estimated monoterpene-derived SOA in the US originated from  $\text{NO}_3$  oxidation [141]. Combined with Kurtén et al. [94], the present study elucidates the ring-opened fate of 6 of the 8 most abundantly emitted monoterpenes globally [64], nearly 11% of total global BVOC emissions, as well as  $\alpha$ -thujene as a structural analog to  $\alpha$ -pinene. This dataset is a significant milestone in understanding the gas-phase mechanisms that do or do not lead to SOA and may be a jumping off point to reframe the simpler monoterpene SOA yield parameterizations necessary to improve larger scale modeling efforts.

## 2.3 Methods

In order to assess the fate of the alkyl and alkoxy radical intermediates, we have calculated the rate constant for each possible reaction using quantum chemical methods and multi-conformer transition state theory (MC-TST). From these rate constants we are able to calculate branching ratios for these radical intermediates. For each monoterpene studied, we assumed the dominant  $\text{NO}_3$  addition pathway leading to the more stable tertiary alkyl radical. We then calculated the ring opening rate constant for each nitroxy-alkyl isomer (2 for endocyclic monoterpenes and 1 for exocyclic monoterpenes) and alkoxy scission

rate constant for each nitroxy-alkoxy stereoisomer (4 for endocyclic monoterpenes and 2 for exocyclic monoterpenes). Nitroxy-alkoxy reactant stereoisomer structures are shown in Figure 2.2, and the nitroxy-alkyl stereoisomer structures correspond to these, omitting the alkoxy stereocenter.

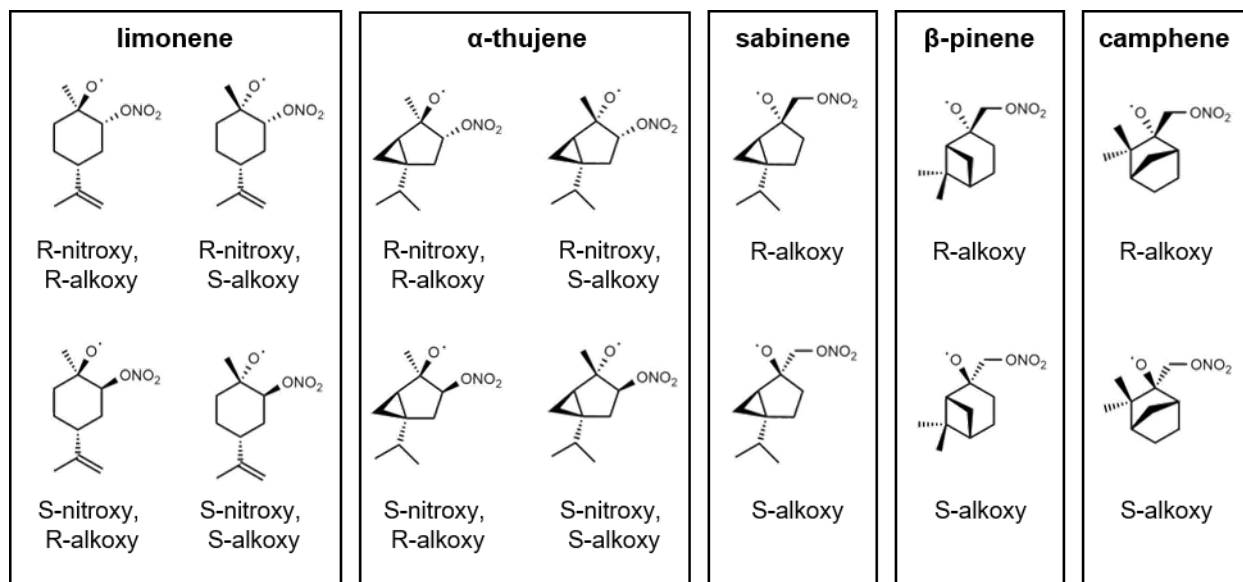


Figure 2.2: Molecular structures of nitroxy-alkoxy stereoisomers of limonene,  $\alpha$ -thujene, sabinene,  $\beta$ -pinene, and camphene assessed in this study.

Rate constants were calculated using the procedure described in Møller et al. [118], with some modifications similar to those used in Kurtén et al. [94] and Draper et al. [36]. Briefly, systematic conformer sampling of each reactant, product, and transition state species was performed with the Spartan'16 and Spartan'18 software (Wavefunction, Inc.) using the MMFF method [67]. The keywords KEEPALL and FFHINT were applied to the conformer search to ensure all conformers were stored in the output and that a neutral charge was applied to the radical center of each molecule. Geometry optimizations and frequency calculations were then performed with Gaussian 09 and 16 [52, 53] using DFT methods. Prior to conformer sampling, an arbitrary transition state structure for each reaction of interest was optimized at the B3LYP/6-31+G(d) level, with the TS search preceded by a partial optimization constraining the length of the bond being broken to 2.1 Å for alkoxy scissions and 2.08 Å for alkyl ring opening reactions [94]. The unconstrained transition state geometry

was then found via a transition state optimization, also at the B3LYP/6-31+G(d) level, and this geometry was used as the input for the transition state conformer sampling, with the breaking bond length again constrained to the value actually found in the TS optimization. Each identified conformer was then optimized at the B3LYP/6-31+G(d) level (constrained optimization followed by transition state optimization for transition states). Unique geometries (determined based on electronic energy and dipole moment) [118] within 2 kcal/mol of the lowest energy conformer were then re-optimized at the  $\omega$ B97X-D/aug-cc-pVTZ level. [23, 87] Finally, single-point energies were calculated using ROHF-DLPNO-CCSD(T)/aug-cc-pVTZ with tight pair natural orbital criteria for the lowest energy conformer of each species using ORCA 4.2.1 [123, 145] to obtain a more accurate electronic energy. These DLPNO-CCSD(T) calculations have been used in place of canonical coupled cluster calculations previously for similar molecules [36] as they maintain high accuracy without being prohibitively expensive computationally for the size of molecules in this study. [145, 121] For the lowest energy conformer of each transition state, intrinsic reaction coordinate (IRC) calculations were run at the B3LYP/6-31+G(d) level to determine the reactant and product conformer connected to the transition state. These geometries were then optimized at the  $\omega$ B97X-D/aug-cc-pVTZ level and forward/reverse energy barriers were used in conjunction with the imaginary frequency of the transition state to calculate the Eckart tunneling correction factor [38]. Rate constants were then calculated using multi-conformer transition state theory (MC-TST) [118].

For the bicyclic monoterpenes (i.e.  $\alpha$ -thujene, sabinene,  $\beta$ -pinene, and camphene), the initial alkyl radical may rearrange to open the minor 3-, 4-, or 5-membered ring. These reaction dynamics were simulated for sabinene and are in progress for  $\alpha$ -thujene,  $\beta$ -pinene, and camphene using the Master Equation Solver for Multi Energy-well Reactions (MESMER) software [60] to determine whether the ring-opening channel is likely to be competitive with peroxy radical formation via O<sub>2</sub> addition. The zero-point corrected energy, vibrational frequencies, and rotational constants were taken from the  $\omega$ B97X-D/aug-cc-pVTZ calculations.

Simulation conditions and parameters used were the same as those employed in simulation for the  $\alpha$ -pinene ring-break analog [94]. The Inverse Laplace Transform (ILT) method was used for the barrierless association reactions modeled ( $\text{NO}_3$  and  $\text{O}_2$  addition), since no transition state was available for those. Pre-exponential factors used were  $1.2 \times 10^{-12}$  and  $6 \times 10^{-12}$   $\text{cm}^3 \text{ molec}^{-1} \text{ s}^{-1}$  for  $\text{NO}_3$  addition and  $\text{O}_2$  addition respectively. A value of -0.5 was used as a modified Arrhenius parameter for both reactions. The transition state for the ring-break reaction was calculated as described above and was modeled using standard RRKM theory with Eckart tunneling correction. Exponential-down collisional energy transfer was used for modeling sabinene- $\text{ONO}_2$  species energy distribution, with parameter  $\Delta E_{\text{down}} = 225 \text{ cm}^{-1}$ . Lennard-Jones parameter values were  $\varepsilon = 600 \text{ K}$  and  $\sigma = 6.5 \text{ \AA}$ .  $\text{N}_2$  was assigned as the bath gas, with Lennard-Jones parameters  $\varepsilon = 91.85 \text{ K}$  and  $\sigma = 3.919 \text{ \AA}$ . Simulated energy grains spanned  $50 \text{ k}_B\text{T}$  above the highest stationary point, with a grain size value of  $15 \text{ cm}^{-1}$ . A very high  $\text{NO}_3$  concentration ( $10^{18} \text{ molec cm}^{-3}$ ) was used to ensure rapid formation of the modeled sabinene- $\text{ONO}_2$  intermediate at the start of the simulation (i.e. as close to  $t=0$  as possible). This unrealistic value was used solely for ease of simulation and has no effect on the other reaction steps. The  $\text{O}_2$  concentration used was  $5.34 \times 10^{18} \text{ molec cm}^{-3}$  (0.2 atm).

## 2.4 Results & Discussion

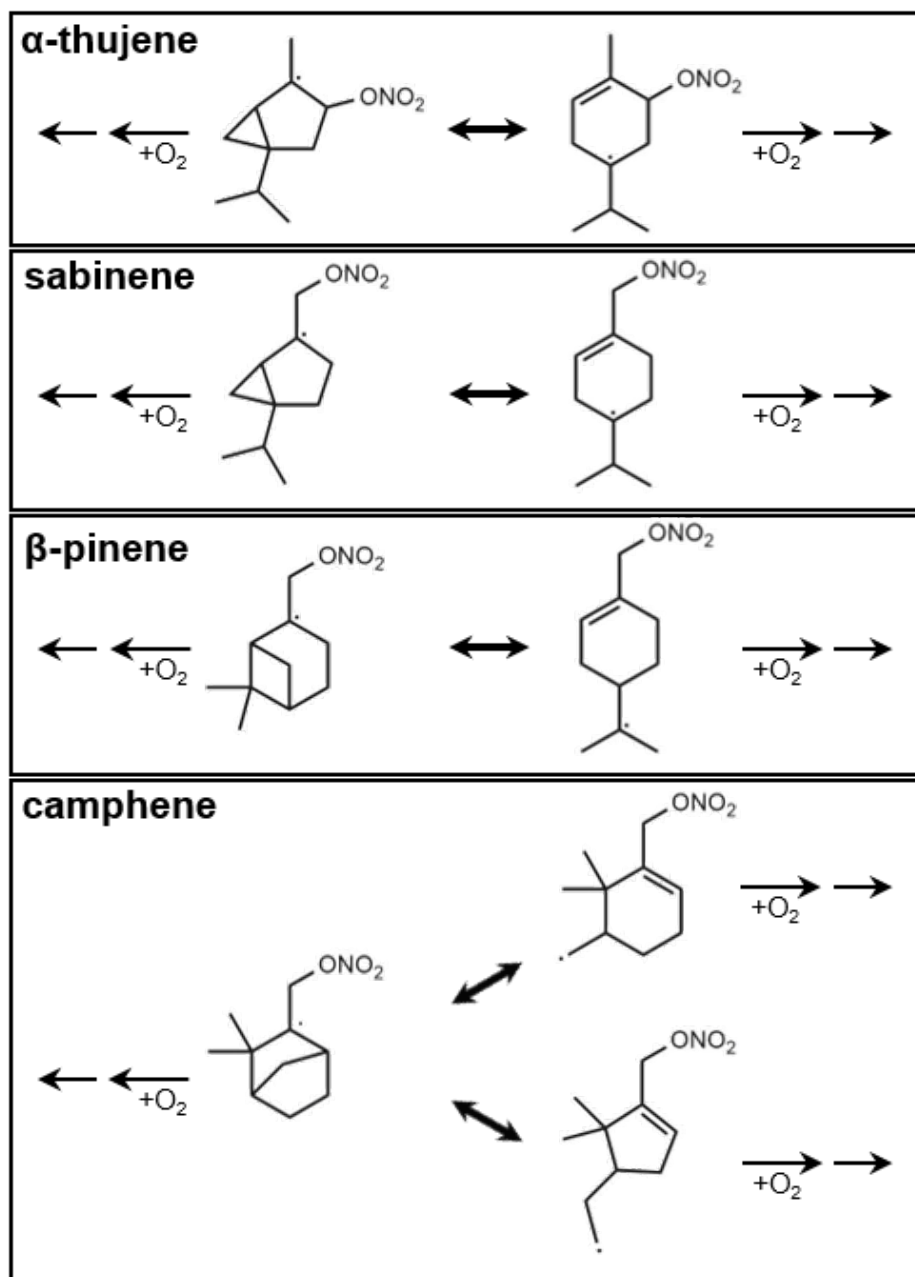
### 2.4.1 Nitroxy alkyl radical ring opening reactions

We start by comparing the branching ratios for  $\text{O}_2$  addition and the ring opening rearrangement of our initial nitroxy-alkyl radicals.  $\text{O}_2$  addition to alkyl radicals is extremely fast in the atmosphere (pseudo-1<sup>st</sup> order rate  $\sim 10^7 \text{ s}^{-1}$ ) [134] due to the high abundance of  $\text{O}_2$ , and therefore this is generally assumed to be the dominant path during VOC oxidation. However, radical addition to an unsaturated VOC is an exothermic process, and some of that extra



energy may allow the adduct to overcome the energy barrier of a subsequent unimolecular reaction. For bicyclic compounds where the initial radical center is  $\alpha$  to a strained ring, it may be energetically favorable to cleave an adjacent C–C bond to release that ring strain, resulting in a rearrangement of the radical and formation of a new double bond to maintain saturation. Scheme 2.1 shows these reactions for each of the bicyclic monoterpenes studied here.

The energy diagram and MESMER simulation are shown in Figure 2.3 for sabinene. We can see from the MESMER simulation (Figure 2.3b) that the ring-opening reaction has a larger branching ratio ( $\sim 80\%$ ) than the  $O_2$  addition pathway ( $\sim 20\%$ ). The analogous reaction was studied in Kurtén et al. for  $\alpha$ -pinene and was found to not be competitive with  $O_2$  addition. The forward barrier for  $\alpha$ -pinene was  $\sim 14$  kcal/mol, [94] whereas we can see it is only 9.90 kcal/mol for sabinene (Figure 2.3a). While we have not yet completed the MESMER simulations for the remaining bicyclic monoterpenes in this study, we can hypothesize whether the ring-opening reaction might be competitive based on their forward barrier energies and assuming that the  $NO_3$  addition reaction releases a comparable amount of energy as calculated for sabinene. Both  $\alpha$ -thujene (12.8 kcal/mol (R) and 12.5 kcal/mol (S)) and  $\beta$ -pinene (13.0 kcal/mol) have forward barriers between sabinene and  $\alpha$ -pinene, calculated based on the zero-point corrected DLPNO-CCSD(T) single point energies, so it is possible that one or both of these can undergo the ring-opening reaction competitively with  $O_2$  addition. Camphene almost certainly has too high of an energy barrier ( $>24.9$  kcal/mol) for this reaction to occur. For sabinene, this ring opening pathway appears to be less important for  $NO_3$ -initiated oxidation than observed in previous work for the OH counterpart due to the lower exothermicity of  $NO_3$  addition compared to OH addition and the slightly higher energy barrier for subsequent ring opening [168], perhaps indicating that alkyl radical ring opening in OH + monoterpene adducts might be somewhat more favorable and should be explored in future studies.



Scheme 2.1: Ring opening radical rearrangement reactions for nitroxy-alkyl radicals from bicyclic monoterpenes

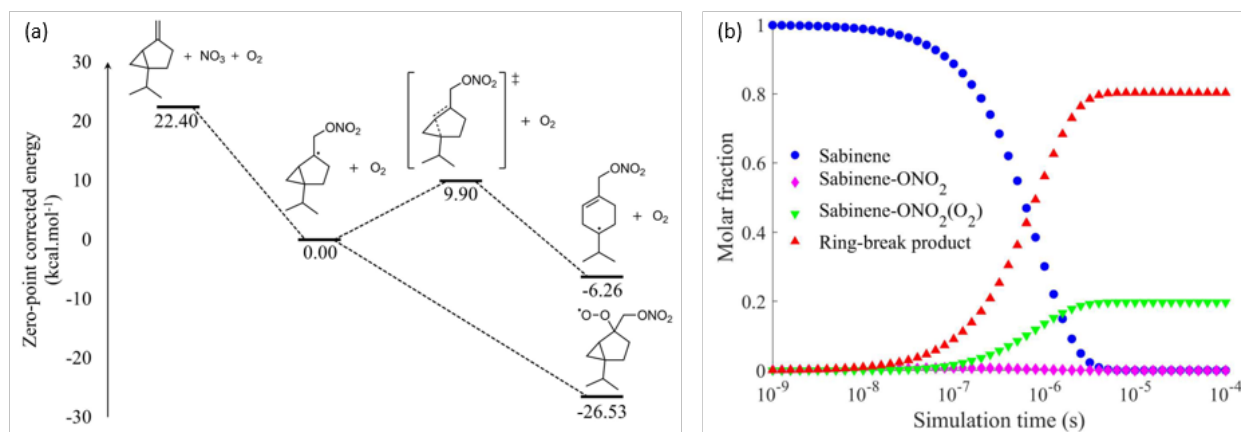


Figure 2.3: Zero-point corrected energy diagram calculated at the  $\omega$ B97X-D/aug-cc-pVTZ level (a) and species time evolution profile from MESMER simulation at 298.15 K and 760 Torr (b) comparing the sabinene +  $\text{NO}_3$  alkyl ring-opening reaction vs.  $\text{O}_2$  addition

## 2.4.2 Nitroxy alkoxy radical $\beta$ -scission reactions

In Table 2.1, we have compiled the zero-point corrected forward barriers and MC-TST rate constants for each alkoxy scission reaction studied (see labeling scheme in Figure 2.4). For completeness, we have also included the barriers and rate constants for  $\alpha$ -pinene and  $\Delta$ -3-carene calculated using the same methods in Kurtén et al. [94]. Energy barriers are compared to those predicted from the structural activity relationship (SAR) describing this chemistry [165]. For  $\alpha$ -thujene and limonene, the SAR accurately predicts the relative favorability of each scission pathway, where the release of (5- or 6-membered) ring strain and extra stability afforded to the transition state by the  $-\text{ONO}_2$  group  $\beta$  to the alkoxy group (as well as the destabilization of a radical center on a cyclopropyl group in  $\alpha$ -thujene) leads to the right side scission (R $\beta$ 1) being most favorable, leading to loss of  $\text{NO}_2$  and oxidative chain termination. However, the SAR predictions are less accurate for the other monoterpenes studied here. The SAR correctly predicts the most favorable scission pathway for sabinene but suggests opposite relative favorability for the other two channels. For  $\beta$ -pinene and camphene, the SAR does not predict the lowest energy pathway calculated here. These observed inconsis-

tencies indicate that the bicyclic structure of these monoterpenes may introduce additional layers of complexity not fully incorporated into the SAR.

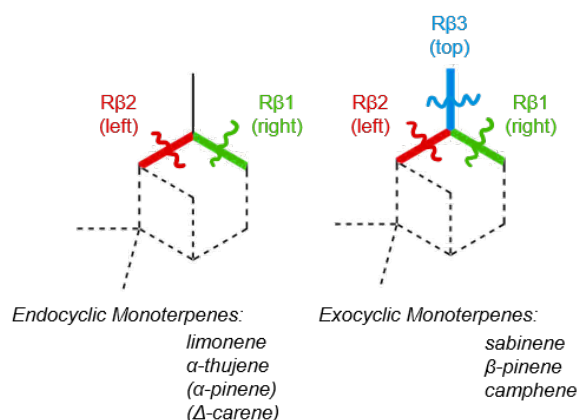


Figure 2.4: Reaction labeling scheme for nitroso-alkoxy scission reactions. Rate constants were calculated for the “right” and “left” C–C scissions for endocyclic monoterpenes and for the “right,” “left,” and “top” C–C scissions for exocyclic monoterpenes with all molecules drawn in comparable orientation, as shown in Figure 2.2 above..

In general, we find that scissions resulting in a radical center on a 3-, 4-, or 5-membered ring structure have the highest energy barrier, whereas the SAR indicates ring substituents (except a cyclopropyl ring)  $\beta$  to the alkoxy group significantly decrease the overall scission barrier, tipping the scales over other substituent effects [165]. Interestingly, for  $\beta$ -pinene we find all three scission pathways are competitive and each stereoisomer has a slight preference for a different pathway: the S-alkoxy isomer preferentially cleaving the right side C–C bond opening up the 6-membered ring and the R-alkoxy isomer preferentially cleaving the top C–C bond, leaving the 6-membered ring intact. For all of the exocyclic monoterpenes we observe this top scission to be more favorable than the left scission that would result in a radical centered on a strained ring, though it is only ever observed to be most favorable in  $\beta$ -pinene. These observations indicate that the SAR may both overestimate the impact of  $\beta$  ring substituents and underestimate the contribution of the  $-\text{ONO}_2$  group somewhat.

Additionally, some experimental evidence in the bulk liquid phase indicates that an  $\alpha$ -cyclopropyl group will increase the lability of other  $C_\alpha-C_\beta$  bonds during similar alkoxy

Table 2.1: Barriers (zero-point corrected transition state - reactant electronic energy) and Multi-Conformer Transition State Theory (MC-TST) rate constants calculated at the  $\omega$ B97X-D/aug-cc-pVTZ level for alkoxy  $\beta$ -scission reactions at 298.15 K.

	Barrier (this study) (kcal mol <sup>-1</sup> )			Rate Coefficient (this study) (s <sup>-1</sup> )			SAR predicted barrier (kcal mol <sup>-1</sup> )		
	R $\beta$ 1 (right)	R $\beta$ 2 (left)	R $\beta$ 3 (top)	R $\beta$ 1 (right)	R $\beta$ 2 (left)	R $\beta$ 3 (top)	R $\beta$ 1 (right)	R $\beta$ 2 (left)	R $\beta$ 3 (top)
limonene adduct stereoisomer									
R-nitroxy, R-alkoxy	8.49	11.49	-	6.75 x 10 <sup>6</sup>	1.65 x 10 <sup>4</sup>	-	6.5	9.3	15.9
R-nitroxy, S-alkoxy	8.74	11.18	-	3.32 x 10 <sup>6</sup>	1.38 x 10 <sup>5</sup>	-			
S-nitroxy, R-alkoxy	8.32	11.21	-	6.83 x 10 <sup>6</sup>	6.44 x 10 <sup>4</sup>	-			
S-nitroxy, S-alkoxy	8.05	10.10	-	6.32 x 10 <sup>6</sup>	4.02 x 10 <sup>5</sup>	-			
$\alpha$ -thujene adduct stereoisomer	Barrier (this study)			Rate Coefficient (this study)			SAR predicted barrier		
R-nitroxy, R-alkoxy	6.41	15.73	-	1.37 x 10 <sup>8</sup>	2.46 x 10 <sup>1</sup>	-	4.1	9.3	15.9
R-nitroxy, S-alkoxy	6.61	15.46	-	6.69 x 10 <sup>7</sup>	7.55 x 10 <sup>1</sup>	-			
S-nitroxy, R-alkoxy	7.01	14.86	-	7.70 x 10 <sup>7</sup>	1.82 x 10 <sup>2</sup>	-			
S-nitroxy, S-alkoxy	6.87	14.59	-	5.11 x 10 <sup>7</sup>	1.57 x 10 <sup>2</sup>	-			
sabinene adduct stereoisomer	Barrier (this study)			Rate Coefficient (this study)			SAR predicted barrier		
R-alkoxy	10.11	15.38	11.79	1.56 x 10 <sup>5</sup>	70.4	2.02 x 10 <sup>4</sup>	6.9	9.3	13.1
S-alkoxy	9.46	15.21	11.04	5.98 x 10 <sup>5</sup>	55.1	4.66 x 10 <sup>4</sup>			
$\beta$ -pinene adduct stereoisomer	Barrier (this study)			Rate Coefficient (this study)			SAR predicted barrier		
R-alkoxy	10.25	10.52	9.20	4.95 x 10 <sup>5</sup>	1.69 x 10 <sup>5</sup>	1.39 x 10 <sup>6</sup>	9.3	5.1	13.1
S-alkoxy	10.20	11.85	11.61	2.10 x 10 <sup>5</sup>	2.62 x 10 <sup>4</sup>	1.33 x 10 <sup>4</sup>			
camphene adduct stereoisomer	Barrier (this study)			Rate Coefficient (this study)			SAR predicted barrier		
R-alkoxy	4.30	0.87	11.19	1.66 x 10 <sup>9</sup>	1.37 x 10 <sup>12</sup>	2.34 x 10 <sup>4</sup>	2.3	2.5	13.1
S-alkoxy	5.36	1.90	14.14	6.04 x 10 <sup>8</sup>	1.88 x 10 <sup>11</sup>	2.39 x 10 <sup>2</sup>			
$\alpha$ -pinene adduct stereoisomer	Barrier <sup>15</sup>			Rate Coefficient <sup>15</sup>			SAR predicted barrier		
R-nitroxy, R-alkoxy	6.1	10.6	-	1.7 x 10 <sup>8</sup>	1.3 x 10 <sup>5</sup>	-	6.5	5.1	15.9
R-nitroxy, S-alkoxy	4.8	9.4	-	1.5 x 10 <sup>9</sup>	3.6 x 10 <sup>6</sup>	-			
S-nitroxy, R-alkoxy	6.7	10.4	-	7.3 x 10 <sup>7</sup>	3.7 x 10 <sup>5</sup>	-			
S-nitroxy, S-alkoxy	8.6	10.5	-	2.2 x 10 <sup>6</sup>	1.0 x 10 <sup>5</sup>	-			
$\Delta$ -carene adduct stereoisomer	Barrier <sup>15</sup>			Rate Coefficient <sup>15</sup>			SAR predicted barrier		
R-nitroxy, R-alkoxy	8.4	7.4	-	8.2 x 10 <sup>6</sup>	2.7 x 10 <sup>7</sup>	-	6.5	9.3	15.9
R-nitroxy, S-alkoxy	9.2	8.3	-	1.7 x 10 <sup>6</sup>	8.4 x 10 <sup>6</sup>	-			
S-nitroxy, R-alkoxy	8.4	8.4	-	3.3 x 10 <sup>6</sup>	6.2 x 10 <sup>6</sup>	-			
S-nitroxy, S-alkoxy	8.6	8.1	-	2.6 x 10 <sup>6</sup>	9.0 x 10 <sup>6</sup>	-			

scission reactions. This observation can be explained by a stability boost from overlap of the C–C bonding orbital with the forming C=O bond [15, 148]. This effect would further promote the right and/or top side scissions for  $\alpha$ -thujene and sabinene – for sabinene perhaps indicating that the effect may not necessarily be underestimated by the SAR. The bulk phase experimental evidence suggests that this effect is not observed for  $\alpha$ -cyclobutyl groups however, and those scissions are governed by radical stability alone [15], still suggesting some amount of underestimation of the  $-\text{ONO}_2$  group for the other exocyclic species with larger secondary rings ( $\beta$ -pinene and camphene).

### 2.4.3 Proposed fate of each monoterpene

Proposed mechanisms for each monoterpene studied (as well as  $\alpha$ -pinene and  $\Delta$ -3-carene reproduced from Kurtén et al. [94] for completeness) are shown from Scheme 2.2 to Scheme 2.8. We can see that certain structural features favor specific reaction pathways. However, we also see that each unique permutation of similar structural features leads to each monoterpene having its own unique reactivity beginning early in the oxidative chain. It logically follows then that the SOA yield from each monoterpene would be different. Broadly, we see that monoterpenes with the potential for multiple generations of radical propagation reactions here are the same monoterpenes that exhibit moderate to high SOA yields in the laboratory [54, 124]. Conversely,  $\alpha$ -pinene, which has been shown to have negligible SOA yields in  $\text{NO}_3$  oxidation, has a dominant termination pathway (RO scission leading to  $\text{NO}_2$  loss) quite early in its oxidative chain suggesting it will have a significantly lower yield of low volatility products that would be expected to dominate SOA formation and growth. Experimental SOA yields from  $\text{NO}_3$  radical chemistry have not yet been measured for  $\alpha$ -thujene or camphene, but mechanistically we would expect  $\alpha$ -thujene to fall on the lower end of the spectrum due to the availability of the analogous  $\text{NO}_2$  loss seen in  $\alpha$ -pinene, and we would expect camphene to fall on the higher end of the spectrum since its dominant scission pathways

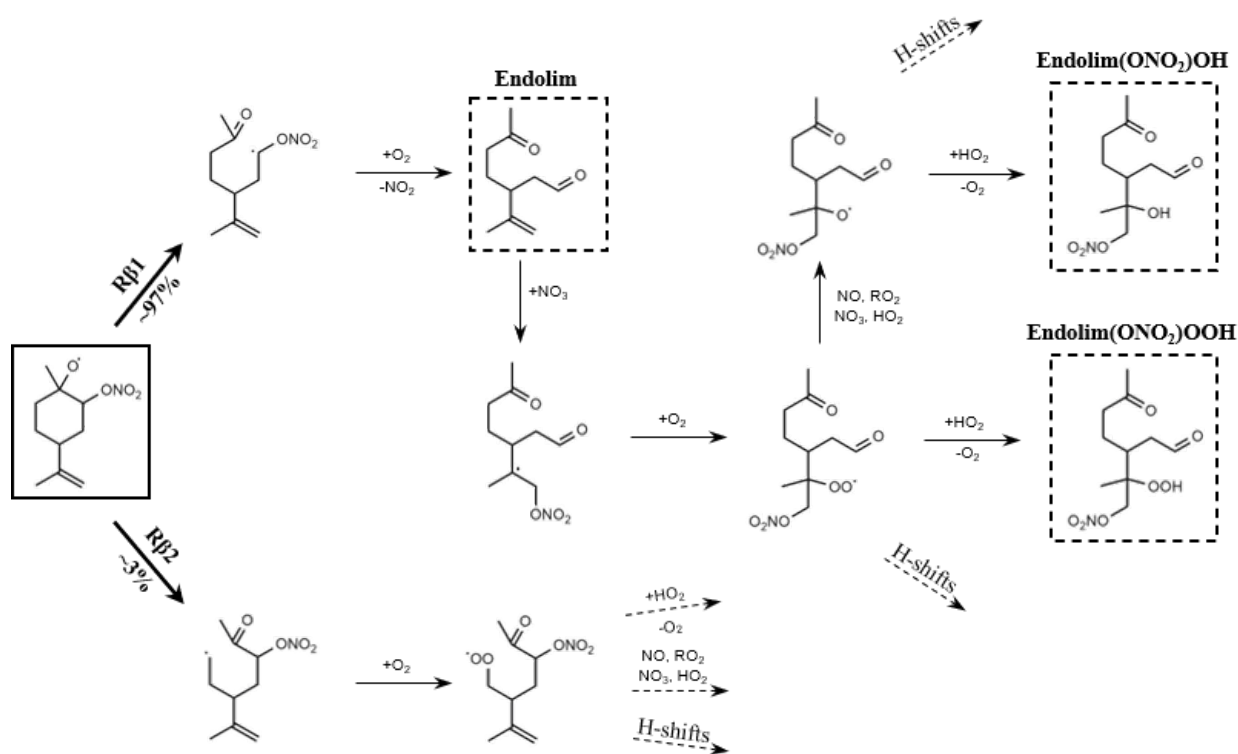
continue radical propagation, and are calculated to be extremely fast, even compared to the quite fast scission pathways of the other monoterpenes studied.

## **Limonene**

Beginning with the simplest monoterpene studied here, insofar as it is only monocyclic and therefore does not have the additional mechanistic complexity afforded by a secondary ring structure, the proposed fate of limonene is shown in Scheme 2.2. We assume  $\text{NO}_3$  addition will occur over the endocyclic double bond as shown by previous studies [157, 56], and no available alkyl radical rearrangement pathway exists, so we consider just the right and left side alkoxy scission reactions. Calculated rate constants indicate a vast majority ( $\sim 97\%$ ) of limonene intermediates will favor the right side scission, leading to  $\text{NO}_2$  loss and closed shell endolim. While the non-dominant left side scission produces a primary alkyl radical that is expected to undergo further generations of radical propagation, the dominance of the pathway leading to an early radical termination might suggest a fairly low SOA yield and organonitrates yield. However, limonene has an additional double bond, which likely undergoes a second generation of  $\text{NO}_3$  addition. Endolim( $\text{ONO}_2$ )OOH and endolim( $\text{ONO}_2$ )OH have both been observed in experiments [50], and their precursor  $\text{RO}_2$  and RO intermediates are likely susceptible to additional radical propagation reactions leading to even more highly oxidized organonitrates [36], supporting the relatively high SOA and organonitrates yield observed for limonene [54].

## **$\alpha$ -Thujene**

Next we show our proposed mechanism for  $\alpha$ -thujene in Scheme 2.3. Based on the structural similarities to  $\alpha$ -pinene (location of strained secondary ring with respect to double bond) we expected  $\alpha$ -thujene to have a similar fate to that of  $\alpha$ -pinene proposed in Kurtén et al. [94]



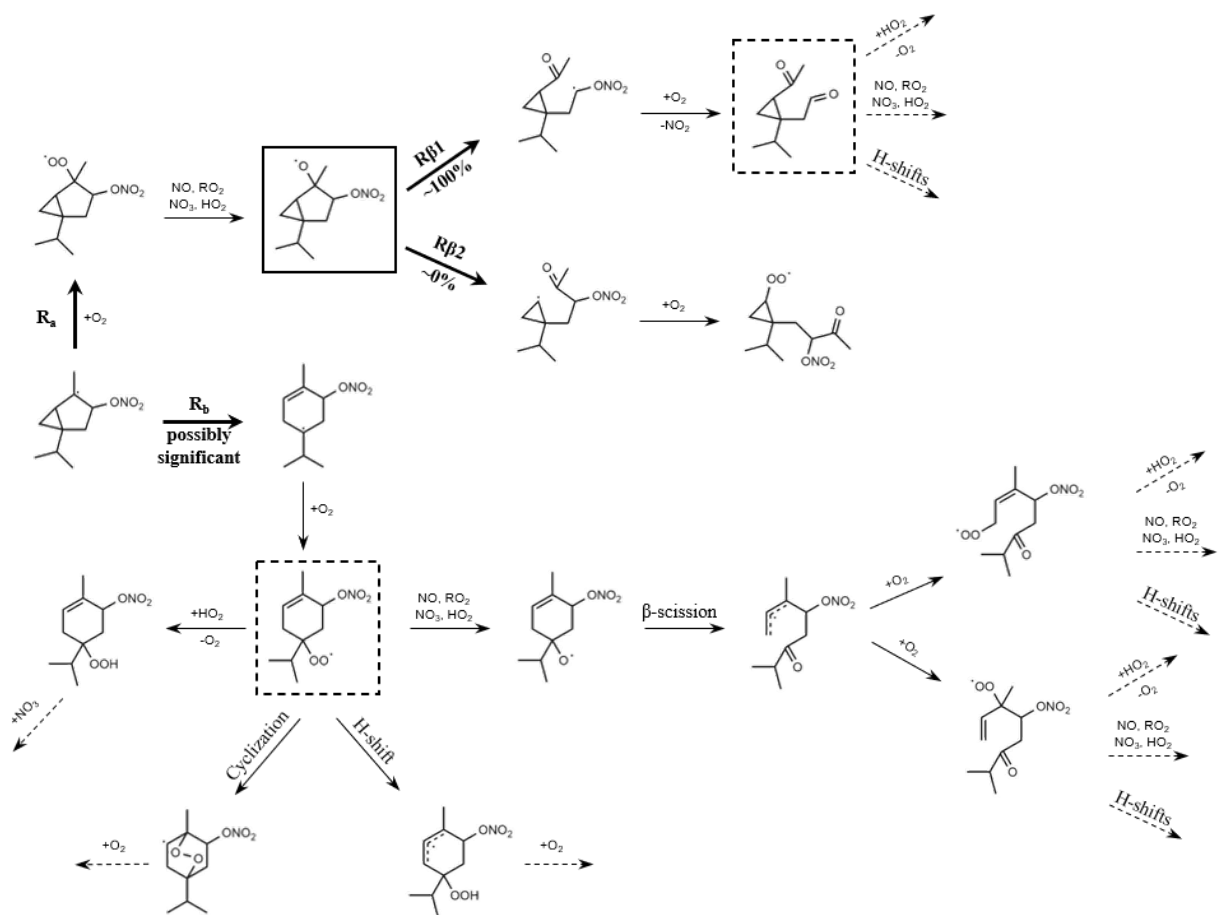
Scheme 2.2: Proposed fate of limonene +  $\text{NO}_3$  beginning from the 1<sup>st</sup>-generation nitroxy-alkoxy radical outlined in black. Bold arrows show the  $\beta$ -scission reactions studied here, including calculated, stereoisomer-averaged branching ratios. Dashed boxes indicate selected products observed experimentally.



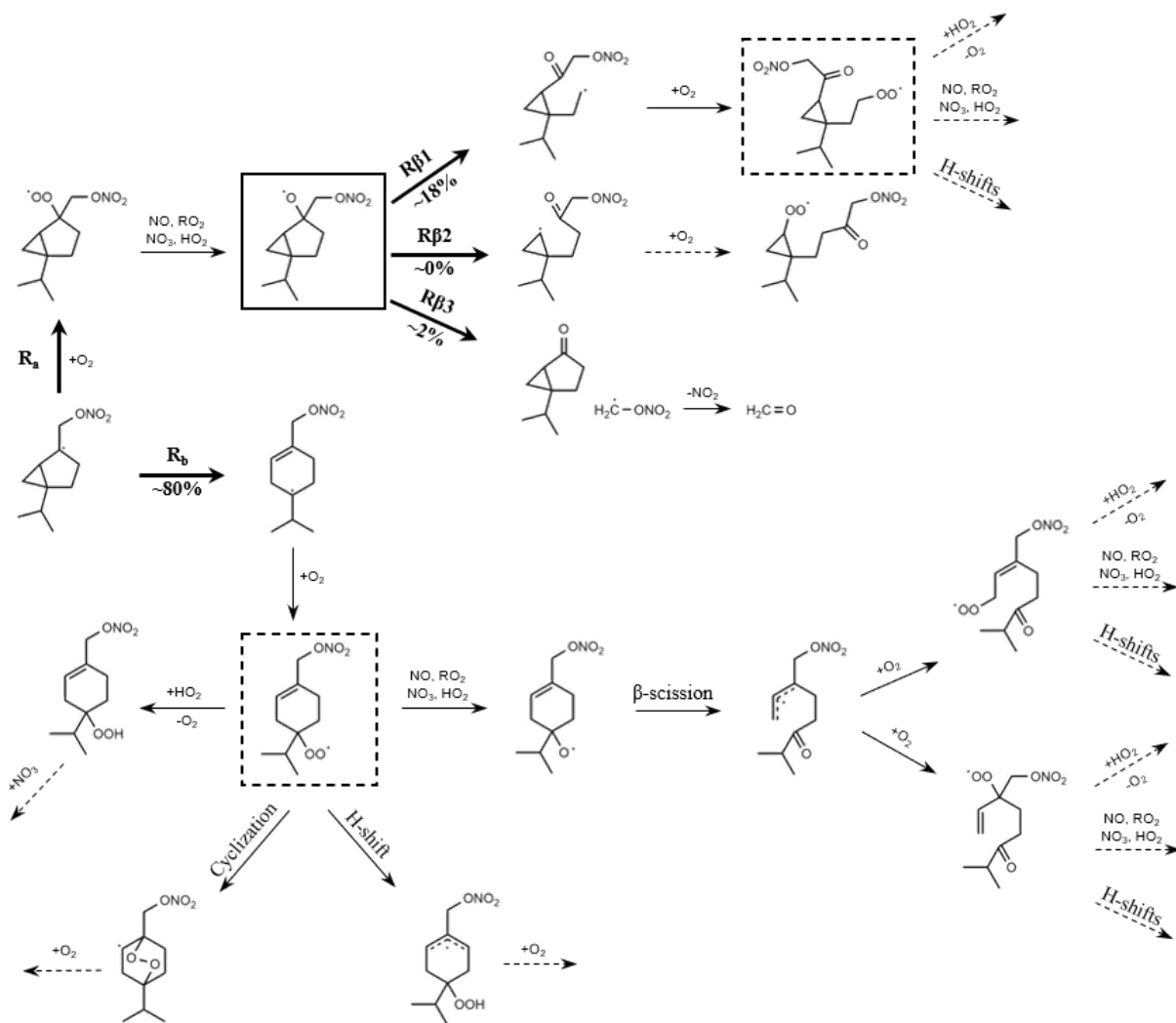
– dominance of the right side alkoxy scission resulting in loss of  $\text{NO}_2$  and early termination of the radical. However, since  $\alpha$ -thujene has a 3-membered ring instead of a 4-membered ring, the additional ring strain may be significant enough that the earlier alkyl ring opening radical rearrangement reaction is favorable. This radical rearrangement would allow for additional radical propagation reactions as well as 2<sup>nd</sup> generation  $\text{NO}_3$  radical oxidation to the newly formed double bond, which we expect to lead to a much larger distribution of highly oxidized products than would be observed for  $\alpha$ -pinene. For the percentage that do undergo the more typical  $\text{O}_2$  addition and alkoxy scission, the right side scission is indeed dominant, as predicted, perhaps even with an extra boost from the  $\alpha$ -cyclopropyl group described above. This pathway likely leads to a non-trivial yield of fairly volatile closed shell products, which may make the overall SOA yield from  $\alpha$ -thujene low.

## Sabinene

Sabinene (Scheme 2.4) differs from  $\alpha$ -thujene only in its exocyclic double bond compared to  $\alpha$ -thujene's endocyclic double bond. Since the most favorable  $\text{NO}_3$  addition pathway results in the same tertiary radical center as  $\alpha$ -thujene, sabinene undergoes the alkyl radical ring opening reaction in high yield, leading to further radical propagation and the possibility for 2<sup>nd</sup> generation  $\text{NO}_3$  oxidation. Along the traditional  $\text{RO}_2$  pathway for the other 20%, sabinene also favors the right side alkoxy scission. However, unlike in  $\alpha$ -thujene, this pathway does not terminate the radical right away and instead forms a primary radical that can undergo additional radical propagation steps leading to highly functionalized low volatility products. The combination of the  $\alpha$ -cyclopropyl group with the extra stabilization of the  $-\text{ONO}_2$  group additionally makes the top scission favorable enough that that pathway occurs too, albeit in small yield.



Scheme 2.3: Proposed fate of  $\alpha$ -thujene +  $\text{NO}_3$  beginning from the 1<sup>st</sup>-generation nitroxy-alkyl radical. The 1<sup>st</sup>-generation nitroxy-alkoxy radical is outlined in black. Bold arrows show the reactions studied here, including calculated, stereoisomer-averaged branching ratios. Dashed boxes indicate predicted major product channels.



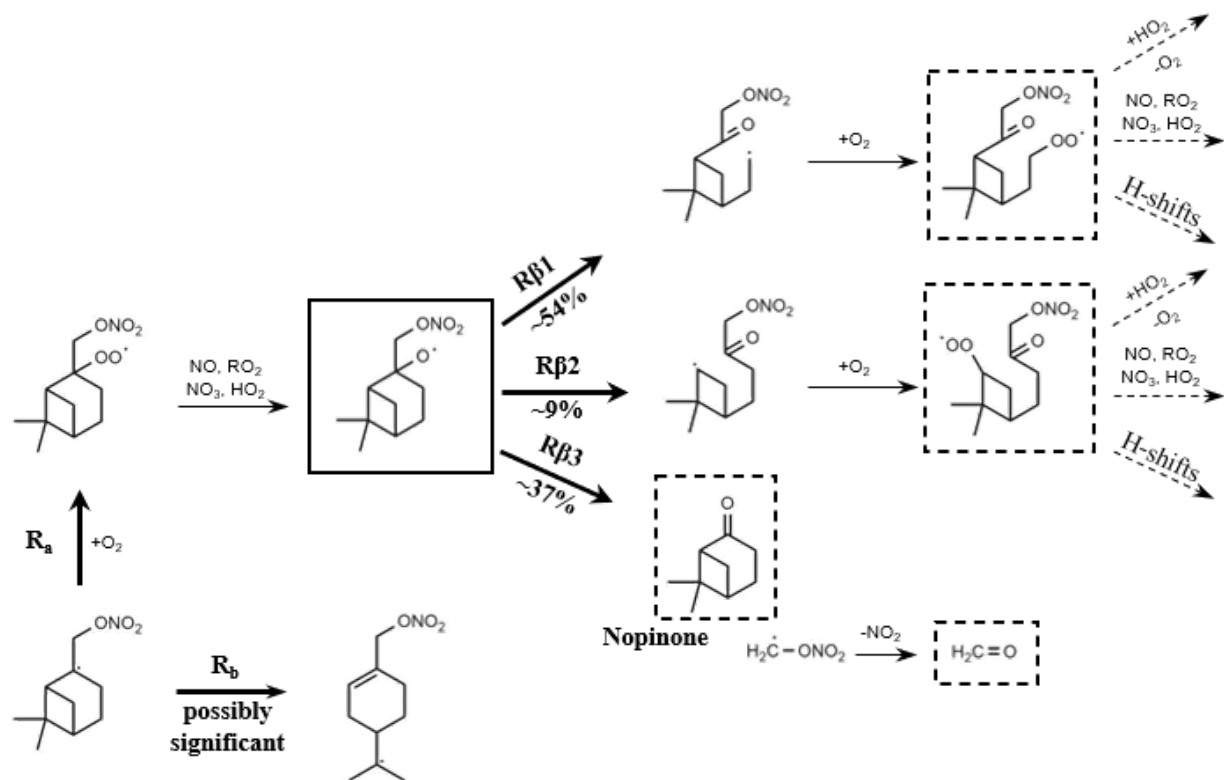
Scheme 2.4: Proposed fate of sabinene +  $\text{NO}_3$  beginning from the 1<sup>st</sup>-generation nitroxy-alkyl radical. The 1<sup>st</sup>-generation nitroxy-alkoxy radical is outlined in black. Bold arrows show the reactions studied here, including calculated, stereoisomer-averaged branching ratios. Dashed boxes indicate predicted major product channels.

## **$\beta$ -Pinene**

The mechanism for  $\beta$ -pinene is shown in Scheme 2.5. It is not yet clear whether the alkyl radical ring opening reaction is competitive with  $O_2$  addition to form an  $RO_2$  at the tertiary site. However, the alkoxy scission calculations are unique from the other monoterpenes studied here insofar as all three scission pathways have significant branching ratios, and the most favorable pathway is different for the two stereoisomers – R-alkoxy favoring the top scission and S-alkoxy favoring the left scission. From visual inspection, the S-peroxy (and thus S-alkoxy) stereoisomer may be favored over the R-peroxy due to slightly less steric congestion on the “front” side of the molecule, but this is speculation and we are not sure what the actual distribution of stereoisomers is likely to be. In any case, this is an interesting example where all three scission pathways are slightly suboptimal (left leaving a radical center on a strained ring, top leaving a  $C_1$  radical with some extra stabilization from the  $-ONO_2$  group, and right leaving a primary radical), so it seems that the energy cost of these suboptimal radical configurations are comparable. In terms of subsequent chemistry, both the left and right scission pathways have potential for continued radical propagation and multifunctional products, whereas the top scission leads to closed shell nopinone. In one chamber study, however, nopinone was only measured in 1-2% yield [68], so we may be overestimating the relative rate constant for the top scission.

## **Camphene**

Camphene’s mechanism is shown in Scheme 2.6. Since its secondary ring structure is a 5-membered ring, camphene’s initial oxidation seems to be driven less by the artifacts of a strained ring than the other bicyclic monoterpenes studied. The ring strain released from camphene’s 5-membered ring provides even less energy to overcome the alkyl radical ring opening barrier, so this channel is not expected to occur. Our calculations indicate that even

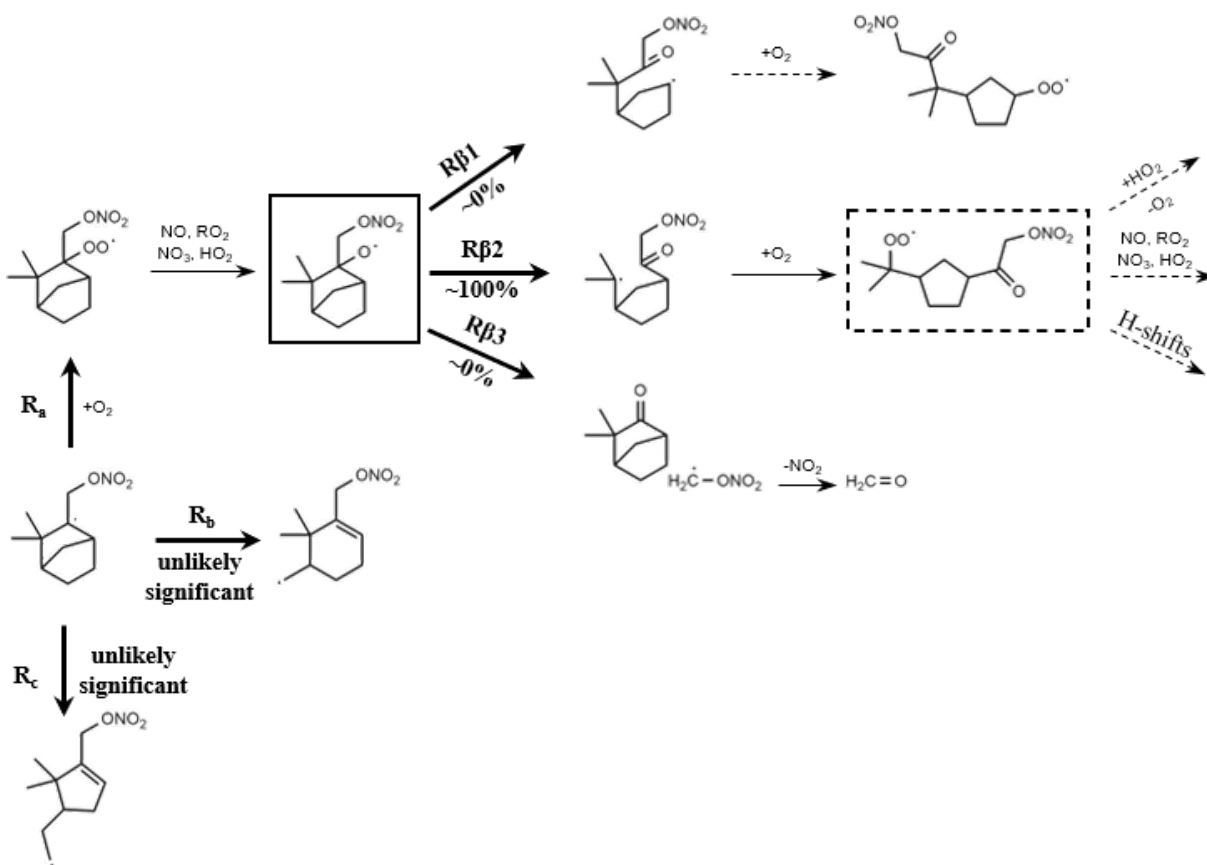


Scheme 2.5: Proposed fate of  $\beta$ -pinene +  $\text{NO}_3$  beginning from the 1<sup>st</sup>-generation nitroxy-alkyl radical. The 1<sup>st</sup>-generation nitroxy-alkoxy radical is outlined in black. Bold arrows show the reactions studied here, including calculated, stereoisomer-averaged branching ratios. Dashed boxes indicate predicted major product channels.

here, however, the right side scission leading to a radical center on the 5-membered ring is less favorable than the left scission, which leaves a tertiary radical center. That said, in terms of absolute energy, the right scission is faster than the dominant scission barrier for any of the other monoterpenes studied here. While it is unclear if  $\alpha$ -cyclobutyl or  $\alpha$ -cyclopentyl groups might afford any of the extra stability that is observed for  $\alpha$ -cyclopropyl groups in the gas-phase, we note that both C atoms cleaved in the dominant left scission are  $\alpha$  to a cyclopentyl group, so if there is even a small amount of extra stability from those groups (and thus extra lability of the cleaved C-C bond), this effect may explain the discrepancy with the SAR prediction as opposed to overestimating the barrier reduction from forming a radical centered on the 5-membered ring.

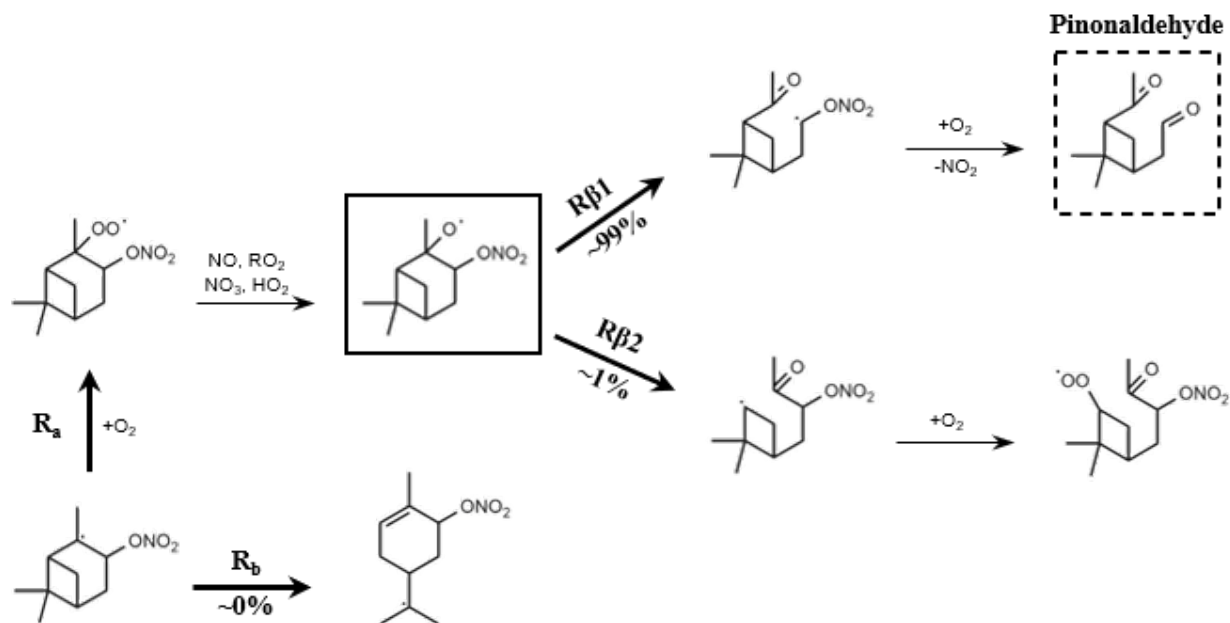
### **$\alpha$ -Pinene & $\Delta$ -Carene**

Analogous mechanisms for  $\alpha$ -pinene and  $\Delta$ -3-carene were published in Kurtén et al. [94], but we include them here in Scheme 2.7 and Scheme 2.8, respectively, so that the  $\text{NO}_3$  radical oxidation mechanism for all of the cyclic monoterpenes most prevalent in the atmosphere are compiled in one place.  $\alpha$ -pinene remains the only cyclic monoterpene with an overwhelmingly dominant preference for right side scission that leads to  $\text{NO}_2$  loss and early radical termination, consistent with its very low observed SOA yields, organonitrate yields [54], and high product yield of pinonaldehyde [68, 169, 135].  $\Delta$ -3-carene, continuing the trend of completely unique monoterpene reactivity, has a preference for the left side alkoxy scission, likely due to the extra stability of the  $\alpha$ -cyclopropyl group. Incidentally, this alkyl radical center is now  $\alpha$  to the cyclopropyl group, which provides a suitable geometry and a sufficient energy bonus from the 3-membered ring that a ring opening rearrangement can occur at this later stage in the mechanism, thus providing two channels of further radical propagation reactions as well as an opportunity for 2<sup>nd</sup> generation  $\text{NO}_3$  addition. These later



Scheme 2.6: Proposed fate of camphene + NO<sub>3</sub> beginning from the 1<sup>st</sup>-generation nitroxy-alkyl radical. The 1<sup>st</sup>-generation nitroxy-alkoxy radical is outlined in black. Bold arrows show the reactions studied here, including calculated, stereoisomer-averaged branching ratios. Dashed boxes indicate predicted major product channels.

stage radical propagation reactions are explored in detail in Draper et al. [36], and these pathways support the high SOA and organonitrates yields observed in chamber studies [54].

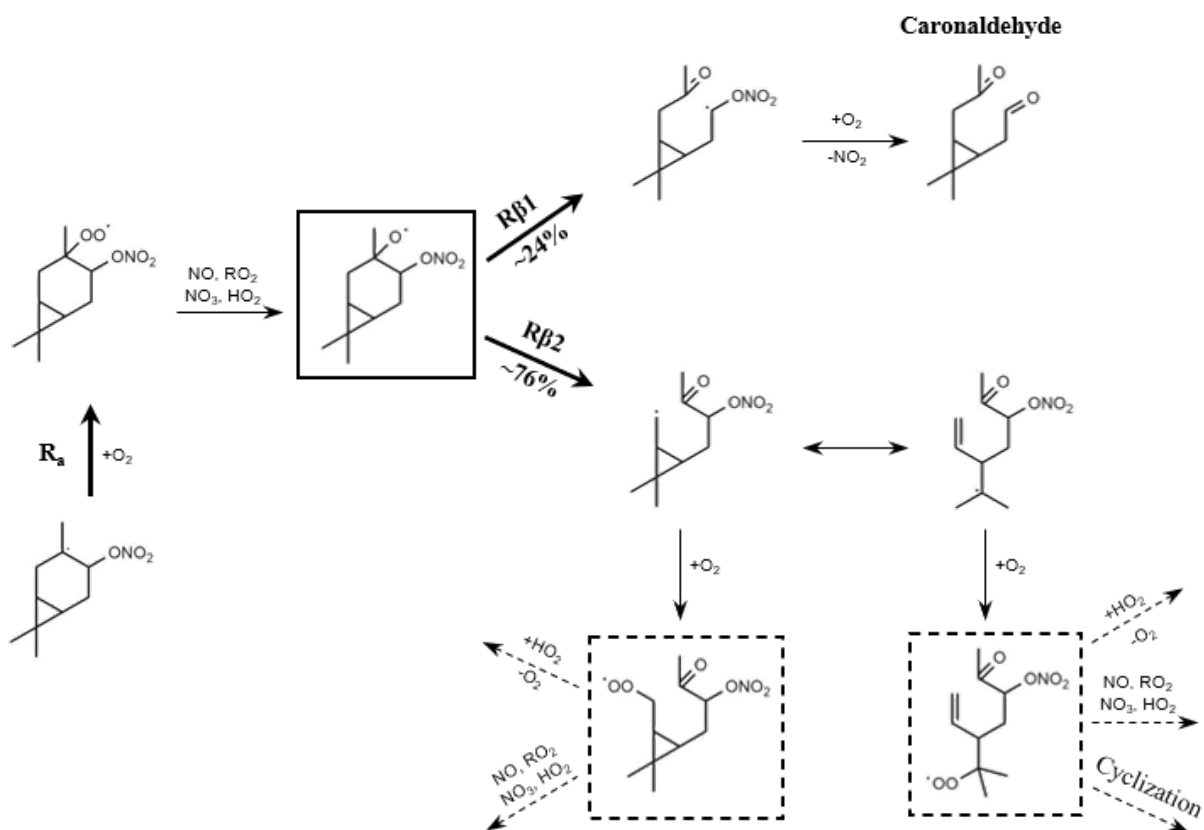


Scheme 2.7: 1<sup>st</sup>-generation mechanism proposed in Kurtén et al. [94] for  $\alpha$ -pinene +  $\text{NO}_3$  beginning from the 1<sup>st</sup>-generation nitroxy-alkyl radical. The 1<sup>st</sup>-generation nitroxy-alkoxy radical is outlined in black. Bold arrows show the reactions corresponding to those studied here, including calculated, stereoisomer-averaged branching ratios. Dashed boxes indicate predicted major product channels.

## 2.5 Conclusions

Assessing the fate of 1<sup>st</sup>-generation alkyl and alkoxy radicals for several cyclic monoterpenes, we find that none of these seven monoterpenes, including those studied in Kurtén et al., is expected to have the same combination of alkyl and alkoxy fate as another. This is in spite of the fact that they each share structural features such as double bond location, secondary ring size, and secondary ring location with at least one other. As both the alkyl and alkoxy radical are expected to form at or near the beginning of the oxidation mechanism (i.e. before the radical is terminated), these results indicate that all of these monoterpenes are likely to





Scheme 2.8: 1<sup>st</sup>-generation mechanism proposed in Kurtén et al. [94] for  $\Delta$ -3-carene +  $\text{NO}_3$  beginning from the 1<sup>st</sup>-generation nitroxy-alkyl radical. The 1<sup>st</sup>-generation nitroxy-alkoxy radical is outlined in black. Bold arrows show the reactions corresponding to those studied here, including calculated, stereoisomer-averaged branching ratios. Dashed boxes indicate predicted major product channels.

have quite different oxidation mechanisms, product yields, and SOA yields from each other. These findings support the variability observed in SOA yields in experimental studies, but call into question the oft-made assumption that a single monoterpene can be considered representative of all monoterpenes.

# Chapter 3

## Formation of Highly Oxidized Molecules from $\text{NO}_3$ Radical Initiated Oxidation of $\Delta$ -3-Carene: A Mechanistic Study

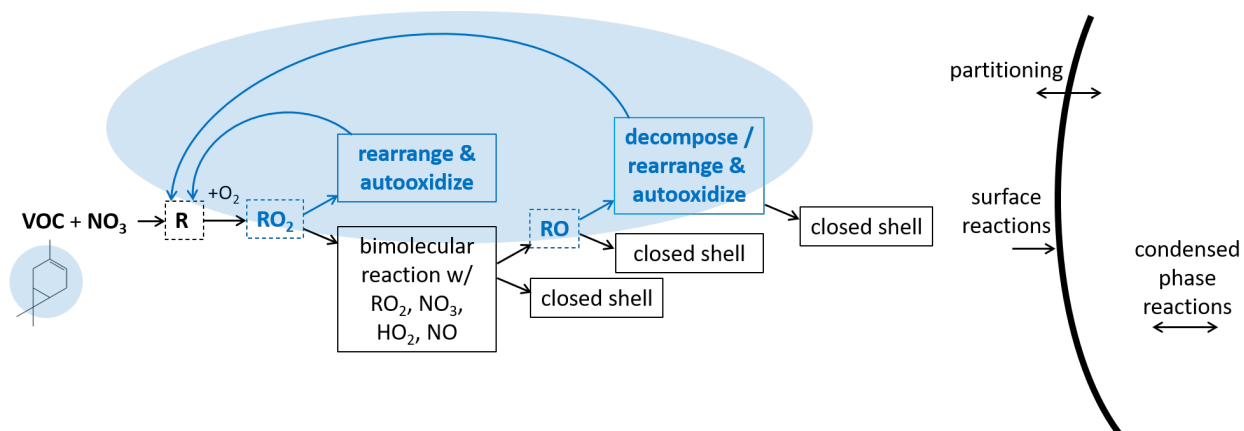


Figure 3.1: Overview schematic: Chapter 3 explores the second generation peroxy radical and alkoxy radical unimolecular reactions available to  $\Delta$ -3-carene following  $\text{NO}_3$  oxidation.

## 3.1 Abstract

$\text{NO}_3$  radical oxidation of most monoterpenes is a significant source of secondary organic aerosol (SOA) in many regions influenced by both biogenic and anthropogenic emissions, but there are very few published mechanistic studies of  $\text{NO}_3$  chemistry beyond simple first generation products. Here, we present a computationally derived mechanism detailing the unimolecular pathways available to the second generation of peroxy radicals following  $\text{NO}_3$  oxidation of  $\Delta$ -3-carene, defining generations based on the sequence of peroxy radicals formed rather than number of oxidant attacks. We assess five different types of unimolecular reactions, including peroxy and alkoxy radical ( $\text{RO}_2$  and  $\text{RO}$ ) hydrogen shifts,  $\text{RO}_2$  and  $\text{RO}$  ring closing (e.g., endoperoxide formation), and  $\text{RO}$  decomposition. Rate constants calculated using quantum chemical methods indicate that this chemical system has significant contribution from both bimolecular and unimolecular pathways. The dominant unimolecular reactions are endoperoxide formation,  $\text{RO}$  H-shifts, and  $\text{RO}$  decomposition. However, the complexity of the overall reaction is tempered as only one or two radical propagation pathways dominate the fate of each radical intermediate. Chemical ionization mass spectrometry (CIMS) measurements using the  $\text{NO}_3^-$  reagent ion during  $\Delta$ -3-carene +  $\text{NO}_3$  chamber experiments show products consistent with each of the three types of unimolecular reactions predicted to be important from the computational mechanism. Moreover, the SIMPOL group contribution method for predicting vapor pressures suggests that a majority of the closed-shell products inferred from these unimolecular reactions are likely to have low enough vapor pressure to be able to contribute to SOA formation.

## 3.2 Introduction

The 2013 IPCC assessment report illustrates that the greatest source of uncertainty in global climate modeling comes from aerosol [119]. Particulate matter in the atmosphere can influence atmospheric radiative balance both directly by scattering or absorbing light and indirectly by affecting the formation, reflectivity, and lifetime of clouds, and it is therefore an important factor limiting our understanding of climate as a whole. Secondary organic aerosol (SOA), which forms through secondary reactions of gas-phase emissions such as oxidation of volatile organic compounds (VOCs), contributes a major fraction of the global submicron aerosol [152]. It has been shown through numerous field studies, laboratory measurements, and the occasional modeling study that  $\text{NO}_3$  radical oxidation of monoterpenes is a significant, though often overlooked, source of SOA [124, 141, 74]. For example, Pye et al. incorporated  $\text{NO}_3$  + monoterpene chemistry into GEOS-Chem, parametrized using laboratory  $\text{NO}_3$  +  $\beta$ -pinene SOA yields [62]. They found that SOA from monoterpenes approximately doubled in regions where monoterpene chemistry is important, compared to simulations where  $\text{NO}_3$  chemistry was omitted. However, the significance of this chemistry is complicated by the fact that while most abundantly emitted monoterpenes (e.g.,  $\beta$ -pinene,  $\Delta$ -3-carene, and limonene) have moderate-to-high SOA yields with  $\text{NO}_3$  radical, the single most abundantly emitted monoterpene ( $\alpha$ -pinene) has a negligible SOA yield with  $\text{NO}_3$  [124, 54]. This presents a challenge to modelers as most models do not consider  $\text{NO}_3$  chemistry and those that do are subject to uncertainties due to poorly understood terpene species-dependence of SOA formation and corresponding poorly characterized regional variability of SOA precursors.

At a glance, the structural difference between  $\alpha$ -pinene and other bicyclic monoterpenes that would lead to such large differences in condensable products is not obvious. Structures of two of the most prevalent monoterpenes,  $\alpha$ -pinene and  $\Delta$ -3-carene, are shown in Figure 3.2a, highlighting that these molecules differ only by the location and size of the small secondary

ring structure. Both of these molecules are expected to undergo the same known atmospheric oxidation pathways in the gas phase, which is summarized in Figure 3.2b, where products may contribute to SOA formation or growth through thermodynamic partitioning or reactive uptake. For  $\text{NO}_3$  radical-initiated oxidation, the  $\text{NO}_3$  radical adds to the double bond, forming an alkyl radical (R). In the oxygen-rich atmosphere, oxygen rapidly adds to the alkyl radical, forming a peroxy radical ( $\text{RO}_2$ ) [7]. The peroxy radical will likely undergo a bimolecular reaction with another radical species, which at night when  $\text{NO}_3$  chemistry is most important is predominantly  $\text{NO}_3$ ,  $\text{HO}_2$ , or  $\text{RO}_2$ . These reactions lead either to alkoxy radicals (RO) or to closed-shell products like hydroperoxides, alcohols, and aldehydes or ketones [128]. Under conditions where the  $\text{RO}_2$  lifetime is long enough (on the order of seconds), research in the past few years has demonstrated that peroxy radicals with suitable substituents are able to undergo internal hydrogen shifts, regenerating an alkyl radical, which subsequently forms a new peroxy radical, thus initiating a chain of “autoxidation” [27, 130, 117, 14]. Alkoxy radicals are short-lived and can either react with oxygen, decompose, or isomerize. RO reactions often lead to closed shell products, though both decomposition and isomerization reactions can also lead to the formation of new alkyl radical, and subsequently peroxy radical, species [129]. Because multiple cycles of radical propagation reactions may occur before terminating to a closed shell product, we will differentiate between different peroxy or alkoxy radicals as different generations with the counter triggered by a backward arrow to an  $\text{RO}_2$  in Figure 3.2b.

Kurtén et al. used computational chemistry to compare rate constants for the first generation radical ( $\text{RO}_2$  and RO) rearrangement reactions following  $\text{NO}_3$  oxidation of  $\alpha$ -pinene and  $\Delta$ -3-carene. They found that the potential unimolecular reactions of the first generation peroxy radicals were calculated to be too slow to contribute significantly to the final product distribution. Instead, they identified the first generation  $\text{NO}_3$ -substituted RO as the point where the mechanisms for these two monoterpenes diverge, likely explaining the large difference in SOA yields from the two [94]. As shown in Figure 3.3, the  $\alpha$ -pinene-derived  $\text{O}_2\text{NO}-\text{RO}$

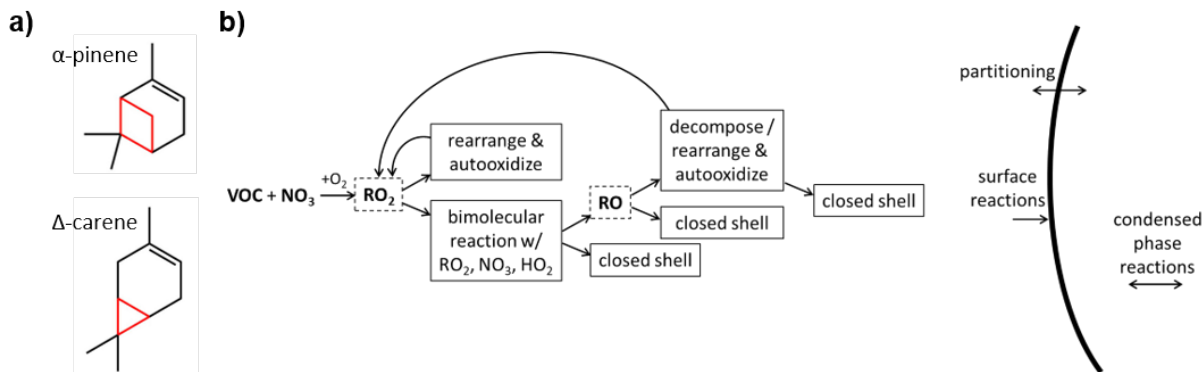


Figure 3.2: (a) Structures of  $\alpha$ -pinene and  $\Delta$ -3-carene highlighting the secondary rings in red to show the only structural variation between the two prevalent monoterpenes, and (b) the general oxidation scheme of  $\text{NO}_3$  oxidation of volatile organic compounds (VOCs) in the atmosphere. We note that not all pathways are available to all VOCs and some pathways may only become available for later generations of chemistry.

overwhelmingly favors the pathway leading to closed-shell pinonaldehyde, whereas the corresponding  $\Delta$ -3-carene-derived  $\text{O}_2\text{NO}-\text{RO}$  is more likely to undergo the radical-retaining pathway, enabling further generations of  $\text{RO}_2$  and  $\text{RO}$  radical rearrangement reactions, which we expect to lead to condensable products. In this study, we expand upon the mechanism presented in Kurtén et al. and calculate rate constants for various unimolecular reactions of the probable second generation  $\text{RO}_2$  and  $\text{RO}$  generated by  $\Delta$ -3-carene +  $\text{NO}_3$  chemistry. We then use these rate constants to predict the most probable second generation reaction products. These predicted products are then compared to compounds observed in the gas phase during chamber experiments of  $\Delta$ -3-carene +  $\text{NO}_3$  chemistry.

Beginning from the radical end points from the Kurtén et al.  $\Delta$ -3-carene mechanism shown in Figure 3.4a (mechanism leading to these radical end points shown in black in Scheme 3.1), we developed a computational mechanism for the next generation of chemistry, surveying five different types of unimolecular reactions as shown in Figure 3.4b: internal  $\text{RO}_2$  and  $\text{RO}$  hydrogen shifts (H-shifts),  $\text{RO}_2$  and  $\text{RO}$  ring closing, and  $\text{RO}$  decomposition. Published structure activity relationships (SARs) exist for many, though not all, of the possible reaction pathways assessed in this study [165, 166]. However, explicit calculations of reaction barriers

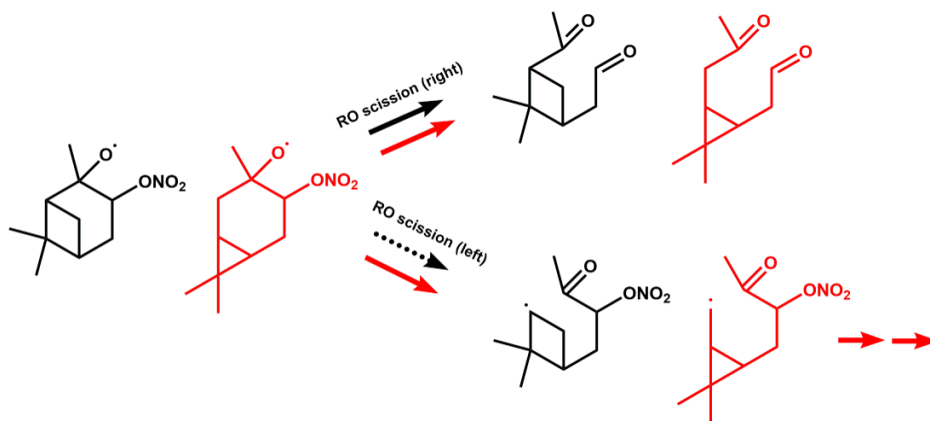


Figure 3.3: Schematic showing the RO scission of  $\alpha$ -pinene +  $\text{NO}_3$  mechanism (black) compared to  $\Delta$ -3-carene +  $\text{NO}_3$  mechanism (red), comparing scission of the right (top) or left (bottom) C–C bond. The dashed arrow for the left scission of the  $\alpha$ -pinene RO indicates this reaction is not expected to be competitive with the right scission due to the unfavorability of the alkyl radical on the strained ring. All other reactions (solid arrows) are expected to occur with an approximate 50/50 branching for the two  $\Delta$ -3-carene RO pathways [94].

and rate constants for case studies such as this are valuable for several reasons. First, SARs are not available for any  $\text{RO}_2$  reactions, and existing SARs for alkoxy reactions lack certain substituent effects like the influence of  $-\text{ONO}_2$  groups on RO H-shifts [166]. Additionally, although it has been observed that unimolecular reaction rates increase with increased functionalization [27, 130, 117, 14], this phenomenon has not been systematically quantified, so computing rate constants for case studies like the complex multifunctional compounds in this study (i.e., a  $\text{C}_{10}$  organonitrate) improves our understanding of these processes for more atmospherically relevant species [117]. Finally, results from this study can provide additional validation of the applicability of existing SARs to more complex molecules.

Accounting for all plausible hydrogen shifts, we compute forward reaction barrier heights and rate constants for all relevant reactions using quantum chemical methods that include coupled-cluster energy corrections. For a few reactions, higher-level calculations were omitted as the barrier heights computed at a lower level of theory indicated that they would not be competitive. The resulting detailed mechanism could be applied to a kinetics model or used



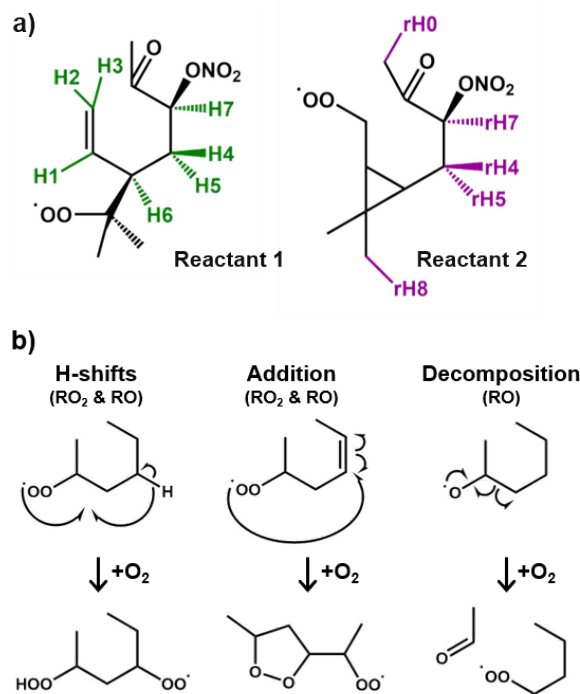


Figure 3.4: (a) Radical end points from  $\Delta$ -3-carene + NO<sub>3</sub> mechanism in Kurtén et al. (2017), which comprise our reactants in this study with the hydrogens investigated in this study labeled and color-coded to differentiate Reactant 1 and Reactant 2, and (b) schematic showing types of rearrangement reactions included in this study.

to develop a parametrization that can be implemented in regional or global models in order to improve estimates of SOA formation.

Because our mechanism includes predictions of the distribution of product isomers, the results of this study are important for the interpretation of experimental data. The widespread application of chemical ionization mass spectrometry (CIMS) measurements to atmospheric chemistry has enabled characterization of the multitude of oxidized organic molecules resulting from complex chemistry. However, although some techniques can be applied to obtain chemical information beyond molecular formula, such as the use of multiple reagent ions selective toward different functional groups [17], mass spectra alone do not provide enough information to explain observed SOA formation [95]. Two molecules with the same formula can vary by orders of magnitude in vapor pressure, depending on the identity and location of functional groups. In this study, we compare our computational mechanism to laboratory

measurements of the gas phase products of  $\text{NO}_3$  oxidation of  $\Delta$ -3-carene performed by CIMS using  $\text{NO}_3^-$  reagent ion. Because  $\text{NO}_3^-$  is selective toward highly oxidized organic species and only a small number of other molecules such as sulfuric acid, it is particularly suited to validate this mechanism focusing on autoxidation pathways [14, 77, 39].

## 3.3 Methods

### 3.3.1 Computational

The computational mechanism presented in this study was developed according to the methods described in Møller et al. [118] and incorporating many of the modifications described in Kurtén et al. [94] due to the size of the molecules studied here. Because our reactant  $\text{RO}_2$  structures are composed of 17 non-hydrogen atoms, use of the multi-conformer transition state theory (MC-TST) framework was prohibitively expensive at any reasonable level of theory. We therefore made some additional modifications to the computational approach and calculated all rate constants using the lowest-conformer transition state theory (LC-TST) framework [118]. These modifications lead to a much larger uncertainty for the absolute rate constants (approximately an order of magnitude) than the complete treatment prescribed in Møller et al. However, we expect the uncertainty from each modification to systematically bias absolute rate constants in the same direction for each reaction. For example, MC-TST accounts for the full population of conformers, so only including the lowest energy conformer by calculating rate constants with LC-TST will bias the absolute rate constants high. Likewise, Møller et al. showed that for these types of systems, increasing the level of theory decreases the calculated absolute rate constant. Therefore, this approach should provide reasonable relative rate constants, which likely overestimate the absolute rate constants, but are sufficient for comparative mechanism development [94]. Additionally, due to the size of

our reactants, and thus computational cost, we have chosen to investigate only the S-nitroso stereoisomer of (+)- $\Delta$ -3-carene as the (+)- $\Delta$ -3-carene enantiomer was used in the experimental portion of this study. Given that the stereocenter is far from the peroxy/alkoxy group and is freely able to rotate (because the 6-membered ring in  $\Delta$ -3-carene has already opened for both of our reactants), we do not expect qualitative differences in the overall mechanism for the R-nitroso stereoisomer.

Systematic conformer sampling for all reactants and products was performed with the Spartan'16 (Wavefunction, Inc.) software using the MMFF force field and ensuring the correct neutral charge was applied to all radical centers using the FFHINT keyword [118]. MMFF conformer sampling for the transition state structures was performed using constrained optimizations with the relevant bond lengths (and/or angles) constrained based on a B3LYP/6-31+G(d) transition state optimization of an arbitrary conformer using Gaussian 09 [101, 12, 52]. Constraints for H-shift, C–C scission, and addition reactions are included in Table B.1. In addition, partial bonds were drawn in Spartan to describe the breaking and/or forming bonds of the transition state. This improves the MMFF optimization of the conformer sampling and the resulting geometries are closer to the local energy minima than those from a conformer sampling where the bonds of the transition state are drawn according to either the reactant or the product. Following the MMFF conformer sampling for reactants, products, and transition states, we calculated B3LYP/6-31+G(d) single point energies for all conformers and applied a 5 kcal/mol cutoff at this stage, as suggested in Møller et al. for larger molecules [118]. The use of partial bonds was tested with an H-shift reaction between a hydroxy and a peroxy radical group of a model compound, and all of the unique transition state conformers (within 2 kcal/mol of the lowest energy conformer after the B3LYP/6-31+G(d) optimization) were found using a 5 kcal/mol energy cutoff after the B3LYP/6-31+G(d) single-point calculation. For reactants and products, we performed B3LYP/6-31+G(d) optimizations, and for transition states we performed B3LYP/6-31+G(d) constrained optimizations, using the constraints mentioned above, on all structures within 5

kcal/mol of the lowest single point energy. For transition state structures, we performed full transition state optimizations with frequency calculations on unique conformers (determined by energy and dipole moment) following the constrained optimizations. Intrinsic reaction coordinate (IRC) calculations were then performed on the lowest-energy transition states at the B3LYP/6-31+G(d) level to verify that they connect the desired reactants and products. Because of the high cost of heavier calculations for molecules of this size, optimization and frequency calculations at the  $\omega$ B97X-D/aug-cc-pVTZ level [37, 87, 23] were only performed for the lowest-energy structures found in the B3LYP/6-31+G(d) optimizations.

Although  $\omega$ B97X-D yields reasonable geometries and frequencies, the single point energies should be corrected using a highly correlated wave function-based method, such as CCSD(T) [121]. However, the computational cost of canonical coupled cluster scales exponentially with molecule size and therefore cannot be applied for the studied system sizes. Therefore, on top of the  $\omega$ B97X-D/aug-cc-pVTZ structures DLPNO-CCSD(T) single point energy calculations were performed using ORCA 4.0.1.2 instead of the prohibitively expensive canonical CCSD(T) calculations [123, 144]. The DLPNO-CCSD(T) method scales nearly linearly with system size while still keeping the accuracy of its canonical counterpart and has therefore become a popular choice to correct electronic energies of large molecular systems [144, 120]. In order to check whether a single-reference method can be used for these systems, we tested both restricted open-shell and unrestricted HartreeFock (ROHF and UHF, respectively) reference wave functions for the DLPNO-CCSD(T) calculations and also studied the T1 and T2 diagnostics, as well as the relative difference in DLPNO-CCSD and DLPNO-CCSD(T) total atomization energies. We found that ROHF and UHF wave functions yield similar DLPNO-CCSD(T) single point energies with a mean absolute error of 0.2 kcal/mol, and both T1 and T2 amplitudes and total atomization energies are within acceptable ranges (see Section B.1), thus confirming that single-reference methods can safely be applied. The final single point energy corrections are therefore calculated using ROHF-DLPNO-CCSD(T)/aug-cc-pVTZ with tight pair natural orbital criteria [144].

In the final LC-TST calculations, tunneling was treated using the Eckart model [38]. This requires information on the energy differences (forward and reverse barriers) between the lowest-energy transition state, and the reactant and product connected by IRC paths to this transition state, which may not be the lowest-energy reactants and products used in the overall LC-TST rate expression. Because of computational cost, the forward and reverse barriers needed for the tunneling calculation were estimated using a combination of approaches. Specifically, the  $\omega$ B97X-D zero-point corrected barriers (energy differences between the lowest-energy transition state and the lowest-energy reactant or product) was corrected by the B3LYP/6-31+G(d) energy difference between the lowest-energy conformer, and the conformer actually connected to the transition state via an IRC path.

### 3.3.2 Experimental

We conducted chamber experiments to validate the computational mechanism. Experiments were performed in a 560 L stainless steel chamber, described in detail in De Haan et al. [31], operating in flow-through mode with a 23 min residence time.  $\text{NO}_3$  radical was formed in situ by combining  $\text{O}_3$  ( $\sim 370$  ppb) with  $\text{NO}_2$  ( $\sim 200$  ppb). Ozone was generated by irradiating purified air produced by a zero air generator (model 737-13, Aadco Instruments) with ultraviolet light produced by a PenRay lamp (model 97-0066-01, Analytik Jena).  $\text{NO}_2$  was provided by a commercially prepared gas cylinder (2.56 ppm in air, Airgas Corp.). The concentrations of these compounds in the chamber were monitored with commercial  $\text{O}_3$  (Model 106-L, 2B Technologies) and  $\text{NO}_x$  (Model 405 nm, 2B Technologies) analyzers. Although we did not have  $\text{NO}_3$  radical or  $\text{N}_2\text{O}_5$  measurements available, we estimated steady-state concentrations of  $\text{N}_2\text{O}_5$  ( $\sim 50$  ppb) and  $\text{NO}_3$  ( $\sim 0.6$  ppb) using the home-built kinetics box model described in Draper et al. [35]. Once the oxidants reached steady state,  $\Delta$ -3-carene ( $\sim 50$  ppb) was added to the chamber for an approximate 1:1  $\Delta$ -3-carene to  $\text{NO}_3$  ratio (including both  $\text{NO}_3$  and  $\text{N}_2\text{O}_5$ ). The  $\Delta$ -3-carene source consisted of a home-prepared prepared gas

cylinder containing 23 ppm of (+)- $\Delta$ -3-carene (>90% purity, TCI America.) in nitrogen. Particle number-size distribution in the chamber was monitored with a scanning mobility particle sizer (SMPS) consisting of a differential mobility analyzer (Model 3081, TSI, Inc.) and ultrafine condensation particle counter (Model 3020, TSI, Inc.). Gas-phase products, specifically the highly oxidized molecules that are the focus of the computational mechanism, were measured by chemical ionization mass spectrometry with the  $\text{NO}_3^-$  reagent ion ( $\text{NO}_3^-$  CIMS). This instrument employs a commercial CIMS inlet (Aerodyne, Corp.) based on the design by Eisele and Tanner [40] coupled to a high-resolution time-of-flight mass spectrometer (LTOF analyzer, ToFwerk AG). Kinetics modeling confirmed that >98% of oxidation was  $\text{NO}_3$  radical-initiated and comparison with an experiment conducted using only  $\text{O}_3$  and  $\Delta$ -3-carene confirmed that the product distribution for the  $\text{NO}_3$  experiment did not have any significant contribution from  $\text{O}_3 + \Delta$ -3-carene products (see Section B.2).

$\text{NO}_3^-$  ion counts identified and fit using high-resolution peak fitting. Isotopes were constrained during peak fitting and accounted for when determining parent peak concentrations. The minimum detection limit is taken as 3 standard deviations above the baseline.

## 3.4 Results & Discussion

### 3.4.1 Derived Reaction Mechanism

A summary of the dominant pathways in the  $\Delta$ -3-carene +  $\text{NO}_3$  mechanism leading to the third generation of peroxy radicals is shown in Scheme 3.1. The complete  $\Delta$ -3-carene +  $\text{NO}_3$  mechanism including minor channels and all reactions calculated in this study is included in Scheme B.1. Black-colored structures are reproduced from Kurtén et al. [94], and green and purple structures differentiate pathways originating from the two reactant peroxy radicals (Reactant 1 and 2, respectively) studied in this work (Figure 3.4a, Scheme 3.1). The complete

list of rate constants calculated in this study are compiled in Table 3.1 and Table 3.2. Although each generation of chemistry creates the potential for an exponentially increasing number of products, this mechanism demonstrates that this potential is tempered because each intermediate will often favor a specific reaction channel.

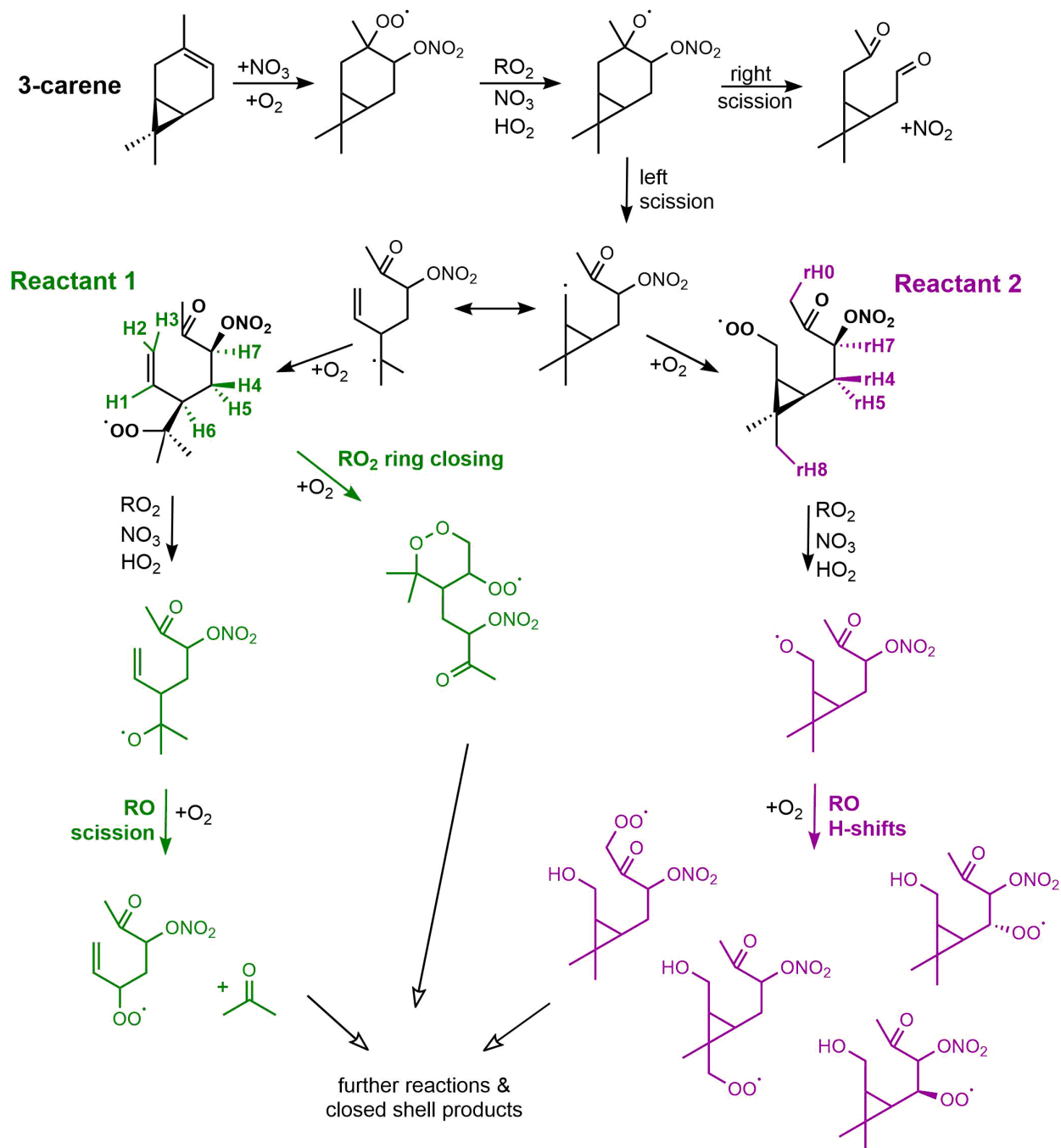
Table 3.1: Barriers and LC-TST Rate Constants<sup>a</sup>

reaction description	$E_b$ (kcal mol <sup>-1</sup> )	$k$ (s <sup>-1</sup> )
RO <sub>2</sub> H-shifts (R8 in Table S4)		
reactant 1 H1	29.0	$5.3 \times 10^{-9}$
reactant 1 H2	66.1	$5.5 \times 10^{-30}$
reactant 1 H3	34.3	$6.7 \times 10^{-13}$
reactant 1 H4	26.8	$2.9 \times 10^{-7}$
reactant 1 H5	25.7	$5.8 \times 10^{-6}$
reactant 1 H6	30.7	$4.2 \times 10^{-6}$
reactant 1 H7	21.7	$8.0 \times 10^{-2}$
reactant 2 rH4	23.2	$6.4 \times 10^{-4}$
reactant 2 rH5	24.2	$1.9 \times 10^{-5}$
reactant 2 rH7	22.2	$5.4 \times 10^{-2}$
RO <sub>2</sub> Ring Closing (R9 in Table S4)		
reactant 1 6-membered endoperoxide	18.1	$4.7 \times 10^{-2}$

<sup>a</sup>Barriers ( $E_b$ , zero-point corrected transition state–reactant electronic energy differences) and lowest-conformer transition state theory (LC-TST) rate constants (298.15 K) calculated for RO<sub>2</sub> H-shifts and RO<sub>2</sub> ring closing. Calculations were performed at the  $\omega$ B97X-D/aug-cc-pVTZ level with single point energy corrections at the ROHF-DLPNO–CCSD(T)/aug-cc-pVTZ level.

### 3.4.2 RO<sub>2</sub> Fate

Starting with Reactant 1 and Reactant 2, we began by surveying the pathways available to these RO<sub>2</sub> radicals. Because our mechanism explicitly calculates only the unimolecular reaction rate constants, we have estimated the pseudo-1<sup>st</sup> order rate constant for bimolecular reactions to be of order  $10^{-2} \text{ s}^{-1}$  based on literature rate constants ( $k_{\text{RO}_2+\text{RO}_2} \sim 10^{-12} \text{ cm}^3 \text{ molec}^{-1} \text{ s}^{-1}$  and  $k_{\text{RO}_2+\text{NO}_3} = 2 \times 10^{-12} \text{ cm}^3 \text{ molec}^{-1} \text{ s}^{-1}$ ) [128, 39] and radical concentrations



Scheme 3.1: Summary of dominant pathways in  $\Delta$ -3-carene+  $\text{NO}_3$  mechanism. Black structures and arrows indicate reactions inferred from literature, culminating in the radical end-points in Kurtén et al. [94] which serve as the “reactants” in this study. Green and purple structures and arrows indicate reactions calculated in this study originating from Reactant 1 and Reactant 2, respectively. For complete mechanism, including all pathways assessed in this study, refer to Scheme B.1.



Table 3.2: Barriers and LC-TST Rate Constants<sup>a</sup>

reaction description	$E_b$ (kcal mol <sup>-1</sup> )	$k$ (s <sup>-1</sup> )	SAR prediction
RO H-shifts (R10 in Table S4)			SAR predicted $k$ (s <sup>-1</sup> )
reactant 1 H0			0.46–17 <sup>b</sup>
reactant 1 H4			0.24
reactant 1 H5			0.24
reactant 1 H7			$1.1 \times 10^7$
reactant 2 rH0	11.8	$3.0 \times 10^4$	$3.4 \times 10^{-2} - 0.51^b$
reactant 2 rH4	8.4	$1.8 \times 10^7$	$3.3 \times 10^6$
reactant 2 rH5	9.5	$1.6 \times 10^6$	$3.3 \times 10^6$
reactant 2 rH7	8.8	$3.7 \times 10^6$	$2.0 \times 10^6$
reactant 2 rH8	8.3	$2.3 \times 10^7$	$3.2 \times 10^5$
RO Addition <sup>c</sup> (R12 in Table S4)			
reactant 1 4-membered endoether	12.3		
reactant 1 5-membered endoether	15.7		
RO decomposition (R11 in Table S4)			SAR predicted $E_b$ (kcal/mol)
reactant 1 C—C scission	7.1	$6.6 \times 10^7$	6.5
reactant 2 C—C scission			20.3

<sup>a</sup>Barriers ( $E_b$ , zero-point corrected transition state–reactant electronic energy differences) and lowest-conformer transition state theory (LC-TST) rate constants (298.15 K) calculated for RO H-shifts, ring closing, and decomposition for alkoxy radicals derived from Reactant 1 and Reactant 2. Calculations were performed at the  $\omega$ B97X-D/aug-cc-pVTZ level with single point energy corrections at the ROHF-DLPNO–CCSD(T)/aug-cc-pVTZ level. SAR predictions of  $E_b$  and  $k$  are included when available.<sup>16,17</sup> <sup>b</sup>Range of SAR-predicted  $k$  values come from structures with H-shifts not easily described by the SAR and therefore calculated using two different assumptions. <sup>c</sup>Note: these barriers were calculated for an arbitrary conformer at the B3LYP/6-31+G(d) level to confirm that the reaction would be slow relative to R1 C—C scission and thus unlikely to contribute to the final product distribution.

representative of the chamber experiments in this study ( $[\text{RO}_2] \approx 0.7$  ppb,  $[\text{NO}_3] \approx 0.4$  ppb) (see Figure B.4). Incidentally, this is a reasonable estimate under certain ambient conditions as well because  $\text{HO}_2$  is a significant bimolecular sink for  $\text{RO}_2$  in the atmosphere (assuming a “typical” ambient  $[\text{HO}_2] \sim 100$  ppt and  $k_{\text{RO}_2+\text{HO}_2} = 2 \times 10^{-11}$  cm<sup>3</sup> molec<sup>-1</sup> s<sup>-1</sup> [128, 72], but  $[\text{HO}_2]$  is assumed to be negligible in these chamber experiments. Therefore, to be competitive,  $\text{RO}_2$  unimolecular rate constants must be comparable to or faster than  $10^{-2}$  s<sup>-1</sup>.

### 3.4.3 RO<sub>2</sub> H-shifts

Hydrogen shifts were calculated for all unique hydrogens greater than a 1,4-H-shift apart with the exception of methyl hydrogens, which have been shown to be slow in other studies [130], and hydrogens on the strained 3-membered ring, which were shown in Kurtén et al. to lead to a highly unstable alkyl radical [94]. This includes all hydrogens labeled in Figure 3.4a

except for rH0 and rH8. The fastest RO<sub>2</sub> H-shifts in each reactant were for the hydrogen  $\alpha$  to the -ONO<sub>2</sub> group and  $\beta$  to the =O group (H7 and rH7). These H-shifts are of order 10<sup>-2</sup> s<sup>-1</sup> and therefore are competitive with bimolecular reaction. However, the alkyl radical at this site leads to rapid loss of NO<sub>2</sub> and termination of the radical as a carbonyl group, so although this pathway contributes to the final product distribution, it does not lead to further oxidation [130]. The remaining RO<sub>2</sub> H-shifts range from approximately 10<sup>-13</sup> to 10<sup>-4</sup> s<sup>-1</sup> and therefore are too slow to contribute significantly to the final product distribution.

Although the majority of these rate constants are too slow to be competitive, it is instructive to look at which of these H-shifts are more favorable than others for this complex, multifunctional molecule. Although a SAR does not currently exist for RO<sub>2</sub> H-shifts, Otkjaer et al. [130] tested the effects of different substituents and transition state ring size for RO<sub>2</sub> H-shifts. Considering only the substituents and transition state ring sizes relevant for this study, we would predict that the =O group would increase H-shift rates and the -ONO<sub>2</sub> group is unlikely to have any significant effect. With respect to transition state ring size, the slowest reactions would be 1,4 H-shifts, and 1,6 H-shifts are likely to be the fastest but comparable to 1,5 and 1,7 H-shifts. Additionally, H-shifts are faster on tertiary carbons and slower on primary carbons [130]. Our results are qualitatively consistent with the trends described in Otkjaer et al. [130] and references therein. The two fastest H-shifts (H7 and rH7), which are somewhat competitive in our mechanism, are  $\alpha$  to a nitrate (-ONO<sub>2</sub>) group and  $\beta$  to a carbonyl (=O), and we attribute the fast rate to the proximity to the carbonyl. After H7 and rH7, the fastest H-shifts were the 1,6-H-shifts from the secondary carbon,  $\beta$  to the nitrate group in Reactant 2 (rH4, rH5). Because we do not expect the nitrate group to have a significant effect, these two hydrogens provide a good baseline of sorts for a molecule of this size where additional substituents or more strained transition states will provide an enhancement or depression of the H-shift rate, respectively. The H-shifts of these corresponding hydrogens in Reactant 1 (H4, H5) are 1 to 2 orders of magnitude slower, perhaps because they are 1,5-H-shifts, which have a slightly more strained transition state. The hydrogen on

the tertiary carbon in Reactant 1 (H6) has a rate constant comparable to H4 and H5, likely due to a net cancellation of the enhancement of the more weakly bound tertiary hydrogen by the more highly strained transition state of the 1,4-H-shift. Overall, the H-shifts from the double-bonded carbons (H1, H2, H3) are the least favorable of the ones tested, which is not surprising because the vinyl C–H bonds are comparatively strong.

### 3.4.4 RO<sub>2</sub> Ring Closing

Reactant 1 arises from the opening of the 3-membered ring, which forms a new double bond. We therefore tested whether the peroxy radical is able to add to the double bond, forming a 6-membered endoperoxide ring. Although it is also possible to add to the other side of the double bond, forming a 5-membered ring, this scenario results in a smaller ring and a primary alkyl radical, so we would expect this pathway to be slower than formation of the 6-membered endoperoxide. This type of endoperoxide formation reaction has been suggested to occur fairly rapidly (up to  $\sim 1 \text{ s}^{-1}$ ) in the ozonolysis of a cyclodiene as well as in the photooxidation of  $\alpha$ -pinene [143, 171]. As with the more well-known H-shift reactions, this reaction results in a similar autoxidation process with O<sub>2</sub> adding to the newly formed alkyl radical. We calculated this ring-closing reaction to have a rate constant of approximately  $5 \times 10^{-2} \text{ s}^{-1}$  for Reactant 1, making it competitive with bimolecular reaction and consistent with the  $\alpha$ -pinene endoperoxide formation reactions in Xu et al. [171] that result in secondary radicals, which are somewhat slower than those leading to tertiary radicals.

### 3.4.5 RO Fate

On the basis of the calculated rate constants described above for RO<sub>2</sub> unimolecular reactions, we expect that the product distribution from Reactant 1 will have some contribution from the endoperoxide channel as well as some closed-shell C<sub>10</sub>H<sub>16</sub>O<sub>4</sub> from the H7 H-shift but a

significant amount of these RO<sub>2</sub> will undergo bimolecular reaction and become RO radicals. For Reactant 2, which does not have an endoperoxide channel available to it, some C<sub>10</sub>H<sub>16</sub>O<sub>4</sub> from the rH7 H-shift will form, and the significant remainder will be converted to RO by bimolecular reactions. We therefore assess the unimolecular reaction pathways available to these alkoxy radical products, including H-shifts, decomposition, and ring closing. Because published SARs are available for both alkoxy H-shifts and alkoxy bond scissions [165, 166], we started by implementing those to estimate which RO pathways are likely to be competitive for the Reactant 1 and Reactant 2 RO radicals.

Alkoxy scission reactions are influenced most strongly by the substituents on the  $\alpha$ - and  $\beta$ -carbons, so any further substituents can be neglected when applying the SAR [165]. The alkoxy radical formed from Reactant 1 has two alkyl groups on each the  $\alpha$ - and  $\beta$ -carbons, which reduce the overall SAR-predicted reaction barrier to 6.5 kcal/mol, compared to the 17.9 kcal/mol “baseline” forward barrier for the unsubstituted RO CH<sub>3</sub>CH<sub>2</sub>O. Reactant 2, on the other hand, has no substituents on the  $\alpha$ -carbon and a cyclopropyl ring on the  $\beta$ -carbon. Scission of a C–C bond adjacent to a cyclopropyl ring leads to an alkyl radical on a highly strained ring, so this substituent results in an increase of the overall reaction barrier to 20.3 kcal/mol. H-shift favorability relies heavily on the structure of a molecule as a whole, because H-shifts can take place between carbons at different distances from the radical center (span) and are impacted by the location of functional groups (substituents) [166]. Because of the wider range of span and substituent permutations, this SAR is less complete, for example, lacking effects from –ONO<sub>2</sub> groups, so we calculated these SAR-predicted rate constants assuming missing substituents would have a negligible effect. SAR-predicted forward energy barriers for alkoxy scission reactions and rate constants for alkoxy H-shift reactions are included in Table 3.2.

Despite the increased uncertainty for the SAR-predicted H-shift rate constants due to missing substituents, the large predicted differences in barrier heights between the Reactant 1 and

Reactant 2 alkoxy scission reactions makes it clear which pathway(s) will be favored by each reactant. We predict an extremely low barrier (6.5 kcal/mol) for the Reactant 1 RO scission, which we estimate to correspond to a rate constant of  $\sim 1 \times 10^8 \text{ s}^{-1}$  from similar alkoxy scission barriers in Kurtén et al. [94]. SAR-predicted rate constants range from  $10^{-2}$  to  $20 \text{ s}^{-1}$  for most available H-shifts in the Reactant 1 RO with one notable exception. Following the qualitative trend of the  $\text{RO}_2$  radicals, the hydrogen  $\alpha$  to the  $-\text{ONO}_2$  group and  $\beta$  to the  $=\text{O}$  group (H7) is predicted to have a rate constant of order  $10^7 \text{ s}^{-1}$ , which will be competitive with RO scission for this reactant. This H-shift leads to rapid loss of  $\text{NO}_2$  and termination of the radical to closed-shell  $\text{C}_{10}\text{H}_{16}\text{O}_3$ , whereas the RO scission pathway will lead to continued radical propagation reactions, so we focus on the RO scission pathway for Reactant 1. In contrast, the predicted barrier for alkoxy scission for the Reactant 2 RO is quite high (20.3 kcal/mol) due to formation of a radical on the strained cyclopropyl ring. We can estimate this barrier to correspond to a rate constant of  $< 10^{-2} \text{ s}^{-1}$  using the  $\text{RO}_2$  ring-closing barrier/rate constant from Table 3.1 as an upper limit as neither the scission or ring-closing reaction require significant tunneling corrections, unlike the H-shift reactions. Because SAR-predicted H-shift rate constants range from  $10^{-2}$  to  $10^6 \text{ s}^{-1}$  with the majority of hydrogens having rate constants above  $10^5 \text{ s}^{-1}$ , we can infer that the Reactant 2 RO will favor H-shifts over scission reactions.

LC-TST calculated rate constants for alkoxy reactions are shown in Table 3.2. Alkoxy scission in Reactant 1 occurs at a calculated rate of  $7 \times 10^7 \text{ s}^{-1}$ , confirming that H-shifts (except for H7) should be negligible in comparison. Rate constants for H-shift reactions in Reactant 2 alkoxy radicals were calculated for all hydrogens labeled in Figure 3.4a, this time also assessing whether methyl hydrogens with rate enhancing substituents at  $\beta$ -positions (rH0 and rH8) might also be competitive, because RO chemistry is typically much faster than  $\text{RO}_2$  chemistry. Calculated rate constants range from  $3 \times 10^4$  to  $2 \times 10^7 \text{ s}^{-1}$ . As expected from the trends observed in the  $\text{RO}_2$  H-shifts, rH4, rH5, and rH7 are among the fastest with the methyl hydrogen rH0 being the slowest. Unexpectedly, however, the fastest RO

H-shift is from the methyl hydrogen rH8, likely due to a combination of a very favorable transition state geometry, as well as some additional stabilization due to the strained ring  $\beta$  to the subsequent alkyl radical. Barrier heights were also calculated for RO addition over the double bond in Reactant 1 but these calculations indicated that this ether-forming reaction is not competitive with the extremely fast RO scission or H-shift reactions. Because our calculated rate constants span many orders of magnitude, it is clear which pathways will dominate, but we note that the barriers for any of the fast RO reactions are quite low and therefore these rate constants calculated using transition state theory will have even larger absolute uncertainties than for the higher barrier RO<sub>2</sub> reactions.

The LC-TST calculations confirmed the qualitative results of the SARs, with two H-shifts being 2 to 6 orders of magnitude faster than predicted by the SAR. The rate constants that deviated most significantly from the SAR predictions were those from methyl hydrogens that were seemingly better represented by the span and substituents included in the SAR. However, these deviations may have come from unincluded substituents like the cyclopropyl ring (rH8) and the fact that assumptions had to be made to combine substituent effects of the  $-C=O$  group at a 1,7 span (rH0). The SAR predicted rate constants well for the H-shifts where we had to assume that, for example an  $-ONO_2$  group has a negligible effect.

### 3.4.6 Computational Summary

From these results, it is evident that three dominant radical pathways emerge from  $\Delta$ -3-carene + NO<sub>3</sub> second generation RO<sub>2</sub> chemistry. Reactant 1 leads to radical products following RO<sub>2</sub> addition to an internal double bond, as well as alkoxy radicals from bimolecular reaction, which subsequently undergo scission reactions leading predominantly to easily identifiable C<sub>7</sub> radical intermediates. Reactant 2 proceeds straight to alkoxy radicals from bimolecular reaction, which predominantly undergo H-shift reactions, retaining their C<sub>10</sub>

backbone. These pathways are summarized in Scheme 3.1, and thus a complete mechanism through second generation products emerges that combines these results with those of Kurtén et al. [94], along with inferred closed-shell products based on known oxidation chemistry (Scheme B.1). Even though assessing the third generation of unimolecular chemistry for this system is computationally unfeasible, understanding the second generation of chemistry helps us understand the balance between bimolecular and unimolecular reactions in the atmosphere, which is a crucial link between known oxidation chemistry and experimental results.

### 3.4.7 Chamber Experiments

Chamber experiments focused specifically on gas-phase  $\text{NO}_3^-$  CIMS measurements to provide comparative measurements of the highly oxidized products formed from  $\text{NO}_3$  radical oxidation of  $\Delta$ -3-carene. SMPS measurements showed new particle formation and subsequent particle growth during these experiments (see Figure B.2) but particle-phase composition was outside the scope of this study. The complete table of identified products is included in Table B.7, and Figure 3.5a,c shows a mass spectrum averaged over the duration of the experiment with structures assigned to the highest intensity peaks. When comparing a CIMS spectrum to the proposed mechanism, we must take into consideration which molecules will be detectable by the selected reagent ion chemistry.  $\text{NO}_3^-$  CIMS will only detect molecules that have a larger binding energy with  $\text{NO}_3^-$  than the binding energy of  $\text{NO}_3^-$  with  $\text{HNO}_3$ . Hyttinen et al. [77] showed that  $\text{C}_6$  molecules containing at least two hydrogen bond (H-bond) donors will bind with  $\text{NO}_3^-$  and are thus detectable by  $\text{NO}_3^-$  CIMS, with increasing oxidation generally leading to stronger binding. Although the products observed in this study seem to have a high enough oxidation state, many of these oxygens come from nitrate or carbonyl functionalities, so some pathways require multiple generations of chemistry to get even one H-bond donor. To ensure that we were assigning detectable structures to our

$\text{NO}_3^-$  CIMS spectrum, we performed ion-clustering calculations on two expected products to investigate whether binding to  $\text{NO}_3^-$  is, in fact, favorable. These results are shown in Section B.3. For the highly oxidized compounds in this study ( $>\text{O}_7$ ), our results indicate that a single H-bond donor is sufficient to bind with  $\text{NO}_3^-$ . Interestingly, despite not containing any H-bond donors, the dipole-dipole interactions in the  $\text{RO}_2$  formed following  $\text{RO}_2$  ring closing from Reactant 1 are sufficient to make clustering with  $\text{NO}_3^-$  competitive with  $\text{HNO}_3(\text{NO}_3^-)$  cluster formation.

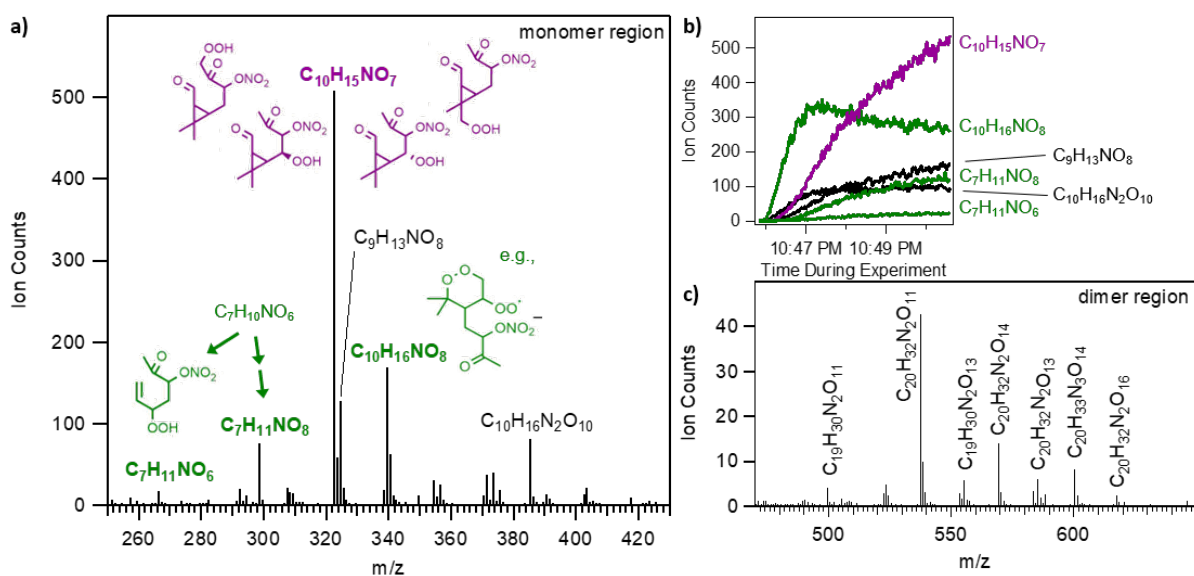


Figure 3.5: (a) Monomer region of average mass spectrum from  $\Delta$ -3-carene +  $\text{NO}_3$  chamber experiment with structures for highest intensity peaks consistent with computational mechanism. M/z values reflect  $\text{NO}_3^-$  adducts ( $\text{M}(\text{NO}_3^-)$ ) as detected, and labeled peaks reflect the product ( $\text{M}$ ) alone.  $\text{C}_7\text{H}_{11}\text{NO}_8$  was not included in the mechanism in this study but is expected to be a third generation product related to  $\text{C}_7\text{H}_{10}\text{NO}_6$ . (b) Time series of the five highest intensity observed peaks as well as  $\text{C}_7\text{H}_{11}\text{NO}_6$  as it is the closed-shell product of one of our explicitly calculated intermediates. (c) Dimer region of mass spectrum with highest intensity peak formulas labeled.

Figure 3.5a shows that three of the five highest intensity observed peaks are consistent with products of the dominant reaction pathways identified in our computational mechanism. The highest intensity peak,  $\text{C}_{10}\text{H}_{15}\text{NO}_7$  most likely arises from Reactant 2 undergoing bimolecular reaction to produce  $\text{RO}$ , which undergoes one of several possible H-shifts with subsequent  $\text{O}_2$  addition. We then assume that the  $\alpha$ -OH H-shift available to this new  $\text{RO}_2$  will be fast



compared to other pathways and result in closed-shell  $C_{10}H_{15}NO_7$  by reaction with  $O_2$  and loss of  $HO_2$ . The second highest intensity peak,  $C_{10}H_{16}NO_8$ , must be a radical species given the even number of hydrogens and single nitrogen. This formula is consistent with the  $RO_2$  radical formed from the  $RO_2$  ring closing of Reactant 1 and subsequent  $O_2$  addition. It is somewhat surprising that we would measure this particular  $RO_2$  at such high intensity given that, as a radical intermediate, it is likely to react away relatively quickly. Additionally, the clustering calculations described above indicate  $NO_3^-$  clustering with this radical may be competitive with  $HNO_3$ , but not strongly, so we would expect to detect this species with lower sensitivity than others with more favorable interactions relative to  $HNO_3$ . Looking at the time series of the species highlighted in Figure 3.5b, however, we see this ion appears earlier than any of the products postulated to come from RO unimolecular reactions, consistent with the fact that it would form directly from unimolecular reactions of Reactant 1 or 2.

Some products remain unexplained or unexplored by the proposed mechanism. For example, formation of a  $C_9$  species is difficult to understand from the chemical pathways considered. Formation of dinitrate species (e.g.,  $C_{10}H_{16}N_2O_{10}$ ) were not explored computationally but given that Reactant 1 and many of its subsequent products and intermediates contain a double bond, these are easily justified by a second  $NO_3$  addition reaction. Dimer formation (for example, via  $RO_2 + RO_2$  reaction) was outside the scope of this study, but as seen in Figure 3.5c, most observed dimers are consistent with predicted monomer building blocks.

### 3.4.8 Implications for SOA Formation

The derived mechanism and experimental results in this study describe autoxidation processes and products in the gas-phase up to the formation of second generation products. This part of the mechanism provides valuable insights into the SOA forming potential of  $\Delta$ -3-carene +  $NO_3$  and can be extrapolated to some of the other monoterpenes that form

SOA from  $\text{NO}_3$  oxidation. To start, we observe a number of dimer species, which have been correlated to new particle formation rates for other chemical systems [89, 103]. Because the dimers in our study are also likely to be the lowest volatility products, we assume that these are the products linked most strongly to initial particle formation and the earliest stages of growth. We have estimated vapor pressures for many of our expected closed-shell products using the SIMPOL.1 group contribution method [132] and tabulated these in Table B.9. For the monomer products with known structures, vapor pressures at 298 K range from  $1.6 \times 10^2$  Torr for caronaldehyde ( $\text{C}_{10}\text{H}_{16}\text{O}_2$ ) to  $5.1 \times 10^8$  Torr for  $\text{C}_{10}\text{H}_{17}\text{NO}_7$  multifunctional hydroperoxides. If we consider “semi-volatile” vapor pressures (defined liberally, encompassing volatility ranges between primarily gas-phase and primarily condensed-phase) as ranging from  $7.6 \times 10^2$  to  $7.6 \times 10^9$  Torr [61], nearly all products in this mechanism would be expected to be able to partition into the particle-phase at least to some degree. Caronaldehyde, analogous to pinonaldehyde in the  $\alpha$ -pinene +  $\text{NO}_3$  system, is one of the few products that is too volatile to contribute significantly to the particle-phase under atmospherically relevant aerosol mass loadings [34], whereas many of the products arising from the unimolecular pathways explored in this study have estimated vapor pressures on the very low end of our defined semivolatile range, and therefore will partition heavily into the particle-phase. The abundance of low volatility, highly oxidized monomers is consistent with observations of relatively small particle number concentrations but fast growth rates in other chamber experiments probing this chemistry [54].

### 3.5 Conclusions

In this work, we have expanded upon the known first generation chemistry of  $\Delta$ -3-carene +  $\text{NO}_3$  to include five different unimolecular reactions available to second generation  $\text{RO}_2$  and  $\text{RO}$  radicals. In doing so, we have also assessed some of the structural features hindering

and enhancing unimolecular reactions for  $C_{10}$  multifunctional molecules. In contrast to some of the chemical systems identified in recent years to undergo rapid and accelerating H-shift and autoxidation reactions leading to very highly oxidized and often extremely low volatility products [27, 14],  $NO_3 +$  monoterpene oxidation products have a much more modest and balanced contribution from both unimolecular and bimolecular radical reactions. This is likely due to the combination of a strained secondary ring, which inhibits H-abstraction or alkyl radical-forming reactions on carbons within that ring, as well as the  $-ONO_2$  group, which does not strongly enhance unimolecular reactions and is also prone to decomposing to  $NO_2$  and a closed-shell product, thus terminating radical propagation. However, we also observed an unexpected enhancement of the RO H-shift rate from a methyl H  $\beta$  to the strained cyclopropyl ring. Understanding this balance between gas-phase bimolecular and unimolecular oxidation pathways is valuable for many chemical systems that, like  $\Delta$ -3-carene +  $NO_3$ , produce SOA but do not necessarily have dominant autoxidation pathways available, whether due to structural features or due to decreased  $RO_2$  lifetimes in more polluted environments.

# Chapter 4

## Observations of semi-volatile organonitrates in nanoparticles in the boreal atmosphere

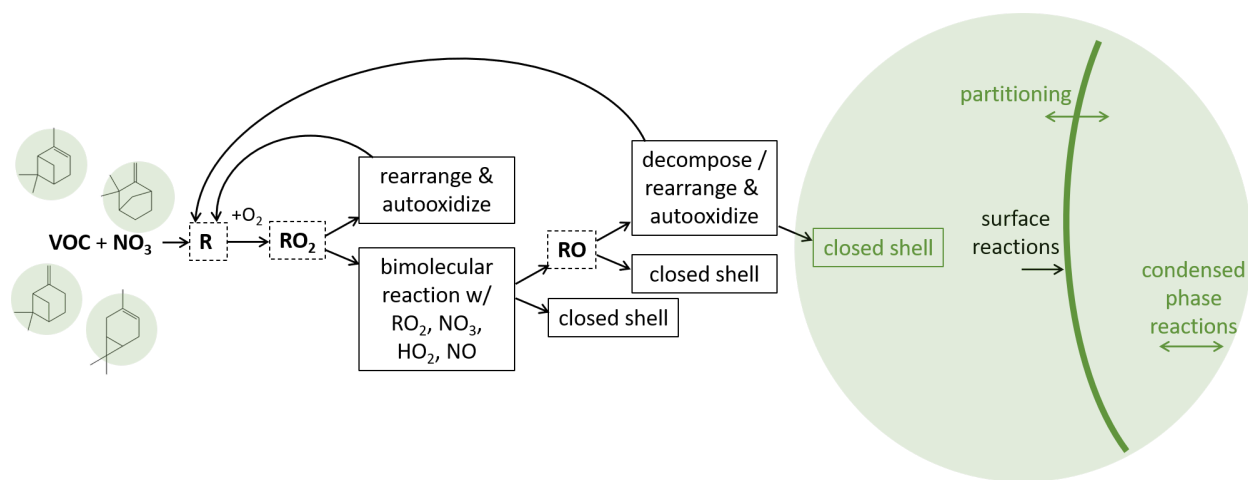


Figure 4.1: Overview schematic: Chapter 4 assesses gas-to-particle partitioning from probable NO<sub>3</sub> oxidation of monoterpenes based on ambient nanoparticle composition measurements.

## 4.1 Abstract

Products consistent with  $\text{NO}_3$  radical-initiated oxidation of monoterpenes have been observed in nanoparticles measured at the SMEAR II station in Hyytiälä, Finland, using the Thermal Desorption Chemical Ionization Mass Spectrometer (TDCIMS). Several organic nitrates, detected as molecular ions and as thermally decomposed fragments, displayed a striking diurnal profile, peaking at night and comprising a significant fraction of total compounds measured by the TDCIMS. Products identified are consistent with first-generation oxidation products, which are assumed to be semivolatile and thus surprising to contribute strongly to nanoparticle composition under ambient conditions. Observed time series are assessed with kinetics and partitioning modeling approaches, using vapor pressures estimated with the SIMPOL.1 group contribution method, to obtain closure between our measurements and known partitioning theory. This work adds to the growing body of literature that suggests  $\text{NO}_3$  oxidation of monoterpenes is a strong contributor to SOA formation in forested environments. Furthermore, it emphasizes the potential importance of this chemistry in the growth of atmospheric nanoparticles.

## 4.2 Introduction

$\text{NO}_3$  radical chemistry has been shown to significantly contribute to the composition of ambient aerosol particles in forested sites around the world [124]. However, the role of this chemistry in new particle formation and early growth are not well understood. As one of the best instrumented sites for studying atmospheric new particle formation, the SMEAR II site in Hyytiälä, Finland is an ideal place to study this phenomenon. Molecular organonitrates, including a number of organonitrate highly oxidized molecules (HOMs), have been observed at Hyytiälä in both the gas-phase as well as in larger accumulation mode aerosol particles

[107, 173, 99]. Here, we investigate the possibility that a few of these molecules contribute to the formation of ambient nanoparticles. In addition to better understanding nanoparticle composition at this site, this work serves to identify potential organonitrate tracers for the Thermal Desorption Chemical Ionization Mass Spectrometer (TDCIMS). Successfully identifying such tracers will enable further research to assess the significance of  $\text{NO}_3$  chemistry in SOA nanoparticle growth in other locations.

In this work, we present observations of size-resolved ultrafine ( $<100$  nm diameter) particle composition at Hyytiälä in spring 2014 during the Biogenic Aerosols - Effects on Clouds and Climate (BAECC) campaign. A number of species show enhancement at night relative to their daytime signal, including some molecular organonitrate ions, but two of the most abundant (nighttime enhanced) ions observed were  $\text{C}_{10}\text{H}_{15}\text{O}_2^-$  and  $\text{C}_{10}\text{H}_{17}\text{O}_2^-$ , which are only minimally oxidized. We show in this work that these two ions are consistent with absorptive partitioning of first generation  $\text{NO}_3$  + monoterpene hydroxynitrate and ketonitrate species. This observation is somewhat puzzling given the discourse on the importance of highly oxygenated molecules for SOA growth. However, it is consistent with previously reported TDCIMS observations that intermediate volatility compounds are key constituents of ambient nanoparticles once they grow beyond  $\sim 10$  nm in diameter [97]. The abundance of these two species in nanoparticle composition suggests that  $\text{NO}_3$  oxidation products should be considered in modeling efforts to simulate new particle formation and growth from the oxidation of biogenic compounds.

## 4.3 Methods

### 4.3.1 Description of Field Site

Measurements took place at the SMEAR II field station in Hyytiälä, Finland (61°51' N, 24°17' E, 181 m above sea level). SMEAR II is situated within a stand of Scots pine and is about 60 km away from the nearest city (Tampere, S-SW, 2014 population  $\sim$ 220,000) [70, 92]. We describe observations made between April 23 and May 1, 2014, during the Biogenic Aerosols-Effects on Clouds and Climate (BAECC) campaign [136]. During this time period, the temperature ranged from minimum  $-4^{\circ}\text{C}$  at night to maximum  $17^{\circ}\text{C}$  during the day and conditions were mostly sunny April 22-26 and subsequently cloudy with a rain event April 28. Winds were from the northwest a majority of the time with wind speeds ranging from 0.5 to  $6.9\text{ m s}^{-1}$ .

### 4.3.2 Instrumentation

The primary measurements discussed in this work are nanoparticle composition from the Thermal Desorption Chemical Ionization Mass Spectrometer (TDCIMS), however datasets from a large number of other co-located instruments were critical for the analysis. Lawler et al. reported measurements from this period, focusing on nanoparticle composition during daytime new particle formation events [97], and a detailed description of the instrumentation and data analysis procedure employed during BAECC can be found there. Below, we briefly describe the aspects of the instrumentation that are pertinent to the current study of nighttime nanoparticle composition.

## TDCIMS

The Thermal Desorption Chemical Ionization Mass Spectrometer (TDCIMS) has been described in detail previously. [98, 156, 155, 167]. Briefly, ambient air is sampled and passed through a unipolar charger, ionizing the particles. These particles are then size-selected using nano differential mobility analyzers (nano-DMAs) at low size resolution, and they are subsequently collected onto a Pt filament via electrostatic precipitation. Following collection, the filament is moved into the ionization region of the TDCIMS inlet and resistively heated to volatilize the particle components. These desorbed compounds are ionized via chemical ionization with  $(\text{H}_2\text{O})_n\text{O}_2^-$  (negative mode) or  $(\text{H}_2\text{O})_n\text{H}_3\text{O}^+$  (positive mode) reagent ions and sampled into a time of flight mass spectrometer (APi-TOF; ToFwerk AG). While both polarities were typically sampled, this analysis focuses on the negative ion mode since it was found to be highly sensitive to oxidized organic compounds. Backgrounds were taken under the same conditions as the collections except the high voltage was not applied to the Pt wire, thereby avoiding particle collection but still allowing comparable exposure of any contamination from e.g. adsorption of gas-phase species. In order to collect sufficient particle mass to analyze, collection (and background) times were 30 minutes each. A single measurement cycle consisted of a collection and background in both positive and negative modes, so the time resolution of the TDCIMS data is approximately 2 hours.

During this measurement period the nano-DMAs within the TDCIMS inlet apparatus were set to 15, 20, 30, or 40 nm mobility diameter, nominally. However, the upstream unipolar charging results in some multiply charged particles as well, so the volume mean diameter of the collected particles was always higher than the nominal setpoint. In order to better assess the actual size distribution of sampled particles and collection efficiency onto the wire, both a Scanning Mobility Particle Sizer (SMPS; TSI 3085 and TSI 3025) with a bipolar neutralizer and a separate Condensation Particle Counter (CPC; TSI 3025) were continuously sampling downstream of the collection wire. The 40 nm setpoint was only used when the main particle



growth mode grew too large and/or the ambient mass concentrations were too low. In this setting, the actual size distribution of sampled particles exceeded the size range of the SMPS (<81 nm), and these periods can be considered to be sampling accumulation mode particles around 100 nm.

### **Additional Datasets**

A number of other meteorological and chemistry measurements were crucial in analyzing this dataset. The SMEAR II field station has been a continuous monitoring site since 1995, so a number of relevant datasets are available as routine measurements, including  $O_3$ ,  $NO_x$ , NO, temperature, relative humidity, radiation, and submicron particle size distributions. These datasets are publicly available and were accessed on the SMEAR website (<https://avaa.tdata.fi/web/smart>). For the chemical species that are either not routinely monitored (e.g.  $HO_x$ ) or for whom SMEAR II monitoring instrumentation was down during the period of interest (e.g. monoterpenes), we relied on published datasets of those species from previous years, using springtime data specifically when possible.

### **4.3.3 Gas / Particle Partitioning Analysis**

Mass spectra of oxidized organic species from the TDCIMS typically include a combination of molecular ions and fragments from either thermal or ionization-induced decomposition processes within the TDCIMS itself [97, 156]. Therefore, unambiguous identification of detected ions can be challenging. A major component of the analysis presented here employs an absorptive partitioning framework shown in equation 4.1 [131] to (1) assist in the identification of parent molecules leading to observed ions and (2) assess the reasonableness of specific semi-volatile species partitioning into nanoparticles under ambient conditions.

$$K_p = \frac{C_{p,i}/TSP}{C_{g,i}} = \frac{f_{om} 760 R T}{MW_{om} \zeta_i p_{L,i}^0 10^6} \quad (4.1)$$

The partitioning coefficient  $K_p$  ( $\text{m}^3 \mu\text{g}^{-1}$ ) is defined in Equation 4.1 for a compound  $i$ . In the first expression,  $C_{p,i}$  ( $\mu\text{g m}^{-3}$ ) and  $C_{g,i}$  ( $\mu\text{g m}^{-3}$ ) are the concentrations of species  $i$  in the particle and gas phases, respectively, and TSP ( $\mu\text{g m}^{-3}$ ) is the total mass concentration of suspended particulate matter. The second expression defines  $K_p$  in terms of the thermodynamic properties of compound  $i$ .  $f_{om}$  is the weight fraction of TSP that is organic material and can act as an absorbing medium (assumed = 1),  $MW_{om}$  ( $\text{g mol}^{-1}$ ) is the average molecular weight of the absorbing organic material,  $p_{L,i}^0$  (Torr) is the vapor pressure of the subcooled liquid of compound  $i$ , and  $\zeta_i$  is the activity of compound  $i$  in the condensed phase (assumed = 1).  $R$  is the universal gas constant ( $8.206 \times 10^{-5} \text{ atm m}^3 \text{ mol}^{-1} \text{ K}^{-1}$ ),  $T$  (K) is the temperature, and 760 ( $\text{Torr atm}^{-1}$ ) and  $10^6$  ( $\mu\text{g g}^{-1}$ ) are conversion factors.

### 4.3.4 Calculations

#### Electron Affinities

We used quantum chemical methods to estimate the electron affinity for the ions detected by the TDCIMS that are assumed to be thermal decomposition products. Electron affinities can be calculated simply as the difference in electronic energy between the neutral and anionic species of interest, M, according to Equations 4.2 and 4.3. If  $EA_M > EA_{O_2}$  then we expect electron transfer to occur on that analyte molecule in the ionization region of the TDCIMS.



For the species of interest as well as  $\text{O}_2$ , we built the reactant and product structures using Spartan’16 software (Wavefunction, Inc.) and ran systematic conformer sampling using the MMFF method [67], ensuring the correct charge was applied (using the FFHINT keyword for radicals to apply a neutral charge to the radical center of the reactants). Conformer geometries were then optimized at the B3LYP/6-31+G(d) level, similar to the method used in Derpmann et al. [33] using Gaussian 09 [52]. This functional is not optimal for computing absolute energies of radicals, but it is computationally efficient, has been widely tested [174, 179, 73], and has been found to accurately predict the energy ordering of conformers [146, 58, 76] so we expect it to be sufficient for this application since we are interested only in relative energies.

## Vapor Pressures

Vapor pressures used in the absorptive partitioning calculations were estimated using the SIMPOL.1 group contribution method due to its simplicity and versatility [132]. However, it is well known that vapor pressure estimates are highly uncertain and predictions for a compound using different methods can span several orders of magnitude, especially for multifunctional oxidized organics which make up SOA [10, 95, 93]. While we cannot assess the uncertainty for the species of interest in this work, we have calculated vapor pressures for these molecules independently using quantum chemical methods with COSMOTherm software, following the same procedure detailed in Kurtén et al. [93], employing systematic conformer searching using Spartan ’16 software [3]. It has been suggested that group con-

tribution methods tend to underpredict vapor pressure [163], whereas the COSMOTherm predictions more likely overestimate the actual vapor pressure [93], so using both here should at least provide upper and lower bounds for the actual vapor pressure of these species.

## 4.4 Results

### 4.4.1 TDCIMS Ambient Observations

The volume median diameter of particles collected by the TDCIMS is shown as black markers in Figure 4.2, with crosses bounding the diameters contributing 90% of collected mass. The period between April 23 and May 2 included multiple new particle formation events with sustained growth over the course of 1-3 days. During these growth events, particle modes remained under 100 nm, and the size set point of the TDCIMS was adjusted to track the mode diameter, achieving collections with volume median diameter ranging from about 25 to 60 nm. The period following the April 23 growth event consisted mainly of larger accumulation mode particles ( $\sim 100$  nm) exceeding the size range of the SMPS downstream of the TDCIMS, so these size ranges are less well constrained, but we expect composition to be dominated by the larger particles and perhaps less indicative of the contributors to the nanoparticle growth events.

Average daytime and nighttime nanoparticle mass spectra from the TDCIMS (negative ion mode) are shown in Figure 4.3a,b. Due to the  $\sim 2$  hour resolution of the TDCIMS, averages were taken from the mass spectrum collected between 11am-2pm each day and 1-3 am each night to get a snapshot of the daytime and nighttime composition without obscuring the signal intensities with diel cycles. Figure 4.3c shows the difference spectrum (nighttime - daytime), highlighting which species are enhanced during the day and which are enhanced at night. Only a handful of species exhibit pronounced daytime/nighttime variability.

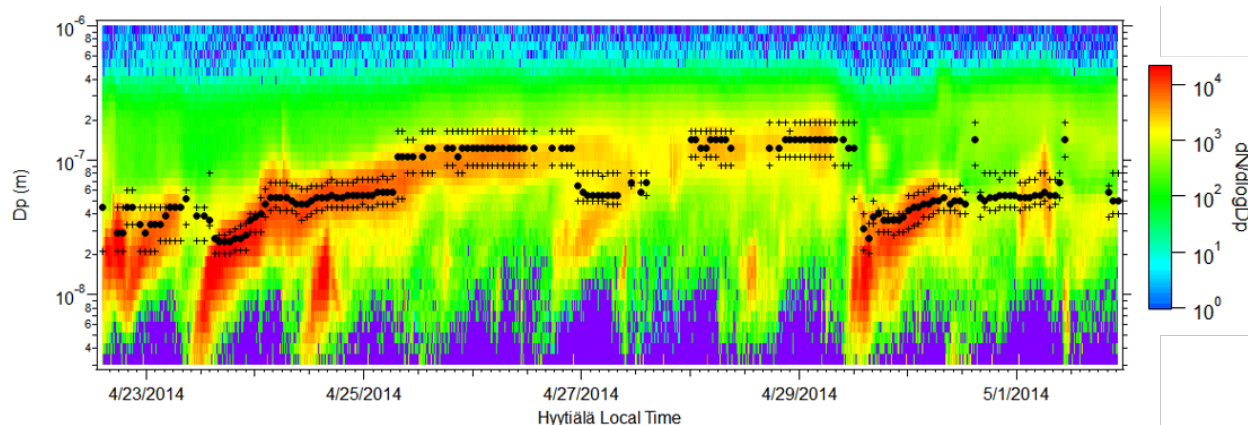


Figure 4.2: Ambient aerosol size distribution ( $dN/d\log D_p$ ), showing particle sizes collected for TDCIMS analysis. Darker markers show volume median diameter of collected particles assessed by direct measurements. Crosses represent the range of particle sizes composing 90% of the total collected mass.

Consistent diel variability requires diel trends in both the production *and* loss of a compound. Production rates of gas-phase species that contribute to SOA do have diel cycles driven by solar radiation, temperature, and emissions of precursors. However, a simplified picture of a particle growth event spanning several days would suggest continued “production” (or accommodation) of material in(to) the particle-phase without a diurnally driven loss mechanism. A diel cycle in the particle-phase could be driven by equilibrium partitioning following the diel temperature cycle, but this cycling would likely be less pronounced for small particles whose composition is expected to be biased toward low-volatility species that would not appreciably re-partition into the gas-phase. It therefore makes sense that relatively few compounds show significant diurnal difference in this dataset. However, of the compounds that *do* show diel variability, a few seem unlikely candidates to have been able to partition into nanoparticles appreciably in the first place.

As mentioned earlier, oxidized organic species often undergo some amount of fragmentation in the TDCIMS inlet due to thermal and/or ionization-induced decomposition. As a result, many of the species observed in TDCIMS spectra have fairly low  $m/z$ , but many of these have low carbon numbers and high O/C and can therefore be attributed to fragments of

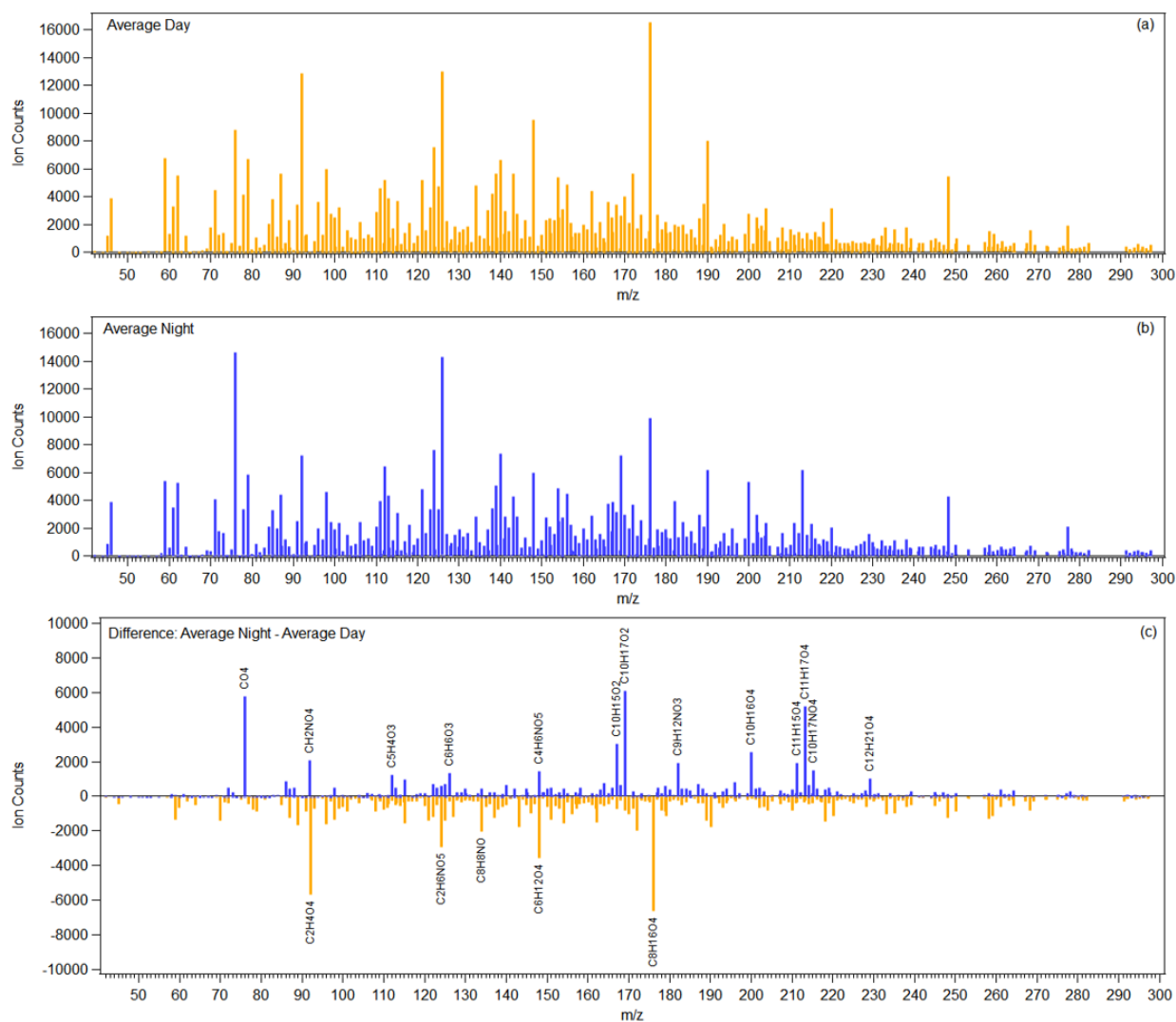


Figure 4.3: TDCIMS-derived average daytime (a) and nighttime (b) mass spectra. Lower plot (c) shows the difference spectrum of nighttime - daytime and highlights the species that dominate nanoparticle composition during each period.

oxidized, multifunctional compounds. However, some of the nighttime enhanced ions have relatively high carbon numbers and comparatively few oxygens. We highlight in particular  $C_{10}H_{15}O_2^-$  and  $C_{10}H_{17}O_2^-$  as two of the most abundant nighttime peaks but having quite low O/C, indicative of being a semi-volatile, early generation oxidation product.

The full time series of these two ions is shown in Figure 4.4 with nighttime periods shaded in grey. These two ions are not only enhanced at night relative to daytime, but they have a very pronounced diurnal cycle, peaking sharply by the end of the night and rapidly disappearing, almost completely, during the day. The combination of the  $C_{10}$  backbone and sharp nighttime peak is suggestive of  $NO_3$  oxidation of monoterpenes, but it is not entirely clear what oxidation product these two ions correspond to.

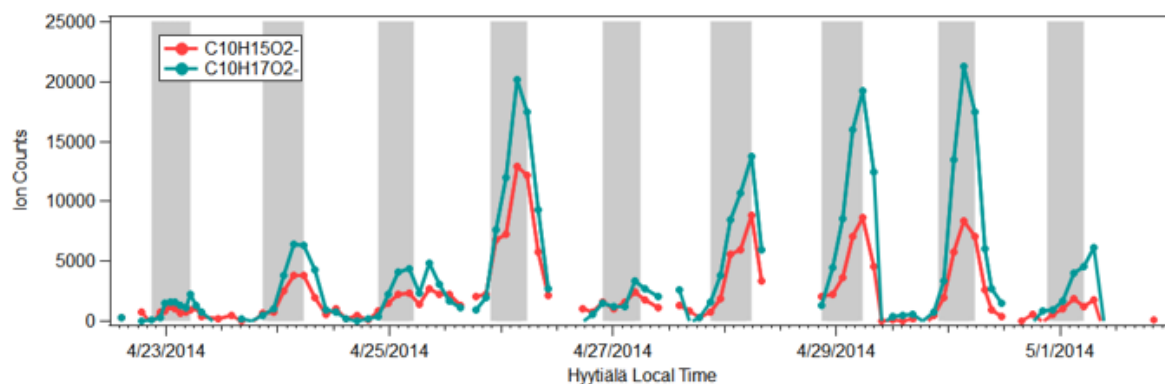


Figure 4.4: Time series of  $C_{10}H_{15}O_2^-$  and  $C_{10}H_{17}O_2^-$  from TDCIMS measurements of nanoparticle composition.

## Supporting Observations

Supporting observations are shown in Figure 4.5.  $NO_2$  concentrations are elevated at night, averaging around 400 ppt most nights and occasionally reaching 1 ppb, and  $O_3$  concentrations range from about 30-50 ppb at night. Monoterpene measurements were not available during this time period, however springtime (April, May 2011) speciated monoterpene diurnal profiles at the SMEAR II site have been published [66], so we extrapolated these diurnal averages for the full time series of interest to estimate monoterpene concentrations.

These speciated measurements indicate that the dominant monoterpene emissions at this site are  $\alpha$ -pinene,  $\Delta$ -3-carene, camphene, and  $\beta$ -pinene in approximately a 10:3:3:1 ratio. The extrapolated  $\alpha$ -pinene time series is included in Figure 4.5, and based on the ratios of other monoterpenes with respect to  $\alpha$ -pinene, we can estimate that the total monoterpene concentration will peak at night around 140 ppt.

## 4.5 Discussion

In the next sections we propose and test a hypothesis to identify the parent molecules present in ambient nanoparticles that lead to the observed  $C_{10}H_{15}O_2^-$  and  $C_{10}H_{17}O_2^-$  ions during TDCIMS analysis. This discussion includes a mechanistic hypothesis, discussion of formation and detectability within the TDCIMS, and partitioning calculations to assess the reasonableness of these species in the sampled nanoparticles.

### 4.5.1 Proposed Mechanism

Given the strong indicators that  $C_{10}H_{15}O_2^-$  and  $C_{10}H_{17}O_2^-$  likely originate from  $NO_3$  oxidation of monoterpenes, we begin by considering the initial steps of monoterpene +  $NO_3$  oxidation. Figure 4.6 shows this mechanism for  $\alpha$ -pinene since it is the most abundant monoterpenes at this site.  $\Delta$ -3-carene, the second most abundant monoterpene at this site, has an analagous mechanism for this first generation chemistry since both  $\alpha$ -pinene and  $\Delta$ -3-carene have an endocyclic double bond in the same position. Camphene and  $\beta$ -pinene are also bicyclic monoterpenes but both have an exocyclic double bond instead of the endocyclic double bond in  $\alpha$ -pinene and  $\Delta$ -3-carene. While their oxidation products are not as directly analagous to  $\alpha$ -pinene, most of their oxidation products in these first few steps will have the same formula and functional groups, so we do not show their mechanisms explicitly here.



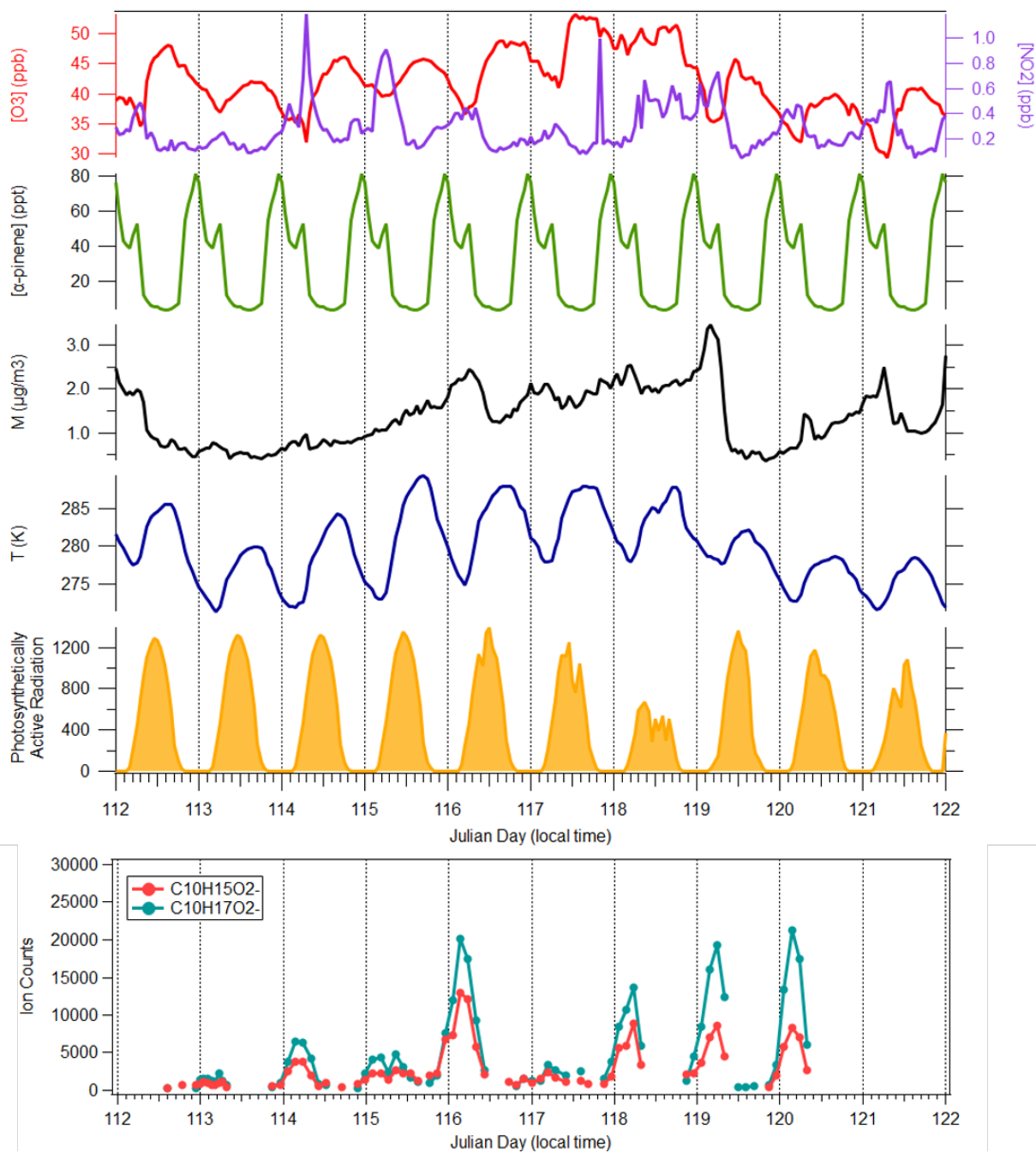


Figure 4.5: Supporting measurements of [O<sub>3</sub>], [NO<sub>2</sub>], estimated concentrations of α-pinene (see text), PM<sub>2.5</sub>, temperature, and photosynthetically active radiation during the observation period, plotted along with the time series of C<sub>10</sub>H<sub>15</sub>O<sub>2</sub><sup>-</sup> and C<sub>10</sub>H<sub>17</sub>O<sub>2</sub><sup>-</sup>.

The  $\text{NO}_3$  radical adds to the double bond, preferentially at the secondary site ( $\sim 65\%$ ) to form a tertiary alkyl radical, and in smaller yield at the tertiary site ( $\sim 35\%$ ) [79, 149]. These alkyl radicals rapidly form peroxy radicals from  $\text{O}_2$  addition. The peroxy radicals then have multiple channels available. Reaction with a  $\text{HO}_2$  radical terminates the radical to a nitrate-hydroperoxide ( $\text{C}_{10}\text{H}_{17}\text{NO}_5$ ). Self reaction with another  $\text{RO}_2$  can result in either an alkoxy radical ( $\text{RO}$ ) or can terminate to a hydroxynitrate ( $\text{C}_{10}\text{H}_{17}\text{NO}_4$ ) and ketonitrate ( $\text{C}_{10}\text{H}_{15}\text{NO}_4$ ), noting that the ketonitrate cannot form if the peroxy group is on a tertiary carbon and therefore would not form from the dominant  $\text{NO}_3$  addition pathway. The alkoxy radical products will decompose, opening the 6-membered ring, and in the case of  $\alpha$ -pinene, decompose into closed shell pinonaldehyde ( $\text{C}_{10}\text{H}_{16}\text{O}_2$ ) [94].

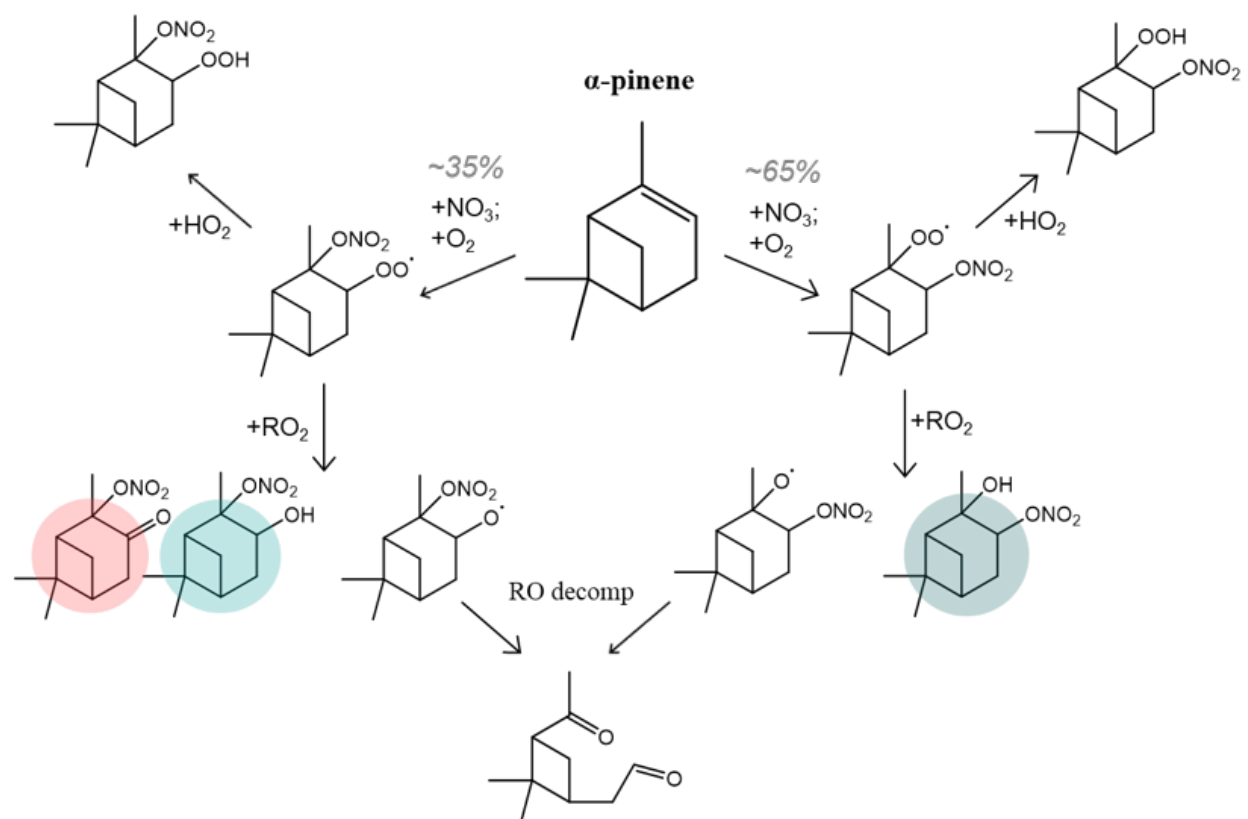


Figure 4.6: Mechanism for  $\text{NO}_3$  initiated oxidation of  $\alpha$ -pinene. Shaded compounds are key intermediates that are discussed in the text and shown again in Figure 4.7.

## Proposed Species Identification

Of the four closed shell products identified above, the hydroxynitrate ( $C_{10}H_{17}NO_4$ ) and ketonitrate ( $C_{10}H_{15}NO_4$ ) are most likely the source of the observed ions. These  $RO_2 + RO_2$  products yield an  $H_{15}$  and  $H_{17}$  product from a single reaction, and while missing the  $-NO_2$  group, both ions' formulas are consistent with having two functional groups.

Organic nitrates are known to dissociate at high temperature ( $\sim 300-400^\circ C$ ), cleaving the  $RO-NO_2$  bond [29, 86]. The TDCIMS desorption period resistively heats the Pt filament at a continuous ramp for 40 s resulting in a final temperature  $\sim 600^\circ C$ . Therefore,  $RO-NO_2$  dissociation is very likely occurring during the desorption process. Thermal dissociation of  $C_{10}H_{15}NO_4$  and  $C_{10}H_{17}NO_4$ , in particular, would therefore result in neutral alkoxy radicals  $C_{10}H_{15}O_2$  and  $C_{10}H_{17}O_2$  and  $NO_2$ . As discussed in Chapters 2 and 3, alkoxy radical lifetimes are extremely short, so the question remains whether these dissociated organic fragments are actually detectable in the TDCIMS. Since the TDCIMS desorption occurs within the ionization region, between the ion source and inlet to the mass spectrometer, it is conceivable that collision with a reagent ion could be competitive with alkoxy decomposition or recombination with  $NO_2$ . If that is the case, then the TDCIMS would be able to see these specific fragments as long as the reagent ion chemistry is sensitive to them.

## Electron Affinity Calculations

In negative ion mode with the  $(H_2O)_nO_2^-$  reagent ion, subsequently referred to as  $O_2^-$ , analyte molecules are likely to be ionized via  $O_2^-$  clustering,  $e^-$  transfer, or proton transfer, as shown in Equations 4.4 - 4.6 [33]. The most straightforward ionization of alkoxy radicals would be  $e^-$  transfer to the radical site, so we calculated the electron affinities for both  $C_{10}H_{15}O_2$  and  $C_{10}H_{17}O_2$  using quantum chemical methods according to the reactions shown in Figure 4.7. As discussed in section 4.3.4, the calculated electron affinity values are not

expected to be accurate absolute values, but we do expect the relative electron affinities to be qualitatively correct. The experimentally determined electron affinity for  $O_2$  is included for reference ( $EA_{O_2} = 0.45$  eV or,  $\Delta E = -0.45$  eV) [2, 42]. Our calculated  $O_2$  electron affinity is 0.59 eV, within about 30% of the experimental value, whereas our calculated electron affinities for  $C_{10}H_{15}O_2$  and  $C_{10}H_{17}O_2$  are  $\geq 2$  eV. It therefore appears that electron transfer to either of these alkoxy radicals is extremely favorable compared to  $O_2$ , so we conclude that these species should be detectable as long as their lifetime is long enough in the ionization region relative to ion-molecule collisions.

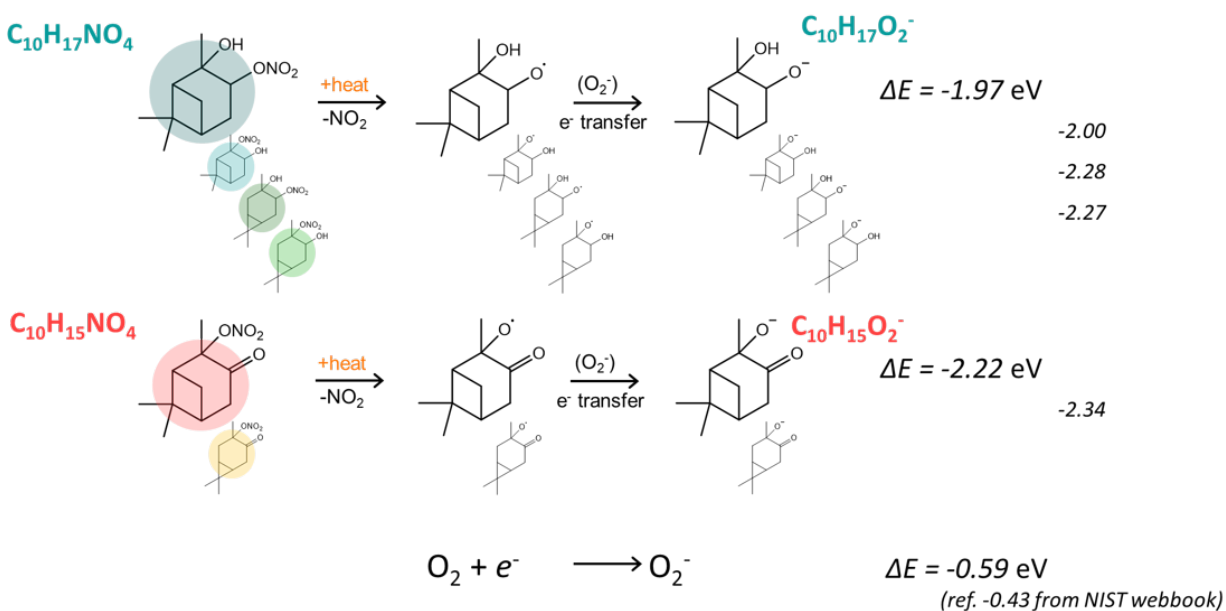


Figure 4.7: Proposed steps that demonstrate the formation of observed ions from key organonitrate precursors show in Figure 4.6. Calculated EA are shown for observed ions as well as minor ions.

## 4.5.2 Partitioning Modeling

From the standpoint of oxidation chemistry alone, it seems entirely reasonable that the  $C_{10}H_{15}O_2^-$  and  $C_{10}H_{17}O_2^-$  ions were originally  $C_{10}H_{15}NO_4$  and  $C_{10}H_{17}NO_4$  and thermally decomposed during analysis. Indeed,  $C_{10}H_{17}NO_4^-$  is observed in the nighttime mass spectrum as well (Figure 4.3), though with lower intensity. However, these are minimally oxidized, 1<sup>st</sup>-generation oxidation products and are expected to be semi-volatile. It is therefore somewhat surprising that they would be present in significant concentration in growing nanoparticles, which intuitively should be composed largely of low volatility species. In order to further validate the identity of these two ions as well as assess whether these products are actually predicted to be able to partition into the particle phase at low mass loadings, we have constructed an observationally constrained kinetics and absorptive partitioning box model to predict the gas-phase formation and partitioning of  $C_{10}H_{15}NO_4$  and  $C_{10}H_{17}NO_4$ .

Based on the supporting chemistry and meteorology measurements between April 23 and May 2, we have been able to estimate the steady state  $NO_3$  radical time series, the time series of the gas-phase monoterpene +  $NO_3$  derived ketonitrate ( $C_{10}H_{15}NO_4$ ) and hydroxynitrate ( $C_{10}H_{17}NO_4$ ) products, and calculate the partitioning of those two species into the particle-phase based on the absorptive partitioning framework [131].

### Calculating $[NO_3]_{ss}$

The steady state  $NO_3$  radical concentration can be calculated according to Equation 4.9 where the production rate ( $P(NO_3)$ ), Equation 4.7) of  $NO_3$  is simply the rate of Reaction 1.4, and the lifetime ( $\tau(NO_3)$ ) Equation 4.8) is the inverse of the sum of the rates of all the reactions that consume  $NO_3$ , here assumed to be reaction with monoterpene (MT), reaction with NO, and photolysis. Photolysis rates (corresponding to Reactions 1.6 and 1.7) were calculated according to the parameterization used in the Master Chemical Mechanism

(Equation 4.10) where  $l$ ,  $m$ , and  $n$  are reaction-specific parameters tabulated in Saunders et al. [149], and therefore the only input is the solar zenith angle ( $\chi$ ). The time series of the solar zenith angle was calculated for the latitude and longitude of the SMEAR II station using the Solar Calculations tool from NOAA [1]. Final photolysis rate time series were corrected using the normalized photosynthetically active radiation (PAR) time series to account for cloudy days. The time series of calculated  $[\text{NO}_3]_{\text{ss}}$  is shown in figure Figure 4.8.

$$P(\text{NO}_3) = k_{\text{NO}_2+\text{O}_3} [\text{NO}_2][\text{O}_3] \quad (4.7)$$

$$\tau(\text{NO}_3) = \frac{1}{\sum k_{\text{MT}+\text{NO}_3}[\text{MT}] + k_{\text{NO}+\text{NO}_3} + j_{1,\text{NO}_3} + j_{2,\text{NO}_3}} \quad (4.8)$$

$$[\text{NO}_3]_{\text{ss}} = \frac{P(\text{NO}_3)}{\tau(\text{NO}_3)} \quad (4.9)$$

$$J = l(\cos \chi)^m \exp(-n \sec \chi) \quad (4.10)$$

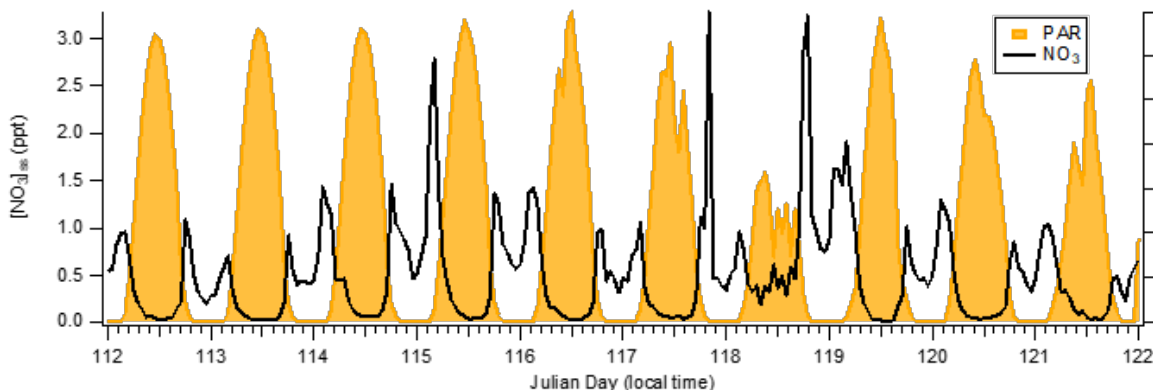


Figure 4.8: Calculated steady state  $\text{NO}_3$  radical time series, overlaid on photosynthetically active radiation (PAR) data to indicate daylight.

## Calculating $[C_{10}H_{15}NO_4]$ and $[C_{10}H_{17}NO_4]$

The gas-phase concentration of the ketonitrate product ( $C_{10}H_{15}NO_4$ ) and hydroxynitrate product ( $C_{10}H_{17}NO_4$ ) can be approximated numerically based on the law of mass action, by taking the production rate minus loss rate and integrating it over some unit time, e.g.  $[C_{10}H_{15}NO_4] = (Production(C_{10}H_{15}NO_4) - Loss(C_{10}H_{15}NO_4))\Delta t$ . Typically the size of  $\Delta t$  would be critical to avoid problems with this calculation, but since we are using observationally constrained precursor concentrations at every time step (as opposed to free modeling all concentrations) the hourly time series used here are sufficient.

The production rate of each of these species is complicated somewhat by the fact that the closed-shell keto- and hydroxynitrate products arise from  $RO_2 + RO_2$  chemistry following the initial monoterpene +  $NO_3$  reaction and  $RO_2$  radicals have multiple loss pathways (Reactions 4.11-4.16), so production rates were calculated in terms of the relevant  $RO_2$  radical, using published rate constants [7, 180, 128, 39, 108, 164] and branching ratios from the Master Chemical Mechanism (v3.3.1, [mcm.leeds.ac.uk/MCM](http://mcm.leeds.ac.uk/MCM)) [149, 79]. For these production rates,  $[HO_2]$  data was needed as well, which was estimated based on published summertime data taken at SMEAR II in 2010 [71]. The gas-phase loss rates of the keto- and hydroxynitrate are less well constrained as the chemical reactivity of these species has not been studied explicitly. We consider photooxidation of both species using rate constants from the Master Chemical Mechanism [149, 79] as well as the photolysis of the ketonitrate [149]. Dry deposition is also expected to be significant for these species [125], but this has not yet been added in the current version of this model.



With the loss rates inadequately constrained, we bound our concentration estimates of these two species with an “instantaneous” concentration and a “cumulative” concentration. The instantaneous concentration is simply the concentration calculated at each time step, while the cumulative concentration adds the instantaneous concentration to the concentration from the previous time bin, leading to a net increase in concentration over time. The calculated instantaneous and cumulative time series for the  $\alpha$ -pinene-derived hydroxynitrate product is shown in Figure 4.9.

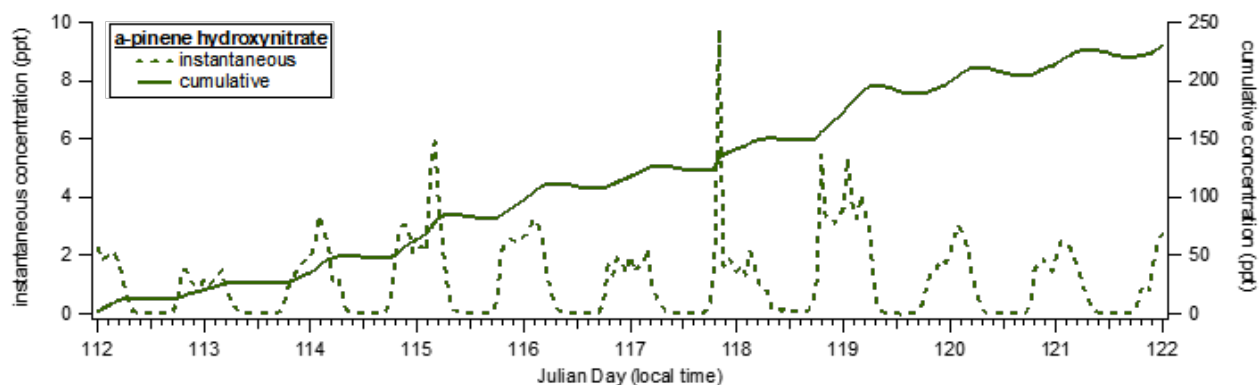


Figure 4.9: The calculated instantaneous and cumulative time series for the  $\alpha$ -pinene-derived hydroxynitrate product during the observation period.



## Vapor Pressure Calculations

With the kinetics calculations complete, providing us with time series of  $C_{10}H_{15}NO_4$  and  $C_{10}H_{17}NO_4$ , the last step is to calculate the partitioning of these species into the particle-phase. In order to do that, we need to estimate the vapor pressures of each molecule. As the vapor pressures are temperature dependent, we calculated the temperature-dependent vapor pressure at each nominal temperature over the range observed during these measurements (270-290 K) using the SIMPOL.1 group contribution method for both the  $C_{10}$  ketonitrate and hydroxynitrate and created a temperature-dependent vapor pressure time series for each. Vapor pressures at 298 K were also estimated using COSMOTerm, and the COSMOTerm temperature-dependent time series was estimated by scaling the SIMPOL.1 time series by the ratio of the COSMOTerm vapor pressure estimate to the SIMPOL.1 vapor pressure estimate at 298 K. Figure 4.10 shows the estimated vapor pressure time series for the ketonitrate product ( $C_{10}H_{15}NO_4$ ) and the hydroxynitrate product ( $C_{10}H_{17}NO_4$ ).

## Model comparison to TDCIMS Observations

The final step is to run the partitioning calculations using Equation 4.1 to obtain the concentration of  $C_{10}H_{15}NO_4$  and  $C_{10}H_{17}NO_4$  in the particle phase. Figure 4.11 shows the modeled fraction each compound contributes to the total particle-phase overlaid with the TDCIMS data represented as fraction of total signal. The left and right axes are adjusted to maximize overlap of the two traces in order to assess the predicted vs observed timing of these species in the particle phase, and in doing so, we see remarkable temporal agreement between the observed and modeled data. This agreement strongly suggests that nighttime production of monoterpene +  $NO_3$  products (combined with decreasing temperatures) are driving partitioning of these species into the particle-phase and increasing temperatures in the morning (combined with lack of production) are driving re-volatization in the morning.

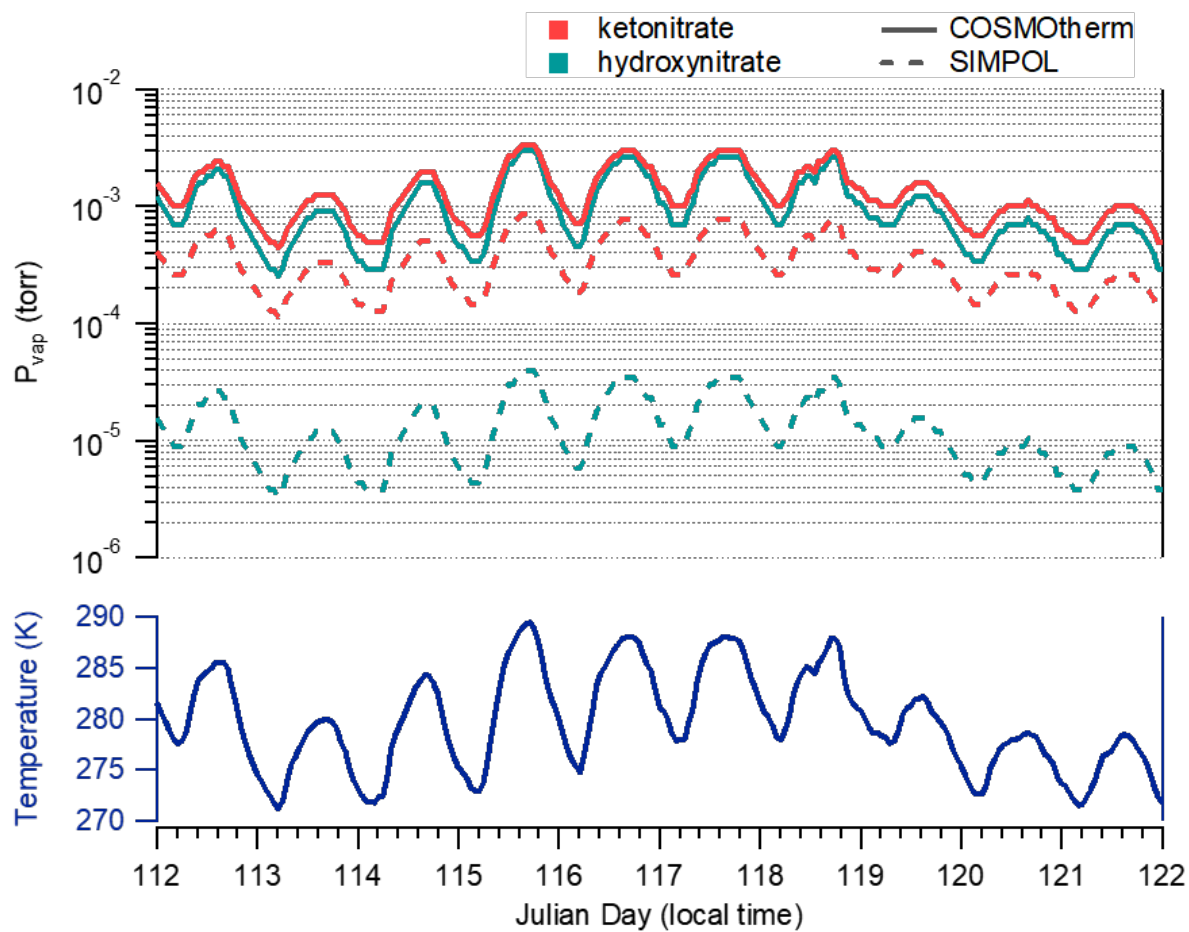


Figure 4.10: Estimated vapor pressures for the ketonitrate product ( $\text{C}_{10}\text{H}_{15}\text{NO}_4$ ) and the hydroxynitrate product ( $\text{C}_{10}\text{H}_{17}\text{NO}_4$ ) using COSMOtherm and SIMPOL.1.

In other words, these two species seem to be undergoing equilibrium absorptive partitioning, enhanced by the fact that production rates are highest while temperatures are low.

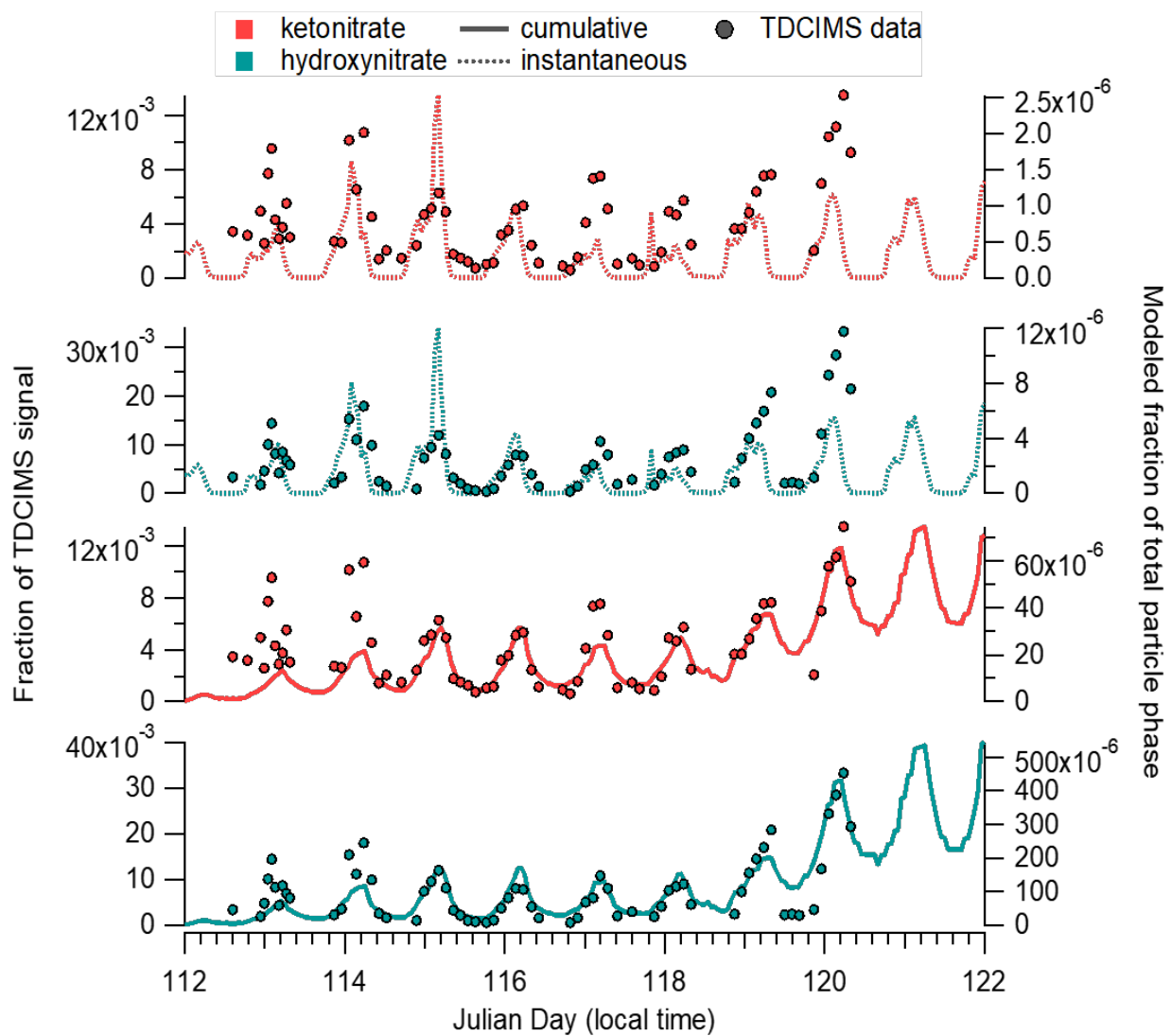


Figure 4.11: Modeled fraction that each compound contributes to the total particle-phase overlaid with the TDCIMS data represented as fraction of total ion signal.

However, it is still unclear whether the high abundance of these ions makes sense in the nanoparticle mass spectra. The modeled temporal variability agrees with observations, but the modeled fractions in the particle phase are orders of magnitude lower than observed, and the relative abundance of the ketonitrate and hydroxynitrate are quite different for the modeled results than the TDCIMS observations. Unfortunately, uncertainties in both the

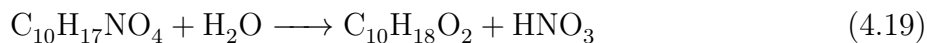
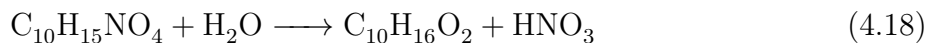
modeled assumptions and TDCIMS observations make it difficult to draw conclusions about the actual particle phase fractions of these two compounds. In the modeling framework, the vapor pressure estimates could be off by orders of magnitude, although there is some indication in the literature that SIMPOL.1 is more likely to underestimate vapor pressures than overestimate [93, 95], which would make these modeled fractions upper limits. On the other hand, it is not possible to calibrate the TDCIMS for the large range of oxidized organic species likely present in nanoparticles, so it is possible that the TDCIMS is just very sensitive to these two ions and they therefore represent a disproportionately large fraction of the total signal.

### 4.5.3 Alternative Mechanisms

We have thus far attributed the observed  $C_{10}H_{15}O_2^-$  and  $C_{10}H_{17}O^-$  ions to 1<sup>st</sup>-generation organonitrates ( $C_{10}H_{15}NO_4$  and  $C_{10}H_{17}NO_4$ ), however one could propose other products that would lead to these two ions in the TDCIMS. While we are in the process of adding these processes to the model described above to assess them in detail, we suspect that neither will be sufficient to explain the observed nanoparticle mass spectra.

### Hydrolysis

Particle-phase hydrolysis of organonitrates is one possibility that could lead to  $C_{10}H_{15}O_2^-$  and  $C_{10}H_{17}O_2^-$  ions in the TDCIMS. Equation 4.17 shows a general hydrolysis reaction, and Equations 4.18 and 4.19 show the hydrolysis reactions of the  $C_{10}$  ketonitrate and hydroxynitrate discussed previously. Since the observed ions only have two oxygens, the hydrolyzed organonitrate would have to be those two compounds specifically. Following hydrolysis, the products would be  $C_{10}H_{16}O_2$  and  $C_{10}H_{18}O_2$ , and assuming ionization by proton transfer ( $[M-H]^-$ ), they would be detected as  $C_{10}H_{15}O_2^-$  and  $C_{10}H_{17}O_2^-$  by the TDCIMS.



Tertiary organonitrates have been shown to have very short lifetimes with respect to hydrolysis, on the order of minutes, whereas primary and secondary organonitrates are unlikely to hydrolyze on the timescale of particle lifetimes [28, 75]. This structural dependence has made it difficult to assess the extent to which hydrolysis occurs in SOA. Chamber studies of SOA formation from  $\text{NO}_3$  + monoterpenes conducted at high relative humidity have suggested that hydrolysis is very fast (<30 min), but only affects up to  $\sim 15\%$  of the particulate organonitrates [162, 11, 16, 110]. On the other hand, regional modeling efforts constrained by ambient data report particulate organonitrate lifetimes to be several hours [139, 51, 100, 176].

For the particular  $\text{NO}_3$ -derived organonitrates considered here, the major  $\text{NO}_3$  addition pathway occurs at the secondary carbon, and therefore a large fraction of the  $\text{C}_{10}\text{H}_{17}\text{NO}_4$  would not undergo efficient hydrolysis. The ketonitrate ( $\text{C}_{10}\text{H}_{15}\text{NO}_4$ ), however, can only form via the minor, tertiary  $\text{NO}_3$  addition channel and therefore could undergo rapid hydrolysis if conditions allow. If we were to attribute the observed  $\text{C}_{10}\text{H}_{15}\text{O}_2^-$  and  $\text{C}_{10}\text{H}_{17}\text{O}_2^-$  ions entirely to hydrolysis products ( $\text{C}_{10}\text{H}_{16}\text{O}_2$  and  $\text{C}_{10}\text{H}_{18}\text{O}_2$ ), the kinetics of the original organonitrate formation and subsequent partitioning into the particle-phase would look the same as discussed earlier, but the formation of the hydrolysis products would be shifted later in time by the hydrolysis lifetime of those organonitrates. If the hydrolysis lifetime is very short, as indicated in laboratory experiments, this time shift might not be substantial enough to notice compared to the 2 hour resolution of the TDCIMS. However, if the hydrolysis lifetime is a few hours, as indicated from modeling of ambient observations, we expect

that the modeled timeseries of the hydrolysis products would be shifted later in time with respect to the observed ions.

That said, even if it cannot be determined whether these ions are thermally decomposed organonitrates or hydrolysis products, the question remains why these semivolatile organonitrates are partitioning into the nanoparticles appreciably in the first place.

## Oligomerization

Another possible pathway is that these  $C_{10}$  ions originate from oligomers that thermally decompose in the TDCIMS inlet. There is a good deal of evidence for particle-phase oligomerization reactions [180], including in monoterpene +  $NO_3$  systems [25, 35], so this is certainly chemistry that could be occurring in the particles. However, if the  $C_{10}$  ions we see originate from oligomers that have decomposed in the TDCIMS inlet, we would expect the diurnal variability of these ions to reflect their significantly lower vapor pressure and not completely re-volatilize every morning.

## 4.6 Conclusions

In this work we have so far investigated the source of two minimally oxidized organic ions,  $C_{10}H_{15}O_2^-$  and  $C_{10}H_{17}O_2^-$ , observed in nanoparticle composition during growth events in the Boreal forest. These are two of only a few ions observed in high abundance that have a striking diurnal profile peaking at night, suggesting that they likely originate from  $NO_3$  radical oxidation of monoterpenes. We propose that these ions form from thermal decomposition of the 1<sup>st</sup>-generation ketonitrate ( $C_{10}H_{15}NO_4$ ) and hydroxynitrate ( $C_{10}H_{17}NO_4$ ) products and we confirm that these two ions should be detectable by the TDCIMS. Kinetic and thermodynamic modeling of the gas-phase formation and subsequent partitioning of these two

compounds into the particle phase using supporting measurements from the SMEAR II site, independent from the TDCIMS observations, shows good temporal agreement with the time series of these two ions in the TDCIMS. However, the magnitude of the modeled fractional contribution of each of these species in the particle phase is significantly lower than the fractional contribution of these ions to the total TDCIMS signal. Since these differences may be driven by uncertainties in the TDCIMS sensitivity to these ions and/or uncertainties in the vapor pressures of these compounds, we cannot say whether the high abundance of these ions observed in the TDCIMS is corroborated entirely by simple equilibrium absorptive partitioning. We want to emphasize that in spite of uncertainties in the overall magnitude of these species in the particle phase, the fact that the modeled and observed time series show remarkable overlap suggests that these ions have been correctly identified and that semivolatile nighttime monoterpene + NO<sub>3</sub> products do contribute to nanoparticle composition at this site. Moreover, equilibrium absorptive partitioning may drive an apparent diurnal cycle in nanoparticle composition.

## 4.7 Ongoing & Future Work

The analysis presented here is not yet complete and has two components in progress. First, as mentioned in section 4.5.3, two other mechanistic pathways could potentially lead to the same ions observed in the TDCIMS: hydrolysis of organonitrates or oligomerization and subsequent decomposition in the TDCIMS inlet. While we suspect that these mechanisms are unlikely to be contributing significantly to our observations, we are expanding the model to include both of these processes so we can compare the three mechanistic hypotheses. The model is also being expanded to include other important mechanistic details such as explicit daytime, 1<sup>st</sup>-generation monoterpene chemistry that could lead to other permutations of similar low-oxidized C<sub>10</sub> compounds, as well as expanding the gas-phase loss mechanisms of

these species to include dry deposition. Finally, we want to assess the impact of this apparent nighttime semivolatile partitioning on the particle growth events and determine the extent to which it seems to be contributing to sub-100 nm particle mass.



# Chapter 5

## Conclusions

In this work we uncovered some of the mechanistic diversity between cyclic monoterpenes that very likely leads to the large range of SOA and product yields observed in laboratory studies. It should be emphasized that the mechanistic diversity observed between different monoterpenes is an important finding in and of itself. Monoterpenes collectively are a significant fraction of BVOC emissions globally, and while  $\alpha$ -pinene is the most abundant on average, several other monoterpenes are emitted in significant amounts and therefore each of the diverse pathways explored in this work have significant impacts on the global scale and larger impacts in the regions where they are most abundant.

We also explored the mechanism by which  $\text{NO}_3 + \Delta$ -3-carene is able to form highly oxidized products, which are expected to be very important for SOA formation and growth. We come to the conclusion that a significant driver for SOA formation may simply be the length of the radical propagation chain, or how many oxidation steps a radical intermediate can undergo before it terminates, whether propagation occurs via unimolecular or bimolecular pathways.

Finally, we observed that semi-volatile organonitrates are likely partitioning onto nanoparticles, simultaneously confirming decades-old understanding of thermodynamic partitioning,

but also somewhat calling into question the community's narrow focus on the extremely low end of the volatility spectrum in recent years.

## 5.1 Future Directions

The future directions of this project are already well underway. The logical next steps for this work are: 1) experimental validation of the inter-terpene mechanism comparisons described in chapter 2; 2) experimental work assessing the particle-phase composition and obtaining closure between particle growth rates, chemical species that are contributing to growth, and concentrations of gas phase compounds that are being taken up; and 3) building and running a comprehensive box model incorporating computationally derived rate constants and working toward agreement between modeled and observed time series to better constrain the complex kinetics at play.

In the past year, we have run chamber experiments for  $\text{NO}_3$  oxidation of  $\alpha$ -pinene,  $\beta$ -pinene,  $\Delta$ -3-carene, and  $\alpha$ -thujene, with a more complete suite of instrumentation than was used in the experiments discussed in chapter 3. This full suite of instruments includes CIMS with  $\text{NO}_3^-$  and  $\text{I}^-$  reagent ions to cover a broader range of oxidized products in the gas-phase as well as the TDCIMS for particle composition. There is now plenty of data to mull over for years to come.

In the longer term, this work has raised important questions of how monoterpene chemistry can be parameterized into models more effectively to capture more of the observed variability, while avoiding becoming too computationally expensive for regional and global models. One potential future direction would be the development of a semi-empirical ultrafine particle growth rate estimator. The inputs and outputs of the parameterization will be based on values that regional and global aerosol microphysics models typically predict and require,

respectively, to capture ultrafine particle growth. We expect the model inputs could be linked to emissions inventories in order to capture regionally-specific monoterpene emissions. Other inputs might include NO<sub>x</sub>, SO<sub>2</sub>, NH<sub>3</sub> and ozone. Outputs would be mass uptake rates that could be converted into size-dependent particulate mass concentrations that could be used to explore the impacts of this special chemistry on climate and air quality.

# Bibliography

- [1] ESRL Global Monitoring Laboratory - Global Radiation and Aerosols. <https://www.esrl.noaa.gov/gmd/grad/solcalc/calcdetails.html>. Accessed: 2020-12-07.
- [2] Oxygen. <https://webbook.nist.gov/cgi/cbook.cgi?ID=C7782447&Mask=20>. Accessed: 2020-12-07.
- [3] Spartan '16.
- [4] J. Almeida, S. Schobesberger, A. Kürten, I. K. Ortega, O. Kupiainen-Määttä, A. P. Praplan, A. Adamov, A. Amorim, F. Bianchi, M. Breitenlechner, A. David, J. Dommen, N. M. Donahue, A. Downard, E. Dunne, J. Duplissy, S. Ehrhart, R. C. Flagan, A. Franchin, R. Guida, J. Hakala, A. Hansel, M. Heinritzi, H. Henschel, T. Jokinen, H. Junninen, M. Kajos, J. Kangasluoma, H. Keskinen, A. Kupc, T. Kurtén, A. N. Kvashin, A. Laaksonen, K. Lehtipalo, M. Leiminger, J. Leppä, V. Loukonen, V. Makhmutov, S. Mathot, M. J. McGrath, T. Nieminen, T. Olenius, A. Onnela, T. Petäjä, F. Riccobono, I. Riipinen, M. Rissanen, L. Rondo, T. Ruuskanen, F. D. Santos, N. Sarnela, S. Schallhart, R. Schnitzhofer, J. H. Seinfeld, M. Simon, M. Sipilä, Y. Stozhkov, F. Stratmann, A. Tomé, J. Tröstl, G. Tsagkogeorgas, P. Vaattovaara, Y. Viisanen, A. Virtanen, A. Vrtala, P. E. Wagner, E. Weingartner, H. Wex, C. Williamson, D. Wimmer, P. Ye, T. Yli-Juuti, K. S. Carslaw, M. Kulmala, J. Curtius, U. Baltensperger, D. R. Worsnop, H. Vehkamäki, and J. Kirkby. Molecular understanding of sulphuric acid-amine particle nucleation in the atmosphere. *Nature*, 502(7471):359–363, 10 2013.
- [5] V. P. Aneja, D. S. Kim, M. Das, and B. E. Hartsell. Measurements and analysis of reactive nitrogen species in the rural troposphere of southeast United States: Southern oxidant study site SONIA. *Atmospheric Environment*, 30(4):649–659, 2 1996.
- [6] R. Atkinson. Rate constants for the atmospheric reactions of alkoxy radicals: An updated estimation method. *Atmospheric Environment*, 41(38):8468–8485, 12 2007.
- [7] R. Atkinson and J. Arey. Atmospheric Degradation of Volatile Organic Compounds. *Chemical Reviews*, 103(12):4605–4638, 12 2003.
- [8] R. W. Atkinson, I. C. Mills, H. A. Walton, and H. R. Anderson. Fine particle components and health - A systematic review and meta-analysis of epidemiological time

- series studies of daily mortality and hospital admissions. *Journal of Exposure Science and Environmental Epidemiology*, 25(2):208–214, 3 2015.
- [9] B. R. Ayres, H. M. Allen, D. C. Draper, S. S. Brown, R. J. Wild, J. L. Jimenez, D. A. Day, P. Campuzano-Jost, W. Hu, J. de Gouw, A. Koss, R. C. Cohen, K. C. Duffey, P. Romer, K. Baumann, E. Edgerton, S. Takahama, J. A. Thornton, B. H. Lee, F. D. Lopez-Hilfiker, C. Mohr, P. O. Wennberg, T. B. Nguyen, A. Teng, A. H. Goldstein, K. Olson, and J. L. Fry. Organic nitrate aerosol formation via  $\text{NO}_3$  + biogenic volatile organic compounds in the southeastern United States. *Atmospheric Chemistry and Physics*, 15(23):13377–13392, 12 2015.
- [10] M. H. Barley and G. McFiggans. The critical assessment of vapour pressure estimation methods for use in modelling the formation of atmospheric organic aerosol. *Atmospheric Chemistry and Physics*, 10(2):749–767, 1 2010.
- [11] J. K. Bean and L. Hildebrandt Ruiz. Gas-particle partitioning and hydrolysis of organic nitrates formed from the oxidation of  $\alpha$ -pinene in environmental chamber experiments. *Atmospheric Chemistry and Physics*, 16(4):2175–2184, 2 2016.
- [12] A. D. Becke. Density-functional thermochemistry. III. The role of exact exchange. *The Journal of Chemical Physics*, 98(7):5648–5652, 4 1993.
- [13] T. Berndt and O. Böge. Products and mechanism of the gas-phase reaction of  $\text{NO}_3$  radicals with  $\alpha$ -pinene. *Journal of the Chemical Society - Faraday Transactions*, 93(17):3021–3027, 1 1997.
- [14] F. Bianchi, T. Kurtén, M. Riva, C. Mohr, M. P. Rissanen, P. Roldin, T. Berndt, J. D. Crouse, P. O. Wennberg, T. F. Mentel, J. Wildt, H. Junninen, T. Jokinen, M. Kulmala, D. R. Worsnop, J. A. Thornton, N. Donahue, H. G. Kjaergaard, and M. Ehn. Highly Oxygenated Organic Molecules (HOM) from Gas-Phase Autoxidation Involving Peroxy Radicals: A Key Contributor to Atmospheric Aerosol, 3 2019.
- [15] M. Bietti, G. Gente, and M. Salamone. Structural effects on the  $\beta$ -scission reaction of tertiary arylcarbinoyloxyl radicals. The role of  $\alpha$ -cyclopropyl and  $\alpha$ -cyclobutyl groups. *Journal of Organic Chemistry*, 70(17):6820–6826, 8 2005.
- [16] C. M. Boyd, J. Sanchez, L. Xu, A. J. Eugene, T. Nah, W. Y. Tuet, M. I. Guzman, and N. L. Ng. Secondary organic aerosol formation from the  $\beta$ -pinene+ $\text{NO}_3$  system: effect of humidity and peroxy radical fate. *Atmospheric Chemistry and Physics*, 15(13):7497–7522, 7 2015.
- [17] P. Brophy and D. K. Farmer. A switchable reagent ion high resolution time-of-flight chemical ionization mass spectrometer for real-time measurement of gas phase oxidized species: Characterization from the 2013 southern oxidant and aerosol study. *Atmospheric Measurement Techniques*, 8(7):2945–2959, 7 2015.
- [18] S. S. Brown and J. Stutz. Nighttime radical observations and chemistry. *Chemical Society Reviews*, 41(19):6405–6447, 9 2012.

- [19] E. C. Browne, K. E. Min, P. J. Wooldridge, E. Apel, D. R. Blake, W. H. Brune, C. A. Cantrell, M. J. Cubison, G. S. Diskin, J. L. Jimenez, A. J. Weinheimer, P. O. Wennberg, A. Wisthaler, and R. C. Cohen. Observations of total RONO<sub>2</sub> over the boreal forest: NO<sub>x</sub> sinks and HNO<sub>3</sub> sources. *Atmospheric Chemistry and Physics*, 13(9):4543–4562, 5 2013.
- [20] A. G. Carlton, P. V. Bhave, S. L. Napelenok, E. O. Edney, G. Sarwar, R. W. Pinder, G. A. Pouliot, and M. Houyoux. Model representation of secondary organic aerosol in CMAQv4.7. *Environmental Science and Technology*, 44(22):8553–8560, 11 2010.
- [21] A. G. Carlton, R. W. Pinder, P. V. Bhave, and G. A. Pouliot. To What Extent Can Biogenic SOA be Controlled? *Environmental Science & Technology*, 44(9):3376–3380, 5 2010.
- [22] A. G. Carlton, C. Wiedinmyer, and J. H. Kroll. A review of Secondary organic aerosol (SOA) formation from isoprene. *Atmospheric Chemistry and Physics*, 9(14):4987–5005, 2009.
- [23] J. D. Chai and M. Head-Gordon. Long-range corrected hybrid density functionals with damped atom-atom dispersion corrections. *Physical Chemistry Chemical Physics*, 10(44):6615–6620, 11 2008.
- [24] S. H. Chung and J. H. Seinfeld. Global distribution and climate forcing of carbonaceous aerosols. *Journal of Geophysical Research Atmospheres*, 107(19):14–1, 10 2002.
- [25] M. S. Claffin and P. J. Ziemann. Identification and Quantitation of Aerosol Products of the Reaction of  $\beta$ -Pinene with NO<sub>3</sub> Radicals and Implications for Gas- and Particle-Phase Reaction Mechanisms. *Journal of Physical Chemistry A*, 122(14):3640–3652, 3 2018.
- [26] J. D. Crouse, H. C. Knap, K. B. Ørnsø, S. Jørgensen, F. Paulot, H. G. Kjaergaard, and P. O. Wennberg. Atmospheric fate of methacrolein. 1. Peroxy radical isomerization following addition of OH and O<sub>2</sub>. *Journal of Physical Chemistry A*, 116(24):5756–5762, 6 2012.
- [27] J. D. Crouse, L. B. Nielsen, S. Jørgensen, H. G. Kjaergaard, and P. O. Wennberg. Autoxidation of organic compounds in the atmosphere. *Journal of Physical Chemistry Letters*, 4(20):3513–3520, 10 2013.
- [28] A. I. Darer, N. C. Cole-Filipiak, A. E. O’Connor, and M. J. Elrod. Formation and stability of atmospherically relevant isoprene-derived organosulfates and organonitrates. *Environmental Science and Technology*, 45(5):1895–1902, 3 2011.
- [29] D. A. Day, P. J. Wooldridge, M. B. Dillon, J. A. Thornton, and R. C. Cohen. A thermal dissociation laser-induced fluorescence instrument for in situ detection NO<sub>2</sub>, peroxy nitrates, alkyl nitrates, and HNO<sub>3</sub>. *Journal of Geophysical Research Atmospheres*, 107(5-6):4–1, 3 2002.

- [30] J. A. de Gouw, A. M. Middlebrook, C. Warneke, P. D. Goldan, W. C. Kuster, J. M. Roberts, F. C. Fehsenfeld, D. R. Worsnop, M. R. Canagaratna, A. A. Pszenny, W. C. Keene, M. Marchewka, S. B. Bertman, and T. S. Bates. Budget of organic carbon in a polluted atmosphere: Results from the New England Air Quality Study in 2002. *Journal of Geophysical Research D: Atmospheres*, 110(16):1–22, 8 2005.
- [31] D. O. De Haan, T. Brauers, K. Oum, J. Stutz, T. Nordmeyer, and B. J. Finlayson-Pitts. Heterogeneous chemistry in the troposphere: Experimental approaches and applications to the chemistry of sea salt particles. *International Reviews in Physical Chemistry*, 18(3):343–385, 7 1999.
- [32] R. Delmas, D. Serça, and C. Jambert. Global inventory of NO<sub>x</sub> sources. *Nutrient Cycling in Agroecosystems*, 48(1-2):51–60, 1997.
- [33] V. Derpmann, S. Albrecht, and T. Benter. The role of ion-bound cluster formation in negative ion mass spectrometry. *Rapid Communications in Mass Spectrometry*, 26(17):1923–1933, 9 2012.
- [34] N. M. Donahue, A. L. Robinson, E. R. Trump, I. Riipinen, and J. H. Kroll. Volatility and Aging of Atmospheric Organic Aerosol. In *Topics in current chemistry*, volume 339, pages 97–143. 2012.
- [35] D. C. Draper, D. K. Farmer, Y. Desyaterik, and J. L. Fry. A qualitative comparison of secondary organic aerosol yields and composition from ozonolysis of monoterpenes at varying concentrations of NO<sub>2</sub>. *Atmospheric Chemistry and Physics*, 15(21):12267–12281, 2015.
- [36] D. C. Draper, N. Myllys, N. Hyttinen, K. H. Møller, H. G. Kjaergaard, J. L. Fry, J. N. Smith, and T. Kurtén. Formation of Highly Oxidized Molecules from NO<sub>3</sub> Radical Initiated Oxidation of  $\delta$ -3-Carene: A Mechanistic Study. *ACS Earth and Space Chemistry*, 3(8):1460–1470, 8 2019.
- [37] T. H. Dunning. Gaussian basis sets for use in correlated molecular calculations. I. The atoms boron through neon and hydrogen. *The Journal of Chemical Physics*, 90(2):1007–1023, 1 1989.
- [38] C. Eckart. The penetration of a potential barrier by electrons. *Physical Review*, 35(11):1303–1309, 6 1930.
- [39] M. Ehn, J. A. Thornton, E. Kleist, M. Sipilä, H. Junninen, I. Pullinen, M. Springer, F. Rubach, R. Tillmann, B. Lee, F. Lopez-Hilfiker, S. Andres, I.-H. Acir, M. Rissanen, T. Jokinen, S. Schobesberger, J. Kangasluoma, J. Kontkanen, T. Nieminen, T. Kurtén, L. B. Nielsen, S. Jørgensen, H. G. Kjaergaard, M. Canagaratna, M. D. Maso, T. Berndt, T. Petäjä, A. Wahner, V.-M. Kerminen, M. Kulmala, D. R. Worsnop, J. Wildt, and T. F. Mentel. A large source of low-volatility secondary organic aerosol. *Nature*, 506(7489):476–9, 2 2014.

- [40] F. L. Eisele and D. J. Tanner. Measurement of the gas phase concentration of H<sub>2</sub>SO<sub>4</sub> and methane sulfonic acid and estimates of H<sub>2</sub>SO<sub>4</sub> production and loss in the atmosphere. *Journal of Geophysical Research*, 98(D5):9001, 1993.
- [41] EPA. 2014 National Emissions Inventory Report, 2014.
- [42] K. M. Ervin, I. Anusiewicz, P. Skurski, J. Simons, and W. C. Lineberger. The only stable state of O<sub>2</sub><sup>-</sup> is the X 2g ground state and it (still!) has an adiabatic electron detachment energy of 0.45 eV. *Journal of Physical Chemistry A*, 107(41):8521–8529, 10 2003.
- [43] M. G. Evans and M. Polanyi. Some applications of the transition state method to the calculation of reaction velocities, especially in solution. *Transactions of the Faraday Society*, 31:875–894, 1935.
- [44] H. Eyring. The activated complex in chemical reactions. *The Journal of Chemical Physics*, 3(2):63–71, 1935.
- [45] C. L. Faiola, A. Buchholz, E. Kari, P. Yli-Pirilä, J. K. Holopainen, M. Kivimäenpää, P. Miettinen, D. R. Worsnop, K. E. Lehtinen, A. B. Guenther, and A. Virtanen. Terpene Composition Complexity Controls Secondary Organic Aerosol Yields from Scots Pine Volatile Emissions. *Scientific Reports*, 8(1), 12 2018.
- [46] C. L. Faiola, I. Pullinen, A. Buchholz, F. Khalaj, A. Ylisirniö, E. Kari, P. Miettinen, J. K. Holopainen, M. Kivimäenpää, S. Schobesberger, T. Yli-Juuti, and A. Virtanen. Secondary Organic Aerosol Formation from Healthy and Aphid-Stressed Scots Pine Emissions. *ACS Earth and Space Chemistry*, 3(9):1756–1772, 9 2019.
- [47] T. Fang, P. S. Lakey, R. J. Weber, and M. Shiraiwa. Oxidative Potential of Particulate Matter and Generation of Reactive Oxygen Species in Epithelial Lining Fluid. *Environmental Science and Technology*, 53(21):12784–12792, 11 2019.
- [48] D. K. Farmer, A. Matsunaga, K. S. Docherty, J. D. Surratt, J. H. Seinfeld, P. J. Ziemann, and J. L. Jimenez. Response of an aerosol mass spectrometer to organonitrates and organosulfates and implications for atmospheric chemistry. *Proceedings of the National Academy of Sciences of the United States of America*, 107(15):6670–5, 4 2010.
- [49] J. A. Faust, J. P. Wong, A. K. Lee, and J. P. Abbatt. Role of Aerosol Liquid Water in Secondary Organic Aerosol Formation from Volatile Organic Compounds. *Environmental Science and Technology*, 51(3):1405–1413, 2 2017.
- [50] C. Faxon, J. Hammes, M. Le Breton, R. K. Pathak, and M. Hallquist. Characterization of organic nitrate constituents of secondary organic aerosol (SOA) from nitrate-radical-initiated oxidation of limonene using high-resolution chemical ionization mass spectrometry. *Atmospheric Chemistry and Physics*, 18(8):5467–5481, 4 2018.



- [51] J. A. Fisher, D. J. Jacob, K. R. Travis, P. S. Kim, E. A. Marais, C. C. Miller, K. Yu, L. Zhu, R. M. Yantosca, M. P. Sulprizio, J. Mao, P. O. Wennberg, J. D. Crouse, A. P. Teng, T. B. Nguyen, J. M. Clair, R. C. Cohen, P. Romer, B. A. Nault, P. J. Wooldridge, J. L. Jimenez, P. Campuzano-Jost, D. A. Day, W. Hu, P. B. Shepson, F. Xiong, D. R. Blake, A. H. Goldstein, P. K. Misztal, T. F. Hanisco, G. M. Wolfe, T. B. Ryerson, A. Wisthaler, and T. Mikoviny. Organic nitrate chemistry and its implications for nitrogen budgets in an isoprene- and monoterpene-rich atmosphere: Constraints from aircraft (SEAC4RS) and ground-based (SOAS) observations in the Southeast US. *Atmospheric Chemistry and Physics*, 16(9):5969–5991, 5 2016.
- [52] M. J. Frisch, G. W. Trucks, H. B. Schlegel, G. E. Scuseria, M. A. Robb, J. R. Cheeseman, G. Scalmani, V. Barone, B. Mennucci, G. A. Petersson, H. Nakatsuji, M. Caricato, X. Li, H. P. Hratchian, A. F. Izmaylov, J. Bloino, G. Zheng, J. L. Sonnenberg, M. Hada, M. Ehara, K. Toyota, R. Fukuda, J. Hasegawa, M. Ishida, T. Nakajima, Y. Honda, O. Kitao, H. Nakai, Vreven, T., J. Montgomery, J. A., J. E. Peralta, F. Ogliaro, M. J. Bearpark, J. Heyd, E. N. Brothers, K. N. Kudin, V. N. Staroverov, R. Kobayashi, J. Normand, K. Raghavachari, A. P. Rendell, J. C. Burant, S. S. Iyengar, J. Tomasi, Cossi, M., N. Rega, N. J. Millam, M. Klene, J. E. Knox, J. B. Cross, V. Bakken, C. Adamo, J. Jaramillo, R. Gomperts, R. E. Stratmann, O. Yazyev, A. Austin, J., R. Cammi, C. Pomelli, J. W. Ochterski, R. L. Martin, K. Morokuma, V. G. Zakrzewski, G. A. Voth, P. Salvador, J. J. Dannenberg, S. Dapprich, A. D. Daniels, Ö. Farkas, J. B. Foresman, J. V. Ortiz, J. Cioslowski, and D. J. Fox. Gaussian 09, revision D.01, 2009.
- [53] M. J. Frisch, G. W. Trucks, H. B. Schlegel, G. E. Scuseria, M. A. Robb, J. R. Cheeseman, G. Scalmani, V. Barone, G. A. Petersson, H. Nakatsuji, X. Li, M. Caricato, A. V. Marenich, J. Bloino, B. G. Janesko, R. Gomperts, B. Mennucci, H. P. Hratchian, J. V. Ortiz, A. F. Izmaylov, J. L. Sonnenberg, D. Williams-Young, F. Ding, F. Lipparini, F. Egidi, J. Goings, B. Peng, A. Petrone, T. Henderson, D. Ranasinghe, V. G. Zakrzewski, J. Gao, N. Rega, G. Zheng, W. Liang, M. Hada, M. Ehara, K. Toyota, R. Fukuda, J. Hasegawa, M. Ishida, T. Nakajima, Y. Honda, O. Kitao, H. Nakai, T. Vreven, K. Throssell, J. A. Montgomery Jr., J. E. Peralta, F. Ogliaro, M. J. Bearpark, J. J. Heyd, E. N. Brothers, K. N. Kudin, V. N. Staroverov, T. A. Keith, R. Kobayashi, J. Normand, K. Raghavachari, A. P. Rendell, J. C. Burant, S. S. Iyengar, J. Tomasi, M. Cossi, J. M. Millam, M. Klene, C. Adamo, R. Cammi, J. W. Ochterski, R. L. Martin, K. Morokuma, O. Farkas, J. B. Foresman, and D. J. Fox. Gaussian 16 {R}evision {C}.01, 2016.
- [54] J. L. Fry, D. C. Draper, K. C. Barsanti, J. N. Smith, J. Ortega, P. M. Winkler, M. J. Lawler, S. S. Brown, P. M. Edwards, R. C. Cohen, and L. Lee. Secondary organic aerosol formation and organic nitrate yield from NO<sub>3</sub> oxidation of biogenic hydrocarbons. *Environmental Science and Technology*, 48(20):11944–11953, 10 2014.
- [55] J. L. Fry, D. C. Draper, K. J. Zarzana, P. Campuzano-Jost, D. A. Day, J. L. Jimenez, S. S. Brown, R. C. Cohen, L. Kaser, A. Hansel, L. Cappellin, T. Karl, A. H. Roux, A. Turnipseed, C. Cantrell, B. L. Lefer, and N. Grossberg. Observations of gas-and

- aerosol-phase organic nitrates at BEACHON-RoMBAS 2011. *Atmos. Chem. Phys.*, 13:8585–8605, 2013.
- [56] J. L. Fry, A. Kiendler-Scharr, A. W. Rollins, T. Brauers, S. S. Brown, H. P. Dorn, W. P. Dubé, H. Fuchs, A. Mensah, F. Rohrer, R. Tillmann, A. Wahner, P. J. Wooldridge, and R. C. Cohen. SOA from limonene: Role of NO<sub>3</sub> in its generation and degradation. *Atmospheric Chemistry and Physics*, 11(8):3879–3894, 4 2011.
- [57] J. L. Fry, A. Kiendler-Scharr, A. W. Rollins, P. J. Wooldridge, S. S. Brown, H. Fuchs, W. Dubé, A. Mensah, M. Dal Maso, R. Tillmann, H. P. Dorn, T. Brauers, and R. C. Cohen. Organic nitrate and secondary organic aerosol yield from NO<sub>3</sub> oxidation of  $\beta$ -pinene evaluated using a gas-phase kinetics/aerosol partitioning model. *Atmospheric Chemistry and Physics*, 9(4):1431–1449, 2 2009.
- [58] A. L. Garden, F. Paulot, J. D. Crouse, I. J. Maxwell-Cameron, P. O. Wennberg, and H. G. Kjaergaard. Calculation of conformationally weighted dipole moments useful in ion-molecule collision rate estimates. *Chemical Physics Letters*, 474(1-3):45–50, 5 2009.
- [59] C. Geron, R. Rasmussen, R. R. Arnts, and A. Guenther. A review and synthesis of monoterpene speciation from forests in the United States. *Atmospheric Environment*, 34(11):1761–1781, 2000.
- [60] D. R. Glowacki, C. H. Liang, C. Morley, M. J. Pilling, and S. H. Robertson. MESMER: An open-source master equation solver for Multi-Energy well reactions. *Journal of Physical Chemistry A*, 116(38):9545–9560, 9 2012.
- [61] A. H. Goldstein and I. E. Galbally. Known and unexplored organic constituents in the earth’s atmosphere, 3 2007.
- [62] R. J. Griffin, D. R. Cocker, R. C. Flagan, and J. H. Seinfeld. Organic aerosol formation from the oxidation of biogenic hydrocarbons. *Journal of Geophysical Research Atmospheres*, 104(D3):3555–3567, 2 1999.
- [63] A. Guenther. A global model of natural volatile organic compound emissions. *Journal of Geophysical Research*, 100(D5):8873–8892, 5 1995.
- [64] A. B. Guenther, X. Jiang, C. L. Heald, T. Sakulyanontvittaya, T. Duhl, L. K. Emmons, and X. Wang. The model of emissions of gases and aerosols from nature version 2.1 (MEGAN2.1): An extended and updated framework for modeling biogenic emissions. *Geoscientific Model Development*, 5(6):1471–1492, 11 2012.
- [65] A. B. Guenther, P. R. Zimmerman, P. C. Harley, R. K. Monson, and R. Fall. Isoprene and monoterpene emission rate variability: model evaluations and sensitivity analyses. *Journal of Geophysical Research*, 98(D7):12609–12617, 7 1993.
- [66] H. Hakola, H. Hellén, M. Hemmilä, J. Rinne, and M. Kulmala. In situ measurements of volatile organic compounds in a boreal forest. *Atmospheric Chemistry and Physics*, 12(23):11665–11678, 12 2012.

- [67] T. A. Halgren. MMFF VII. Characterization of MMFF94, MMFF94s, and other widely available force fields for conformational energies and for intermolecular-interaction energies and geometries. *Journal of Computational Chemistry*, 20(7):730–748, 5 1999.
- [68] M. Hallquist, I. Wängberg, E. Ljungström, I. Barnes, and K. H. Becker. Aerosol and product yields from NO<sub>3</sub> radical-initiated oxidation of selected monoterpenes. *Environmental Science and Technology*, 33(4):553–559, 2 1999.
- [69] M. Hallquist, J. C. Wenger, U. Baltensperger, Y. Rudich, D. Simpson, M. Claeys, J. Dommen, N. M. Donahue, C. George, A. H. Goldstein, J. F. Hamilton, H. Herrmann, T. Hoffmann, Y. Iinuma, M. Jang, M. E. Jenkin, J. L. Jimenez, A. Kiendler-Scharr, W. Maenhaut, G. McFiggans, T. F. Mentel, A. Monod, A. S. Prévôt, J. H. Seinfeld, J. D. Surratt, R. Szmigielski, and J. Wildt. The formation, properties and impact of secondary organic aerosol: Current and emerging issues. *Atmospheric Chemistry and Physics*, 9(14):5155–5236, 2009.
- [70] P. Hari, E. Nikinmaa, T. Pohja, E. Siivola, J. Bäck, T. Vesala, and M. Kulmala. Station for measuring ecosystem-atmosphere relations: SMEAR. In *Physical and Physiological Forest Ecology*, volume 9789400756, pages 471–487. 2013.
- [71] K. Hens, A. Novelli, M. Martinez, J. Auld, R. Axinte, B. Bohn, H. Fischer, P. Keronen, D. Kubistin, A. C. Nölscher, R. Oswald, P. Paasonen, T. Petäjä, E. Regelin, R. Sander, V. Sinha, M. Sipilä, D. Taraborrelli, C. Tatum Ernest, J. Williams, J. Lelieveld, and H. Harder. Observation and modelling of HO<sub>x</sub> radicals in a boreal forest. *Atmospheric Chemistry and Physics*, 14(16):8723–8747, 8 2014.
- [72] F. Holland, A. Hofzumahaus, J. Schäfer, A. Kraus, and H. W. Pätz. Measurements of OH and HO<sub>2</sub> radical concentrations and photolysis frequencies during BERLIOZ. *Journal of Geophysical Research D: Atmospheres*, 108(4):2–1, 2 2003.
- [73] L. F. Holroyd and T. van Mourik. Insufficient description of dispersion in B3LYP and large basis set superposition errors in MP2 calculations can hide peptide conformers. *Chemical Physics Letters*, 442(1-3):42–46, 7 2007.
- [74] C. R. Hoyle, M. Boy, N. M. Donahue, J. L. Fry, M. Glasius, A. Guenther, A. G. Hallar, K. Huff Hartz, M. D. Petters, T. Petäjä, T. Rosenoern, and A. P. Sullivan. A review of the anthropogenic influence on biogenic secondary organic aerosol, 1 2011.
- [75] K. S. Hu, A. I. Darer, and M. J. Elrod. Thermodynamics and kinetics of the hydrolysis of atmospherically relevant organonitrates and organosulfates. *Atmospheric Chemistry and Physics*, 11(16):8307–8320, 8 2011.
- [76] N. Hyttinen, O. Kupiainen-Määttä, M. P. Rissanen, M. Muuronen, M. Ehn, and T. Kurtén. Modeling the Charging of Highly Oxidized Cyclohexene Ozonolysis Products Using Nitrate-Based Chemical Ionization. *Journal of Physical Chemistry A*, 119(24):6339–6345, 6 2015.

- [77] N. Hyttinen, M. P. Rissanen, and T. Kurtén. Computational Comparison of Acetate and Nitrate Chemical Ionization of Highly Oxidized Cyclohexene Ozonolysis Intermediates and Products. *The Journal of Physical Chemistry A*, 121(10):2172–2179, 3 2017.
- [78] M. Jaoui, T. E. Kleindienst, K. S. Docherty, M. Lewandowski, and J. H. Offenberg. Secondary organic aerosol formation from the oxidation of a series of sesquiterpenes:  $\alpha$ -cedrene,  $\beta$ -caryophyllene,  $\alpha$ -humulene and  $\alpha$ -farnesene with O<sub>3</sub>, OH and NO<sub>3</sub> radicals. *Environmental Chemistry*, 10(3):178–193, 2013.
- [79] M. E. Jenkin, S. M. Saunders, and M. J. Pilling. The tropospheric degradation of volatile organic compounds: A protocol for mechanism development. *Atmospheric Environment*, 31(1):81–104, 1 1997.
- [80] K. Jew, D. Herr, C. Wong, A. Kennell, K. Morris-Schaffer, G. Oberdörster, M. K. O’Banion, D. A. Cory-Slechta, and A. Elder. Selective memory and behavioral alterations after ambient ultrafine particulate matter exposure in aged 3xTgAD Alzheimer’s disease mice. *Particle and Fibre Toxicology*, 16(1):45, 11 2019.
- [81] J. L. Jimenez, M. R. Canagaratna, N. M. Donahue, A. S. Prevot, Q. Zhang, J. H. Kroll, P. F. DeCarlo, J. D. Allan, H. Coe, N. L. Ng, A. C. Aiken, K. S. Docherty, I. M. Ulbrich, A. P. Grieshop, A. L. Robinson, J. Duplissy, J. D. Smith, K. R. Wilson, V. A. Lanz, C. Hueglin, Y. L. Sun, J. Tian, A. Laaksonen, T. Raatikainen, J. Rautiainen, P. Vaattovaara, M. Ehn, M. Kulmala, J. M. Tomlinson, D. R. Collins, M. J. Cubison, E. J. Dunlea, J. A. Huffman, T. B. Onasch, M. R. Alfarra, P. I. Williams, K. Bower, Y. Kondo, J. Schneider, F. Drewnick, S. Borrmann, S. Weimer, K. Demerjian, D. Salcedo, L. Cottrell, R. Griffin, A. Takami, T. Miyoshi, S. Hatakeyama, A. Shimono, J. Y. Sun, Y. M. Zhang, K. Dzepina, J. R. Kimmel, D. Sueper, J. T. Jayne, S. C. Herton, A. M. Trimborn, L. R. Williams, E. C. Wood, A. M. Middlebrook, C. E. Kolb, U. Baltensperger, and D. R. Worsnop. Evolution of organic aerosols in the atmosphere. *Science*, 326(5959):1525–1529, 12 2009.
- [82] T. Jokinen, M. Sipilä, H. Junninen, M. Ehn, G. Lönn, J. Hakala, T. Petäjä, R. L. Mauldin, M. Kulmala, and D. R. Worsnop. Atmospheric sulphuric acid and neutral cluster measurements using CI-API-TOF. *Atmospheric Chemistry and Physics*, 12(9):4117–4125, 5 2012.
- [83] H. Junninen, M. Ehn, T. Petäjä, L. Luosujärvi, T. Kotiaho, R. Kostianen, U. Rohner, M. Gonin, K. Fuhrer, M. Kulmala, and D. R. Worsnop. A high-resolution mass spectrometer to measure atmospheric ion composition. *Atmospheric Measurement Techniques*, 3(4):1039–1053, 8 2010.
- [84] M. Kanakidou, K. Tsigaridis, F. J. Dentener, and P. J. Crutzen. Human-activity-enhanced formation of organic aerosols by biogenic hydrocarbon oxidation. *Journal of Geophysical Research: Atmospheres*, 105(D7):9243–9354, 2000.
- [85] L. Kaser, T. Karl, B. Yuan, R. L. Mauldin, C. A. Cantrell, A. B. Guenther, E. G. Patton, A. J. Weinheimer, C. Knote, J. Orlando, L. Emmons, E. Apel, R. Hornbrook,

- S. Shertz, K. Ullmann, S. Hall, M. Graus, J. De Gouw, X. Zhou, and C. Ye. Chemistry-turbulence interactions and mesoscale variability influence the cleansing efficiency of the atmosphere. *Geophysical Research Letters*, 42(24):10894–10903, 12 2015.
- [86] N. I. Keehan, B. Brownwood, A. Marsavin, D. A. Day, and J. L. Fry. A thermal-dissociation–cavity ring-down spectrometer (TD-CRDS) for the detection of organic nitrates in gas and particle phases. *Atmospheric Measurement Techniques*, 13(11):6255–6269, 11 2020.
- [87] R. A. Kendall, T. H. Dunning, and R. J. Harrison. Electron affinities of the first-row atoms revisited. Systematic basis sets and wave functions. *The Journal of Chemical Physics*, 96(9):6796–6806, 5 1992.
- [88] A. Kiendler-Scharr, A. A. Mensah, E. Friese, D. Topping, E. Nemitz, A. S. H. Prevot, M. Äijälä, J. Allan, F. Canonaco, M. Canagaratna, S. Carbone, M. Crippa, M. Dall'Osto, D. A. Day, P. De Carlo, C. F. Di Marco, H. Elbern, A. Eriksson, E. Freney, L. Hao, H. Herrmann, L. Hildebrandt, R. Hillamo, J. L. Jimenez, A. Laaksonen, G. McFiggans, C. Mohr, C. O'Dowd, R. Otjes, J. Ovadnevaite, S. N. Pandis, L. Poulain, P. Schlag, K. Sellegri, E. Swietlicki, P. Tiitta, A. Vermeulen, A. Wahner, D. Worsnop, and H.-C. Wu. Ubiquity of organic nitrates from nighttime chemistry in the European submicron aerosol. *Geophysical Research Letters*, 43(14):7735–7744, 7 2016.
- [89] J. Kirkby, J. Duplissy, K. Sengupta, C. Frege, H. Gordon, C. Williamson, M. Heinritzi, M. Simon, C. Yan, J. Almeida, J. Trostl, T. Nieminen, I. K. Ortega, R. Wagner, A. Adamov, A. Amorim, A. K. Bernhammer, F. Bianchi, M. Breitenlechner, S. Brilke, X. Chen, J. Craven, A. Dias, S. Ehrhart, R. C. Flagan, A. Franchin, C. Fuchs, R. Guida, J. Hakala, C. R. Hoyle, T. Jokinen, H. Junninen, J. Kangasluoma, J. Kim, M. Krapf, A. Kurten, A. Laaksonen, K. Lehtipalo, V. Makhmutov, S. Mathot, U. Molteni, A. Onnela, O. Perakyla, F. Piel, T. Petaja, A. P. Praplan, K. Pringle, A. Rap, N. A. Richards, I. Riipinen, M. P. Rissanen, L. Rondo, N. Sarnela, S. Schobesberger, C. E. Scott, J. H. Seinfeld, M. Sipila, G. Steiner, Y. Stozhkov, F. Stratmann, A. Tomé, A. Virtanen, A. L. Vogel, A. C. Wagner, P. E. Wagner, E. Weingartner, D. Wimmer, P. M. Winkler, P. Ye, X. Zhang, A. Hansel, J. Dommen, N. M. Donahue, D. R. Worsnop, U. Baltensperger, M. Kulmala, K. S. Carslaw, and J. Curtius. Ion-induced nucleation of pure biogenic particles. *Nature*, 533(7604):521–526, 5 2016.
- [90] M. Kulmala and V. M. Kerminen. On the formation and growth of atmospheric nanoparticles. *Atmospheric Research*, 90(2-4):132–150, 11 2008.
- [91] M. Kulmala, J. Kontkanen, H. Junninen, K. Lehtipalo, H. E. Manninen, T. Nieminen, T. Petäjä, M. Sipilä, S. Schobesberger, P. Rantala, A. Franchin, T. Jokinen, E. Järvinen, M. Äijälä, J. Kangasluoma, J. Hakala, P. P. Aalto, P. Paasonen, J. Mikkilä, J. Vanhanen, J. Aalto, H. Hakola, U. Makkonen, T. Ruuskanen, R. L. Mauldin, J. Duplissy, H. Vehkamäki, J. Bäck, A. Kortelainen, I. Riipinen, T. Kurtén, M. V. Johnston, J. N. Smith, M. Ehn, T. F. Mentel, K. E. Lehtinen, A. Laaksonen, V. M. Kerminen,

- and D. R. Worsnop. Direct observations of atmospheric aerosol nucleation. *Science*, 339(6122):943–946, 2 2013.
- [92] M. Kulmala, Rannik, L. Pirjola, M. Dal Maso, J. Karimäki, A. Asmi, A. Jäppinen, V. Karhu, H. Korhonen, S. P. Malvikko, A. Puustinen, J. Raittila, S. Romakkaniemi, T. Suni, S. Yli-Koivisto, J. Paatero, P. Hari, and T. Vesala. Characterization of atmospheric trace gas and aerosol concentrations at forest sites in southern and northern Finland using back trajectories. *Boreal Environment Research*, 5(4):315–336, 2000.
- [93] T. Kurtén, N. Hyttinen, E. Louise D’Ambro, J. Thornton, and N. L. Prisle. Estimating the saturation vapor pressures of isoprene oxidation products C<sub>5</sub>H<sub>12</sub>O<sub>6</sub> and C<sub>5</sub>H<sub>10</sub>O<sub>6</sub> using COSMO-RS. *Atmospheric Chemistry and Physics*, 18(23):17589–17600, 12 2018.
- [94] T. Kurtén, K. H. Møller, T. B. Nguyen, R. H. Schwantes, P. K. Misztal, L. Su, P. O. Wennberg, J. L. Fry, and H. G. Kjaergaard. Alkoxy Radical Bond Scissions Explain the Anomalously Low Secondary Organic Aerosol and Organonitrate Yields From  $\alpha$ -Pinene + NO<sub>3</sub>. *The Journal of Physical Chemistry Letters*, 8(13):2826–2834, 7 2017.
- [95] T. Kurtén, K. Tiusanen, P. Roldin, M. Rissanen, J. N. Luy, M. Boy, M. Ehn, and N. Donahue.  $\alpha$ -Pinene Autoxidation Products May Not Have Extremely Low Saturation Vapor Pressures Despite High O:C Ratios. *Journal of Physical Chemistry A*, 120(16):2569–2582, 4 2016.
- [96] M. J. Lawler, D. C. Draper, and J. N. Smith. Atmospheric fungal nanoparticle bursts. *Science Advances*, 6(3), 2020.
- [97] M. J. Lawler, M. P. Rissanen, M. Ehn, R. L. Mauldin, N. Sarnela, M. Sipilä, and J. N. Smith. Evidence for Diverse Biogeochemical Drivers of Boreal Forest New Particle Formation. *Geophysical Research Letters*, 45(4):2038–2046, 2 2018.
- [98] M. J. Lawler, J. Whitehead, C. O’Dowd, C. Monahan, G. McFiggans, and J. N. Smith. Composition of 15–85 nm particles in marine air. *Atmospheric Chemistry and Physics*, 14(21):11557–11569, 11 2014.
- [99] B. H. Lee, F. D. Lopez-Hilfiker, E. L. D’Ambro, P. Zhou, M. Boy, T. Petäjä, L. Hao, A. Virtanen, and J. A. Thornton. Semi-volatile and highly oxygenated gaseous and particulate organic compounds observed above a boreal forest canopy. *Atmospheric Chemistry and Physics*, 18(15):11547–11562, 8 2018.
- [100] B. H. Lee, C. Mohr, F. D. Lopez-Hilfiker, A. Lutz, M. Hallquist, L. Lee, P. Romer, R. C. Cohen, S. Iyer, T. Kurtén, W. Hu, D. A. Day, P. Campuzano-Jost, J. L. Jimenez, L. Xu, N. L. Ng, H. Guo, R. J. Weber, R. J. Wild, S. S. Brown, A. Koss, J. de Gouw, K. Olson, A. H. Goldstein, R. Seco, S. Kim, K. McAvey, P. B. Shepson, T. Starn, K. Baumann, E. S. Edgerton, J. Liu, J. E. Shilling, D. O. Miller, W. Brune, S. Schobesberger, E. L. D’Ambro, and J. A. Thornton. Highly functionalized organic nitrates in the southeast United States: Contribution to secondary organic aerosol and reactive nitrogen budgets. *Proceedings of the National Academy of Sciences of the United States of America*, 113(6):1516–21, 2 2016.

- [101] C. Lee, W. Yang, and R. G. Parr. Development of the Colle-Salvetti correlation-energy formula into a functional of the electron density. *Physical Review B*, 37(2):785–789, 1 1988.
- [102] T. J. Lee and P. R. Taylor. A diagnostic for determining the quality of single-reference electron correlation methods. *International Journal of Quantum Chemistry*, 36(23 S):199–207, 6 1989.
- [103] K. Lehtipalo, C. Yan, L. Dada, F. Bianchi, M. Xiao, R. Wagner, D. Stolzenburg, L. R. Ahonen, A. Amorim, A. Baccarini, P. S. Bauer, B. Baumgartner, A. Bergen, A. K. Bernhammer, M. Breitenlechner, S. Brilke, A. Buchholz, S. B. Mazon, D. Chen, X. Chen, A. Dias, J. Dommen, D. C. Draper, J. Duplissy, M. Ehn, H. Finkenzeller, L. Fischer, C. Frege, C. Fuchs, O. Garmash, H. Gordon, J. Hakala, X. He, L. Heikkinen, M. Heinritzi, J. C. Helm, V. Hofbauer, C. R. Hoyle, T. Jokinen, J. Kangasluoma, V. M. Kerminen, C. Kim, J. Kirkby, J. Kontkanen, A. Kürten, M. J. Lawler, H. Mai, S. Mathot, R. L. Mauldin, U. Molteni, L. Nichman, W. Nie, T. Nieminen, A. Ojdanic, A. Onnela, M. Passananti, T. Petäjä, F. Piel, V. Pospisilova, L. L. Quéléver, M. P. Rissanen, C. Rose, N. Sarnela, S. Schallhart, S. Schuchmann, K. Sengupta, M. Simon, M. Sipilä, C. Tauber, A. Tomé, J. Tröstl, O. Väisänen, A. L. Vogel, R. Volkamer, A. C. Wagner, M. Wang, L. Weitz, D. Wimmer, P. Ye, A. Ylisirniö, Q. Zha, K. S. Carslaw, J. Curtius, N. M. Donahue, R. C. Flagan, A. Hansel, I. Riipinen, A. Virtanen, P. M. Winkler, U. Baltensperger, M. Kulmala, and D. R. Worsnop. Multicomponent new particle formation from sulfuric acid, ammonia, and biogenic vapors. *Science Advances*, 4(12):eaau5363, 2018.
- [104] K. R. Lemire. Fine particulate matter source attribution for Southeast Texas using  $\text{C}^{14}/\text{C}^{13}$  ratios. *Journal of Geophysical Research*, 107(D22):4613, 11 2002.
- [105] C. W. Lewis, G. A. Klouda, and W. D. Ellenson. Radiocarbon measurement of the biogenic contribution to summertime PM-2.5 ambient aerosol in Nashville, TN. *Atmospheric Environment*, 38(35):6053–6061, 11 2004.
- [106] J. Liebmann, E. Karu, N. Sobanski, J. Schuladen, M. Ehn, S. Schallhart, L. Quéléver, H. Hellen, H. Hakola, T. Hoffmann, J. Williams, H. Fischer, J. Lelieveld, and J. N. Crowley. Direct measurement of NO<sub>3</sub> radical reactivity in a boreal forest. *Atmospheric Chemistry and Physics*, 18(5):3799–3815, 3 2018.
- [107] J. Liebmann, N. Sobanski, J. Schuladen, E. Karu, H. Hellén, H. Hakola, Q. Zha, M. Ehn, M. Riva, L. Heikkinen, J. Williams, H. Fischer, J. Lelieveld, and J. N. Crowley. Alkyl nitrates in the boreal forest: formation via the NO<sub>3</sub>, OH- and O<sub>3</sub>-induced oxidation of biogenic volatile organic compounds and ambient lifetimes. *Atmospheric Chemistry and Physics*, 19(15):10391–10403, 8 2019.
- [108] P. D. Lightfoot, R. A. Cox, J. N. Crowley, M. Destriau, G. D. Hayman, M. E. Jenkin, G. K. Moortgat, and F. Zabel. Organic peroxy radicals: Kinetics, spectroscopy and tropospheric chemistry. *Atmospheric Environment Part A, General Topics*, 26(10):1805–1961, 7 1992.

- [109] C. Liou, J. E. Penner, C. Chuang, J. J. Walton, H. Eddleman, and H. Cachier. A global three-dimensional model study of carbonaceous aerosols. *Journal of Geophysical Research: Atmospheres*, 101(D14):19411–19432, 1996.
- [110] S. Liu, J. E. Shilling, C. Song, N. Hiranuma, R. A. Zaveri, and L. M. Russell. Hydrolysis of organonitrate functional groups in aerosol particles. *Aerosol Science and Technology*, 46(12):1359–1369, 12 2012.
- [111] W. P. Logan. MORTALITY IN THE LONDON FOG INCIDENT, 1952. *The Lancet*, 261(6755):336–338, 2 1953.
- [112] M. Lüpke, M. Leuchner, R. Steinbrecher, A. Menzel, and T. Buckley. Quantification of monoterpene emission sources of a conifer species in response to experimental drought. 2017.
- [113] P. Massoli, H. Stark, M. R. Canagaratna, J. E. Krechmer, L. Xu, N. L. Ng, R. L. Mauldin, C. Yan, J. Kimmel, P. K. Misztal, J. L. Jimenez, J. T. Jayne, and D. R. Worsnop. Ambient Measurements of Highly Oxidized Gas-Phase Molecules during the Southern Oxidant and Aerosol Study (SOAS) 2013. *ACS Earth and Space Chemistry*, 2(7):653–672, 7 2018.
- [114] A. Metzger, B. Verheggen, J. Dommen, J. Duplissy, A. S. Prevot, E. Weingartner, I. Riipinen, M. Kulmala, D. V. Spracklen, K. S. Carslaw, and U. Baltensperger. Evidence for the role of organics in aerosol particle formation under atmospheric conditions. *Proceedings of the National Academy of Sciences of the United States of America*, 107(15):6646–6651, 4 2010.
- [115] C. Mohr, J. A. Thornton, A. Heitto, F. D. Lopez-Hilfiker, A. Lutz, I. Riipinen, J. Hong, N. M. Donahue, M. Hallquist, T. Petäjä, M. Kulmala, and T. Yli-Juuti. Molecular identification of organic vapors driving atmospheric nanoparticle growth. *Nature Communications*, 10(1):4442, 2019.
- [116] J. Moldanova and E. Ljungström. Modelling of particle formation from NO<sub>3</sub> oxidation of selected monoterpenes. *Journal of Aerosol Science*, 31(11):1317–1333, 2000.
- [117] K. H. Møller, K. H. Bates, and H. G. Kjaergaard. The Importance of Peroxy Radical Hydrogen-Shift Reactions in Atmospheric Isoprene Oxidation. *Journal of Physical Chemistry A*, 123(4):920–932, 1 2019.
- [118] K. H. Møller, R. V. Otkjaer, N. Hyttinen, T. Kurtén, H. G. Kjaergaard, and C. Ø. Cost-Effective Implementation of Multi-Conformer Transition State Theory for Peroxy Radical Hydrogen Shift Reactions. *The Journal of Physical Chemistry A*, 120(51):10072–10087, 12 2016.
- [119] G. Myhre, D. Shindell, M. Bréon, F. W. Collins, J. Fuglestedt, J. Huang, D. Koch, J.-F. Lamarque, D. Lee, B. Mendoza, T. Nakajima, A. Robock, G. Stephens, T. Take-mura, and H. Zhang. Climate change 2013 : the Physical Science Basis: Contribution



- of Working Group I Contribution to the Fifth Assessment Report of the Intergovernmental Panel on Climate Change. chapter Anthropoge, pages 659–740. Cambridge, United Kingdom Cambridge University Press, 2014. ©2013, Cambridge, United Kingdom and New York, NY, 2014.
- [120] N. Myllys, J. Elm, R. Halonen, T. Kurtén, and H. Vehkamäki. Coupled Cluster Evaluation of the Stability of Atmospheric Acid-Base Clusters with up to 10 Molecules. *Journal of Physical Chemistry A*, 120(4):621–630, 2 2016.
- [121] N. Myllys, J. Elm, and T. Kurtén. Density functional theory basis set convergence of sulfuric acid-containing molecular clusters. *Computational and Theoretical Chemistry*, 1098:1–12, 12 2016.
- [122] T. Nah, J. Sanchez, C. M. Boyd, and N. L. Ng. Photochemical Aging of  $\alpha$ -pinene and  $\beta$ -pinene Secondary Organic Aerosol formed from Nitrate Radical Oxidation. *Environmental Science & Technology*, 50(1):222–231, 1 2016.
- [123] F. Neese. The ORCA program system. *Wiley Interdisciplinary Reviews: Computational Molecular Science*, 2(1):73–78, 1 2012.
- [124] N. L. Ng, S. S. Brown, A. T. Archibald, E. Atlas, R. C. Cohen, J. N. Crowley, D. A. Day, N. M. Donahue, J. L. Fry, H. Fuchs, R. J. Griffin, M. I. Guzman, H. Herrmann, A. Hodzic, Y. Iinuma, J. L. Jimenez, A. Kiendler-Scharr, B. H. Lee, D. J. Luecken, J. Mao, R. McLaren, A. Mutzel, H. D. Osthoff, B. Ouyang, B. Picquet-Varrault, U. Platt, H. O. T. Pye, Y. Rudich, R. H. Schwantes, M. Shiraiwa, J. Stutz, J. A. Thornton, A. Tilgner, B. J. Williams, and R. A. Zaveri. Nitrate radicals and biogenic volatile organic compounds: oxidation, mechanisms, and organic aerosol. *Atmospheric Chemistry and Physics*, 17(3):2103–2162, 2 2017.
- [125] T. B. Nguyen, J. D. Crouse, A. P. Teng, J. M. Clair, F. Paulot, G. M. Wolfe, and P. O. Wennberg. Rapid deposition of oxidized biogenic compounds to a temperate forest. *Proceedings of the National Academy of Sciences of the United States of America*, 112(5):E392–E401, 2 2015.
- [126] G. Oberdörster, E. Oberdörster, J. Oberdörster, G. Oberdorster, E. Oberdorster, and J. Oberdorster. Nanotoxicology: An emerging discipline evolving from studies of ultrafine particles. *Environmental Health Perspectives*, 113(7):823–839, 2005.
- [127] G. Oberdörster, Z. Sharp, V. Atudorei, A. Elder, R. Gelein, W. Kreyling, and C. Cox. Translocation of inhaled ultrafine particles to the brain. In *Inhalation Toxicology*, volume 16, pages 437–445. *Inhal Toxicol*, 6 2004.
- [128] J. J. Orlando and G. S. Tyndall. Laboratory studies of organic peroxy radical chemistry: An overview with emphasis on recent issues of atmospheric significance. *Chemical Society Reviews*, 41(19):6294–6317, 9 2012.
- [129] J. J. Orlando, G. S. Tyndall, and T. J. Wallington. The Atmospheric Chemistry of Alkoxy Radicals. *Chemical Reviews*, 103(12):4657–4689, 2003.

- [130] R. V. Otkjær, H. H. Jakobsen, C. M. Tram, and H. G. Kjaergaard. Calculated Hydrogen Shift Rate Constants in Substituted Alkyl Peroxy Radicals. *Journal of Physical Chemistry A*, 122(43):8665–8673, 11 2018.
- [131] J. F. Pankow. An absorption model of gas/particle partitioning of organic compounds in the atmosphere. *Atmospheric Environment*, 28(2):185–188, 1 1994.
- [132] J. F. Pankow and W. E. Asher. SIMPOL.1: A simple group contribution method for predicting vapor pressures and enthalpies of vaporization of multifunctional organic compounds. *Atmospheric Chemistry and Physics*, 8(10):2773–2796, 5 2008.
- [133] J. F. Pankow and W. E. Asher. SIMPOL.1: A simple group contribution method for predicting vapor pressures and enthalpies of vaporization of multifunctional organic compounds. *Atmospheric Chemistry and Physics*, 8(10):2773–2796, 5 2008.
- [134] J. Park, C. G. Jongsma, R. Zhang, and S. W. North. OH/OD initiated oxidation of isoprene in the presence of O<sub>2</sub> and NO. *Journal of Physical Chemistry A*, 108(48):10688–10697, 2004.
- [135] V. Perraud, E. A. Bruns, M. J. Ezell, S. N. Johnson, J. Greaves, and B. J. Finlayson-Pitts. Identification of organic nitrates in the NO<sub>3</sub> radical initiated oxidation of  $\alpha$ -Pinene by atmospheric pressure chemical ionization mass spectrometry. *Environmental Science and Technology*, 44(15):5887–5893, 8 2010.
- [136] T. Petäjä, E. J. O’Connor, D. Moiseev, V. A. Sinclair, A. J. Manninen, R. Väänänen, A. Von Lerber, J. A. Thornton, K. Nicoll, W. Petersen, V. Chandrasekar, J. N. Smith, P. M. Winkler, O. Krüger, H. Hakola, H. Timonen, D. Brus, T. Laurila, E. Asmi, M. L. Riekkola, L. Mona, P. Massoli, R. Engelmann, M. Komppula, J. Wang, C. Kuang, J. Bäck, A. Virtanen, J. Levula, M. Ritsche, and N. Hickmon. A field campaign to elucidate the impact of biogenic aerosols on clouds and climate. *Bulletin of the American Meteorological Society*, 97(10):1909–1928, 10 2016.
- [137] U. Platt, D. Perner, A. M. Winer, G. W. Harris, and J. N. Pitts. Detection of NO<sub>3</sub> in the polluted troposphere by differential optical absorption. *Geophysical Research Letters*, 7(1):89–92, 1 1980.
- [138] C. A. Pope and D. W. Dockery. Health effects of fine particulate air pollution: Lines that connect. *Journal of the Air and Waste Management Association*, 56(6):709–742, 2006.
- [139] H. O. Pye, D. J. Luecken, L. Xu, C. M. Boyd, N. L. Ng, K. R. Baker, B. R. Ayres, J. O. Bash, K. Baumann, W. P. Carter, E. Edgerton, J. L. Fry, W. T. Hutzell, D. B. Schwede, and P. B. Shepson. Modeling the Current and Future Roles of Particulate Organic Nitrates in the Southeastern United States. *Environmental Science and Technology*, 49(24):14195–14203, 12 2015.
- [140] H. O. Pye and J. H. Seinfeld. A global perspective on aerosol from low-volatility organic compounds. *Atmospheric Chemistry and Physics*, 10(9):4377–4401, 2010.

- [141] H. O. T. Pye, A. W. H. Chan, M. P. Barkley, and J. H. Seinfeld. Global modeling of organic aerosol: the importance of reactive nitrogen (NO<sub>x</sub> and NO<sub>3</sub>). *Atmospheric Chemistry and Physics*, 10(22):11261–11276, 11 2010.
- [142] S. Reis, R. W. Pinder, M. Zhang, G. Lijie, and M. A. Sutton. Reactive nitrogen in atmospheric emission inventories. *Atmospheric Chemistry and Physics*, 9(19):7657–7677, 10 2009.
- [143] S. Richters, M. Pfeifle, M. Olzmann, and T. Berndt. Endo-cyclization of unsaturated RO<sub>2</sub> radicals from the gas-phase ozonolysis of cyclohexadienes. *Chemical Communications*, 53(29):4132–4135, 4 2017.
- [144] C. Riplinger and F. Neese. An efficient and near linear scaling pair natural orbital based local coupled cluster method. *Journal of Chemical Physics*, 138(3):034106, 1 2013.
- [145] C. Riplinger, B. Sandhoefer, A. Hansen, and F. Neese. Natural triple excitations in local coupled cluster calculations with pair natural orbitals. *Journal of Chemical Physics*, 139(13):134101, 10 2013.
- [146] M. P. Rissanen, T. Kurtén, M. Sipilä, J. A. Thornton, J. Kangasluoma, N. Sarnela, H. Junninen, S. Jørgensen, S. Schallhart, M. K. Kajos, R. Taipale, M. Springer, T. F. Mentel, T. Ruuskanen, T. Petäjä, D. R. Worsnop, H. G. Kjaergaard, and M. Ehn. The formation of highly oxidized multifunctional products in the ozonolysis of cyclohexene. *Journal of the American Chemical Society*, 136(44):15596–606, 11 2014.
- [147] A. W. Rollins, A. Kiendler-Scharr, J. L. Fry, T. Brauers, S. S. Brown, H. P. Dorn, W. P. Dubé, H. Fuchs, A. Mensah, T. F. Mentel, F. Rohrer, R. Tillmann, R. Wegener, P. J. Wooldridge, and R. C. Cohen. Isoprene oxidation by nitrate radical: Alkyl nitrate and secondary organic aerosol yields. *Atmospheric Chemistry and Physics*, 9(18):6685–6703, 2009.
- [148] H. D. Roth and T. Herberitz. The Structure of Simple Vinylcyclopropane Radical Cations: Evidence for Conjugation between Alkene and Cyclopropane Groups. *Journal of the American Chemical Society*, 115(21):9804–9805, 10 1993.
- [149] S. M. Saunders, M. E. Jenkin, R. G. Derwent, and M. J. Pilling. Protocol for the development of the Master Chemical Mechanism, MCM v3 (Part A): Tropospheric degradation of non-aromatic volatile organic compounds. *Atmospheric Chemistry and Physics*, 3(1):161–180, 2 2003.
- [150] D. E. Schraufnagel. The health effects of ultrafine particles, 3 2020.
- [151] M. Shiraiwa, Y. Li, A. P. Tsimpidi, V. A. Karydis, T. Berkemeier, S. N. Pandis, J. Lelieveld, T. Koop, and U. Pöschl. Global distribution of particle phase state in atmospheric secondary organic aerosols. *Nature Communications*, 8(1):1–7, 4 2017.

- [152] M. Shrivastava, C. D. Cappa, J. Fan, A. H. Goldstein, A. B. Guenther, J. L. Jimenez, C. Kuang, A. Laskin, S. T. Martin, N. L. Ng, T. Petaja, J. R. Pierce, P. J. Rasch, P. Roldin, J. H. Seinfeld, J. Shilling, J. N. Smith, J. A. Thornton, R. Volkamer, J. Wang, D. R. Worsnop, R. A. Zaveri, A. Zelenyuk, and Q. Zhang. Recent advances in understanding secondary organic aerosol: Implications for global climate forcing. *Reviews of Geophysics*, 55(2):509–559, 6 2017.
- [153] J. H. Slade, A. P. Ault, A. T. Bui, J. C. Ditto, Z. Lei, A. L. Bondy, N. E. Olson, R. D. Cook, S. J. Desrochers, R. M. Harvey, M. H. Erickson, H. W. Wallace, S. L. Alvarez, J. H. Flynn, B. E. Boor, G. A. Petrucci, D. R. Gentner, R. J. Griffin, and P. B. Shepson. Bouncer Particles at Night: Biogenic Secondary Organic Aerosol Chemistry and Sulfate Drive Diel Variations in the Aerosol Phase in a Mixed Forest. *Environmental Science and Technology*, 53(9):4977–4987, 5 2019.
- [154] J. N. Smith, D. C. Draper, S. Chee, M. Dam, H. Glicker, D. Myers, A. E. Thomas, M. J. Lawler, and N. Myllys. Atmospheric clusters to nanoparticles: Recent progress and challenges in closing the gap in chemical composition, 3 2021.
- [155] J. N. Smith, K. F. Moore, P. H. McMurry, and F. L. Eisele. Atmospheric Measurements of Sub-20 nm Diameter Particle Chemical Composition by Thermal Desorption Chemical Ionization Mass Spectrometry. *Aerosol Science and Technology*, 38(2):100–110, 2 2004.
- [156] J. N. Smith and G. J. Rathbone. Carboxylic acid characterization in nanoparticles by thermal desorption chemical ionization mass spectrometry. *International Journal of Mass Spectrometry*, 274(1-3):8–13, 7 2008.
- [157] M. Spittler, I. Barnes, I. Bejan, K. J. Brockmann, T. Benter, and K. Wirtz. Reactions of NO<sub>3</sub> radicals with limonene and  $\alpha$ -pinene: Product and SOA formation. *Atmospheric Environment*, 40(40):116–127, 2006.
- [158] J. F. Stanton, R. J. Bartlett, and C. M. L. Rittby. Fock space multireference coupled-cluster theory for general single determinant reference functions. *The Journal of Chemical Physics*, 97(8):5560–5567, 10 1992.
- [159] D. Stolzenburg, L. Fischer, A. L. Vogel, M. Heinritzi, M. Schervish, M. Simon, A. C. Wagner, L. Dada, L. R. Ahonen, A. Amorim, A. Baccarini, P. S. Bauer, B. Baumgartner, A. Bergen, F. Bianchi, M. Breitenlechner, S. Brilke, S. B. Mazon, D. Chen, A. Dias, D. C. Draper, J. Duplissy, I. E. Haddad, H. Finkenzeller, C. Frege, C. Fuchs, O. Garmash, H. Gordon, X. He, J. Helm, V. Hofbauer, C. R. Hoyle, C. Kim, J. Kirkby, J. Kontkanen, A. Kürten, J. Lampilahti, M. Lawler, K. Lehtipalo, M. Leiminger, H. Mai, S. Mathot, B. Mentler, U. Molteni, W. Nie, T. Nieminen, J. B. Nowak, A. Ojdanic, A. Onnela, M. Passananti, T. Petäjä, L. L. Quéléver, M. P. Rissanen, N. Sarnela, S. Schallhart, C. Tauber, A. Tomé, R. Wagner, M. Wang, L. Weitz, D. Wimmer, M. Xiao, C. Yan, P. Ye, Q. Zha, U. Baltensperger, J. Curtius, J. Dommen, R. C. Flagan, M. Kulmala, J. N. Smith, D. R. Worsnop, A. Hansel, N. M. Donahue, and P. M. Winkler. Rapid growth of organic aerosol nanoparticles over a wide tropospheric

- temperature range. *Proceedings of the National Academy of Sciences of the United States of America*, 115(37):9122–9127, 2018.
- [160] J. Sun and P. A. Ariya. Atmospheric organic and bio-aerosols as cloud condensation nuclei (CCN): A review, 2 2006.
- [161] S. Szidat, M. Ruff, N. Perron, L. Wacker, H.-A. Synal, M. Hallquist, A. S. Shannigrahi, K. E. Yttri, C. Dye, and D. Simpson. Fossil and non-fossil sources of organic carbon (OC) and elemental carbon (EC) in Göteborg, Sweden. *Atmospheric Chemistry and Physics*, 9(5):1521–1535, 3 2009.
- [162] M. Takeuchi and N. L. Ng. Chemical composition and hydrolysis of organic nitrate aerosol formed from hydroxyl and nitrate radical oxidation of  $\alpha$ -pinene and  $\beta$ -pinene. *Atmospheric Chemistry and Physics*, 19(19):12749–12766, 10 2019.
- [163] R. Valorso, B. Aumont, M. Camredon, T. Raventos-Duran, C. Mouchel-Vallon, N. L. Ng, J. H. Seinfeld, J. Lee-Taylor, and S. Madronich. Explicit modelling of SOA formation from  $\alpha$ -pinene photooxidation: Sensitivity to vapour pressure estimation. *Atmospheric Chemistry and Physics*, 11(14):6895–6910, 2011.
- [164] S. Vaughan, C. E. Canosa-Mas, C. Pfrang, D. E. Shallcross, L. Watson, and R. P. Wayne. Kinetic studies of reactions of the nitrate radical (NO<sub>3</sub>) with peroxy radicals (RO<sub>2</sub>): An indirect source of OH at night? *Physical Chemistry Chemical Physics*, 8(32):3749–3760, 8 2006.
- [165] L. Vereecken and J. Peeters. Decomposition of substituted alkoxy radicals - Part I: A generalized structure-activity relationship for reaction barrier heights. *Physical Chemistry Chemical Physics*, 11(40):9062–9074, 10 2009.
- [166] L. Vereecken and J. Peeters. A structure-activity relationship for the rate coefficient of H-migration in substituted alkoxy radicals. *Physical Chemistry Chemical Physics*, 12(39):12608–12620, 9 2010.
- [167] D. Voisin, J. N. Smith, H. Sakurai, P. H. McMurry, and F. L. Eisele. Thermal Desorption Chemical Ionization Mass Spectrometer for Ultrafine Particle Chemical Composition. *Aerosol Science and Technology*, 37(6):471–475, 6 2003.
- [168] L. Wang and L. Wang. Atmospheric Oxidation Mechanism of Sabinene Initiated by the Hydroxyl Radicals. *Journal of Physical Chemistry A*, 122(44):8783–8793, 11 2018.
- [169] I. Wängberg, I. Barnes, and K. H. Becker. Product and mechanistic study of the reaction of NO<sub>3</sub> radicals with  $\alpha$ -pinene. *Environmental Science and Technology*, 31(7):2130–2135, 7 1997.
- [170] R. J. Weber, A. P. Sullivan, R. E. Peltier, A. Russell, B. Yan, M. Zheng, J. De Gouw, C. Warneke, C. Brock, J. S. Holloway, E. L. Atlas, and E. Edgerton. A study of secondary organic aerosol formation in the anthropogenic-influenced south-eastern United States. *J. Geophys. Res.*, 112:13302, 2007.

- [171] L. Xu, K. H. Møller, J. D. Crouse, R. V. Otkjær, H. G. Kjaergaard, and P. O. Wennberg. Unimolecular reactions of peroxy radicals formed in the oxidation of  $\alpha$ -Pinene and  $\beta$ -Pinene by hydroxyl radicals. *Journal of Physical Chemistry A*, 123(8):1661–1674, 2 2019.
- [172] L. Xu, H. O. Pye, J. He, Y. Chen, B. N. Murphy, and N. L. Ng. Experimental and model estimates of the contributions from biogenic monoterpenes and sesquiterpenes to secondary organic aerosol in the southeastern United States. *Atmospheric Chemistry and Physics*, 18(17):12613–12637, 8 2018.
- [173] C. Yan, W. Nie, M. Äijälä, M. P. Rissanen, M. R. Canagaratna, P. Massoli, H. Junninen, T. Jokinen, N. Sarnela, S. Häme, S. Schobesberger, F. Canonaco, A. S. H. Prevot, T. Petäjä, M. Kulmala, M. Sipilä, D. R. Worsnop, and M. Ehn. Source characterization of Highly Oxidized Multifunctional Compounds in a Boreal Forest Environment using Positive Matrix Factorization. *Atmospheric Chemistry and Physics Discussions*, pages 1–31, 5 2016.
- [174] T. Yanai, D. P. Tew, and N. C. Handy. A new hybrid exchange-correlation functional using the Coulomb-attenuating method (CAM-B3LYP). *Chemical Physics Letters*, 393(1-3):51–57, 7 2004.
- [175] A. Zare, K. M. Fahey, G. Sarwar, R. C. Cohen, and H. O. Pye. Vapor-Pressure Pathways Initiate but Hydrolysis Products Dominate the Aerosol Estimated from Organic Nitrates. *ACS Earth and Space Chemistry*, 3(8):1426–1437, 8 2019.
- [176] A. Zare, P. S. Romer, T. Nguyen, F. N. Keutsch, K. Skog, and R. C. Cohen. A comprehensive organic nitrate chemistry: Insights into the lifetime of atmospheric organic nitrates. *Atmospheric Chemistry and Physics*, 18(20):15419–15436, 10 2018.
- [177] H. Zhang, L. D. Yee, B. H. Lee, M. P. Curtis, D. R. Worton, G. Isaacman-VanWertz, J. H. Offenberg, M. Lewandowski, T. E. Kleindienst, M. R. Beaver, A. L. Holder, W. A. Lonneman, K. S. Docherty, M. Jaoui, H. O. Pye, W. Hu, D. A. Day, P. Campuzano-Jost, J. L. Jimenez, H. Guo, R. J. Weber, J. De Gouw, A. R. Koss, E. S. Edgerton, W. Brune, C. Mohr, F. D. Lopez-Hilfiker, A. Lutz, N. M. Kreisberg, S. R. Spielman, S. V. Hering, K. R. Wilson, J. A. Thornton, and A. H. Goldstein. Monoterpenes are the largest source of summertime organic aerosol in the southeastern United States. *Proceedings of the National Academy of Sciences of the United States of America*, 115(9):2038–2043, 2 2018.
- [178] Q. Zhang, J. L. Jimenez, M. R. Canagaratna, J. D. Allan, H. Coe, I. Ulbrich, M. R. Alfarra, A. Takami, A. M. Middlebrook, Y. L. Sun, K. Dzepina, E. Dunlea, K. Docherty, P. F. DeCarlo, D. Salcedo, T. Onasch, J. T. Jayne, T. Miyoshi, A. Shimo-no, S. Hatakeyama, N. Takegawa, Y. Kondo, J. Schneider, F. Drewnick, S. Borrmann, S. Weimer, K. Demerjian, P. Williams, K. Bower, R. Bahreini, L. Cottrell, R. J. Griffin, J. Rautiainen, J. Y. Sun, Y. M. Zhang, and D. R. Worsnop. Ubiquity and dominance of oxygenated species in organic aerosols in anthropogenically-influenced Northern Hemisphere midlatitudes. *Geophysical Research Letters*, 34(13), 7 2007.

- [179] Y. Zhao and D. G. Truhlar. Density functionals with broad applicability in chemistry. *Accounts of Chemical Research*, 41(2):157–167, 2 2008.
- [180] P. J. Ziemann and R. Atkinson. Kinetics, products, and mechanisms of secondary organic aerosol formation. *Chemical Society Reviews*, 41(19):6582–6605, 9 2012.

# Appendix A

## Abstract for Dummies

Inspired by the xkcd comic “Up Goer Five” (<http://xkcd.com/1133/>), the abstract for this dissertation is presented below “explained using only the ten hundred words people use the most often.”

Some tree smells make more drops in the air than others. This seems weird because these tree smells look the same and should act the same. We have looked at how each tree smell makes drops in the air at night to figure out why they do not act the same. In the middle of the time they are changing to new things they must pick which direction they will go. The ones that pick one direction will stay as air, and the ones that pick the other direction will have many more things to do in their life and will make drops. We like to pretend that all tree smells make the same drops in the air, but this game does not let us know what the air is really like. We hope our study will help make this problem better.



# Appendix B

## Supplementary Information for Chapter 3

### B.1 Computational

Table B.1: Constraints applied to B3LYP/6-31+G\* constrained optimizations of transition states for each type of reaction.

Type of Reaction	bonds constrained (participating in TS)
RO <sub>2</sub> H-shifts	C-H, H-O, O-O
RO <sub>2</sub> Ring Closing	O-O, C-O
RO H-shifts	C-H, H-O
RO Ring Closing	C-O, O-C
RO Decomposition	C-C

## The usage of single-reference ROHF-DLPNO-CCSD(T) method

We have tested whether single-reference methods can be used for our systems by computing four different diagnostic parameters: the T1 values (T1), the largest T2 amplitudes (T2), the difference in the final DLPNO-CCSD(T) energy from using either ROHF or UHF reference wave functions ( $\Delta\text{EROHF-UHF}$ ), and the percentage contribution of the triples correction to the CCSD(T) atomization energy ((T)-%). Generally, larger diagnostic values mean that the system potentially has more multi-reference character. Table B.1 shows that our reaction pathway contains one system (H2ts) for which the diagnostic values are larger than they should be for a single-reference system, i.e.,  $T1 > 0.02$ ,  $T2 > 0.2$  and  $\Delta\text{EROHF-UHF} > 1$  kcal/mol [102, 158]. This indicates that H2ts may have multireference character, and the energies calculated for H2ts might thus be very inaccurate. However, we expect the H2ts reaction to be so slow that despite these large error margins, we can rule out its contribution to any final product formation. Since we do not expect the multireference character of H2ts affect the overall results, and all other diagnostic values are within an acceptable range, the single-reference ROHF-DLPNO-CCSD(T) method can be used for the studied reactions. Additionally, we have assessed the accuracy of the DLPNO-CCSD(T) method for open-shell peroxy radical H-shift reactions similar to those carried out in this study by comparing forward and reverse reaction barriers for a set of four test systems studied previously, as shown in Figure B.1 and Table B.3.

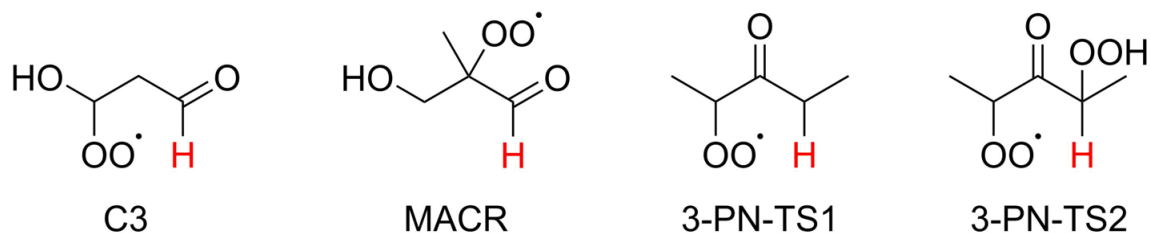


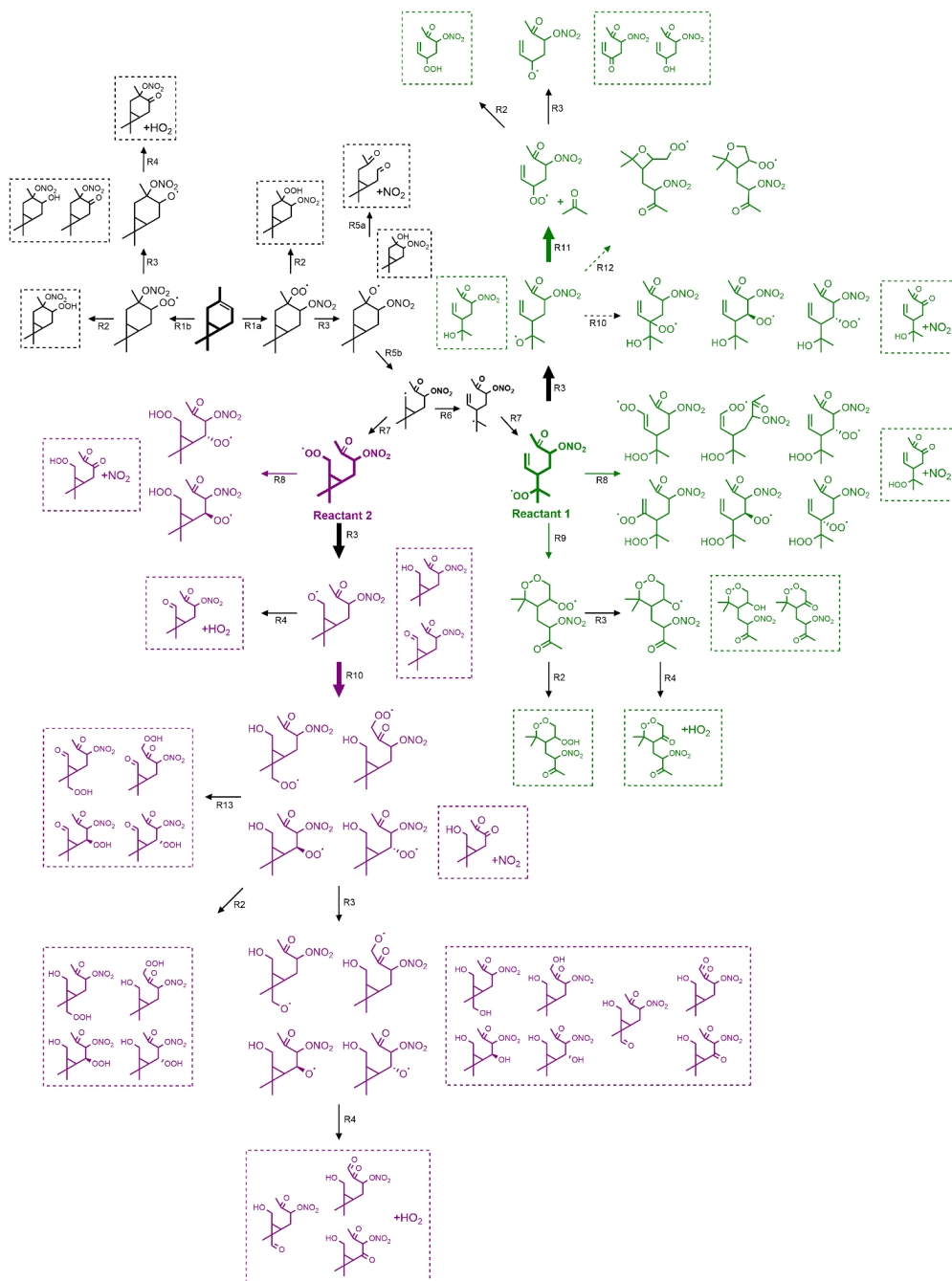
Figure B.1: Structures of the four systems used to assess the accuracy of DLPNO for peroxy H-shift reactions [118]. The hydrogen in red is the one being abstracted in the forward reaction.

Table B.2: T1 values, largest T2 amplitudes,  $\Delta E_{\text{ROHF-UHF}}$  (in kcal/mol) and the triples correction percentage from the atomization energy.

File Name	T1	T2	$\Delta E_{\text{ROHF-UHF}}$	(T)-%
H1p	0.015	0.090	0.00	2.19
H1ts	0.018	0.081	0.06	2.28
H2p	0.015	0.090	0.01	2.20
<b>H2ts</b>	0.029	0.202	1.02	2.43
H3p	0.015	0.090	0.01	2.20
H3ts	0.018	0.086	0.15	2.27
P_RO2add	0.015	0.090	0.01	2.15
P_ROscis	0.017	0.084	0.01	2.04
rH0p_RO	0.016	0.074	0.12	2.02
rH0ts_RO	0.019	0.133	0.47	2.30
rH4ts_RO	0.019	0.120	0.36	2.40
rH5p_RO	0.016	0.073	0.05	2.12
rH5ts_RO	0.019	0.123	0.34	2.04
rH7p_RO	0.015	0.055	0.03	2.08
rH7ts_RO	0.020	0.144	0.50	2.13
rH8p_RO	0.015	0.071	0.01	2.05
rH8ts_RO	0.018	0.103	0.23	2.13
rReactant	0.016	0.078	0.04	2.05
R_ROscis	0.016	0.083	0.03	2.12
R	0.019	0.135	0.12	1.92
TS_RO2add	0.020	0.114	0.53	2.01
TS_ROscis	0.020	0.168	0.76	2.01
H4ts	0.019	0.093	0.15	2.29
H5ts	0.019	0.094	0.08	2.29
H6ts	0.019	0.094	0.53	2.31
H7ts	0.017	0.079	-0.03	2.31
rH4ts	0.018	0.087	0.14	2.27
rH5ts	0.018	0.087	0.12	2.27
rH7ts	0.019	0.095	0.18	2.29
rR	0.019	0.151	0.10	2.15

Table B.3: Forward and reverse reaction barriers as well as reaction energies (product minus reactant) calculated using  $\omega$ B97X-D/aug-cc-pVTZ (abbreviated wB), CCSD(T)-F12a/VDZ-F12// $\omega$ B97X-D/aug-cc-pVTZ (abbreviated F12), and DLPNO-CCSD(T)/def2-QZVPP// $\omega$ B97X-D/aug-cc-pVTZ (abbreviated DLPNO) for a set of four test systems previously studied [118, 26, 27]. The F12 and DLPNO calculations are single-point energy calculations on the  $\omega$ B97X-D/aug-cc-pVTZ geometry. All values include a  $\omega$ B97X-D/aug-cc-pVTZ ZPVE correction.

Level of theory	Forward barrier (kcal/mol)	Reverse barrier (kcal/mol)	Reaction energy (Product minus reactant; kcal/mol)
C3			
wB	18.73	14.04	4.69
F12	19.74	18.11	1.64
DLPNO	20.05	18.15	1.90
MACR			
wB	20.63		
F12	20.26		
DLPNO	21.38		
3-Pentanone-TS1			
wB	24.22	18.99	5.23
F12	23.63	20.26	3.37
DLPNO	24.19	20.71	3.47
3-Pentanone-TS2 (S,S)			
wB	20.22		
F12	20.53		
DLPNO	21.40		
3-Pentanone-TS2 (R,S)			
wB	20.64		
F12	20.78		
DLPNO	21.70		



Scheme B.1: Derived  $\Delta$ -3-carene +  $\text{NO}_3$  reaction mechanism. Black structures and arrows indicate reactions inferred from literature. Green and purple arrows indicate reactions explicitly calculated in this study, while green and purple structures broadly indicate species originating from (bolded) Reactant 1 and Reactant 2, respectively. Bold arrows indicate a pathway is strongly favorable, plain arrows indicate a pathway is competitive but not strongly so, and dashed arrows indicate a pathway is unlikely to be competitive, and all arrows are labeled according to reaction type, as listed in Table S4. Possible closed-shell products are boxed.

Table B.4: Reactions and rate constants (k) included in the full mechanism shown in Scheme B.1 [7, 128, 6, 94, 134, 130]

Label	Reaction	k (298 K)	Reference
R1a,b	$\Delta\text{-3-carene} + \text{NO}_3 \rightarrow \text{O}_2\text{NO-R}$	$9.1 \times 10^{-12}$ $\text{cm}^3 \text{ molecule}^{-1} \text{ s}^{-1}$  Branching ratios: a) 0.65 b) 0.35	Atkinson & Arey <sup>6</sup>
R2	$\text{RO}_2 + \text{HO}_2 \rightarrow \text{ROOH} + \text{O}_2$	$10^{-11}$ $\text{cm}^3 \text{ molecule}^{-1} \text{ s}^{-1}$	Orlando & Tyndall <sup>7</sup>
R3	bimolecular radical propagation reactions:  $\text{RO}_2 + \text{RO}_2 \rightarrow 2\text{RO} + \text{O}_2$ $\quad \quad \quad \rightarrow \text{ROH} + \text{R}'(\text{O}) + \text{O}_2$ $\text{RO}_2 + \text{NO}_3 \rightarrow \text{RO} + \text{NO}_2 + \text{O}_2$	$\text{RO}_2$ : $10^{-12}$ $\text{cm}^3 \text{ molecule}^{-1} \text{ s}^{-1}$  $\text{NO}_3$ : $\sim 10^{-12}$ $\text{cm}^3 \text{ molecule}^{-1} \text{ s}^{-1}$	Orlando & Tyndall <sup>7</sup>
R4	$\text{RO} + \text{O}_2 \rightarrow \text{R}'(\text{O}) + \text{HO}_2$	$9 \times 10^{-15}$ $\text{cm}^3 \text{ molecule}^{-1} \text{ s}^{-1}$	Atkinson <sup>8</sup>
R5a	$\Delta\text{-3-carene O}_2\text{NO-RO C-C scission (right)}$	$\sim 2 \times 10^6 \text{ s}^{-1}$	Kurten et al. <sup>9</sup>
R5b	$\Delta\text{-3-carene O}_2\text{NO-RO C-C scission (left)}$	$\sim 9 \times 10^6 \text{ s}^{-1}$	Kurten et al. <sup>9</sup>
R6	$\Delta\text{-3-carene O}_2\text{NO-R ring opening}$	$\sim 2 \times 10^8 \text{ s}^{-1}$	Kurten et al. <sup>9</sup>
R7*	$\text{R} + \text{O}_2 \rightarrow \text{RO}_2$	$\sim 10^7 \text{ s}^{-1}$	Park et al. <sup>10</sup>
R8	2 <sup>nd</sup> generation $\text{RO}_2$ H-shifts	See Table 1	
R9	2 <sup>nd</sup> generation $\text{RO}_2$ addition	See Table 1	
R10	2 <sup>nd</sup> generation $\text{RO}$ H-shifts	See Table 2	
R11	2 <sup>nd</sup> generation $\text{RO}$ C-C scission (decomposition)	See Table 2	
R12	2 <sup>nd</sup> generation $\text{RO}$ addition	See Table 2	
R13	3 <sup>rd</sup> generation $\text{RO}_2$ $\alpha\text{-OH-H-shift} + \text{O}_2$	estimated competitive	Otkjaer et al. <sup>11</sup>

\*This reaction is only mentioned explicitly twice in Scheme 1, but it is implied for every reaction forming an  $\text{RO}_2$ .

Table B.5: Barrier heights ( $E_b$ ; kcal/mol) and LC-TST rate constants at 298.15 K ( $k$ ;  $s^{-1}$ ) calculated at different levels of theory: B3LYP barriers (B3LYP/6-31+G\* transition state – reactant electronic energy),  $\omega$ B97X-D barriers ( $\omega$ B97X-D/aug-cc-pVTZ zero point corrected transition state – reactant electronic energy), and DLPNO barriers ( $\omega$ B97X-D/aug-cc-pVTZ zero point corrected transition state – reactant electronic energy with single point energy corrections at the ROHF-DLPNO-CCSD(T)/aug-cc-pVTZ level). All rate constants use the  $\omega$ B9X-D/aug-cc-pVTZ partition functions and include an Eckart tunneling coefficient (see Table B.3).

Reaction Description	B3LYP $E_b$	$\omega$ B97X-D $E_b$	$\omega$ B97X-D $k$	DLPNO $E_b$	DLPNO $k$
RO <sub>2</sub> H-shifts (R8 in Table 1)					
Reactant 1 H1	34.0	29.5	$1.0 \times 10^{-9}$	29.0	$5.3 \times 10^{-9}$
Reactant 1 H2	66.4	66.0	$2.6 \times 10^{-30}$	66.1	$5.5 \times 10^{-30}$
Reactant 1 H3	40.3	34.9	$2.3 \times 10^{-13}$	34.3	$6.7 \times 10^{-13}$
Reactant 1 H4	32.0	27.0	$1.9 \times 10^{-7}$	26.8	$2.9 \times 10^{-7}$
Reactant 1 H5	29.8	25.7	$5.8 \times 10^{-6}$	25.7	$5.8 \times 10^{-6}$
Reactant 1 H6	33.0	30.2	$9.1 \times 10^{-6}$	30.7	$4.2 \times 10^{-6}$
Reactant 1 H7	24.5	21.5	$1.0 \times 10^{-1}$	21.7	$8.0 \times 10^{-2}$
Reactant 2 rH4	26.5	23.3	$5.5 \times 10^{-4}$	23.2	$6.4 \times 10^{-4}$
Reactant 2 rH5	29.2	24.2	$2.1 \times 10^{-5}$	24.2	$1.9 \times 10^{-5}$
Reactant 2 rH7	23.9	20.7	$4.3 \times 10^{-1}$	22.2	$5.4 \times 10^{-2}$
RO <sub>2</sub> Ring Closing (R9 in Table 1)					
Reactant 1 6-membered endoperoxide	16.1	19.0	$1.0 \times 10^{-2}$	18.1	$4.7 \times 10^{-2}$
RO H-shifts (R10 in Table 1)					
Reactant 2 rH0	13.7	9.6	$7.8 \times 10^5$	11.8	$3.0 \times 10^4$
Reactant 2 rH4	11.0	7.4	$8.8 \times 10^7$	8.4	$1.8 \times 10^7$
Reactant 2 rH5	12.8	8.5	$8.1 \times 10^6$	9.5	$1.6 \times 10^6$
Reactant 2 rH7	10.7	7.0	$5.6 \times 10^7$	8.8	$3.7 \times 10^6$
Reactant 2 rH8	11.5	7.6	$6.8 \times 10^7$	8.3	$2.3 \times 10^7$
RO Addition (R12 in Table 1)					
Reactant 1 4-membered endo-ether	12.3	--	--	--	--
Reactant 1 5-membered endo-ether	15.7	--	--	--	--
RO decomposition (R11 in Table 1)					
Reactant 1 C-C scission	4.1	5.2	$1.8 \times 10^9$	7.1	$6.6 \times 10^7$

Table B.6: Forward and reverse IRC barriers (kcal/mol) used to calculate the Eckart Tunneling Coefficient. IRC barriers were calculated by correcting the  $\omega$ B97X-D/aug-cc-pVTZ forward/reverse barriers (difference in zero-point corrected energies between the lowest-energy transition state and the lowest-energy – reactant/product) by the difference in energies between the lowest energy reactant or product, and the energy of the reactant or product connected to the transition state, both calculated at the B3LYP/6-31+G\* level.

<b>Reaction Description</b>	<b>IRC forward barrier</b>	<b>IRC reverse barrier</b>	<b>Eckart Tunneling Coefficient</b>
RO <sub>2</sub> H-shifts (R8 in Table 1)			
Reactant 1 H1	27.9	4.5	11.5
Reactant 1 H2	64.7	38.9	$3.5 \times 10^7$
Reactant 1 H3	29.5	8.8	20.6
Reactant 1 H4	22.9	9.0	53.8
Reactant 1 H5	21.3	8.8	53.0
Reactant 1 H6	25.1	28.7	$2.6 \times 10^5$
Reactant 1 H7	20.2	45.7	$4.2 \times 10^3$
Reactant 2 rH4	23.3	11.6	134.2
Reactant 2 rH5	23.3	6.1	29.7
Reactant 2 rH7	20.7	51.4	$6.7 \times 10^3$
RO <sub>2</sub> Ring Closing (R9 in Table 1)			
Reactant 1 6-membered endoperoxide	15.6	16.2	1.5
RO H-shifts (R10 in Table 1)			
Reactant 2 rH0	9.2	20.5	38.6
Reactant 2 rH4	8.5	14.9	16.5
Reactant 2 rH5	8.2	12.6	17.3
Reactant 2 rH7	8.4	61.9	23.5
Reactant 2 rH8	8.4	14.1	17.8
RO decomposition (R11 in Table 1)			
Reactant 1 C-C scission	7.1	24.9	1.4



## B.2 Experimental

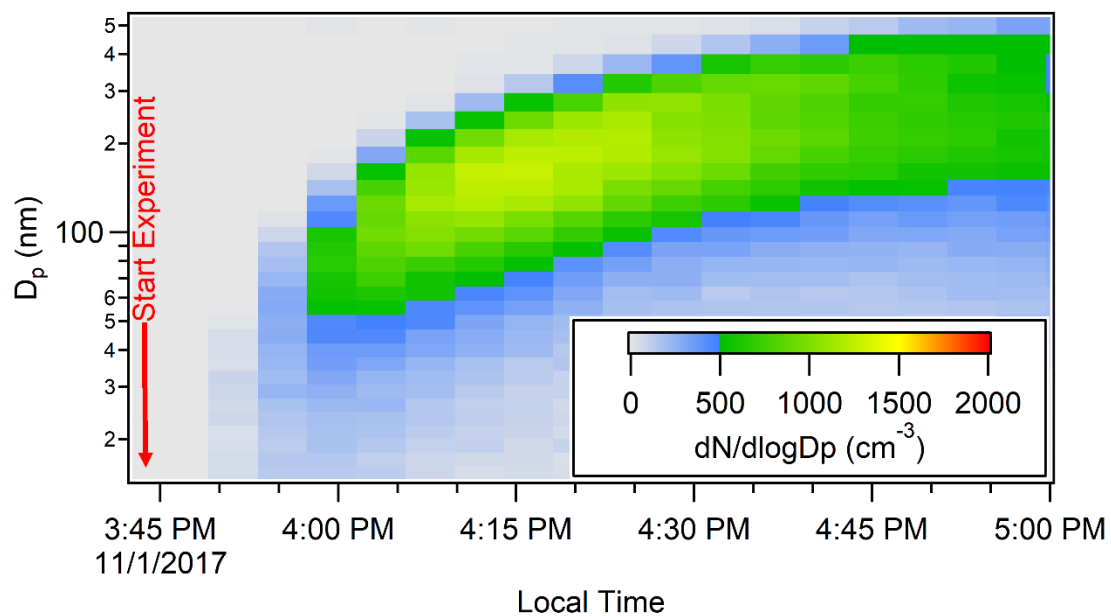


Figure B.2: Particle size distribution during an  $\text{NO}_3 + \Delta\text{-3-carene}$  experiment. Experiment was unseeded and thus particle formation and growth is initiated by gas-phase chemistry.

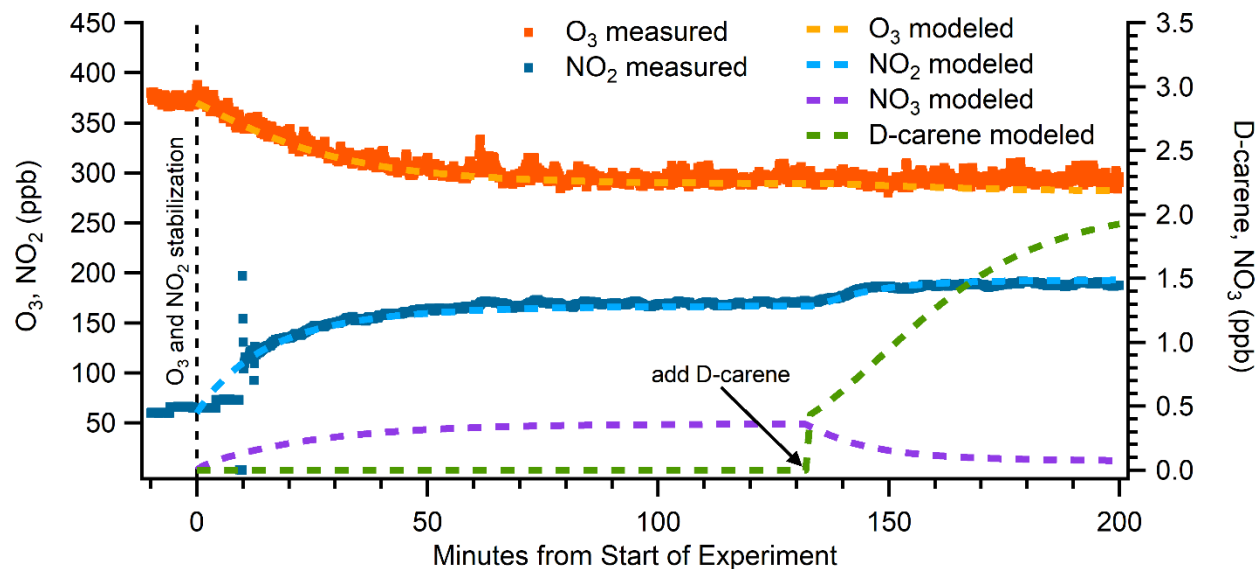


Figure B.3: Kinetics model prediction of trace gas evolution during an  $\text{NO}_3 + \Delta\text{-3-carene}$  experiment using home built model described in detail in Draper et al. [35]. Model agrees well with measurements when available (i.e.  $\text{O}_3$  and  $\text{NO}_2$ ). Particle size distribution during an  $\text{NO}_3 +$  experiment. Experiment was unseeded and thus particle formation and growth is initiated by gas-phase chemistry.

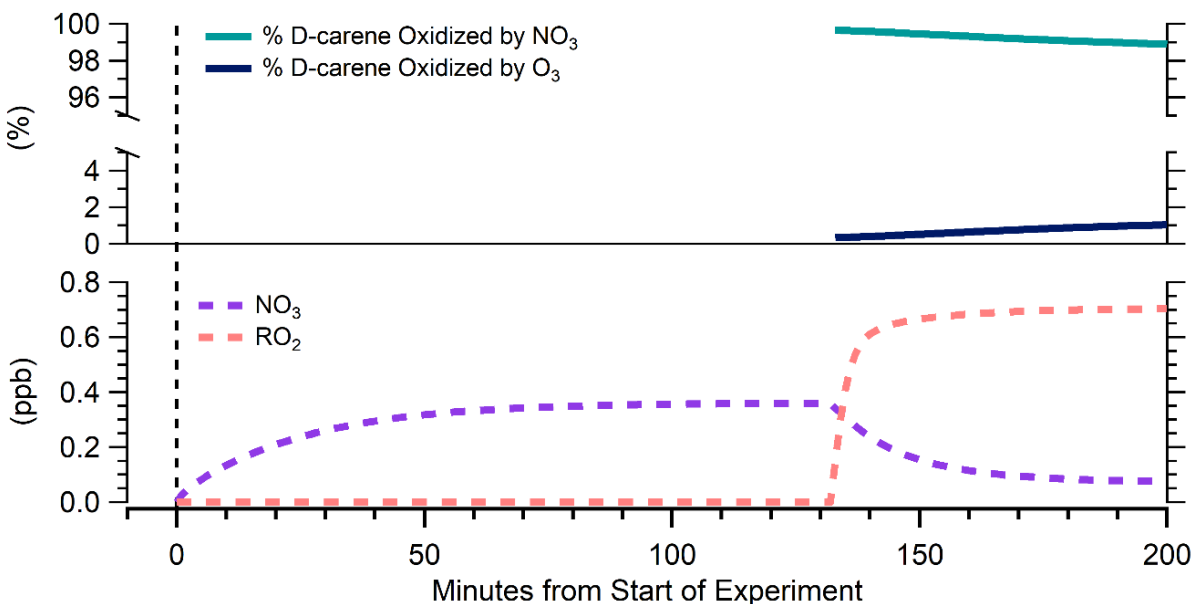


Figure B.4: Additional kinetics modeling results showing that  $>98\%$  of  $\Delta\text{-3-carene}$  was oxidized by  $\text{NO}_3$  during  $\text{NO}_3$  experiments (where  $\text{NO}_3$  was generated via reaction of  $\text{O}_3$  and  $\text{NO}_2$ ), so we expect negligible contribution from  $\Delta\text{-3-carene} + \text{O}_3$  products (top), and predicted concentrations of the two dominant bimolecular radical sinks for  $\text{RO}_2$  in these chamber experiments (bottom).

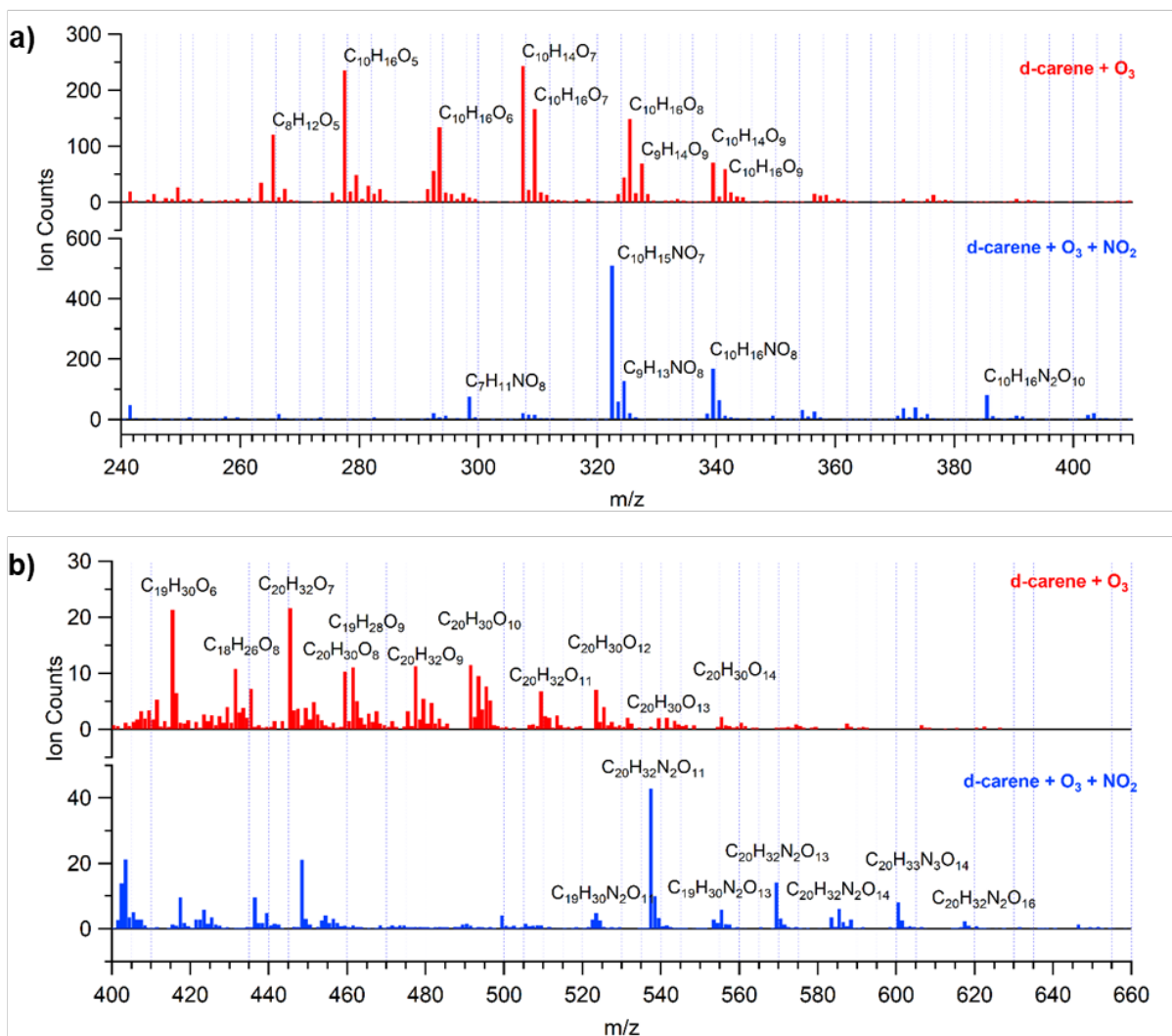


Figure B.5: Comparison of  $\text{NO}_3^-$  CIMS spectra obtained during  $\text{O}_3 + \Delta\text{-3-carene}$  experiments (red) and  $\text{NO}_3 + \Delta\text{-3-carene}$  experiments (blue) confirming that  $\text{NO}_3 + \Delta\text{-3-carene}$  experiments have negligible effect from  $\Delta\text{-3-carene}$  ozonolysis. Several identified peaks are labeled in the monomer region (a) and dimer region (b).

Table B.7:  $\text{NO}_3^-$  CIMS high resolution (HR) peak list from  $\Delta$ -3-carene +  $\text{NO}_3$  experiment.

m/z	HR peak ID ( $\text{NO}_3^-$ cluster)	Product Formula ( $\text{NO}_3^-$ subtracted)	Normalized Average Peak Intensity
61.9878	NO3	(reagent ion)	0.566234
124.983	NO3(HNO3)	(reagent ion)	0.212594
323.073	C10H15N2O10	C10H15NO7	0.0406579
340.075	C10H16N2O11	C10H16NO8	0.0141936
325.052	C9H13N2O11	C9H13NO8	0.00855313
386.068	C10H16N3O13	C10H16N2O10	0.00584364
538.188	C20H32N3O14	C20H32N2O11	0.0058255
299.036	C7H11N2O11	C7H11NO8	0.0056182
341.047	C9H13N2O12	C9H13NO9	0.0027949
372.065	C10H16N2O13	C10H16NO10	0.0027374
341.083	C10H17N2O11	C10H17NO8	0.00249576
355.062	C10H15N2O12	C10H15NO9	0.00238796
357.078	C10H17N2O12	C10H17NO9	0.00180811
339.068	C10H15N2O11	C10H15NO8	0.00165636
404.042	C9H14N3O15	C9H14N2O12	0.00162291
570.178	C20H32N3O16	C20H32N2O13	0.00151544
295.078	C9H15N2O9	C9H15NO6	0.0015102
374.068	C9H16N3O13	C9H16N2O10	0.00144452
374.081	C10H18N2O13	C10H18NO10	0.00140622
309.057	C9H13N2O10	C9H13NO7	0.00138411
267.046	C7H11N2O9	C7H11NO6	0.00131115
293.062	C9H13N2O9	C9H13NO6	0.00121794
326.072	C10H16NO11	C10H16O8	0.00120147
403.071	C10H17N3O14	C10H17N2O11	0.00112153
308.062	C10H14NO10	C10H14O7	0.00106661
601.184	C20H33N4O17	C20H33N3O14	0.000994894
391.071	C9H17N3O14	C9H17N2O11	0.000954367
586.173	C20H32N3O17	C20H32N2O14	0.000711924
437.068	C14H17N2O14	C14H17NO11	0.000688006
418.058	C10H16N3O15	C10H16N2O12	0.000662835
556.163	C19H30N3O16	C19H30N2O13	0.000572091
524.173	C19H30N3O14	C19H30N2O11	0.000527701
554.183	C20H32N3O15	C20H32N2O12	0.000396236
523.178	C20H31N2O14	C20H31NO11	0.000372292
584.158	C20H30N3O17	C20H30N2O14	0.000365971
491.188	C20H31N2O12	C20H31NO9	0.000278355
423.065	C14H17NO14	C14H17O11	0.000266776
500.064	C14H18N3O17	C14H18N2O14	0.000263211
187.979	NO3(HNO3)2	(reagent ion)	0.000241605
618.163	C20H32N3O19	C20H32N2O16	0.000189133
424.073	C14H18NO14	C14H18O11	0.000178714
490.204	C20H32N3O11	C20H32N2O8	0.000169137
250.056	C8H12NO8	C8H12O5	0.000149432
647.153	C20H31N4O20	C20H31N3O17	0.000126088
496.167	C19H30NO14	C19H30O11	0.000031383

### B.3 NO<sub>3</sub><sup>-</sup> Clustering Calculations

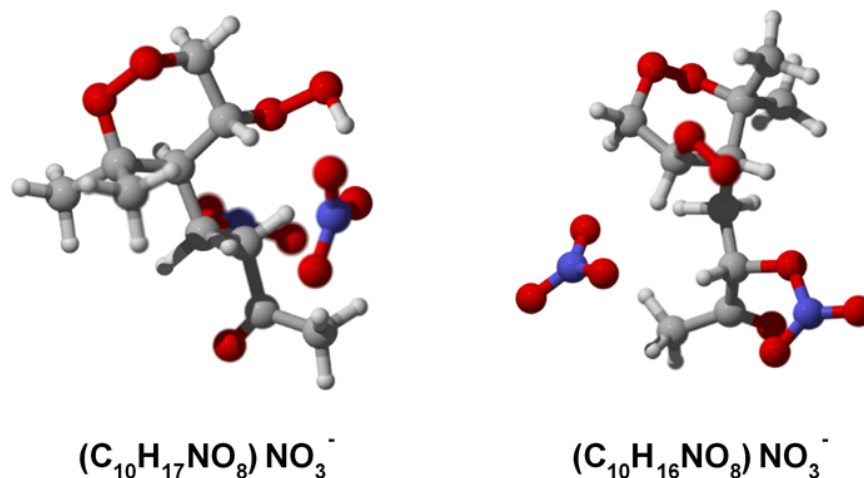



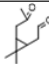
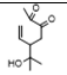
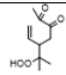
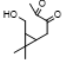
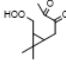
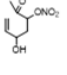
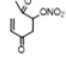
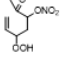
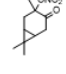
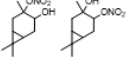
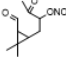
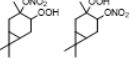
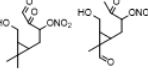
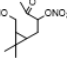
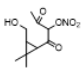
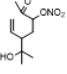
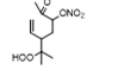
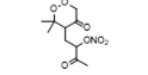
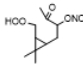
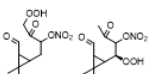
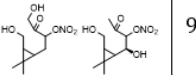
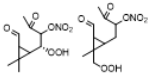
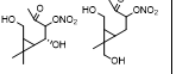
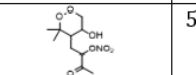
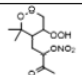
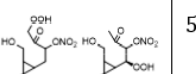
Figure B.6: Optimized  $\omega$ B97X-D//6-31++G\*\* geometries of NO<sub>3</sub><sup>-</sup> clusters tested, including a closed-shell ROOH (C<sub>10</sub>H<sub>17</sub>NO<sub>8</sub>) and its corresponding open-shell RO<sub>2</sub> (C<sub>10</sub>H<sub>16</sub>NO<sub>8</sub>). For the ROOH, clustering is driven mainly by H-bonding of the single -OOH group, whereas for the RO<sub>2</sub>, clustering is driven by a combination of weaker intramolecular forces (i.e. dipole-dipole interactions) since the RO<sub>2</sub> lacks any H-bond donors.

Table B.8: Electronic energy differences ( $\Delta E$ ) at the  $\omega$ B97X-D/6-31+G\*,  $\omega$ B97X-D/6-31++G\*\*, and ROHF-DLPNO-CCSD(T)/aug-cc-pVTZ// $\omega$ B97X-D/6-31++G\*\* (abbreviated as “DLPNO”) levels of theory for the clustering reactions of NO<sub>3</sub><sup>-</sup> with HNO<sub>3</sub> as well as the ROOH and RO<sub>2</sub> shown in Figure B.5. The (ROOH)NO<sub>3</sub><sup>-</sup> cluster is several kcal/mol more strongly bound than the (HNO<sub>3</sub>)NO<sub>3</sub><sup>-</sup> cluster and therefore will be detectable in the NO<sub>3</sub><sup>-</sup> CIMS. The NO<sub>3</sub><sup>-</sup> cluster is only slightly more strongly bound than the (HNO<sub>3</sub>)NO<sub>3</sub><sup>-</sup> cluster, so it is likely detectable with the NO<sub>3</sub><sup>-</sup> CIMS, but with lower sensitivity.

NO <sub>3</sub> <sup>-</sup> cluster with:	$\omega$ B97X-D/6-31+G* $\Delta E$ (kcal/mol)	$\omega$ B97X-D/6-31++G** $\Delta E$ (kcal/mol)	DLPNO $\Delta E$ (kcal/mol)
HNO <sub>3</sub>	-29.8	-30.8	-29.4
C <sub>10</sub> H <sub>17</sub> NO <sub>8</sub> (ROOH)	-36.8	-37.2	-37.9
C <sub>10</sub> H <sub>16</sub> NO <sub>8</sub> (RO <sub>2</sub> )	-30.4	-31.3	-31.5

## B.4 Estimated vapor pressures

Table B.9: Vapor pressure ( $P_{\text{vap}}$ ) estimates for predicted closed-shell molecules at 298 K using SIMPOL.1 [133].

Name	Structure	$P_{\text{vap}}$ (torr)	Name	Structure	$P_{\text{vap}}$ (torr)
$\Delta$ -3-carene		2.1	$\text{C}_{10}\text{H}_{16}\text{O}_2$		$1.6 \times 10^{-2}$
$\text{C}_{10}\text{H}_{16}\text{O}_3$		$2.1 \times 10^{-4}$	$\text{C}_{10}\text{H}_{16}\text{O}_4$		$1.1 \times 10^{-4}$
		$2.5 \times 10^{-4}$			$1.4 \times 10^{-4}$
$\text{C}_7\text{H}_{11}\text{NO}_5$		$2.2 \times 10^{-4}$	$\text{C}_7\text{H}_9\text{NO}_5$		$3.8 \times 10^{-3}$
$\text{C}_7\text{H}_{11}\text{NO}_6$		$1.2 \times 10^{-4}$	$\text{C}_{10}\text{H}_{15}\text{NO}_4$		$2.0 \times 10^{-3}$
$\text{C}_{10}\text{H}_{17}\text{NO}_4$		$1.2 \times 10^{-4}$	$\text{C}_{10}\text{H}_{15}\text{NO}_5$		$1.0 \times 10^{-4}$
$\text{C}_{10}\text{H}_{17}\text{NO}_5$		$6.4 \times 10^{-5}$	$\text{C}_{10}\text{H}_{15}\text{NO}_6$		$6.8 \times 10^{-7}$
		$1.3 \times 10^{-5}$			$1.6 \times 10^{-6}$
		$1.3 \times 10^{-5}$			
$\text{C}_{10}\text{H}_{17}\text{NO}_6$		$6.4 \times 10^{-6}$	$\text{C}_{10}\text{H}_{15}\text{NO}_7$		$1.0 \times 10^{-4}$
		$7.8 \times 10^{-6}$			$3.7 \times 10^{-7}$
		$9.2 \times 10^{-8}$			
					
$\text{C}_{10}\text{H}_{17}\text{NO}_7$		$5.7 \times 10^{-6}$	$\text{C}_{10}\text{H}_{17}\text{NO}_8$		$3.2 \times 10^{-6}$
		$5.1 \times 10^{-8}$			